UNIVERSITY OF BRASÍLIA

INSTITUTE OF PHYSIC

Laboratório de Síntese de Nanomateriais e Caracterização Magnética-LSNCM

Programa de Pós-Graduação em Física

Tuning the physical properties in Fe doped ITO films by controlling intrinsic and extrinsic defects

Ajustando as propriedades físicas em filmes de ITO dopados com Fe através do controle de defeitos intrínsecos e extrínsecos

Doctoral Thesis

Carlos Adolfo Vilca Huayhua

Brasília-DF

2026

UNIVERSITY OF BRASÍLIA

INSTITUTE OF PHYSIC

Laboratório de Síntese de Nanomateriais e Caracterização Magnética-LSNCM

Programa de Pós-Graduação em Física

Carlos Adolfo Vilca Huayhua

Tuning the physical properties in Fe doped ITO films by controlling intrinsic and extrinsic defects

Ajustando as propriedades físicas em filmes de ITO dopados com Fe através do controle de defeitos intrínsecos e extrínsecos

Doctoral thesis presented as a partial requirement for the degree of doctor in Physics, from the Graduate Program in Physics of the University of Brasília.

Advisor: Dr. José Antonio Huamani Coaquira
Co-advisor: Dr. Fermin Fidel Herrera Aragón

Brasília-DF

2026

CARLOS ADOLFO VILCA HUAYHUA

TUNING THE PHYSICAL PROPERTIES IN FE DOPED ITO FILMS BY CONTROLLING INTRINSIC AND EXTRINSIC DEFECTS
AJUSTANDO AS PROPRIEDADES FÍSICAS EM FILMES DE ITO DOPADOS COM FE ATRAVÉS DO CONTROLE DE DEFEITOS INTRÍNSECOS E EXTRÍNSECOS

Thesis presented as a partial requirement for obtaining the title of Doctor of Physics, from the University of Brasília, approved by the Committee formed by professors:

Prof. Dr. José Antonio Huamani Coaquira
University of Brasília, UnB

Prof. Dr. Ricardo Gargano
University of Brasília, UnB

Prof. Dr. Luiz Carlos Camargo Miranda Nagamine
University of São Paulo, USP

Prof. Dr. Ramón Raudel Peña Garcia
Universidade Federal Rural de Pernambuco,
UFRPE

Brasília, March 05, 2026

Este trabajo esta dedicado a mi familia

Acknowledgements

Estou profundamente grato aos professores José A. H. Coaquira e Fermín F. H. Aragón pela confiança e apoio que depositaram em mim ao longo de todo este processo. A sua experiência e apoio foram fundamentais para o desenvolvimento desta investigação. Aprendi muito sobre física exponencialmente.

Estou grato à minha família por todo o sacrifício e apoio incondicional ao longo da minha vida. Eu não teria conseguido sem todos vós.

Estou grato à minha querida e traumatizada Lizz, que me acompanhou durante os meus estudos de pós-graduação. Apesar da distância, senti como se ela estivesse sempre ao meu lado.

Aos meus amigos e colegas de laboratório, Bill, Joel, Sonia, Chilo, Cristel, Emanuel, Jessica, Israel, João, John, Juliani, Lucas e JR, pela amizade e colaboração.

Estou grato ao Professor Sebastião pelo apoio e pela disponibilidade dos equipamentos do seu laboratório, que foram importantes na seleção dos parâmetros físicos iniciais utilizados neste trabalho.

Agradeço ao Professor Leonardo Villegas e ao Luis Ribeiro a colaboração nas simulações de primeiros princípios. Agradeço também ao Professor J.A. Guerra por me ter proporcionado a oportunidade de desenvolver e caracterizar filmes no seu laboratório, e aos seus alunos que me ajudaram a aprender novas e robustas ferramentas e técnicas de investigação.

Agradeço ao Professor Alysson M. Almeida Silva, Waldemar A. de Almeida Macedo pelas medias XPS

Expresso minha gratidão ao CNPq e à CAPES, agências brasileiras de fomento à pesquisa, pela bolsa de doutorado..

Para que pelear por un pedazo de tierra,
si tenemos todo un universo para invadir
(Carlos Vilca)

Abstract

Transparent conducting magnetic oxides, such as transition-metal–doped indium tin oxide (ITO), have attracted growing interest for their potential applications in optoelectronic and spintronic devices, due to the high charge carrier density and the possibility of achieving room-temperature ferromagnetism. In this thesis, we report a comprehensive study of physical properties of Sn doped In_2O_3 and Fe-doped ITO thin films grown by the sputtering technique. Firstly, the critical concentration of tin was investigated, where the characterization of optical and electrical properties demonstrated that Sn exhibits good solubility within the In_2O_3 matrix without the formation of secondary phases, showing a uniform distribution of atoms throughout the film. Hall effect measurements revealed that a ~10% Sn concentration yielded the highest density of n-type charge carriers, attributed to the effective substitution of In^{3+} ions for Sn^{4+} in the lattice. Additionally, thermal annealing carried out in vacuum controlled levels led to the controlled formation of oxygen vacancies, removal of interstitial oxygen, and V_O–Sn defect migration, which is an essential issue for the enhancing of the conductivity of ITO compound. The increase in charge carrier density caused a shift of the Fermi level towards and above the conduction band, resulting in a highly degenerate transparent conductive oxide. This effect was accompanied by a widening of the optical bandgap in accordance with the Burstein-Moss model. These results are consistent with computational models based on the density functional theory (DFT).

Subsequently, upon the introduction of Fe ions at low concentrations (<4%), the ITO films preserved their cubic bixbyite structure, exhibiting a good Fe solubility within the lattice, as evidenced by X-ray diffraction (XRD). The optical bandgap was reduced due to the emergence of Fe-related localized states and intrinsic defects inside the gap. Therefore, the Fe doping introduced an additional degree of freedom, thereby altering the electrical properties and giving rise to the coexistence of weak ferromagnetism and paramagnetism at room temperature. These properties showed a strong dependence on temperature and atmosphere of thermal annealing. In this context, the annealing in an air atmosphere facilitated oxygen diffusion at the surface, leading to a saturation magnetization reduction and affecting the electrical conductivity. In contrast, high-vacuum annealing promoted the formation of oxygen vacancies, which enhanced room-temperature ferromagnetism due to the formation of bound magnetic polarons. Furthermore, low-temperature resistivity measurements revealed an anomalous resistivity behavior caused by interactions between Fe-localized states and conduction electrons. Additionally, the presence of Fe-related electronic states influenced the methane gas sensing properties and the UV-light-induced photocurrent, significantly improving their sensitivity. These findings suggest that Sn/Fe co-doped In_2O_3 films exhibit strong potential for a wide range of technological applications.

keywords: Fe doped ITO thin films; engineering defects; Room temperature ferromagnetism; impedance; gas sensor; photocurrent.

Resumo

Óxidos magnéticos condutores transparentes, como o óxido de índio-estanho (ITO) dopado com metais de transição, têm despertado crescente interesse devido às suas potenciais aplicações em dispositivos optoeletrônicos e espintrônicos, em razão da elevada densidade de portadores de carga e da possibilidade de se obter ferromagnetismo à temperatura ambiente. Nesta tese, é apresentado um estudo abrangente das propriedades físicas de filmes finos de In_2O_3 dopados com Sn e de ITO dopado com Fe, crescidos pela técnica de sputtering. Inicialmente, foi investigada a concentração crítica de estanho, na qual foram observadas propriedades ópticas e elétricas ótimas, demonstrando que o Sn apresenta boa solubilidade na matriz de In_2O_3 sem a formação de fases secundárias, com uma distribuição uniforme dos átomos em todo o filme. Medidas de efeito Hall revelaram que uma concentração de $\sim$10% de Sn resultou na maior densidade de portadores de carga do tipo n, atribuída à substituição efetiva de íons In^{3+} por íons Sn^{4+} na rede cristalina. Além disso, variações na pressão de vácuo durante o recozimento térmico levaram à formação de vacâncias de oxigênio, à remoção de oxigênio intersticial e à migração de defeitos do tipo V_O–Sn, processos essenciais para o aumento da condutividade do ITO. O incremento na densidade de portadores de carga provocou um deslocamento do nível de Fermi acima da banda de condução, resultando em um óxido condutor transparente altamente degenerado. Esse efeito foi acompanhado por um alargamento da banda proibida óptica, em concordância com o modelo de Burstein-Moss. Esses resultados são consistentes com modelos computacionais baseados na teoria do funcional da densidade (DFT).

Posteriormente, com a introdução de íons Fe em baixas concentrações (<4%), os filmes de ITO preservaram sua estrutura cúbica do tipo bixbyita, apresentando boa solubilidade na rede cristalina, conforme evidenciado por difração de raios X (DRX). A banda proibida óptica foi reduzida devido ao surgimento de estados localizados associados ao Fe e a defeitos intrínsecos dentro da banda proibida. Portanto, a dopagem com Fe introduziu um grau adicional de liberdade, alterando as propriedades elétricas e provocando a coexistencia de ferromagnetismo fraco e paramagnetismo à temperatura ambiente. Essas propriedades mostraram forte dependência na temperatura e atmosfera de tratamento térmico. Nesse contexto, tratamentos térmicos em atmosfera de ar facilitaram a difusão de oxigênio na superfície, reduzindo a magnetização de saturação e afetando a condutividade elétrica. Em contraste, o recozimento em alto vácuo promoveu a geração de vacâncias de oxigênio, o que intensificou o ferromagnetismo à temperatura ambiente devido à formação de polarons magnéticos ligados. Além disso, análises de resistividade em baixas temperaturas revelaram um comportamento anômalo da resistividade, causado pela interação entre estados localizados do Fe e elétrons de condução. Adicionalmente, a presença de estados eletrônicos relacionados ao Fe influenciou as propriedades de detecção de gás metano e a fotocorrente induzida por luz UV, melhorando significativamente sua sensibilidade. Esses

resultados indicam que filmes de In_2O_3 codopados com Sn e Fe apresentam grande potencial para uma ampla gama de aplicações tecnológicas.

Palavras-chave: Filmes finos de ITO dopados com Fe; engenharia de defeitos; ferromagnetismo à temperatura ambiente; impedância; sensor de gás; fotocorrente

List of figures

Figure 2.2.1–(a) Magnetic semiconductor, (b) non-magnetic semiconductor, (c) DMS dilute magnetic semiconductor. "Source: Author's own elaboration." 35

Figure 2.3.1–(a) Indium Oxide (b) Indium Tin Oxide, (c) Iron doped Indium Tin Oxide. "Source: Author's own elaboration". 37

Figure 2.4.1–(a) Crystal structures of In_2O_3 showing the occupational sites (b-site and d-site) of In, (b) Occupation of Sn^{4+} in the two sites b and d forming a complex in combination with an interstitial oxygen (O_i). "Source: Author's own elaboration." 38

Figure 2.6.1–(a) Real (Re Z) and complex (-Im Z) part impedance diagrams, (b) impedance as a function of frequency, the inset shows the equivalent circuit representing the impedance curves. 42

Figure 2.7.1–(a) Dependence of resistivity on temperature for semiconductor systems (blue lines) and metals (red lines), (b) band model for metallic and semiconductor behavior, N_F represents the Fermi level. "Source: Author's own elaboration." 44

Figure 2.8.1–(a) Transmittance spectra measured in the UV-vis and infrared regions, inset: refractive index and absorption coefficient as a function of wavelength. "Source: Author's own elaboration". 46

Figure 2.8.2–Trajectory of a electron scattering off the ion, according to the Drude model. 48

Figure 2.9.1–Representation of two linked magnetic polarons generated by oxygen vacancies. "Source: Author's own elaboration". 53

Figure 2.10.1–(a) Schematic diagram showing the reaction on the surface of the material grains in the presence of atmospheric oxygen and (b) Photocurrent curves, the lead-colored bands, represent when UV light is off. 54

Figure 2.11.1–(a) Diagram showing the reaction on the surface of the material grains in the presence of atmospheric oxygen and (b) after the reaction of the surface with the gas to be measured. "Source: Author's own elaboration". 55

Figure 3.1.1–Schematic of the manufacturing process for In and Sn metal targets. 57

Figure 3.1.2–Commercial two-inch targets (a) In_2O_3(90%)/SnO_2(10% wt.) (b) Metallic Fe. 57

Figure 3.2.1–(a) Vacuum sputtering station, (b) magnetrons used for co-sputtering deposition, (c) films deposited on substrates. 58

Figure 4.1.1–(a) XRD patterns of the different $(In_{1-x}Sn_x)_2O_3$ films (x=0, 0.05, 0.10, 0.12, 0.15). (b) Rietveld Refinement fit for the In_2O_3 doped with 5%Sn.The blue circles represent the experimental data Y_{Obs}, the orange line represents the fit Y_{Cal}, the green line the difference between Y_{Obs}-Y_{Cal}, the pink line is the phase of In_2O_3 and the sky blue line is a metallic phase of indium. 66

Figure 4.1.2 – Lattice constant as a function of Sn concentration. Data reported by Park *et al.* (PARK et al., 2011) and Binczycka *et al.* (BINCZYCKA et al., 2005) are included for comparison. The dashed line is a guide to the eye. 67
Figure 4.1.3 – (a) Atomic distribution of elements of Sn-doped In_2O_3 along the film (b) chemical composition by EDS and XRD analysis for the films with different nominal Sn concentrations (0, 5, 10, 12, 15%). 69
Figure 4.1.4 – AFM images of films for different concentrations of Sn (a) 0% , (b) 4.9% , (c) 7.6%, (d) 10.7%, (b) 12.2% Sn. 70
Figure 4.1.5 – XPS spectra of films for different concentrations of Sn (a) Survey, (b) O 1s orbital, (c) Tin (Sn) peaks related to $3d_{3/2}$ and $3d_{5/2}$ orbitals, (d) indium (In) peaks related to $3d_{3/2}$ and $3d_{5/2}$ orbitals. 71
Figure 4.1.6 – Charge carrier measurements obtained by Hall effect for In_2O_3 films doped with different Sn concentrations. Experimental results were included: Khan et al. (KHAN et al., 2020), Khan et al. (KHAN et al., 2022), Sato et al. (SATO et al., 2010) Wen et al. (WEN et al., 1992). 73
Figure 4.1.7 – UV-vis transmittance spectra obtained for Sn doped In_2O_3. A good fited transmittance spectra are represented by the solid red lines using the Tauc Lorentz and Hamberg models. 75
Figure 4.1.8 – (a) Bandgap, the light blue line represents the value of the bandgap bulk for In_2O_3. (b) Urbach energy for In_2O_3 and Sn doped In_2O_3 films, the red inset line shows the fit over the absorption region using the band fluctuation model. 76
Figure 4.1.9 – (a) Photocurrent response of the 4.9% Sn-doped In_2O_3 thin film under UV illumination (light ON, sky blue). The inset shows the photoresponse (PR) extracted for all films. (b) Gas sensing response to methane (CH_4) at an operating temperature of 200 °C. The inset presents the corresponding gas sensing response (GSR) for the different films. 78
Figure 4.1.10 – (a) In_2O_3 crystal structure doped with 9.24 % Sn, (b) In_2O_3 structures doped with 12.4 % Sn, with a contribution of 2.1% O^{int}; and (c) In_2O_3 doped with 12.4 % Sn with a contribution of 4.2% O^{int} obtained by DFT. 80
Figure 4.1.11 – Band structure for In_2O_3 with different Sn concentration (a) 0% Sn (b) 1Sn ~ 3.1% Sn, (c) 3Sn ~ 9.4% Sn, (d) 9.4% Sn + 2.1% O^{int}, (e) 12.5% Sn + 2.1% O^{int}, (f) 12.5% Sn + 4.2% O^{int}, the dashed red line represent the position of Fermi level. 80
Figure 4.1.12 – Calculated Projected density of states PDOS for In_2O_3 doped (a) 0% Sn, (b) 3.1% Sn, (c) 9.4% Sn, (d) 9.4% Sn + 2.1% O^{int}, (e) 12.5% Sn + 2.1% O^{int}, (f) 12.5% Sn + 4.2% O^{int}, the dashed red line represent the position of Fermi level. 82
Figure 4.1.13 – (a) Electronic transition values between the valence band and the Fermi energy $(E_F - E_V)$, (b) Charge carriers obtained from Equation 57 for Sn-doped In_2O_3 systems obtained by DFT calculation. 83

Figure 4.2.1–XPS survey spectrum of ITO films annealed at different temperatures. . . . 86
Figure 4.2.2–(a) High-resolution for O 1s, (b) Sn 3d, (c) In 3d peak. (d) The variation of areal ratio of oxygen vacancies and (e) areal ratio of Sn^{4+} as a function of annealing temperature. 87
Figure 4.2.3–(a) XRD patterns of the ITO films and their corresponding Rietveld refinements. The black spheres denote the experimental intensities (Y_{Obs}), while the orange line represents the calculated profile (Y_{Cal}). The green line represents the difference $Y_{\mathrm{Obs}} - Y_{\mathrm{Cal}}$. The blue markers indicate the Bragg positions of the cubic In_2O_3 phase. 88
Figure 4.2.4–(a) Lattice parameter (a) and (b) average crystallite size ($< D >$) at annealing temperature function, inset shown the ratio texture from 440/222 plane . . . 90
Figure 4.2.5–Charge carrier measurements obtained by Hall (N_{Hall}) and electrical resistivity (ρ) for ITO films annealed at different temperatures. 91
Figure 4.2.6–UV-Vis-NIR transmittance spectra obtained for ITO; the red lines show the fit of the transmittance spectra using the Tauc-Lorentz and Hamberg models. The gray color curve represents the substrate transmittance. 92
Figure 4.2.7–Optical constants obtained from fitting the T-L/Hamberg model, (a) refractive index (n) as a function of wavelength, inset shows the dependence of n on the annealing temperature, for wavelengths of 632 and 2500nm, (b) extinction coefficient (k) as a function of wavelength, inset shows k as a function of the number of carriers. 93
Figure 4.2.8–(a) Optical bandgap (E_g^{Opt}) vs. N_{Hall} funtion, the inset shows the fit over the absorption region using the BF method. (b) Urbach energy (E_U) as a function of annealing temperature 94
Figure 4.2.9–Photocurrent curves as a function of time for the ITO:AG film. The shaded regions indicate the intervals during which the sample was exposed to UV light. (b) Percent photoresponse (PR) as a function of annealing temperature; the inset shows the dependence of the PR on the Sn^{2+} and V_O defects. . . . 96
Figure 4.2.10–The photocurrent curves show the exponential fit of the decay curve using Equation 62. 97
Figure 4.3.1–Scanning electron microscopy (SEM) images of the cross-sections of Sn-doped In_2O_3 films annealed at different vacuum pressures at 600° for 2 hours, as shown in (a) air atmosphere, (b) 1×10^{0} mbar, (c) 2.3×10^{-1} mbar, (d) 2.3×10^{-2} mbar, (e) 5.0×10^{-5} mbar, and (f) 2.3×10^{-6} mbar. 101
Figure 4.3.2–3D AFM images of Sn doped In_2O_3 films annealed at different pressures (a) air atmosphere, (b) 1×10^{0} mbar, (c) 2.3×10^{-1} mbar, (d) 5.0×10^{-5} mbar, and (e) 2.3×10^{-6} mbar. 102

Figure 4.3.3 (a) X-ray diffraction patterns of Sn-doped In_2O_3 films annealed at various pressures. The as-grown (AG) XRD pattern is included for comparison. (b) Rietveld refinement of the sample annealed at 10^{-6} mbar. 103
Figure 4.3.4 Dependence of mean crystallite size on lattice parameters, with the arrow indicating an increase in the vacuum pressure (VP). 104
Figure 4.3.5 UV-visible transmittance measurements of ITO thin films subjected to various vacuum pressures during thermal treatment. The inset displays the main near-infrared region with wavelength from 1000 to 2400 nm spectra. 106
Figure 4.3.6 (a) Dependence of bandgap energy on increasing vacuum pressures, compared with the bandgap of In_2O_3 (~3.6 eV (KHAN et al., 2012)), showing higher values for ITO films. The inset illustrates the band fluctuation model for a vacuum of 10^{-6} mbar. (b) Urbach energy variation as a function of vacuum pressure. The error bars were derived from analyses of approximately 10 different regions in the absorption spectrum. 107
Figure 4.3.7 (a) Variation in resistivity and carrier concentration (n) based on electrical measurements as a function of the vacuum pressure. (b) γ parameters versus VP assessed via equation 3. The mobility (μ) obtained from optical and Hall effect measurements is displayed in the inset. The dashed lines are shown only as a guide to the eye. 109
Figure 4.3.8 (a) Photocurrent as a function of time under alternating light and dark conditions for the sample annealed at a vacuum of 1.0×10^{-2} mbar. (b) Photosensitivity (PS = I_{Light}/I_{Dark}) as a function of crystallite size, showing a decrease in PS with increasing crystallite size. The inset shows the PS response as a function of the vacuum pressure, indicating the influence of environmental conditions on the photocurrent response. The dashed lines are provided only as a guide for the eyes. 111
Figure 4.3.9 (a)-(e) Bode plots at different vacuum pressures and their respective equivalent circuits. The red dots are the experimental data and the solid green line is the fit. The letters present the following: resistance (R), inductance (L), capacitance (C), and Warburg component (W). (f) The mounted circuit was divided into four component groups: group 1 (G_1), group 2 (G_2), group 3 (G_3), and group 4 (G_4). 112
Figure 4.3.10 Band structures calculated via DFT for (a) pristine ITO, (b) ITO with 1 oxygen vacancy, (c) 2 oxygen vacancies, (d) 3 oxygen vacancies, and (e) 1 oxygen interstitial. The projected density of states (PDOS) for In, Sn, and O orbitals is also shown. The blue line indicates the Fermi energy level. 114

Figure 4.3.11 – Carrier concentration as a function of oxygen vacancies, calculated via DFT. The inset shows the observed shift between the Fermi energy (E_F) and the valence band maximum (E_V) due to oxygen defects. Dashed lines are included as a visual guide. 115
Figure 4.4.1 – Schematic representation of the substrate arrangement during the DC sputtering process. The substrates are positioned at different distances (x) from the center of the metallic In–Sn target, which is located 15 mm above the substrate plane. Using this configuration one can obtain films which thickness depends on the x position. 119
Figure 4.4.2 – XRD patterns of Sn-doped In_2O_3 thin films annealed under high vacuum at different substrate positions (x= 0 – 20 mm). The blue circles represent the experimental data (Y_{Obs}), and the orange lines correspond to the calculated diffraction patterns from Rietveld refinement (Y_{Cal}). The green lines show the difference curves ($Y_{\mathrm{Obs}} - Y_{\mathrm{Cal}}$), while the vertical bars mark the expected Bragg peak positions for the cubic bixbyite phase. Major diffraction peaks are indexed. The S-factor (S = WRp/Rp) is provided for each refinement, indicating the fit quality. 121
Figure 4.4.3 – (a) Lattice parameter as a function of the (x) position. The green line represents the bulk lattice parameter of In_2O_3. (b) Texture coefficients (TC) for the (222) and (400) crystallographic planes, showing the TC ratio (400)/(222) as a function of the substrate position. 122
Figure 4.4.4 – (a)–(e) Resistivity vs. temperature curves measured from 80 K to 300 K for Sn-doped In_2O_3 (ITO) thin films with different thicknesses (t_{XRD}). The experimental data are shown as black symbols, while the red lines represent the fits using (Equation 71). The semiconductor-to-metal transition temperature (T_{SM}) is indicated for each film. 124
Figure 4.4.5 – Semiconductor-to-metal transition temperature (T_{SM}) as a function of film thickness (t_{XRD}) for Sn-doped In_2O_3 (ITO) thin films. This figure includes data from this work (black circles) and previously reported values by Kaushik et al. (KAUSHIK; KUMAR; SUBRAHMANYAM, 2017a), Guo et al. (GUO et al., 2011), and Lin et al. (LIN et al., 2010). The inset shows the correlation between T_{SM} and the Hall carrier concentration (N_{Hall}), highlighting the influence of charge density on the transition temperature. 126
Figure 4.4.6 – Fermi wavelength (λ_F) as a function of carrier concentration for ITO films. Blue squares correspond to samples thermal annealing (TA) in air, red circles to vacuum-annealed samples ref.* (HUAYHUA, 2022), and black spheres to samples studied in this work. The dashed line is a guide to the eye. 127

Figure 4.4.7–(a) UV–Visible transmittance spectra of ITO thin films with varying thicknesses (t_{XRD} = 199–552 nm), measured in the range of 300–2500 nm. Thinner films exhibit fewer interference fringes and stronger free-carrier absorption in the near-infrared (NIR) region. The gray curve corresponds to the borosilicate glass substrate. (b) Transmittance spectrum and corresponding fit for the t_{XRD} = 552 nm sample using the combined Tauc–Lorentz and Hamberg (T–L/Hamberg) models (PFLUG et al., 2004). 128
Figure 4.4.8–Refractive index (n) and extinction coefficient (k) of Sn-doped In_2O_3 thin films, extracted using the Tauc–Lorentz/Hamberg model across the 500–2500 nm spectral range. Curves are shown for different film thicknesses (t_{opt}), along with DFT-calculated values for pristine ITO. 130
Figure 4.4.9–(a) Optical bandgap energy (E_g^{opt}) as a function of carrier concentration (N_{Hall}), determined using the Dolgonos–Hamberg (DH) and Band Fluctuation (BF) models. (b) Urbach energy (E_U) derived from exponential tail fitting and broadening parameter (Γ) as functions of N_{Hall}. Inset: fitting curves for the optical absorption edge using both models. 132
Figure 4.4.10–Electronic band structures calculated via DFT for ITO with different defect configurations: (a) 4.2% interstitial oxygen (O_i), (b) 2.1% interstitial oxygen, (c) pristine ITO, and (d) 2% oxygen vacancies (V_O). The red dashed line indicates the Fermi level. 134
Figure 4.4.11–Projected density of states (PDOS) calculated via VASP for In, Sn, and O orbitals in Sn-doped In_2O_3 (ITO) with different defect configurations: (a) pristine ITO ($In_{29}Sn_3O_{48}$), (b) ITO with 2% oxygen vacancies (V_O), (c) ITO with 2.1% interstitial oxygen (O_i), and (d) ITO with 4.2% O_i. The red vertical dashed line indicates the Fermi level. 135
Figure 4.5.1–XRD patterns of Fe-doped ITO films at different AT, refined using Rietveld method. Black circles represent the experimental data (Y_{Obs}), the red line corresponds to the calculated fit (Y_{Cal}), the sky-blue line shows the difference between Y_{Obs} and Y_{Cal}, and the black vertical lines indicate the peak positions of the phase. 140
Figure 4.5.2–Representative EDS spectrum of Fe-doped ITO thin films. The characteristic emission lines of O (K_α at 0.52 keV), Fe (L_α at 0.704 keV), In (M_α at 0.45 keV, L_α at 3.29 keV, L_β at 3.45 keV), and Sn (M_α at 0.49 keV, L_α at 3.44 keV, L_β at 3.66 keV, $L_{\beta 2}$ at 3.93 keV) are indicated. The inset highlights the low-energy region, where the Fe–L_α peak is resolved from the nearby Sn–M line. 141

Figure 4.5.3–(a) UV–Visible transmittance spectra of Fe doped ITO thin films with varying annealing temperature (400-700°C), measured in the range of 300–2500 nm. The red line represents the fit T-L/Hamberg model, (b) optical constants, refraction index (n) and extinction coefficient (k) obtained from fitting T-L/Hamberg model. 143

Figure 4.5.4–(a) Fit over the absorption region using the band fluctuation model (BF), (b) Optical bandgap (E_g^{Opt}) and Urbach energy for Fe-doped ITO films at different annealing temperatures, (c) E_g^{Opt} at Hall carrier concentration function. 145

Figure 4.5.5–Hall carrier concentration (N_{Hall}), electrical resistivity (ρ), and Hall mobility (μ_{Hall}) measured for Fe-doped ITO films as a function of the annealing temperature. 147

Figure 4.5.6–(a)-(e) Resistivity vs. temperature curves measured from 80 K to 300 K for Fe doped ITO thin films with different anneling temperatures. The experimental data are shown as black symbols, while the red lines represent the fits using (Equation 82). (f) Correction resistivity parameters a function of the annealing temperature, (g) Activation energy (E_a) vs. carrier concentration ($n^{1/3}$), inset: Resistivity ln ρ vs. 1/T. 148

Figure 4.5.7–Magnetization as a function of the applied external magnetic field (H) for Fe-doped ITO films, (a) M vs H at 2 K, inset coercive field, (b) M vs H at 300K, inset ferromagnetic contribution curves at room temperature, (c) Fe atomic concentration estimated from SQUID measurements and EDS. . . . 151

Figure 4.5.8–(a) Saturation magnetization of the FM contribution (M_S) determined at 300 K as a function of annealing temperature, (b) M_S as a function of carrier concentration. In this plot are included values reported by Kitagawa et al. (KITAGAWA; NAKAMURA, 2025). The yellow shaded region shows the increase in magnetization for larger charge carriers density. 153

Figure 4.5.9–Magnetic susceptibility (χ) as a function of temperature for samples annealed at different temperatures. 154

Figure 4.5.10Photocurrent as a function of time for the film annealed at 600 °C. The dark-shaded regions indicate the intervals when the sample was not exposed to UV illumination. The inset shows the exponential fitting of the decay curve using Equation 86. (b) Photoresponse ratio (PR = $I_{\text{UV}}/I_{\text{dark}}$) as a function of annealing temperature. 155

Figure 4.6.1–(a) X-ray diffraction patterns of the Fe-doped ITO films annealed at different vacuum levels, (b) Rietveld refinement of the XRD pattern of the film annealed in 10^{-6} mbar. The black circles represent the experimental data Y_{Obs}, the blue line represents the fit Y_{Cal}, the green line the difference between Y_{Obs}-Y_{Cal}, the black line the phase and finally wRp/RP=1.26 the quality of the fit. . . . 159

Figure 4.6.2–(a) Lattice parameter obtained from Rietveld refinements and (b) crystallite size $< D >$, as a function of the vacuum pressure level used during the annealing of the Fe-doped ITO films. 161
Figure 4.6.3–XPS spectra of the Fe-doped ITO films annealed at different vacuum pressure levels (a) Survey, (b) O 1s orbital, (c) Tin (Sn) peaks related to $3d_{3/2}$ and $3d_{5/2}$ orbitals, (d) indium (In) peaks related to $3d_{3/2}$ and $3d_{5/2}$ orbitals. . . . 162
Figure 4.6.4–(a) UV–Vis transmittance spectra. In the inset is shown the fit using Tauc-Lorentz oscillator layer model. (b) Optical bandgap (E_g^{Opt}), Urbach energy (E_U) as a function of the vacuum pressure level used during the annealing of the Fe-doped ITO films. The inset shows the fit using the band fluctuation model. 164
Figure 4.6.5–Carrier concentration (N_{Hall}) and electrical resistivity (ρ) as a function of the vacuum pressure level used during the annealing of the Fe-doped ITO films.166
Figure 4.6.6–(a) Resistivity measured over a temperature range of 80-300K, (b) ln ρ vs. 1000/T, the curves show the fits of the different charge transport mechanisms, the red line represents the fit of the Thermal activation conduction band (TACB), the light blue line represents the nearest neighbor hopping (NNH) behavior, the fit of the Mott-VRH model is shown in the inset of the figure. (c) TACB at vacuum annealing function. 167
Figure 4.6.7–(a) Frequency dependence of the Real part (Re Z) and (b) imaginary part (-Im Z) of the AC impedance, for films annealed at different vacuum pressures. . 169
Figure 4.6.8–(a)-(f) Nyquist plots, fitted EIS curves of ITO films annealed at different vacuum pressure. The inset of figure (b) is shown the equivalent electrical circuit. 170
Figure 4.6.9–(a) Methane (CH_4) gas-sensing response at an operating temperature of 200 °C. (b) Photocurrent response of the Fe-doped ITO film annealed at a pressure of 10^{-1} mbar. The UV light-off periods are represented by the gray shaded regions. The insets display the response and recovery times for gas sensing and photocurrent measurements, respectively. 172
Figure 4.6.10–Gas sensor response to methane gas and photoresponse under UV illumination as a function of the crystallite size ($< D >$) determined for the Fe-doped ITO films annealed at different vacuum pressure levels. 174
Figure 4.6.11–Magnetic moment as a function of the applied external magnetic field (H) for Fe-doped ITO films annealed at different vacuum levels, (a) 2 K, inset coercive field, and (b) 300K, inset ferromagnetic contribution curves at room temperature. 176
Figure 4.6.12–Saturation magnetization (M_S) at 300 K as a function of vacuum pressure level used for the annealing process (bottom axis) and oxygen vacancy concentration (top axis) determined from XPS analysis. 177

List of Tables

Table 4.1.1 Results of structural paramenters of In_2O_3 films with different Sn doped obtained from the XRD Rietveld refinement, lattice parameter (a), average crystallite size ($< D >$), Sn concentration obtained by XRD (Sn_{XRD}) and EDS Sn_{EDS}, average roughness (Rq) from AFM micrography. $O^{Non-Struc}/O^{Struc}$, Sn^{2+}/Sn^{4+} ratio obtained by XPS with an adjustment error below 0.5%, the S=wRp/Rp represents the quality of the fit using the Rietveld method. 68

Table 4.1.2 Electrical resistivity (ρ), carrier concentration (N_{Hall}) and Hall mobility (μ_{Hall}) obtained by four-point probe method. Transmittance (T_{max}) and results obtained from the adjustments of the transmittance spectra using the Tauc Lorentz and the Hamberg model, thickness (t_{Opt}), carrier concentration (N_{Opt}), electron effective mass (γ). 74

Table 4.1.3 Photocurrent parameters: recovery times (τ_{rec}) and response times (τ_{res}); photoresponse ($PR = I_{UV}/I_{dark}$); UV-light-saturated photocurrent (I_{UV}) and saturated dark current (I_{dark}). Parameters of the methane gas sensing response: response time (t_{res}) and recovery time (t_{rec}); gas sensor response ($GSR = R_{air}/R_{gas}$). 77

Table 4.2.1 Parameters obtained by XPS, ratio Sn/In, V_O/O_T and In-I/In-II. Results of structural and morphological paramenters of ITO films obtained from the XRD Rietveld refinement. The lattice parameter ($a = b = c$), average crystallite size ($< D >$),and residual strain ($< \varepsilon >$). the texture coefficient (TC) calculated using Equation 59 and goodness-of-fit (G) is also included to show the quality of the Rietveld refinement. 89

Table 4.2.2 Results obtained from the adjustments of the transmittance spectra using the Tauc Lorentz model and the Hamberg model, thickness (t), carrier concentration (n_{Opt}), reduced effective mass (γ), Transmittance (T) and Electrical measurement sheet resistance ($R_\square$), resistivity (ρ), carrier concentration (N_{Hall}) and Hall mobility (μ_{Hall}) using the Van der Pauw configuration. 95

Table 4.2.3 Results of resistance (R), inductance (L), capacitance (C), wolbur (W), obtained from the adjustments of the Nyquids curves, the error was obtained below 0.5%. 97

Table 4.3.1 Structural parameters, including lattice constants and crystallite size, are obtained from XRD analysis. Thickness measurements are assessed using cross-sectional SEM images and transmittance data, under vacuum conditions ranges from room atmosphere to 2.3×10^{-6} mbar, as described in the text. . . 100

Table 4.3.2–Resistivity, carrier concentration (n_{Hall}), and mobility (μ) values for ITO thin films were measured using the van der Pauw method. Additionally, the parameter γ was determined from both transmittance and Hall effect measurements. 110
Table 4.3.3–Values obtained from the impedance measurements, where the equivalent circuit is showing and all electrical components of each of the equivalent circuits. 110
Table 4.3.4–Effective mass of free electrons, transition between E_F-E_V and charge carriers, calculated for indium tin oxide with different defects by DFT. 116
Table 4.4.1–Structural parameters obtained from X-ray diffraction analysis for Sn-doped In_2O_3 thin films deposited at different substrate positions. Parameters include the lattice constant ($a = b = c$), average full width at half maximum ($\langle FWHM \rangle$), texture coefficients (TC) for the (222) and (400) planes, and the S-factor ($S = WRp/Rp$) indicating the quality of the Rietveld refinement. Film thickness (t_{XRD}) was estimated using the absorption-based method described in the text, with an uncertainty of approximately 12% which does not affect the uncertainty of the resistivity and carrier concentration 120
Table 4.4.2–Electrical properties of the ITO films measured at different sample positions (x), including the sheet resistance ($R_\square$), resistivity (ρ), carrier concentration (N_{Hall}), and mobility (μ_{Hall}). Also reported the extrapolated resistivity (ρ_0) at $T = 0$ K, and the fitting parameters m and K, obtained from temperature-dependent resistivity measurements. 125
Table 4.4.3–Parameters of the fits of the transmittance spectra using the Tauc–Lorentz/ Hamberg models, thickness (t_{Opt}), carrier concentration (N_{Opt}), plasma frequency (ω_P), dynamical resistivity (ρ_{Dyn}), optical mobility (μ_{Opt}) and reduce effective mass (γ). The results are shown for different sample positions. . . . 131
Table 4.4.4–DFT-calculated effective mass (γ_{DFT}), energy difference between the Fermi level and the valence band maximum ($E_F - E_V$), theoretical carrier concentration (N_{DFT}), e plasma frequency (ω_p(DFT)) for Sn-doped In_2O_3 (ITO) with different defect types, obtained using both VASP and Quantum ESPRESSO. Literature values from DMo13 Scott et al. (BREWER; F, 2004) and VASP Chem et al. (CHEN et al., 2015) are included for comparison. 136
Table 4.5.1–Structural parameters obtained from the Rietveld refinement: lattice parameter ($a = b = c$), average $\langle FWHM \rangle$, goodness-of-fit (G), and texture coefficients (TC) for the (222) and (400) reflections. Atomic concentrations per formula unit of In, Sn, Fe, O, fraction of Fe atoms per cation (At. Fe) were determined by EDS, with an estimated uncertainty below 14%. 139

Table 4.5.2–Results obtained from the adjustments of the transmittance spectra using the Tauc Lorentz and the Hamberg model, thickness (t), carrier concentration (N_{Opt}), effective mass (γ), Transmittance (T_{max}), refraction index (n) and extinction coefficient (k) at λ = 632.8 nm. (* Ref (POLYANSKIY, 2024)) . . 143
Table 4.5.3–Electrical characterization at room temperature using the four-point probe method, showing the sheet resistance ($R_{\square}$), electrical resistivity (ρ), carrier concentration (N_{Hall}), and Hall mobility (μ_{Hall}) for the Fe-doped ITO films. . 147
Table 4.5.4–Parameters obtained from the fits of the low temperature resistivity curves employed Equation 82. 149
Table 4.5.5–Parameters obtained from the fit of magnetization vs. magnetic field curves to the Brilloiun function, M_S (2K) is the saturation magnetization at 2K, spin angular moment (S), fraction paramagnetic of Fe (x_{PM}), temperature independent susceptibility (χ_0), interaction temperature (T_0), coercive field (H_C), M_S (300K) is the saturation magnetization at 300K, fraction ferromagnetic of Fe (x_{FM}), $x_{Tot} = x_{PM} + x_{FM}$ for the Fe-doped ITO films. 152
Table 4.5.6–Parameters extracted from the exponential fitting of Equation 86, including the response time (τ_R), recovery time (τ), and photoresponse ratio (PR) for the Fe-doped ITO films. 156
Table 4.6.1–Results of structural and morphological paramenters of ITO films obtained from the XRD Rietveld refinement. The lattice parameter ($a = b = c$), average crystallite size ($< D >$),and residual strain ($< \varepsilon >$). the texture coefficient (TC) calculated using Equation 88 and goodness-of-fit (G) are also included. Integrated areas of the Sn/In, V_O/O_T, Sn^{4+}/Sn^{2+} ratios obtained by XPS. . . . 161
Table 4.6.2–Thickness (t), Transmittance (T) values at a wavelength of ∼ 580 nm, obtained from the fits of the transmittance spectra using the Tauc Lorentz model, and carrier concentration (n_{Hall}, resistivity (ρ), mobility (μ_{Hall}) determined from Hall effect measurements. 165
Table 4.6.3–Thermal activation conduction band (TACB) energy E_{TACB}, nearest neighbor hopping (NNH) activation energy E_{NNH} and Mott characteristic temperature T_{Mott} obtained from different temperature range for Fe-doped ITO films annealed at different vacuum levels. 168
Table 4.6.4–Equivalent circuit parameters obtained from the fits of the EIS data of Fe-doped ITO thin films annealed at different vacuum levels. 171
Table 4.6.5–Parameters of the methane gas sensing response: response time (t_{res}) and recovery time (t_{rec}); gas sensor response ($GSR = R_{air}/R_{gas}$). Photocurrent parameters: recovery times (τ_{rec}) and response times (τ_{res}); photoresponse ($PR = I_{UV}/I_{dark}$); UV-light-saturated photocurrent (I_{UV}) and saturated dark current (I_{dark}). 174

Table 4.6.6 Parameters obtained from the fit of M vs. H curves to the Brilloiun function, M_S (2K) is the saturation magnetization at 2K, temperature independent susceptibility (χ_0), spin angular moment (S), interaction temperature (T_0), fraction paramagnetic of Fe (x_{PM}), M_S (300K) is the saturation magnetization at 300K, fraction ferromagnetic Fe ions (x_{FM}) for the Fe-doped ITO films. . . 177

List of abbreviations and acronyms

ITO	Indium Tin Oxide
AZO	Aluminum-doped Zinc Oxide
FTO	Fluorine-doped Tin Oxide
TCO	Transparent Conductor Oxide
DMS	Diluted Magnetic Semiconductor
TM	Transition Metal
RT	Room Temperature
RTF	Room Temperature Ferromagnetism
FM	Ferromagnetism
PM	Paramagnetism
DC	Direct Current
AC	Alternating Current
RF	Radio Frequency
BF	Band Fluctuation
TL	Tauc–Lorentz
NIR	Near infrared
FWHM	Full Width at Half Maximum
GB	Grain boundaries
VB	Valence Band
CB	Conduction Band
VP	Vacuum Pressure
AT	Annealing Temperature
WS	Williamson–Hall
SLG	Soda Lime Glass

AG	As Grown
TC	Texture Coefficient
RKKY	Ruderman-Kittel-Kasuya-Yosida
GSAS	General Structure Analysis System
EDS	Energy-Dispersive Spectroscopy
XRD	X-Ray Diffraction
AFM	Atomic Force Microscopy
XPS	X-Ray Photoelectron Spectroscopy
VASP	Vienna Ab initio Simulation Packag
DFT	Density Functional Theory
PBE	Perdew–Burke–Ernzerho
PAW	Projector Augmented-Wave
DOS	Density of States
PDOS	Projected Density of States
WLE	Weak Localization Effect

List of symbols

Symbol	Description
V_O	Oxygen vacancy
O_i	Oxygen interstitial
$< D >$	Average crystallite size
$< \varepsilon >$	Strain
a	Lattice parameter
t_{XRD}	Film thickness from XRD
t_{Opt}	Film thickness from Transmittance
T_{SM}	Semiconductor-to-metal transition temperature
R	Electrical resistance
L	Inductance
C	Capacitance
W	Warburg
$R_{\square}$	Sheet resistance
σ	Electrical conductivity
ρ	Electrical resistivity
ρ_0	Electrical resistivity grain boundary scattering
$\rho_{1/2}$	Electron–electron interactions
$\rho_{4.5}$	Two magnon scattering
ρ_{Dyn}	Electrical dynamical resistivity
ρ_S	Kondo-like spin-dependent scattering
N_{Hall}	Hall carrier concentration
N_{Opt}	Optical carrier concentration
μ_{Hall}	Hall mobility
μ_{Opt}	Optical mobility

μ_{BND}	Mobility limited by grain boundaries
k_B	Boltzmann constant
ω	frequency
ω_P	Plasma frequency
m^*	Electron effective mass
M_{Mol}	Molar mass
ε	complex refractive index
n	Refractive index
k	Extinction coefficient
Γ	Width of the electronic transition
E_g^{Opt}	Optical bandgap
E_U	Urbach energy
α	Absorption coefficient
E_F	Fermi energy
G	Goodness-of-fit
M	Magnetization
μ_B	Bohr magneton
B_S	Brillouin function
H	Applied magnetic field
S	Spin angular moment
T_0	Interaction temperature
T_{Mot}	Temperature of Mott
H_C	Coercive field
χ	Magnetic susceptibility
λ_F	Fermi wavelength
h	Plank constant

T	Temperature
E_{TACB}	Thermal activation conduction band
E_{NNH}	Nearest neighbor hopping
t_{res}	Response time
t_{rec}	Recovery time

Contents

1 Introduction and objectives **30**

1.1 Introduction 30

1.2 Objectives 32

1.2.1 Specific objectives 32

2 Theoretical concepts **34**

2.1 Transparent Conductor Oxide 34

2.2 Diluted Magnetic Semiconductor 35

2.3 Indium Tin Oxide and Fe doped 36

2.4 Engineering of Defects 37

2.5 Electrical Conduction Mechanisms 38

2.5.1 DC Electrical Conduction 38

2.6 Impedance Spectroscopy 41

2.7 Metal Insulator Transition 44

2.8 Optical Properties 45

2.8.1 Transparent region 45

2.8.2 Optical constants n y k 45

2.8.3 Tauc Lorentz 46

2.8.4 Drude model 47

2.8.4.1 Drude Model for Electrical Conductivity 48

2.8.5 Hamberg model 50

2.9 Magnetic Properties 51

2.9.1 Ruderman-Kittel-Kasuya-Yosida model (RKKY) 51

2.9.2 Mean-field Zener model 51

2.9.3 Double exchange coupling model 52

2.9.4 Bound magnetic polarons model 52

2.10 Photoconductivity 52

2.11 Gas Sensor Properties 54

3 Materials and experimental methods **56**

3.1 Targets 56

3.2 Deposition of films via sputtering technique 57

3.3 Thermal Annealing 59

3.4 Film Characterization 59

3.4.1 X-ray Diffraction 59

3.4.2 UV-visible Spectroscopy 60

3.4.3 Scanning Electron Microscopy (SEM) and X-Ray Photoelectron Spectroscopy (XPS) . . . 60
3.4.4 Atomic Force Microscopy . . . 60
3.4.5 Electrical Measurements DC and AC . . . 60
3.4.6 Magnetic measurements . . . 61
3.4.7 Gas sensor measurement . . . 61
3.4.8 Photocurrent measurement . . . 61
3.4.9 DFT calculations . . . 61

4 Experimental results and discussion . . . 63
4.1 Dynamic defect compensation in Sn-doped In_2O_3 thin films: correlating structural, electrical, and optical properties through experiment and DFT calculation . . . 63
4.1.1 Experimental details . . . 63
4.1.2 Theoretical calculation . . . 64
4.1.3 Structural properties . . . 65
4.1.4 EDS and AFM results . . . 68
4.1.5 XPS analysis . . . 69
4.1.6 Electrical properties . . . 72
4.1.7 Optical properties . . . 73
4.1.8 Photocurrent measurements and methane gas detection . . . 76
4.1.9 Ab-initio investigation of the electronic properties . . . 79
4.1.10 Conclusion . . . 83
4.2 Pos-growth thermal annealing effect on the physical properties of ITO thin films 85
4.2.1 Experimental details . . . 85
4.2.2 XPS Surface analysis . . . 85
4.2.3 Structural properties . . . 87
4.2.4 Electrical properties and Optical properties . . . 91
4.2.5 Photocurrent measurements . . . 95
4.2.6 Conclusion . . . 98
4.3 Tailoring structural, electrical, and optical properties of ITO thin films via vacuum-pressure annealing: An experimental and theoretical study . . . 99
4.3.1 Experimental details . . . 99
4.3.2 Theoretical Approach . . . 99
4.3.3 Morphological characterization . . . 100
4.3.4 Structural Characterization . . . 102
4.3.5 Optical and DC electrical properties . . . 105
4.3.6 AC electrical properties . . . 110
4.3.7 Theoretical Results and Discussions . . . 113
4.3.8 Conclusions . . . 116

4.4 Tuning the structural, electrical, and optical properties of ITO thin films via thickness control and vacuum annealing 118
4.4.1 Experimental details 118
4.4.2 Theoretical Approach 118
4.4.3 Structural characterization 120
4.4.4 Electrical properties 123
4.4.5 Optical properties 128
4.4.6 Theoretical Results 133
4.4.7 Conclusions 137
4.5 Room-Temperature Ferromagnetism and Anomalous Transport in Vacuum-Annealed Fe-Doped ITO Thin Films 138
4.5.1 Experimental details 138
4.5.2 Structural properties 139
4.5.3 Optical properties 141
4.5.4 Electrical properties 146
4.5.5 Magnetic properties 151
4.5.6 Photocurrent 155
4.5.7 Conclusion 156
4.6 Influence of the thermal annealing carried out in different vacuum levels on the optoelectronic, magnetic properties and gas-sensor response of Fe doped ITO films 158
4.6.1 Experimental details 158
4.6.2 Structural properties 158
4.6.3 XPS analysis 162
4.6.4 Optical and electrical properties 163
4.6.5 Electrical properties at low temperature 166
4.6.6 AC electrical properties 168
4.6.7 Gas sensor and Photocurrent Response 171
4.6.8 Magnetic properties 175
4.6.9 Conclusion 178

5 General conclusions 179

6 Future works 181

Bibliography 182

Appendix 198

APPENDIX A Articles published within the context of this thesis 199

APPENDIX B Articles published outside the context of this thesis 202

1

Introduction and objectives

1.1 Introduction

Thin films' technologies based on transparent semiconductor oxides (TCOs) are arousing great interest due to their diverse optoelectronic applications for the construction of various electronic devices. In_3O_2, when doped with Sn (Indium Tin Oxide, ITO), is known to belong to the family of TCOs. This structure has a low electrical resistivity of $\sim 10^{-4}$ Ω-cm and high optical transmittance (>80%) in the visible region of the electromagnetic spectrum. These properties together, lead to applications such as functional glass technologies (SZYMANIEC et al., 2025), surface plasmon resonance (SHARIKA et al., 2022), transistors (LU et al., 2022), thermoelectrics (MURMU et al., 2021), solar cells (ZHENG et al., 2023; RAMANATHAN et al., 2025), gas sensors (DAMSHEKAN; MOGHIM; BAHROLOLOOM, 2023), among others. There are several methods to obtain these materials, such as DC sputtering (MARKOV et al., 2023), electron beam evaporation (YAMAGUCHI et al., 2004), pulsed laser (LIU et al., 2023), ultrasonic spray pyrolysis (KOC; KALELI; ÖZTÜRK, 2022), forced Hydrolysis (MADRIGAL-DIAZ et al., 2026) and others. Regarding DC sputtering growth, it is a physical technique that allows the growth of high-quality films under vacuum conditions with good homogeneity and reproducibility.

Understanding the microstructure of ITO is essential, as it strongly depends on the fabrication technique, as well as on the growth conditions and parameters. These factors lead to variations in the microstructure, thereby modifying the physical properties of the material. However, numerous experimental studies have reported that a Sn concentration in the range of approximately 5–12% is optimal for enhancing the optoelectronic properties of ITO (KHAN et al., 2022; PARK et al., 2011; FENG et al., 2026). When this concentration is exceeded, native defects or the formation of complexes begin to occur, resulting in a reduction of the electrical conductivity of ITO (FRANK; KöSTLIN, 1982; GONZáLEZ et al., 2001). Furthermore, although post-deposition thermal annealing in vacuum is commonly used to enhance the crystallinity of

ITO thin films and improve their electrical conductivity, the specific influence of the low pressure in a vacuum environment on defect formation and evolution is still not fully understood. In addition, growths under oxygen-deficient conditions cause changes in the preferential orientations in the (222) and (400) planes (NAJWA et al., 2019; HUANG et al., 2024; ASADIAN; BAKOUEI; GHAMSARI, 2026).

Another parameter to be considered is the film thickness. It is well known that for thicknesses greater than 200 nm, the resistivity and electron charge carrier density do not exhibit significant variations. Moreover, the thickness of relatively thick films (above 200 nm) can lead to a decrease in the transmittance of ITO films (KIM et al., 2018; ZHU et al., 2026). Recent studies have shown that thermal annealing under vacuum conditions is more effective for thin films with thicknesses below 200 nm, due to the generation of vacancies and/or the removal of interstitial oxygen, which activates the Sn^{4+} charge and increases the charge carrier concentration (HUAYHUA et al., 2025).

In this context, an increase in electron-donor-type defects is desirable to enhance the electrical properties. Chen et al. and Fereidooni et al. conducted first-principles DFT calculations combined with experimental results, demonstrating an improvement in optical and electrical properties attributed to the presence of oxygen vacancies (CHEN et al., 2014; FEREIDOONI et al., 2023). Currently, there is significant interest in identifying the optimal doping level that achieves the maximum electron carrier density, as well as the optimal transmittance and thickness for the fabrication of optoelectronic devices (TORASA; SRITHANACHAI, 2022). Additionally, with the introduction of other defects, it is possible to influence the formation of oxygen vacancies, as reported in the work of Chakraborty et al. The authors showed that an increase in oxygen vacancies can be achieved with the insertion of Fe into the ITO matrix, causing an increase in electronic charge carriers (CHAKRABORTY et al., 2020a). However, the introduction or generation of a high density of defects can alter its electrical properties. Reports in the literature have indicated an increase in surface resistance with increasing Fe concentration, which was associated with an effective decrease in charge carriers, since Fe acts as a acceptor-type carrier (ARAGóN et al., 2021). Demonstrating the complexity of defective ITO structures, the manipulation of defects within the ITO lattice remains a challenge in the pursuit of optimizing its physical properties.

ITO is known to have good optoelectronic properties, and when doped with transition metals, an additional degree of freedom is introduced, forming a dilute magnetic conductive oxide (DMC-O). In recent years, these materials have been the subject of considerable interest due to their ability to exhibit ferromagnetism at room temperature (RT), depending on the transition metal (TM) and the film fabrication process. Stankiewicz et al. reported that ITO films doped with 8% Co exhibit ferromagnetic properties at room temperature. Their magnetic behavior is consistent with the bound magnetic polaron percolation model (STANKIEWICZ; VILLUENDAS; BARTOLOMé, 2007). Additionally, interactions between Fe and Sn dopants

under reduced oxygen partial pressure were also studied, favoring the generation of free electrons. In the case of Fe-Sn co-doped In_3O_2, a minor fraction of the Fe^{3+} ion is reduced to Fe^{2+} by consuming some electrons from the crystal lattice, suggesting that Fe doping may help modify the electrical conductivity. According to the literature, conduction electrons derived from Sn doping act as mediators of the magnetic coupling between distant Fe^{3+} ions. This carrier-mediated magnetic coupling is useful for spin-based applications (SHANKER et al., 2015). This shows that the excess charge generated by Sn^{4+} substituting In^{3+} and/or the formation of oxygen vacancies provides itinerant electrons that become polarized by magnetic ions, thereby promoting ferromagnetic behavior in ITO structures. Peleckis et al. reached a similar conclusion, indicating that introducing Ni atoms into the ITO lattice results in a material that exhibits magnetic ordering at room temperature which was associated with Zener–Ruderman-Kittel-Kasuya-Yoshida model (RKKY) (PELECKIS; WANG; DOU, 2006; KITAGAWA; NAKAMURA, 2025). On the other hand, Kitagawa et al. doped ITO with Mn and found ferromagnetism at temperatures above 400 K and a high charge carrier density of $\sim 10^{21}$ cm^{-3}. The authors suggest that the room-temperature ferromagnetism observed in Mn-doped ITO films is not only mediated by charge carriers, but also due to the percolation of bound magnetic polarons (BMPs) (KITAGAWA; NAKAMURA, 2023), showing that the combination of oxygen vacancies and itinerant electrons is a promising approach to promote ferromagnetism in DMC-O. However, there are some controversies in the literature, some studies have shown that increasing the charge carrier density of In_3O_2 co-doped with Sn and Fe contributes little to ferromagnetism (ZHOU et al., 2012; XING; CHEN; SUN, 2013) and that it is the localized charges resulting from the generation of oxygen vacancies that enhance ferromagnetism (CHAKRABORTY et al., 2020a). Venkatesan et al. experimentally concluded that room-temperature ferromagnetism in Fe- and Mn-doped indium tin oxide thin films is due to the presence of a magnetite impurity phase. The formation of these magnetite clusters was also reported by Ohno et al. (OHNO et al., 2007) and the Mn ions would have a paramagnetic behavior up to 4 K (VENKATESAN et al., 2008). This suggests that the control and manipulation of magnetic ions in the ITO structure are important for understanding the ferromagnetic properties and remain a challenge today.

1.2 Objectives

In this work, we investigated the influence of the Fe and Sn doping of In_2O_3 films grown by sputtering technique. Also, the generation of structural defects by controlling the growth parameters and thermal annealing conditions were studied systematically.

1.2.1 Specific objectives

- Melting high purity Sn and In metals in the predetermined proportions in an arc voltaic furnace.

- Sn-doped In_2O_3 thin films were deposited on glass substrates by the sputtering technique using previously prepared metallic targets.

-Growing Fe-doped ITO films using commercial targets (Fe and ITO) on fuse silica and quartz substrates via RF sputtering technique.

- Performing heat treatments at different temperatures and controlled atmospheres (air, vacuum), in order to improve the electrical, optical and magnetic properties by tuning structural defects.

- In order to determine the film thickness, morphology and structural properties cross sectional scanning electron microscope (SEM) images and transmittance measurements were carried out. Meanwhile, the chemical composition and structural characterization were obtained by energy dispersive spectroscopy (EDS), x-ray photoelectrons spectroscopy (XPS) and X-ray diffraction (XRD) experiments.

- Obtaining optical properties such as transparency, energy gap width, refractive index, and extinction coefficient. UV-Vis spectroscopy measurements were carried out.

- In order to determine the magnetic properties and gain insight into the origin of room-temperature ferromagnetism, magnetic measurements were carried out over a broad range of temperatures (2–300 K) and applied magnetic fields (up to 7 T). Additionally, to assess the different charge transport mechanisms, electrical resistivity measurements were performed over a wide temperature range.

- To perform CH_4 gas sensing measurements and photocurrent measurements under UV illumination in order to understand the effects of intrinsic and extrinsic defects.

- To provide physical support to the experimental results, first-principles density functional theory (DFT) calculations were carried out in this work.

2

Theoretical concepts

2.1 Transparent Conductor Oxide

Transparent conductive oxides (TCOs) are based on solid solutions of metal oxides. Compounds such as indium tin oxide (ITO), aluminum-doped zinc oxide (ZnO:Al), fluorine-doped tin oxide (FTO), indium-doped cadmium oxide, among others, are known as TCOs materials (DIXON et al., 2016). These materials are commonly fabricated as thin films. They exhibit transmittance values above 80 %, low electrical resistivity, and a bandgap greater than 3 eV, making them suitable for various optoelectronic devices. TCOs consist of a metallic component A combined with a non-metallic component B, typically oxygen, forming compound semiconductors A_YB_Z with diverse physicochemical properties. These properties can be tailored through doping, A_YB_Z:X (where X represents the dopant), which can be metals, metalloids, or non-metals from the periodic table. Such dopants are usually effectively incorporated into the semiconductor matrix, creating a charge imbalance that is compensated by an abundance of electrons (n-type) or holes (p-type) (GUILLéN; HERRERO, 2019; AFRE et al., 2018). Commonly, TCOs exhibit n-type conductivity due to donor-type defects, which shift the Fermi level towards the conduction band. Upon increased doping, the impurity electronic states begin to overlap with the conduction band, facilitating electron transport at room temperature and inducing a semiconductor-to-metal transition. Each TCO compound represents a solubility limit. For example, ZnO:Al exhibits active donor Al concentrations below 2 % (EFAFI et al., 2014), while in the case of ITO, the solubility limit is below 10 % Sn (KHAN et al., 2020). Above these doping concentrations, the formation of complexes with native defects can be favored, which deactivate the charges of donor ions, thereby altering the properties of the TCOs. However, the study of defect engineering in these materials is of great interest today, as it allows the exploration of new mechanisms in various electronic devices.

2.2 Diluted Magnetic Semiconductor

Diluted magnetic semiconductors (DMS) are composed of diamagnetic semiconductor hosts into which magnetic impurities, such as transition metals (TM), are introduced at low concentrations Figure 2.2.1. These materials may exhibit paramagnetic or ferromagnetic behavior because the dopant elements possess partially filled 3d electron shells. Interest in DMS over recent decades, such as TM doped ZnO, CuO, ITO, TiO_2 (NORTON et al., 2006; ELSHARAWY et al., 2023; MAJUMDAR et al., 2010; MATSUMOTO et al., 2001) and others, has arisen from the observation that these materials can exhibit ferromagnetic ordering at room temperature or even at higher temperatures. This has led to extensive research on DMS due to the possibility of controlling electron spin at temperatures above 300 K, enabling the development of new technological devices, ranging from non-volatile memory to enhanced data-processing capabilities with reduced energy consumption, thus contributing significantly to the field of spintronics (BABU et al., 2016).

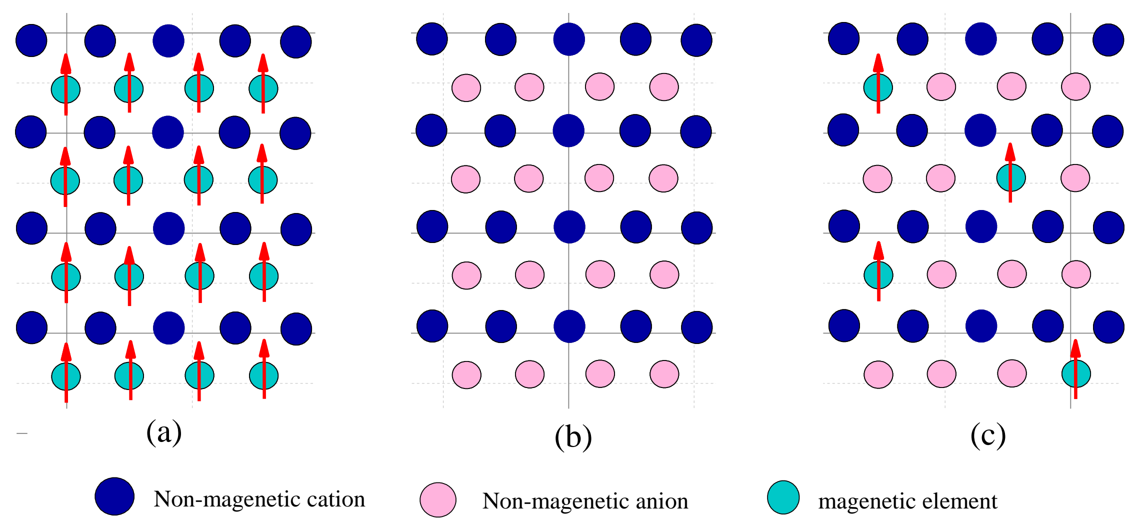

Figure 2.2.1 – (a) Magnetic semiconductor, (b) non-magnetic semiconductor, (c) DMS dilute magnetic semiconductor. "Source: Author's own elaboration."

The incorporation of magnetic elements during sample preparation is a complex process and often leads to controversial results when interpreting the properties of DMS. Therefore, controlling the positions adopted by magnetic impurities within the semiconductor lattice such as interstitial or substitutional sites, as well as the formation of agglomerates or clusters remains a major challenge. Depending on the chemical environment, these configurations naturally influence the magnetic and optoelectronic properties, opening new theoretical perspectives for understanding DMS.

ITO exhibits high solubility, which allows doping with relatively high concentrations of magnetic impurities. This favors the formation of intrinsic defects in the host lattice that act as charge-compensating centers or neutral centers through the generation of complexes within

the high-dilution limit. Consequently, the band structure is modified, leading to alterations in optical, electrical, and magnetic properties. A key discussion regarding the magnetic properties of Fe-doped ITO concerns the existence of exchange interactions between delocalized itinerant carriers and localized states in the outer *d* shell of the magnetic ion. This has stimulated debate on the origin of ferromagnetism: some authors suggest that room-temperature ferromagnetism is mediated by itinerant electrons through $s-d$ or $p-d$ exchange interactions, while another possible mechanism involves polaron formation associated with F-centers mediated by oxygen vacancies. Kitagawa et al. demonstrated that ferromagnetism may arise from a combination of both mechanisms (KITAGAWA; NAKAMURA, 2023). However, determining which mechanism is dominant remains an open question in degenerate semiconductors.

2.3 Indium Tin Oxide and Fe doped

Indium oxide is a transparent semiconductor in the visible range of the electromagnetic spectrum, with a wide energy bandgap of 3.7 eV (WALSH et al., 2022a) and exhibits n-type charge carriers. The most stable crystal structure is the cubic bixbyite type (space group T7h, Ia3), showing a lattice parameter of $a = b = c = 10.117$ Å (MAREZIO, 1966) and a density of 7.12 g/cm^3. This structure is composed of 80 atoms, of which 32 correspond to indium and 48 to oxygen (see Figure 2.3.1(a)). Indium atoms can occupy nonequivalent sites surrounded by six oxygen atoms: eight indium atoms are located in the octahedral site known as site *b*, and 24 in the octahedral site known as site *d*, as shown in Figure 2.4.1.

Regarding the structure of In_2O_3, when In^{3+} ions are substituted by Sn^{4+} ions (ITO) (see Figure 2.3.1(a)), this provides an extra electron for conduction. Thus, a transparent conductive oxide is formed, which, in addition to its high transmittance (>85%), exhibits low resistivity. According to experimental results, the Sn concentrations in the In_2O_3 structure range from approximately 5–15%, where the maximum n-type charge carrier density is reached. Moreover, the generation of oxygen vacancies in the lattice can also contribute up to two electrons, leading to an increase in charge carriers, reaching values of 10^{20}–10^{21}cm^{-3}. The energy bandgap values of ITO vary between 3.5 and 4.2 eV. Depending on growth conditions, it is possible to control the bandgap, texturization, resistivity, charge carriers, defects, mobility, transmittance, among other physical parameters, for optimizing ITO in the field of optoelectronics. However, the introduction of magnetic ions at low concentrations into the ITO lattice provides an additional degree of freedom through the emergence of magnetic properties, resulting in a Diluted Magnetic Conductive Oxide as shown in the Figure 2.3.1(c). Fe is one of the most commonly used transition metals due to its high magnetic moment, which arises from the partially filled 3*d* orbital shells. This induces changes in the physical properties of ITO, where the interaction between conduction electrons and magnetic ions can generate spin-polarized currents. Such interactions may lead to room-temperature ferromagnetism.

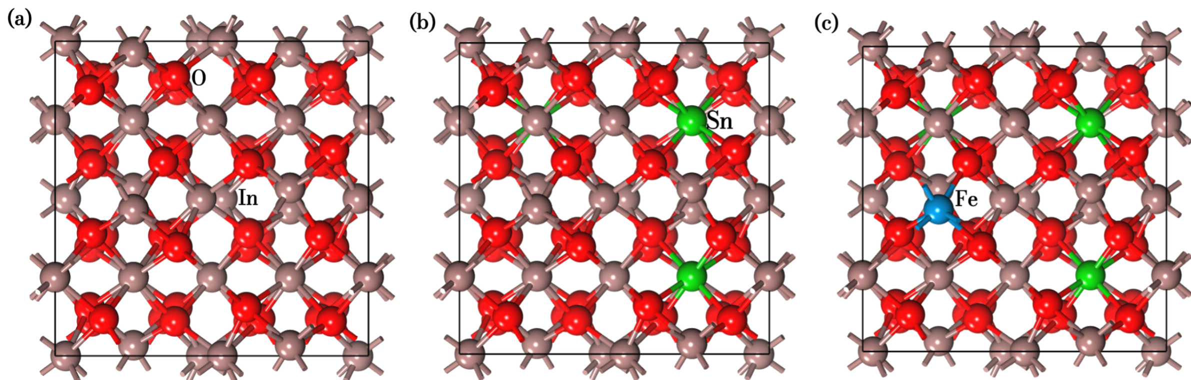

Figure 2.3.1 – (a) Indium Oxide (b) Indium Tin Oxide, (c) Iron doped Indium Tin Oxide. "Source: Author's own elaboration".

2.4 Engineering of Defects

The development of defect engineering in materials such as semiconductors has attracted significant interest in recent years due to the strategic incorporation of defects within the crystalline lattice. These defects induce structural irregularities that can be exploited to tailor electronic, optical, magnetic, and mechanical properties, enabling efficient functionalization for use in emerging technologies such as hydrogen production (XU et al., 2025), enhancing photocatalytic activity for green energy production (TRIPATHY; BARAL, 2025), optoelectronics, and spintronics (FUKUMURA et al., 2004).

For decades, the conductive properties of indium tin oxide (ITO) have been continuously investigated. Its high electrical conductivity is mainly attributed to the substitutional incorporation of Sn^{4+} ions at In^{3+} sites and to the presence of oxygen vacancies (V_O), as mentioned previously. On the other hand, the structure of ITO is relatively complex and consists of two tetrahedral sites, referred to as the *b* and *d* sites, as shown in Figure 2.4.1(a). Regardless of which site is occupied by Sn^{4+}, an extra electron is donated, leading to an increase in conductivity. However, once a critical Sn concentration of approximately 10% is exceeded, intrinsic defects begin to form with higher density in order to minimize their formation energy and reach thermodynamic equilibrium. Consequently, the electrical conductivity is affected by the generation of Sn^{4+}–O_i complexes (see Figure 2.4.1(b)) and oxygen vacancies associated with Sn^{2+}-V_O, which act as charge compensators as evidenced in this thesis.

The emergence of O_i and/or Sn^{2+} defects gives rise to electronic states near the valence band with acceptor-like character, while in some cases, defects such as V_O introduce deep levels. These types of defects are particularly interesting in highly degenerate doped systems, where they can have a strong impact on applications such as photocurrent generation and gas sensing, as will be discussed in this thesis.

However, incorporation of transition metals into the In_2O_3 lattice leads to the emergence

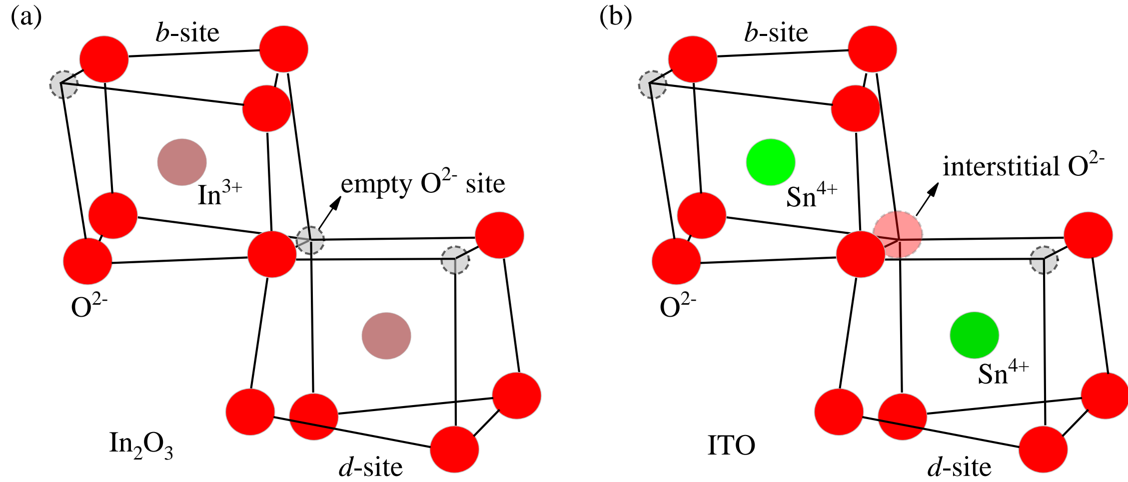

Figure 2.4.1 – (a) Crystal structures of In_2O_3 showing the occupational sites (*b*-site and *d*-site) of In, (b) Occupation of Sn^{4+} in the two sites *b* and *d* forming a complex in combination with an interstitial oxygen (O_i). "Source: Author's own elaboration."

of an additional degree of freedom, giving rise to paramagnetic and/or ferromagnetic properties at room temperature, in contrast to Sn incorporation. The location of the transition metal at the *b* and *d* sites is particularly important, since transition metals are more sensitive to the surrounding chemical environment. Yan et al. conducted a combined theoretical and experimental study, in which they observed that oxygen vacancies induce the formation of Fe^{2+} ions at the 24*d* sites, contributing to room-temperature ferromagnetism (RT). However, Fe^{3+} ions occupying the 8*b* sites do not contribute to room-temperature ferromagnetism, instead exhibiting paramagnetic behavior. These results are both controversial and intriguing, as they indicate that the magnetic properties of Fe-doped In_2O_3 can be tuned by manipulating the oxidation states and the occupation sites of the dopant (YAN et al., 2014).

These emerging perspectives pose new challenges for researchers, who must undertake in-depth studies of complex systems induced by such defects, which are expected to have future scientific and industrial applications.

2.5 Electrical Conduction Mechanisms

2.5.1 DC Electrical Conduction

Electrical conductivity

Electrical conductivity is the ability of materials to allow the flow of electric current through them. This property is directly related to the density of charge carriers (n), electrical resistivity (p) and their mobility in the material (μ). Using the following equation,

$$\sigma = q(n\mu_e + p\mu_p) = 1/\rho \tag{1}$$

Where q is the electron charge, For n-type systems, such as ITO, electrical conductivity is primarily governed by free electrons due to extrinsic doping. However, increased doping can affect the mobility of charge carriers, and consequently, their electrical conductivity. Therefore, an attempt is made to find a balance between these physical magnitudes to achieve optimal values that are useful in different applications.

Electrical resistivity (ρ) can be experimentally determined using the four-point probe method in the Van der Pauw configuration through the following relationship.

$$\rho = \frac{\pi}{2\ln 2}(R_{21,34} + R_{32,41}) \times t \tag{2}$$

where $R_{21,34}$, $R_{32,41}$ are the Van der Pauw configurations and t thickness.

Hall effect

The Hall effect is a physical phenomenon observed when an electric current is passed through a sample, to which a uniform external magnetic field is applied. This separates the electrons from the holes, developing a potential proportional to the current and the magnetic field called the Hall voltage. This effect is the basis for determining the sign of the charge carriers in a material, and is a useful technique for characterizing the electrical transport properties of metals and semiconductors.

The physical principle of the Hall effect occurs when a stream of electrons moves along a direction $\vec{v}$, perpendicular to the applied magnetic field, $\vec{B}$, these electrons experience a force, $\vec{F}$, called the Lorentz force $\vec{F} = q(\vec{E} + \vec{v} \times \vec{B})$, In response to this force, the electrons move in a curved path (sideways) along the material, these electrons create a build-up of negative charge, leaving a positive charge on the other side edge of the material, and hence a Hall voltage (V_H) is produced as:

$$V_H = \frac{IB}{qN_{Hall}t} \tag{3}$$

here I is the current, t thickness and N_{Hall} is carrier concentration.

$V_H > 0$ if the carriers have a positive charge and will be deterred upwards.

$V_H < 0$ if the negative charges are in the majority and the current is in the same direction.

Mobility

Mobility describes how fast charge carriers move within a material. It can be obtained either by applying a magnetic field, yielding the Hall mobility (μ_{Hall}), or by using radiation in the infrared region of the electromagnetic spectrum, yielding the optical mobility (μ_{opt}). In this

context, the optical mobility μ_{opt} is associated only with scattering events occurring within the crystallites, whereas the Hall mobility μ_{Hall} also accounts for scattering effects originating from grain boundaries or twin defects (REY et al., 2013). This difference arises from the presence of potential barriers at extended defects, which limit carrier mobility.

The optical carrier mobility, μ_{opt}, can be obtained from the dispersion relation based on Drude-Sommerfeld theory (MAIER et al., 2007) can be defined as:

$$\mu_{opt} = q\tau/m^* \tag{4}$$

τ is the mean time in which the electron collides with other electrons or ionic impurities and m^* is the effective electron mass in the conduction band.

And the Hall mobility μ_{Hall}, is obtained by:

$$\mu_{Hall} = \sigma/qN_{Hall} \tag{5}$$

It has been observed that in ITO films the increase in charge carriers induces greater absorption of photons, decreasing transmittance (HUAYHUA et al., 2025). These effects suggest that the increase in electronic mobility would be an important parameter to improve the conductivity and transmittance of ITO films. This presents several contributions as shown in the Equation 6 (SHARIKA et al., 2022; REY et al., 2013):

$$\mu_{Tot} = \mu_{GB} + \mu_{Lattice} + \mu_{Impurity} + \ldots \tag{6}$$

Grain boundaries (GB) cause electronic defects located at the grain boundaries that are capable of trapping free carriers. This creates a depletion zone on each side of the grain barrier, generating a potential barrier of height ϕ_b. For degenerate semiconductors, the Fermi level can be greater than the barrier height ϕ_b, facilitating electrical mobility, which is obtained through the following equation (REY et al., 2013):

$$\mu_{GB} = \gamma_{eff} \frac{4\pi m^* e}{h^3} \frac{\Lambda}{\Lambda + \frac{3}{4} w_b} \frac{L_g}{n_c} \ln\left\{1 + \exp\left[\frac{-(\phi_b - E_F)}{k_B T}\right]\right\} \tag{7}$$

where γ_{eff} is a correcting factor ranging from 0 to 1, L_g is the average distance between neighboring GBs, Λ is the mean free path of carriers, within grains and finally w_b is the GB potential barrier width.

Lattice scattering

Here is an expression of the variation of mobility due to lattice dispersion with temperature (BARDEEN; SHOCKLEY, 1950; RAMAIAH et al., 2000):

$$\mu_{Lattice} = \frac{(8\pi)^{1/2} q \hbar^4 C}{3 E_L m^{*5/2} (k_B T)^{3/2}} \tag{8}$$

Where $\hbar$ is the reduced Planck constant, k_B is the Boltzmann constant, and $C_{ii} = (C_{11} + B_{12} + 2C_{32}/2)$ is the elastic constant for longitudinal acoustic waves. E_L is the displacement of the conduction band edge with temperature per unit expansion.

Impurity scattering

This analytical expression for the mobility μ_{Impurity} in degenerately doped semiconductors is caused by scattering from ionized dopant atoms and predominates at carrier concentrations above approximately 10^{19} cm^{-3} (ELLMER; MIENTUS, 2008; PISARKIEWICZ; ZAKRZEWSKA; LEJA, 1989).

$$\mu_{Impurity} = \frac{3(\epsilon_r \epsilon_0)^2 h^3}{Z^2 m^{*2} e^3} \frac{n}{N_i} \frac{1}{F_{ii}^{np}(\zeta_d)} \tag{9}$$

here:

$$\zeta_d = (3\pi^2)^{1/3} \frac{\epsilon_r \epsilon_0 h^2 n^{1/3}}{m^* e^2} \tag{10}$$

and the screening function F_{ii}^{np}

$$F_{ii}^{np} = \left[1 + \frac{4\zeta_{np}}{\zeta_d}(1 - \frac{\zeta_{np}}{8})\right] \ln(1 + \zeta_d) - \frac{\zeta_d}{1 + \zeta_d} - 2\zeta_{np}\left(1 - \frac{5\zeta_{np}}{16}\right) \tag{11}$$

here $\zeta_{np} = 1 - m_0^*/m^*$ which describes the nonparabolicity of the conduction band, m^* effective masses in the conduction band and m_0^* at the conduction band edge.

2.6 Impedance Spectroscopy

Electrochemical impedance spectroscopy (EIS) is widely used to study mass transfer, charge transfer, and diffusion processes through the response to an alternating electrical excitation, which allows the intrinsic properties of materials to be explored via changes in the inductance, resistance, or capacitance of an electrochemical system. It is well known that Ohm's law applies to all currents and electrical potentials, $R = E/I$, where the ideal resistance is independent of frequency (i.e., the current and the potential are in phase). In this case, however, the impedance depends on frequency, and when a small excitation signal is applied, a phase shift (ϕ) is introduced (MAGAR; HASSAN; MULCHANDANI, 2021). Therefore, the excitation signal can be expressed as a function of time, as shown in Equation 12.

$$E_t = R_0 \sin(\omega t) \tag{12}$$

where E_t is the potential at time t, E_0 is the amplitude of the signal, and ω is the radial frequency. The correlation between the radial frequency (ω) and the applied frequency (f) is calculated by ($\omega = 2\pi f$). In a linear system, the signal is shifted in phase (ϕ) and has a different amplitude than I_0 (Equation 13).

$$I_t = I_0 \sin(\omega t) \tag{13}$$

Therefore, the impedance of the entire system can be obtained from Equation 12 and Equation 13. Rewriting the impedance as an Euler relation $\exp(j\phi) = \cos\phi + i\cos\phi$ we have:

$$Z = \frac{E_t}{I_t} = Z_0 \exp(j\phi) = Z_0(\cos\phi + j\cos\phi) = Re(Z) + Im(Z) \tag{14}$$

Therefore, the impedance expression is divided into a real part (representing the x-axis) and an imaginary part (y-axis), obtaining a Nyquist diagram, as shown in Figure 2.6.1(a). These curves are represented by an equivalent electrical circuit (see inset Figure 2.6.1(b)) involving electrical components such as resistors, capacitors, and/or inductors. This designed equivalent circuit provides valuable information for understanding and evaluating the individual components of the EIS system.

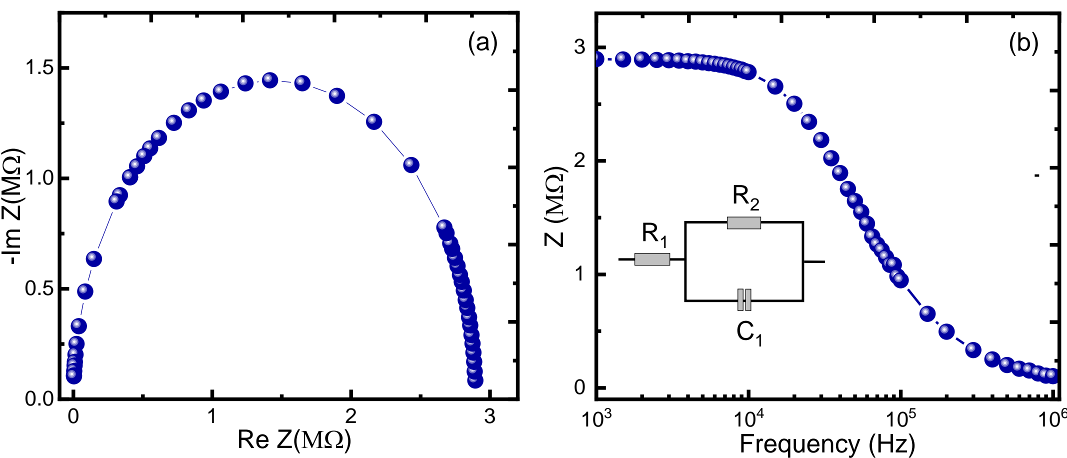

Figure 2.6.1 – (a) Real (Re Z) and complex (-Im Z) part impedance diagrams, (b) impedance as a function of frequency, the inset shows the equivalent circuit representing the impedance curves.

Resistor

Resistance (R) indicates the extent to which an electrical circuit opposes the flow of electric current, as represented by Ohm's Law. The impedance of R is given by the Equation 15, where its impedance is equal to its resistance.

$$Z_R = R \tag{15}$$

Capacitors

Capacitors are devices that have the property of storing electric charge due to the presence of an electric field. A capacitor commonly consists of two parallel plates separated by a distance,

with a dielectric material between the plates. Its main function is the storage of electric potential energy. The impedance of the capacitor is given by the Equation 16.

$$Z_C = \frac{-1}{\omega C} j \tag{16}$$

CPE

The Constant Phase Elements (CPE) circuit component can be used to represent a Double Layer Capacitor, which exhibits deviations from the behavior of an ideal capacitor. The impedance of a CPE is given by the Equation 17:

$$Z_{\text{CEP}} = \frac{1}{T(j\omega)^{\phi}} \tag{17}$$

Here, T is a parameter related to capacitance, and ϕ is the exponent representing the constant phase, with values in the range $0 < \phi < 1$. If the phase is ϕ=1, the behavior corresponds to that of an ideal capacitor.

Inductor

An inductor is an electrical device capable of storing energy created in a magnetic field. These components are usually coils made of charge-conductive materials and serve to oppose sudden variations in the electric current of a circuit. The impedance of the inductor is defined in a manner opposite to that of the capacitor and can be expressed by Equation 18.

$$Z_L = j\omega L \tag{18}$$

Warburg

The Warburg component represents the diffusion effects experienced by ionic species; its contribution increases as the frequency decreases and is described by the Equation 19. In practice, two types of Warburg impedance for finite diffusion are commonly distinguished: the short-circuit Warburg, which exhibits higher capacitive resistance due to species reflected at the far end of the finite diffusion layer, and the open-circuit Warburg, which shows higher capacitive resistance due to species absorbed at the beginning of the finite diffusion layer (SANTOS, 2007).

$$Z_{\text{W}} = \frac{\sigma_w}{\sqrt{2\pi f}} - j\frac{\sigma_w}{\sqrt{2\pi f}} \tag{19}$$

here σ_w is the Warburg coefficient, expressed by:

$$\sigma_w = \frac{RT}{Az^2F^2\sqrt{2}}\left(\frac{1}{\sqrt{D_0}c_0^b} + \frac{1}{\sqrt{D_R}c_R^b}\right) \tag{20}$$

Where R and F are the gas and Faraday constants, D is the diffusion coefficient, and c^b is the concentration of the species in the bulk. The subscripts O and R indicate the oxidized and reduced species.

2.7 Metal Insulator Transition

The metal-insulator transition (MIT) temperature is of great scientific interest, both from the fundamental physics perspective and for technological applications. Depending on its temperature dependence, materials can generally be classified as metals or insulators, with electrical resistivity being a key property characterizing this behavior. In insulators, electrical resistivity decreases with temperature (dR/dT < 0), whereas in metals the opposite occurs (dR/dT > 0) (MATTONI, 2017), as shown in Figure 2.7.1(a). This phenomenon enables the study of new material functionalities.

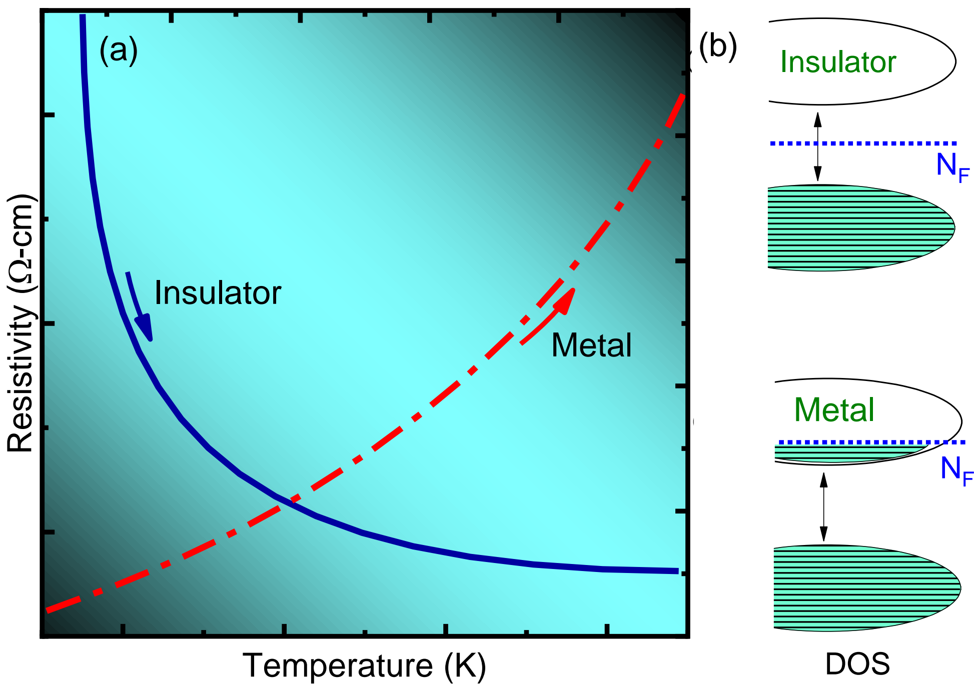

Figure 2.7.1 – (a) Dependence of resistivity on temperature for semiconductor systems (blue lines) and metals (red lines), (b) band model for metallic and semiconductor behavior, N_F represents the Fermi level. "Source: Author's own elaboration."

According to the band theory model, insulators or semiconductors exhibit an energy gap between the valence band, which contains occupied states, and the conduction band, which is unoccupied. As the temperature increases, electrons can be excited from the valence band to the conduction band, thereby reducing electrical resistivity. This behavior is observed in semiconductors such as In_2O_3, ZnO, SnO_2, among others. In contrast, extrinsic defects combined with native defects (especially donors) generated in these materials shift the Fermi energy towards the conduction band, causing overlap, as illustrated in Figure 2.7.1(b). This shift causes the

semiconductor to behave as a metal at room temperature. ITO exhibits a metal-insulator transition temperature of approximately 100 K (HUAYHUA et al., 2025), which can be altered by changes in its physical characteristics, such as thickness, Sn concentration, and native defect density. These changes induce structural disorder, activating or deactivating conduction electrons. Variations in resistivity as a function of temperature are explained within the framework of quantum corrections to conductivity, where quantum interference effects dominate at low temperatures. At these temperatures, the inelastic collision frequency is sufficiently low for electrons to experience elastic collisions without losing phase coherence (KAUSHIK; KUMAR; SUBRAHMANYAM, 2017a), and is explained through electron-electron interactions and weak localization.

2.8 Optical Properties

2.8.1 Transparent region

In transparent conducting oxides (TCOs), one of the most important properties is optical transmittance, which typically exceeds 80% in the visible region. Figure 2.8.1 shows the evolution of transmittance as a function of wavelength, which can be affected by impurities within the lattice, charge carriers, and film thickness. By irradiating the sample with UV–visible radiation (200–800 nm), it is possible to obtain information about the optical bandgap and estimate the film thickness from the oscillations observed in the visible region, which arise as a consequence of optical interference effects. On the other hand, the infrared region provides valuable information about the electrical conductivity of the samples. Additionally, optical constants such as the refractive index and the extinction coefficient can be extracted (see the inset of Figure 2.8.1). These parameters are essential for understanding the interaction of light with TCO materials.

In ITO films, high doping with transition metals and growth under oxygen-deficient conditions are some of the factors that induce the formation of defects such as interstitial atoms, vacancies, and structural imperfections. These defects can promote charge trapping centers and scattering. As a result, incident photons interact with these scattering centers, affecting the optical absorption. Moreover, increased doping may lead to a decrease in the transmittance of the films. Hsu et al. observed an increase in the transmittance of Ni-doped ITO films after thermal treatment (HSU et al., 2005), attributed to the annihilation of certain impurities. It is also necessary for the thicknesses of ITO films to be appropriate for their fabrication. Sobri achieved 90% transmittance in transition metal-doped films with thicknesses below 10 nm (SOBRI et al., 2014).

2.8.2 Optical constants n y k

The refractive index (n) of a medium is defined as the ratio between the speed of light in vacuum and the speed of light in that medium, expressed as

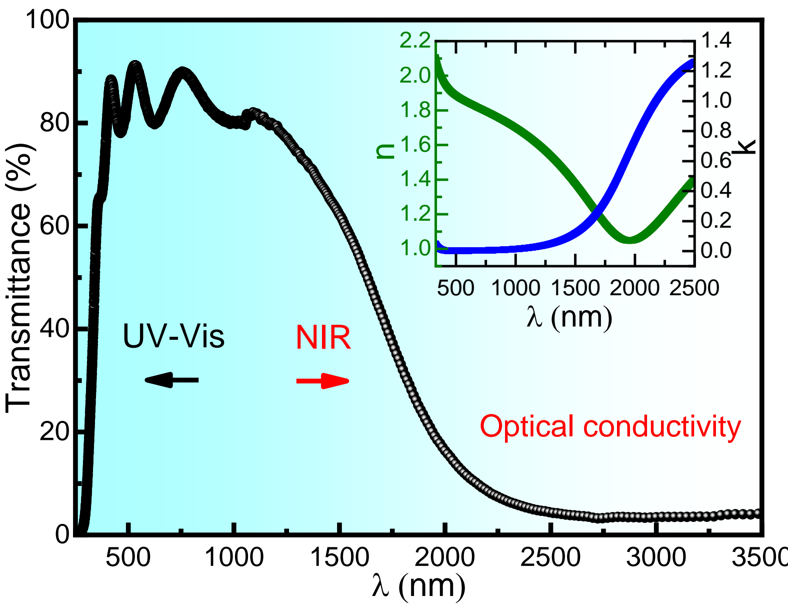

Figure 2.8.1 – (a) Transmittance spectra measured in the UV-vis and infrared regions, inset: refractive index and absorption coefficient as a function of wavelength. "Source: Author's own elaboration".

$$n = c/v \tag{21}$$

where c is the speed of light in vacuum and v is the speed of light in the medium. For transparent materials, the amplitude of the incident wave remains constant as it propagates through the material. However, in a more realistic case, the materials exhibit absorption; therefore, a parameter k, known as the extinction coefficient, is introduced. In this case, the amplitude of the incident wave undergoes a logarithmic variation during its propagation in the medium, causing the refractive index to become a complex quantity, expressed as $N = n + ik$. Here, the real part n accounts for light propagation, while the imaginary part k describes attenuation. These two constants, n and k, can also be represented in terms of dielectric function (see Equation 22), which constitutes a more general concept applicable to both transparent and absorbing materials.

$$\varepsilon = \varepsilon_1 + i\varepsilon_2 \tag{22}$$

If ε_2=0, the medium does not exhibit absorption losses and, therefore, the complex refractive index reduces to the real refractive index.

2.8.3 Tauc Lorentz

For the study of the optical properties of semiconductors, various models have been developed to parameterize their optical constants over specific ranges of the electromagnetic spectrum. However, modeling analyzes require an appropriate optical model that incorporates the

optical properties of the materials (the complex refractive index ($N = n + ik$) (VYGRANENKO; LAVAREDA, 2024) or the dielectric function $\varepsilon = \varepsilon_1 + i\varepsilon_2$, the thickness, and other topographic parameters of each layer in the investigated structure.

The Tauc–Lorentz model, based on the combination of absorption near the band edge (Tauc), which corresponds to the real part, and the imaginary part arising from interband electronic transitions (Lorentz oscillators), is one of the classical dispersion models for the dielectric functions of materials, in which the material can be described as a set of non-interacting oscillators (LIKHACHEV; MALKOVA; POSLAVSKY, 2015). In this model, the imaginary part of the dielectric function is given by:

$$\varepsilon_2(E) = \begin{cases} \frac{AE_0C(E-E_g)^2}{(E^2-E_0^2)^2+C^2E^2}\frac{1}{E}, & E > E_g \\ 0, & E \geq E_g \end{cases} \tag{23}$$

where E_g is the bandgap of the material, A is the oscillator amplitude, E_0 is the energy (position) of the Lorentz peak, and C is the broadening parameter. This model can be generalized for the case of multiple Tauc-Lorentz oscillators. In the other hand, the real part of the dielectric function is given by:.

$$\varepsilon_1(E) = \varepsilon_\infty + \frac{2}{\pi}P\int_{E_g}^{\infty}\frac{x\varepsilon_2(x)}{x^2 - E^2}dx \tag{24}$$

where ε_∞ represents the value of the real part of the dielectric function ε at infinite energy and is an additional fitting parameter in the oscillator model, P stands for the Cauchy principal part of the integral.

2.8.4 Drude model

The Drude model is based on classical mechanics, which considers the valence electrons of the atoms forming a solid as free charged particles moving through a background of much heavier, immobile positive charges. In this model, neither the details of the crystal structure nor the type of atom constituting the solid are taken into account. The model also assumes that, in the interval between collisions, electrons are scattered by ions treated as rigid and impenetrable spheres, and electron–electron interactions are neglected, so that each electron moves independently. Furthermore, under the influence of an external electric field, regardless of the drift velocity acquired by the electron, this velocity is lost after each collision. Consequently, the applied external electric field can only exert its influence during the time between collisions (see Figure 2.8.2). The probability dP that an electron will undergo a collision in a time interval dt is given by $dP = dt/\tau$. The mean time between collisions, τ, is assumed to be independent of the electron's position and velocity; however, the larger its value, the greater the influence of the external field on the electrons.

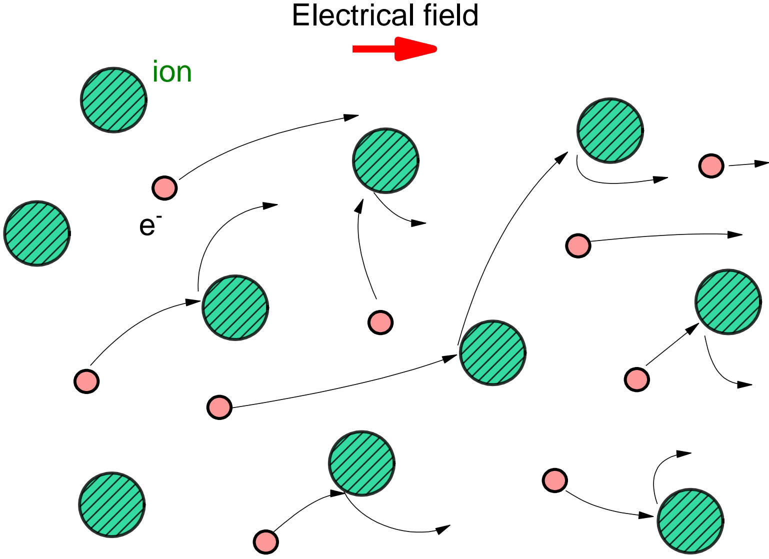

Figure 2.8.2 – Trajectory of a electron scattering off the ion, according to the Drude model.

2.8.4.1 Drude Model for Electrical Conductivity

Consider Ohm's vector law:

$$J = \sigma E \tag{25}$$

In addition, the current density of a gas of electrons is given by:

$$J = nqv \tag{26}$$

where n is the electron density, $q = e$ is the electron charge, and v is the velocity of the electrons. Combining Equation 25 and Equation 26, the conductivity is obtained:

$$\sigma = \frac{J}{E} = ne\frac{v}{E} \tag{27}$$

The ratio $v/E = \mu_q$ is called mobility.

The equation of motion for a charge q in the presence of an electric field E is given by Newton's 2nd Law:

$$\frac{d\vec{v}}{dt} + \frac{\vec{v}}{\tau} = \frac{e\vec{E}}{m} \tag{28}$$

The force exerted by the magnetic field on the charge is negligible to a first approximation, since in low velocity regimes$v << c$ we have $|\vec{E}| >> |\vec{v} \times \vec{B}|$.

Solving the differential equation above in the harmonic regime, $\vec{E} = \vec{E_0}\exp(-i\omega t)$, we can assume $\vec{v} = \vec{v_0}\exp(-i\omega t)$ to obtain:

$$\vec{v} = \frac{e\tau}{m(1+i\omega\tau)}\vec{E} \tag{29}$$

Combining Equation 27 and Equation 29 gives us the electrical conductivity of the material:

$$\sigma(\omega,\tau) = \frac{ne^2\tau}{m(1+i\omega\tau)} = \frac{ne^2}{m^*}\left(\frac{i\omega\tau^2+\tau}{1+\omega^2\tau^2}\right) \tag{30}$$

Here, conductivity $\sigma^* = \sigma_1 + i\sigma_2$ is a complex value that results in a real and imaginary part:

$$\sigma_1 = \frac{ne^2\tau}{m^*(1+i\omega^2\tau^2)} = \frac{\sigma_0}{1+i\omega^2\tau^2} \tag{31}$$

$$\sigma_2 = \frac{ne^2\omega\tau^2}{m^*(1+i\omega^2\tau^2)} = \frac{\sigma_0\omega\tau}{1+i\omega^2\tau^2} \tag{32}$$

These equations govern the absorption of light due to charge carriers within a TCO, as a function of frequency. Here σ_0 is the DC conductivity of the material:

$$\sigma_0 = \frac{ne^2\tau}{m^*} \tag{33}$$

The electrical permittivity is given by: $\varepsilon = \varepsilon_\infty + i\sigma/\varepsilon_0\omega$ (JACKSON, 2021). By substituting Equation 30 into the last permittivity expression, the real and imaginary components of the permittivity are obtained (SALES, 2022),

$$\varepsilon = \varepsilon_1 + i\varepsilon_2 \tag{34}$$

here,

$$\varepsilon_2 = \frac{\sigma_0}{\varepsilon_0\omega}\left(\frac{1}{1+i\omega^2\tau^2}\right) \tag{35}$$

$$\varepsilon_1 = \varepsilon_\infty - \frac{\sigma_0\tau}{\varepsilon_0}\left(\frac{1}{1+i\omega^2\tau^2}\right) \tag{36}$$

This last Equation 36 has two terms, which means that for some combination of values between the parameters and the frequency, it will be zero. This frequency is known as the plasma frequency ω_p given by,

$$\omega_p = \sqrt{\frac{ne^2}{\epsilon_0 m^*}}, \tag{37}$$

2.8.5 Hamberg model

This model is based on the energy-loss model, in which the electric field interacts not only with free electrons but also with bound electrons, phonons, and other fundamental excitations. These interactions arise from elementary excitations and are described by the following dielectric function ε (SALES, 2022).

$$\varepsilon = 1 + \varepsilon_{Valence-e} + \varepsilon_{Phonos} + \varepsilon_{Free-e} + \ldots \tag{38}$$

Where $\varepsilon_{Valencia}$ is the contribution of valence electrons, ε_{Phonos} phonons and ε_{Free-e} free carriers. Consequently, the energy-loss model will help us to describe these new contributions. The underlying concept of the energy-loss model is explained for the case of scattering by ionized impurities, where an ion moves with a constant velocity v within the electron sea of a semiconductor.

The Hamberg model is primarily focused on modeling the absorption and reflection of free carriers in the infrared regime. At first, a dielectric function $\varepsilon(k, \omega)$, is introduced, which depends on frequency and wave number. From this function, an average dynamic resistivity $\rho(\omega)$ and the corresponding dielectric function $\varepsilon(\omega)$ are obtained, as developed by (SALES, 2022; PFLUG et al., 2004).

$$\varepsilon(\omega) = \varepsilon_\infty + \varepsilon_{IR}(\omega) \tag{39}$$

here we have;

$$\varepsilon_{IR}(\omega) = \frac{i}{\varepsilon_0(\omega)\left(\rho(\omega) - \frac{i\omega}{\varepsilon_0 \omega_p^2}\right)}, \tag{40}$$

where ω_p is the plasma frequency, given by,

$$\omega_p = \sqrt{\frac{N_e e^2}{\epsilon_0 m^*}}, \tag{41}$$

with the dynamic resistivity is expressed as:

$$\rho(\omega) = i\frac{Z^2 n_i}{6\pi\varepsilon_0 N_e^2 \omega}\int_0^\infty k^2 \left[\frac{1}{\varepsilon(k,\omega)} - \frac{1}{\varepsilon(k,0)}\right] dk, \tag{42}$$

Instead of a damping and a plasma frequency, this model comprises more physical parameters as density of electrons N_e and impurities n_i as well as the effective electron mass m^*.

2.9 Magnetic Properties

Magnetism is a phenomenon present in all materials or substances, which are influenced, to a greater or lesser extent, by the presence of a magnetic field. Accordingly, materials are classified as diamagnetic, paramagnetic, or ferromagnetic. The underlying principles and mechanisms of magnetism are complex and require the framework of quantum mechanics, which is based on the orbital and spin motions of electrons and on the manner in which they interact with each other.

The focus of this work is on the study of ferromagnetism in diluted magnetic semiconductors, a form of magnetism in which materials can become magnetized and retain their magnetization even after the removal of the externally applied magnetic field. These materials are characterized by their strong interaction with magnetic fields, which constitutes a crucial factor in many industrial and technological applications. Consequently, explaining the origin of ferromagnetism in such systems remains a significant challenge, for which several theoretical models have been proposed.

2.9.1 Ruderman-Kittel-Kasuya-Yosida model (RKKY)

Proposed by Yosida (YOSIDA, 1996) to explain the possible origin of ferromagnetism in DMS, Xing et al. used this model to interpret the results of Ni-doped ITO (PELECKIS; WANG; DOU, 2006). The authors described the magnetic interaction between a single localized magnetic ion and the conduction band electrons. Due to this interaction, conduction electrons near the magnetic ion become polarized and act by generating an effective magnetic field that polarizes other nearby magnetic ions, with the polarization decaying in an oscillatory manner. This oscillation mediates ferromagnetic or antiferromagnetic exchange coupling, depending on the distance between the magnetic ions. This model is effective when a high concentration of delocalized carriers is present in the host material.

2.9.2 Mean-field Zener model

The interaction mechanism proposed by Zener is based on the strong coupling between the spin of the incomplete d-shell of an atom and the s orbital electrons. The minimum energy of this coupling corresponds to the state in which the spin of the s-shell electron aligns parallel to that of the d-shell. This $s-d$ interaction mechanism proposed by Zener assumes a uniform polarization of conduction electrons. The Zener model was used by Dietl et al. (DIETL et al., 2000) to explain magnetic ordering in diluted magnetic semiconductors (DMS). In this case, the charge carriers (electrons or holes) in the semiconductor mediate the coupling between the spins of the magnetic ions via an indirect exchange interaction of the RKKY type, based

on the $sp - d$ coupling between the magnetic ion states and the free charge carriers in the host matrix. This model has been successfully used to explain the origin of ferromagnetism in systems such as GaMnAs, GaN, and ZnO, where the long-range ferromagnetic coupling of Mn ions is mediated by holes. Although this model suggests that hole mediation is dominant, the theoretical prediction by Sato et al. (SATO; KATAYAMA-YOSHIDA, 2001) shows that high Curie temperature ferromagnetism can also be achieved in n-type ZnO doped with magnetic elements.

2.9.3 Double exchange coupling model

The double-exchange interaction is explained by the hopping of itinerant electrons between two neighboring transition-metal (TM) ions with mixed oxidation states, mediated by oxygen p orbitals (ZENER, 1951). In this mechanism, the parallel alignment of the localized t_{2g} spins and the e_g electrons minimizes the kinetic energy during electron hopping. In diluted magnetic semiconductors (DMSs), the $3d$ levels of TM ions occupying tetrahedral sites are split by the crystal field into a lower-energy doublet and a higher-energy triplet, for example, the t_{2g} levels. The spin-up (↑) and spin-down (↓) states are further split by exchange splitting. In Co-doped ZnO, the spin-up Co $3d$ states lie at lower energy than the spin-down states and are strongly hybridized with O $2p$ states. Conversely, the spin-down states of Co ions are located close to the conduction band of the ZnO host. If neighboring Co ions exhibit parallel alignment of their magnetic moments, electrons in the partially filled Co $3d$ orbitals can hop from one ion to another, thereby stabilizing the ferromagnetic ground state.

2.9.4 Bound magnetic polarons model

The ferromagnetic ordering of transition metal (TM) ions in DMS materials is also described by the bound magnetic polaron (BMP) model. In this model, the formation of bound magnetic polarons is explained by the exchange interaction between multiple localized TM ion spins and weakly localized charge carriers. The overlap of neighboring magnetic polarons leads to a long-range ferromagnetic state, and the ferromagnetic transition occurs when the polaron percolation size equals the sample size. Recently, Coey et al. (COEY; VENKATESAN; FITZGERALD, 2005) applied this model to diluted magnetic oxides. They proposed that the ferromagnetic exchange coupling of TM ions in n-type diluted magnetic oxides is mediated by shallow donor electrons trapped by oxygen vacancies, which tend to form bound magnetic polarons within their hydrogenic orbitals Figure 2.9.1.

2.10 Photoconductivity

Photoconductivity is a phenomenon observed when photons emitted from a light source of radiation hit a material, whether insulating or semiconductor, if the energy of the incident

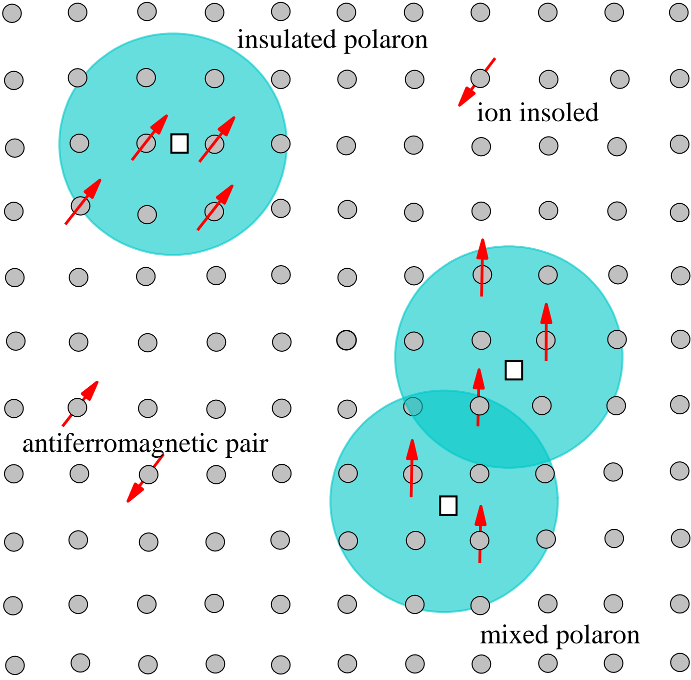

Figure 2.9.1 – Representation of two linked magnetic polarons generated by oxygen vacancies. "Source: Author's own elaboration".

photon is high enough to excite an electron from the valence, or electrons located in defect states, to the conduction band. Photo-excited electron-hole pairs are produced, participating in electrical conductivity, as shown in the experimental scheme of Figure 2.10.1(a). This behavior is often used for the design of practical optical detectors. When the material is initially in the absence of a light source, the conductivity is traditionally represented by:

$$\sigma = q(n\mu_e + p\mu_p) \tag{43}$$

Where q is the electron charge, n, p carrier concentration μ_e, μ_p are the electron and hole mobilities, respectively. After the emission of photons on the material, the conductivity changes and an increase in (Δn) and (Δp) results from photo-excitation. This process increases the electrical conductivity.

$$\sigma = q((n + \Delta n)\mu_e + (p + \Delta p)\mu_p) \tag{44}$$

Photocurrent

Photocurrent is the photo-induced electric current generated in a semiconductor material or a photosensitive device when exposed to light radiation (see Figure 2.10.1(b)), and is directly proportional to the intensity of that radiation. Several mechanisms in semiconductors have been studied, showing dependence on the active area, the wavelength of the incident light, the activation energy, and lattice defects (SILVA et al., 2026; LEE et al., 2017).

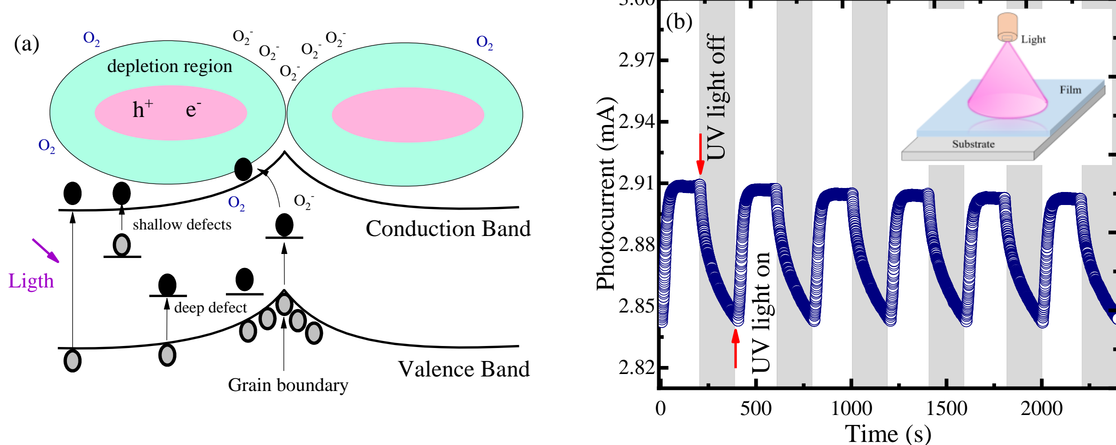

Figure 2.10.1 – (a) Schematic diagram showing the reaction on the surface of the material grains in the presence of atmospheric oxygen and (b) Photocurrent curves, the lead-colored bands, represent when UV light is off.

Typically, photocurrent is measured as the ratio between the current under illumination (I_{UV}) and the dark current (I_{dark}) PR= I_{UV}/I_{dark}. This photocurrent detection is applied in photovoltaic energy technologies, enabling devices such as solar cells (SZMYTKOWSKI, 2007), as well as optical sensors (FERNANDES et al., 2002), highlighting the fundamental role of photocurrent in optoelectronics

2.11 Gas Sensor Properties

Metal oxide-based sensors remain of interest today, as they represent non-invasive, low-cost alternatives that enable easy diagnostics. Numerous materials such as SnO_2, ZnO, TiO_2, In_2O_3, WO_2, among others, exhibit attractive physicochemical properties, including fast response times. There is a growing demand for the development of sensing devices capable of operating efficiently under varying atmospheric conditions, ranging from standard atmospheric conditions (temperature 273 K, pressure 1 Pa) to extreme temperatures and pressure variations. These sensors are also expected to be selective to specific gases, making them useful for monitoring applications across various terrestrial and space-related technological fields. The operating mechanism of these metal oxides begins with the interaction between ambient oxygen atoms and the surface of the metal oxide. This interaction results in the withdrawal of electrons from the oxide, leading to the formation of different ionic oxygen species (O_2^-, O^-, O^{2-}) on the surface (DEY, 2018), depending on the operating temperature.

$$O_{2(gas)} \rightarrow O_{2(ads)}, \tag{45}$$

$$O_{2(ads)} + e^- \rightarrow O_{(ads)} \;(T < 473 \text{ K}), \tag{46}$$

$$O_{2\,(ads)}^{-} + e^{-} \rightarrow 2O^{-}{}_{(ads)} \; (\, 373 \text{ K} < \text{T} < 473 \text{ K}), \tag{47}$$

$$2O_{2\,(ads)}^{-} + 2e^{-} \rightarrow 2O^{2-}{}_{(ads)} \; (\, \text{T} > 473 \text{ K}). \tag{48}$$

This process increases the depletion region and consequently raises the potential barrier (Schottky barrier) at the grain boundaries, which hinders electron transport and increases electrical resistance, as illustrated in Figure 2.11.1(a). When the metal oxide comes into contact with a reducing gas, such as CO, CH_4, or H_2, the gas molecules react with the adsorbed oxygen species, releasing the previously trapped electrons back into the material. This reduces the potential barrier, facilitates electron mobility, and consequently decreases the electrical resistance (see Figure 2.11.1(b)).

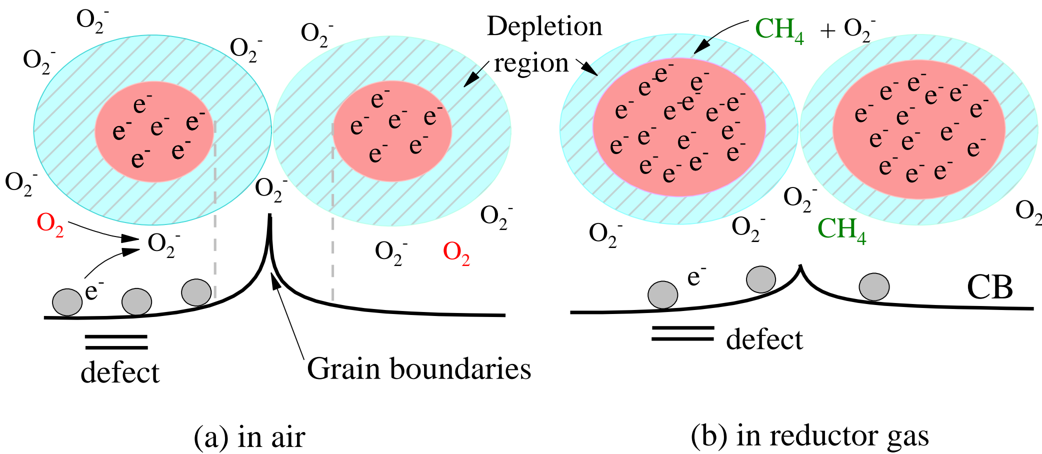

Figure 2.11.1 – (a) Diagram showing the reaction on the surface of the material grains in the presence of atmospheric oxygen and (b) after the reaction of the surface with the gas to be measured. "Source: Author's own elaboration".

3

Materials and experimental methods

Two film batches were grown. The first batch consists of $(In_{1-x}Sn_x)_2O_3$ thin films using the DC sputtering technique in the LSNCM/IF-UnB. These films were fabricated using metallic $In_{1-x}Sn_x$ targets with different x. For the second batch, commercial ITO and Fe targets were used to deposit Fe-doped ITO films using the RF sputtering technique, in collaboration with PUCP-Peru University.

3.1 Targets

For the fabrication of the metallic targets, indium (In) and tin (Sn) metallic pieces were used, which were purchased from Sigma-Aldrich with a purity of 99.99%. Both metals were weighed in the appropriate proportions to obtain different concentrations of Sn in molar fraction ($In_{0.95}Sn_{0.05}$, $In_{0.90}Sn_{0.10}$, $In_{0.88}Sn_{0.12}$, and $In_{0.85}Sn_{0.15}$).

The melting process was carried out in an arc furnace, which was previously purged three times with high-purity argon (Ar). Subsequently, a continuous flow of Ar was maintained throughout the melting process and a current of 50 A was applied, resulting in a homogeneous metallic alloy. After removal from the furnace, the alloy was pelletized using a die with a diameter of 1.5 cm under a pressure of 2 tons, yielding an $In_{1-x}Sn_x$ target, as shown in Figure 3.1.1. From the targets, ITO films were grown using the homemade DC sputtering technique. This process was carried out in the Laboratory of Synthesis of Nanomaterials and Magnetic Characterization (LSNCM) at the Institute of Physics, UnB.

For the deposition of Fe-doped ITO thin films, commercially available targets were used. The ITO target consisted of In_2O_3 (90 wt%) / SnO_2 (10 wt%), with a diameter of 2 inches and a thickness of 0.125 inches, and was acquired from Plasmaterials, Inc. The metallic Fe target had a diameter of 2 inches and a thickness of 0.15 inches and was purchased from Beijing Xing Rong Yuan Technology Co. Both targets had a purity of 99.99% (see Figure 3.1.2). The deposition of

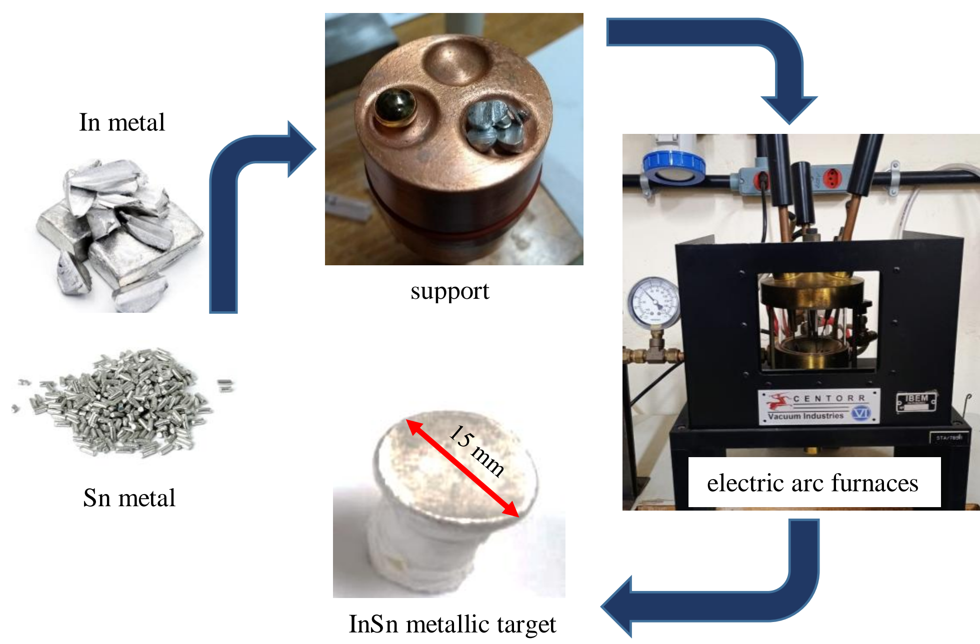

Figure 3.1.1 – Schematic of the manufacturing process for In and Sn metal targets.

Fe doped ITO was performed using the RF magnetron sputtering technique, at the Department of Sciences, Physics Section, Pontifical Catholic University of Peru (PUCP).

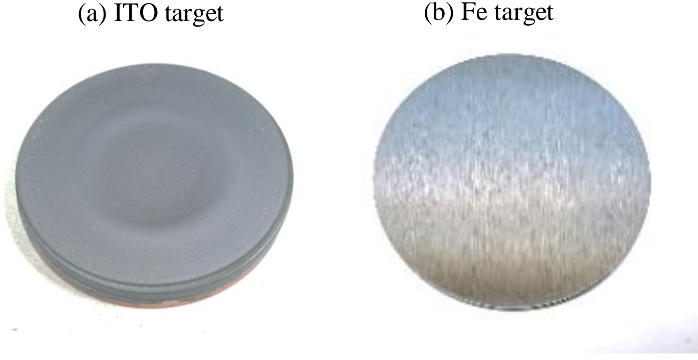

Figure 3.1.2 – Commercial two-inch targets (a) In_2O_3(90%)/SnO_2(10% wt.) (b) Metallic Fe.

3.2 Deposition of films via sputtering technique

Sputtering is a physical deposition technique and is essential for the growth of thin films under high-vacuum conditions, as it enables the deposition of metallic and oxide compounds over large areas while maintaining a uniform thickness across the substrates, thereby facilitating large-scale production. In addition, the use of magnetrons enhances ion bombardment, increasing the film deposition rates and consequently reducing sputtering times. The good adhesion achieved

on the substrates allows deposition at room temperature, and the vacuum conditions inherent to this technique ensure high purity of the sputtered material.

Sputtering consists of bombarding the surface of a solid material, referred to as the target, with highly energetic ions. As a result, atoms are ejected from the target and directed toward the substrate, where they adhere and bond with each other to form a thin film. During transport, the sputtered atoms are mainly influenced by the pressure inside the chamber, which affects the number of collisions occurring during film growth. The fewer collisions the sputtered atoms experience, the longer their mean free path, and consequently the higher the resulting deposition rate. In contrast, an increase in pressure leads to lower deposition rates.

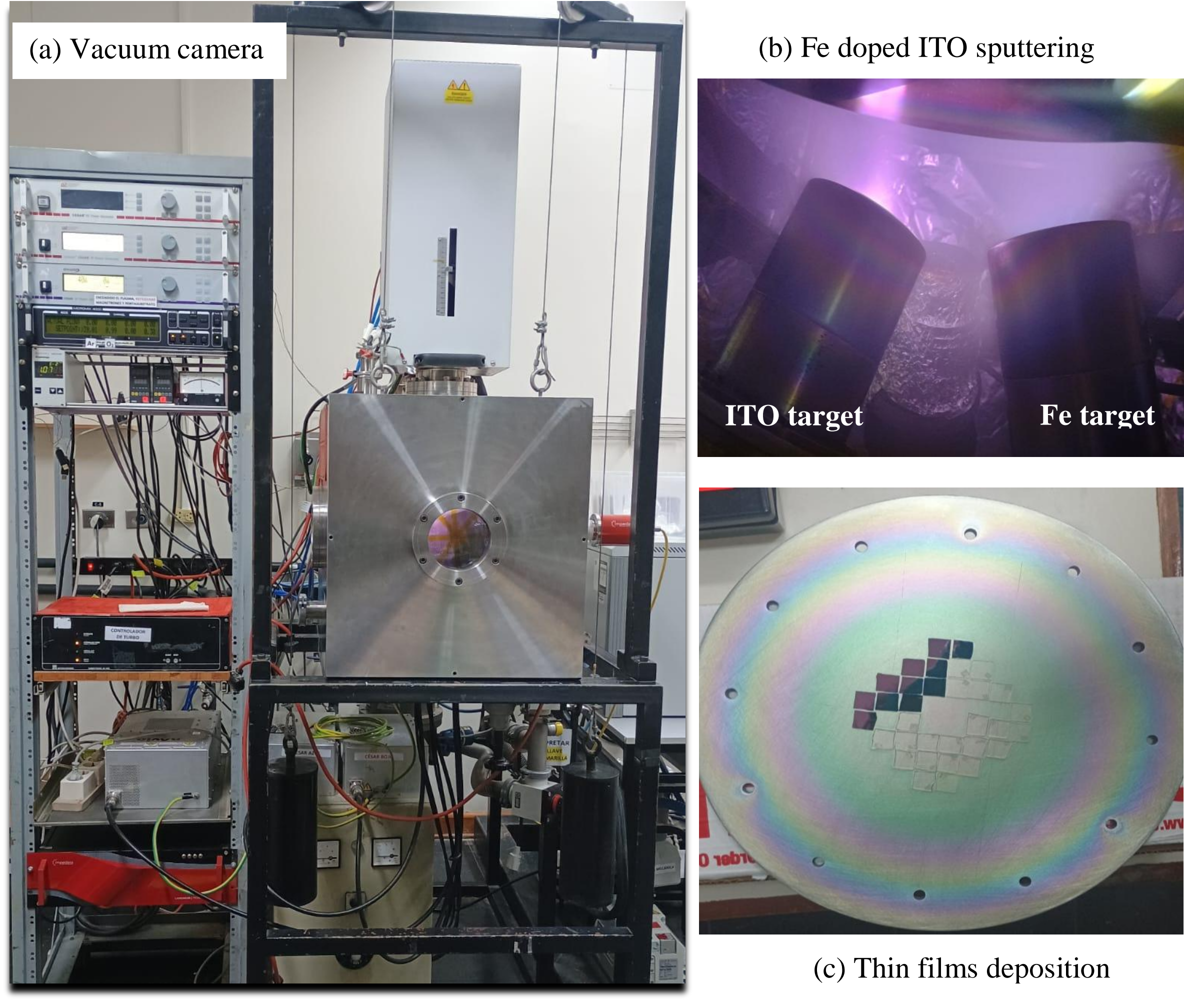

Figure 3.2.1 – (a) Vacuum sputtering station, (b) magnetrons used for co-sputtering deposition, (c) films deposited on substrates.

For the growth of ITO and Fe-doped ITO thin films, borosilicate glass, quartz, and/or fused silica substrates with dimensions of 1.0 cm × 1.0 cm and 0.5 cm × 0.5 cm were used. Prior to deposition, the substrates were cleaned with isopropyl alcohol and acetone to remove surface contaminants and then carefully dried using clean paper towels. Once cleaned and dried, the

substrates were placed inside the vacuum chamber at a distance of 7.5 cm from the target.

Subsequently, high vacuum was achieved using a turbomolecular pump, reaching a base pressure of 1.0×10^{-6} mbar. Afterward, high-purity argon gas (Ar^+) or gas mixtures of argon with reactive gases such as oxygen (Ar^+/O_2) were introduced into the chamber. The working pressure was regulated by adjusting the gas inlet flow rates through a microvalve. Once the working pressure was selected, the RF or DC power supply was increased and kept constant. In addition, the substrate temperature was maintained at room temperature throughout the entire deposition process.

3.3 Thermal Annealing

Thin films deposited by the sputtering technique generally exhibit an amorphous structure. After thermal annealing, it is possible to obtain structures with a higher degree of crystallinity. In this context, post-deposition thermal annealing treatments were carried out in an air atmosphere using a commercial furnace. Additionally, thermal annealing under vacuum conditions was performed. For this purpose, the films were placed inside a quartz tube connected to a turbomolecular pump capable of reaching a vacuum level of the order of $\sim 10^{-7}$ mbar. Once the desired vacuum level was achieved, the tube was introduced into a tubular furnace and the thermal annealing process was performed.

Annealing temperatures of up to 600 °C were used for films deposited on borosilicate substrates. For films grown on quartz or silicon substrates, the temperature could be increased up to 1000 °C. These thermal annealing processes were carried out at the LSNCM laboratory, which is equipped with furnaces and vacuum facilities.

3.4 Film Characterization

3.4.1 X-ray Diffraction

After growth and thermal annealing treatments of the films, X-ray diffraction measurements were carried out. By analyzing the obtained diffractograms, were determine the crystalline quality and identify the phases present in the films by comparing them with the crystallographic database. Rietveld refinement (GSAS - General Structure Analysis System) of the diffractograms will be performed to obtain information on lattice parameters, crystallite size, and microdeformations. These measurements were obtained using a Rigaku X-ray Diffraction equipment in the Bragg Brentano configuration, at the X-ray Diffraction Laboratory of the Institute of Geosciences, University of Brasília.

3.4.2 UV-visible Spectroscopy

To obtain TCO films with good optical properties, it is necessary to measure transmittance in the UV-visible range. These spectra also allow us to obtain information about film thickness, especially when corrugated, using the envelope method. With absorbance values, we can determine the energy gap width, refractive index, and extinction coefficient using UV-Vis spectroscopy, in addition to performing ellipsometry measurements.

A UV-2600 spectrophotometer from the Optical Characterization Laboratory of the Applied Physics group in the Institute of Physics of the University of Brasília were used to perform these measurements. Ellipsometry measurements were also performed, in collaboration with the Materials Characterization Laboratory of PUCP-Perú.

3.4.3 Scanning Electron Microscopy (SEM) and X-Ray Photoelectron Spectroscopy (XPS)

Scanning Electron Microscopy (SEM) allows us to analyze the surface and determine film thickness, as well as obtain compositional information. Additionally, by integrating an Energy Dispersive X-ray (EDS) detector with an electron microscope, we can determine the chemical composition of the material. The film images were obtained with a scanning electron microscope at the Multiuser Microscopy and Microanalysis Laboratory (LMM) at the Institute of Biological Sciences at the University of Brasília. Furthermore, we performed XPS measurements on the samples to provide information about the composition of the MT-doped ITO. The XPS measurements will be performed at the CDTN in Belo Horizonte, in collaboration with Dr. Waldemar Macedo and Department of Mechanical Engineering, in the Laboratory of Ceramic and Nanostructured Materials, at FT/UnB.

3.4.4 Atomic Force Microscopy

Morphological properties can also influence the electrical and optical characteristics of a material; therefore, it is necessary to understand its surface. This analysis allows the determination of surface roughness and grain size, which are crucial for interpreting surface resistance results. These measurements were performed at the Applied Physics Center of the Institute of Physics, University of Brasília (IF-UnB).

3.4.5 Electrical Measurements DC and AC

In order to carried out the electrical characterization we used the electrical measurements station of LSNCM. The Hall effect station were used to carried out resistivity and charge carrier density measurements using the four-probe method in the Van der Pauw configuration, applying a magnetic field up to 0.4 T. Furthermore, measurements of the resistivity as a function of temperature can provide further information. In this case, a commercial cryostat (Janis Inc.) were

used to cool the samples to 77 K and perform measurements in the range of 77 K to 300 K. AC Electrical characterization was carried out by impedance spectroscopy at room temperature using an Agilent 4284A LCR meter. Measurements were performed over a broad frequency range (1KHz-1MHz), and the acquired data were processed and analyzed using a LabVIEW-based data acquisition and analysis program.

3.4.6 Magnetic measurements

To characterize the magnetic properties of samples containing Fe magnetic measurements were performed using the SQUID magnetometer, Quantum Design, at LSNCM. Measurements were performed with varying magnetic fields up to 7 T and temperatures from 2 K to 400 K to obtain hysteresis and magnetization as a function of temperature curves.

3.4.7 Gas sensor measurement

To determine the gas sensor properties of the films, the electrical resistance was measured in the presence of gas (4 % CH_4/He)/air. The sensor test was carried out using a gas flow of 150 cm^3/min a test chamber with a volume of 128 cm^3. Besides measurements in the presence of hydrogen gas (H_2), using the same configurations were carried out. The electrical resistance data were recorded using a data acquisition system (KEITHLEY, model 196) and the temperature of the sensor material was controlled by a temperature controller (LAKESHORE, model 331).

3.4.8 Photocurrent measurement

The photocurrent responses for UV light were used at room temperature, UV light sensing tests were carried out in a closed chamber equipped with a ~26 mW/cm^2 UV lamp (OceanTech), implemented with a two-probe measurement station. A constant voltage of between 1-15 V (depending on the film resistance) were applied to the film electrode using a standard power supply, while the UV illumination was periodically switched on and off in cycles of 2.5 min. The corresponding photocurrent response was recorded in real time using a digital multimeter (Keithley model 196).

3.4.9 DFT calculations

Density functional theory (DFT) calculations were performed, employed the Vienna Ab initio Simulation Package (VASP) and the Quantum ESPRESSO package under the GNU General Public License. The study focused on indium oxide ($In_{32}O_{48}$), The Kohn-Sham (KS) equations were solved using the projector-augmented wave (PAW) method, with the KS states expanded by using plane waves. The electronic and structural properties were described through the Perdew Burke Ernzerhof (PBE) Exchange correlation functional. For the integration of the Brillouin zone (BZ), a Γ-centered k-mesh of $4 \times 4 \times 4$ was used for the optimization process,

and $8 \times 8 \times 8$ for electronic properties (density of states and bands structure). During structural optimization, the self-consistent cycle converged with a total energy criterion of 10^{-6} eV, and atomic forces were minimized to less than 0.01 eV $Å^{-1}$. A plane-wave energy cutoff of 600 eV was applied in all simulations. This simulations employed VASP software, was performed using the supercomputers of Santos Dumont LNCC, CENAPAD and to the "Centro Nacional de Processamento de Alto Desempenho em São Paulo". Simulations using QUANTUM ESPRESSO was performed using the computing facilities of INKARI-IAAPP of the National University of San Agustín of Arequipa.

4

Experimental results and discussion

4.1 Dynamic defect compensation in Sn-doped In_2O_3 thin films: correlating structural, electrical, and optical properties through experiment and DFT calculation

There is a growing interest in understanding the relationship between the extrinsic doping (Sn) and intrinsic defects, such as oxygen vacancies and interstitial oxygens, which determines the electrical transport properties of ITO. In this context, in the following section, we investigate the effects of Sn doping on the In_2O_3 matrix by combining experimental results and DFT-based approach, providing insight into the defect-driven mechanisms that control the structural, optical, and electrical behavior of ITO. **(Under submission process)**

4.1.1 Experimental details

ITO thin films were grown using a metallic targets with different stoichiometries $In_{0.95}Sn_{0.05}$, $In_{0.90}Sn_{0.10}$, $In_{0.88}Sn_{0.12}$ and $In_{0.85}Sn_{0.15}$. For the fabrication of the targets, metallic pieces of In and Sn purchased from Sigma–Aldrich with a purity of 99.99% were used. Both pieces were weighed in the appropriate proportions to obtain different Sn concentrations in atom fraction. The melting process was carried out in an arc furnace by applying a current of 50 A in the presence of high–purity Ar^+, resulting in a homogeneous metallic mixture. Subsequently, the metallic mixture was pelletized using a die with a diameter of 1.5 cm under a pressure of 2 tons. Glass substrates of 0.5 cm × 0.5 cm dimension were used to grown the films, these one were previously cleaned in isopropyl alcohol and acetone PA in ultrasound for 15 min. The distance (target–substrates) was 15 mm, a vacuum of 10^{-5} mbar was established as base pressure, then Ar was introduced maintaining a sputtering pressure of 4.2×10^{-2} mbar, later we applied a potential difference of 1400 V, the growth lasted 2 hours. After the growth of the

films, thermal annealing were carried out at 500 °C for 2 h, using a heating rate of 600 °C/h under vacuum conditions with a pressure of 2.3×10^{-6} mbar during annealing. Subsequently, the films was characterized by performing X–ray diffraction (XRD) measurements using a Rigaku diffractometer with Cu–Kα radiation (λ = 1.5418 Å) in the range of $20° \leq 2\theta \leq 70°$. XPS spectra were acquired (60 scans) using a pass energy of 0.25 eV and a step size of 0.1 eV. A Flood Gun was employed for charge compensation with a current of 0.21 μA, and the spectra were calibrated using a reference of 284.6 eV for C 1s. The peaks were fitted with CasaXPS using a combination of Gaussian and Lorentzian functions over a background resembling the Shirley function. UV–Vis spectra were collected using a Ellipsometer, in transmittance mode due to the dimensions of the films, in the spectra range of (250–2500 nm). For micrographs, a Nanosurf Flex-Axiom AFM microscope with a Nanosurf C3000 controller allowing 24-bit resolution was used scanned in an area of 5.0×5.0 μm^2 for different positions on the surface of the films. Resistivity measurements were performed at room temperature using a four-point system using the van der Pauw configuration, using a current measurement equipment and Keithley voltmeter. The photocurrent responses for UV light were used at room temperature, UV light sensing tests were carried out in a closed chamber equipped with a ~26 mW/cm^2 UV lamp (OceanTech), implemented with a two-probe measurement station. A constant voltage of 1.5 V was applied to the film electrode using a standard power supply, while the UV illumination was periodically switched on and off in cycles of 2.5 min. The corresponding photocurrent response was recorded in real time using a digital multimeter (Keithley model 196). finally to measure the properties of the gas sensor, the electrical resistance was measured in the presence of gas (4 % CH_4/He)/air corresponding to a concentration of 40000 ppm, the sensor test was carried out using a gas flow of 150 cm^3/min a test chamber with a volume of 128 cm^3. The electrical resistance data were recorded using a data acquisition system (KEITHLEY, model 196) and the temperature of the sensor material was controlled by a temperature controller (LAKESHORE, model 331).

4.1.2 Theoretical calculation

Self-consistent calculations were performed with the Vienna *Ab initio* Simulation Package (VASP) software (KRESSE; FURTHMüLLER, 1996; HAFNER, 2008), based on density functional theory (DFT) (HOHENBERG; KOHN, 1964; KOHN; SHAM, 1965). The Perdew–Burke–Ernzerhof (PBE) functional (PERDEW; BURKE; ERNZERHOF, 1996) was used to describe exchange and correlation effects, with the valence atomic configurations $5s^2$ $5p^1$ $4d^{10}$ for In, $2s^2$ p^4 for O and $5s^2$ $5p^2$ $4d^{10}$ for Sn, respectively. The Kohn–Sham (KS) equations were solved using the projector augmented-wave (PAW) method (BLöCHL, 1994) with KS wavefunctions expanded in a plane-wave basis set. Applying a cutoff energy of 600 eV and $4 \times 4 \times 4$ k-points to give sufficient convergence to optimize the In_2O_3 unit cell with 80 atoms, the In ions were then replaced by Sn ions obtaining four structures with different stoichiometry. We adopted a total energy convergence criterion of 10^{-6} eV for self-consistent electronic cycles, and the interatomic forces were required to be less than 0.01 eV/Å during structural optimization.

The $In_{31}Sn_1O_{48}$, $In_{30}Sn_2O_{48}$, represent low concentrations of 3.2% and 6.3% and for higher concentrations $In_{29}Sn_3O_{48}$ 9.2% and $In_{28}Sn_4O_{48}$, 12.4% interstitial oxygens were introduced in the 12.4% Sn doped structure representing more realistic conditions of the experimental results. Finally, we proceeded to perform the parameterization, DOS, PDOS and band structure calculations on each of the structures using K-point $8 \times 8 \times 8$. Structural visualizations and analyses were carried out using the VESTA software (MOMMA; IZUMI, 2008), while the VASPKIT toolkit was used for data post-processing (WANG et al., 2021).

4.1.3 Structural properties

Figure 4.1.1(a) presents the XRD patterns of bixbyite-type cubic In_2O_3 thin films in agreement with the standard JCPDS card no. 06-0416 (space group $Ia\bar{3}$, No. 206) with nominal Sn concentrations of 0, 5, 10, 12, and 15%. All films exhibit good crystalline quality, showing the characteristic diffraction peaks of the In_2O_3 matrix, indexed to the (211), (222), (231), (400), (332), (431), (440), and (622) planes, with a pronounced preferential orientation along the thermodynamically favored (222) direction. Within the detection limit of the XRD equipment, no secondary phases associated with SnO_2 and/or SnO are observed, suggesting that Sn ions are predominantly incorporated into the In_2O_3 lattice. However, a weak additional reflection appears at $2\theta \approx 32°$ for the film doped with 4.9% Sn, as highlighted in Figure 4.1.1(b), which can be attributed to a minor metallic In phase, which has also been reported in previous studies and is commonly associated with thermal treatments carried out under reducing atmospheres, such as vacuum conditions (VILCA-HUAYHUA et al., 2020).

In order to provide a more quantitative structural analysis, Rietveld refinements were performed for all films using the GSAS software package (TOBY; DREELE, 2013), employing Lorentzian peak-shape functions. A representative refinement is shown in Figure 4.1.1(b). The blue symbols correspond to the observed diffraction data (Obs), while the continuous orange line represents the calculated pattern (Cal). The difference curve (Obs–Cal) is displayed as green dots, which linearity indicating a good agreement between the experimental and calculated diffraction profiles. The vertical tick marks denote the Bragg reflection positions expected for the crystalline In_2O_3 phase (pink) and the minor metallic In phase (sky blue). Moreover, within the bixbyite In_2O_3 crystal structure, Sn atoms substitute In at the (0.25, 0.25, 0.25) crystallographic b-site, which are energetically more favorable to be occupied compared to d-sites (TRIPATHI et al., 2012; BINCZYCKA et al., 2005), leading to the formation of a substitutional solid solution. The Sn concentration was quantitatively determined by refining the site-occupation factor during the Rietveld analysis, which enables a reliable and direct estimation of the Sn content incorporated into the In_2O_3 lattice (see Figure 4.1.3 (b)).

For the undoped In_2O_3 film, the lattice parameter (a = 10.116 ± 0.001 Å) obtained from the refinement shows in agreement with the reported bulk In_2O_3 value of 11.117 Å (MAREZIO, 1966) (Table 4.1.1). However, a clear reduction in the lattice constant is observed

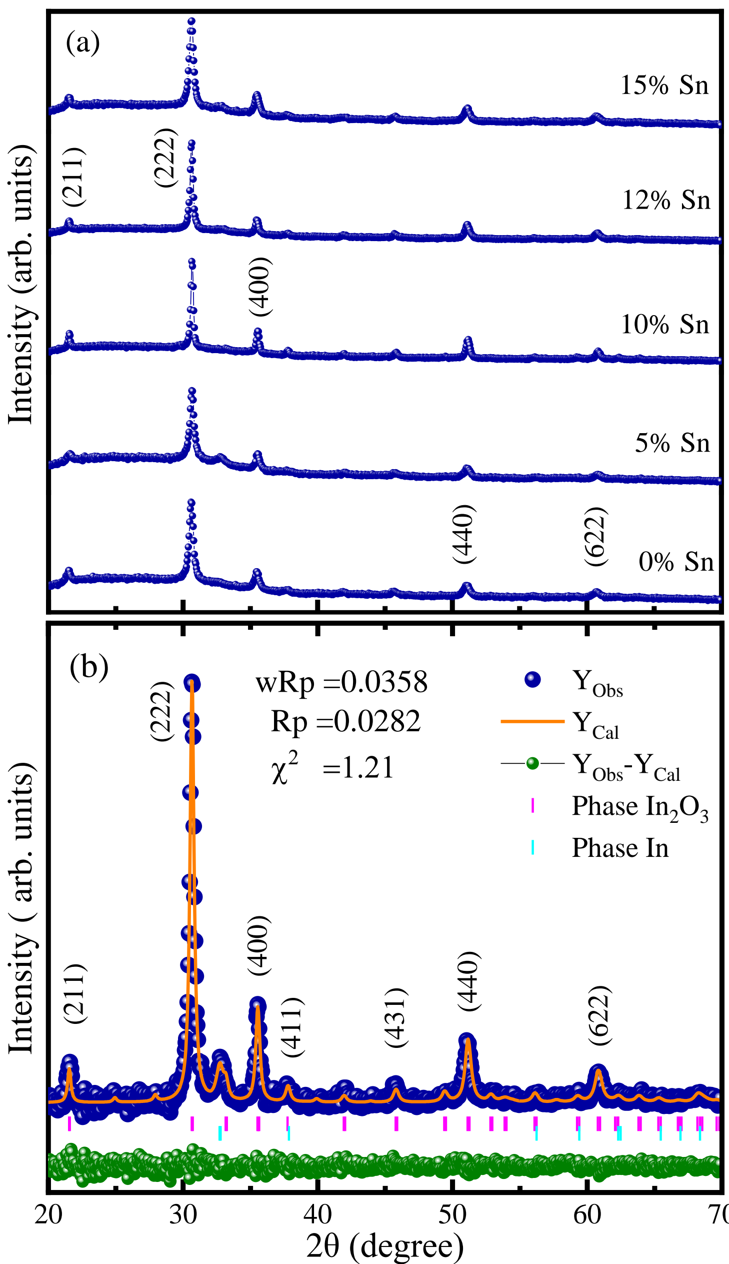

Figure 4.1.1 – (a) XRD patterns of the different $(In_{1-x}Sn_x)_2O_3$ films (x=0, 0.05, 0.10, 0.12, 0.15). (b) Rietveld Refinement fit for the In_2O_3 doped with 5%Sn.The blue circles represent the experimental data Y_{Obs}, the orange line represents the fit Y_{Cal}, the green line the difference between Y_{Obs}-Y_{Cal}, the pink line is the phase of In_2O_3 and the sky blue line is a metallic phase of indium.

for Sn concentrations around 5-7.6%, which can be attributed to the substitution of In^{3+} ions (ionic radius: 0.81 Å) by smaller Sn^{4+} ions (ionic radius: 0.71 Å) within the In_2O_3 lattice. This substitutional incorporation leads to a contraction of the lattice parameter as the Sn^{4+} content increases, consistent with the formation of a substitutional solid solution.

Furthermore, the reduction of the lattice parameter *a* up to a critical Sn concentration, followed by its subsequent increase, is a particularly intriguing observation. A plausible explanation can be associated with the aliovalent substitution of In^{3+} by Sn^{4+} ions, which requires

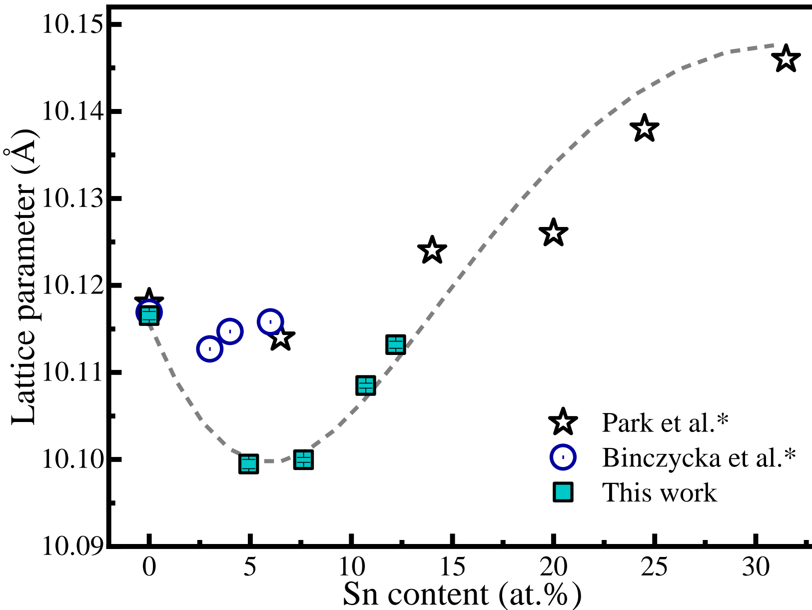

Figure 4.1.2 – Lattice constant as a function of Sn concentration. Data reported by Park *et al.* (PARK et al., 2011) and Binczycka *et al.* (BINCZYCKA et al., 2005) are included for comparison. The dashed line is a guide to the eye.

charge compensation mechanisms within the lattice, at low Sn concentrations, this compensation is primarily achieved through the formation of oxygen vacancies (O^{Vac}). However, these defect mechanisms cannot increase indefinitely, and beyond a certain Sn content, alternative compensation processes become energetically favorable. According to Frank et al., oxygen interstitials (O^{int}), in two types, may form in Sn-doped In_2O_3 structure, one loosely bound to Sn ions and another forming a strongly bound Sn_2O_4 complex. The authors report that at low Sn doping levels (Sn ≤ 4 at.%), the carrier concentration is mainly governed by loosely bound Sn–O defect complexes. In contrast, at higher Sn concentrations, an expansion of the lattice parameter a is observed, as shown in Figure 4.1.2. This lattice expansion can be correlated with an increased concentration of O^{int} and a partial change in the oxidation state of Sn from Sn^{4+} to Sn^{2+}, as evidenced by the XPS analysis (discussed in more detail below). The substitutional incorporation of Sn^{2+} ions (ionic radius = 1.22 Å) in place of In^{3+} ions (ionic radius = 0.81 Å) would naturally lead to an increase in the lattice parameter. This behavior is consistent with experimental values reported by Park et al., who demonstrated that the lattice constant of ITO films begins to increase for Sn concentrations above 6.3% (PARK et al., 2011).

The average crystallite size ($\langle D \rangle$) was estimated using the Scherrer equation, $\langle D \rangle = K\lambda/\beta_{\text{Sample}} \cos\theta$, where β_{Sample} denotes the full width at half maximum (FWHM) associated with size induced broadening of the diffraction peaks, the constant K is the Scherrer shape factor, which depends on the crystallite morphology; a value of $K \approx 0.9$ is commonly adopted for approximately spherical crystallites. Instrumental broadening was corrected by subtracting the instrumental contribution from the measured FWHM, according to $\beta_{\text{Sample}} = \beta_{\text{Meas.}} - \beta_{\text{Inst.}}$. The average crystallite size was subsequently extracted from the corrected peak broadening and are

Table 4.1.1 – Results of structural paramenters of In_2O_3 films with different Sn doped obtained from the XRD Rietveld refinement, lattice parameter (a), average crystallite size ($< D >$), Sn concentration obtained by XRD (Sn_{XRD}) and EDS Sn_{EDS}, average roughness (Rq) from AFM micrography. $O^{Non-Struc}/O^{Struc}$, Sn^{2+}/Sn^{4+} ratio obtained by XPS with an adjustment error below 0.5%, the S=wRp/Rp represents the quality of the fit using the Rietveld method.

Sn doped (at.%)	a (Å)	$< D >$ (nm)	Sn_{XRD} (%)	Sn_{EDS} (%)	Rq (nm)	O^{N-S}/O^{S}	Sn^{2+}/Sn^{4+}	S
0	10.116	24 ± 2	-	-	2.1 ± 0.1	0.82	-	1.25
5	10.099	23 ± 2	6.1 ± 0.1	4.9 ± 0.2	5.1 ± 0.3	1.27	0.14	1.27
10	10.100	45 ± 1	4.9 ± 0.1	7.6 ± 0.2	3.6 ± 0.4	1.20	0.35	1.25
12	10.108	43 ± 1	13.4 ± 0.1	10.7 ± 0.2	1.5 ± 0.1	2.79	0.63	1.26
15	10.113	24 ± 2	15.6 ± 0.1	12.2 ± 0.2	6.7 ± 0.5	1.63	0.90	1.25

summarized in Table 4.1.1.

The $\langle D \rangle$ exhibits a nontrivial dependence on the Sn dopant concentration. Specifically, $\langle D \rangle$ increases from approximately 24 nm to about 45 nm at a nominal Sn content of 12%, followed by a decrease to nearly 24 nm when the Sn concentration is further increased to 15% (see Table 4.1.1). This behavior reveals a non-monotonic evolution of the crystallinity as a function of dopant content. Such a trend points to a competition between dopant-assisted grain growth and defect-induced lattice disorder, which cooperation will be discussed in greater detail throughout the manuscript.

4.1.4 EDS and AFM results

Figure 4.1.3(a) shows the EDS analyses of In_2O_3 thin films with different Sn concentrations, revealing the constituent elements of ITO (In, Sn, and O). A homogeneous atomic distribution is observed throughout the films, indicating that Sn is well incorporated into the In_2O_3 lattice. In addition, the Sn atomic percentages were determined, yielding chemical compositions of 4.9%, 7.6%, 10.7% and 12.2%. As shown in Figure 4.1.3(b), where the nominal Sn content is plotted along the x-axis and the experimentally determined concentrations (from EDS and XRD) along the y-axis, these values are in close agreement with the nominal target compositions and lie within the experimental uncertainty. This result demonstrates a strong correlation between the Sn concentrations obtained from EDS and those inferred from XRD analysis. From this point onward, the Sn concentrations used throughout the manuscript refer to the values obtained from EDS.

To assess the film morphology, atomic force microscopy (AFM) measurements were performed on the Sn-doped In_2O_3 films. The corresponding images are shown in Figure 4.1.4, revealing average surface roughness values in the range of 1.5–7 nm. For the film doped with 10.7% Sn, a minimum root-mean-square roughness of approximately 1.5 nm is obtained (see Figure 4.1.4 (d)), indicating a smoother surface and an overall improvement in surface quality.

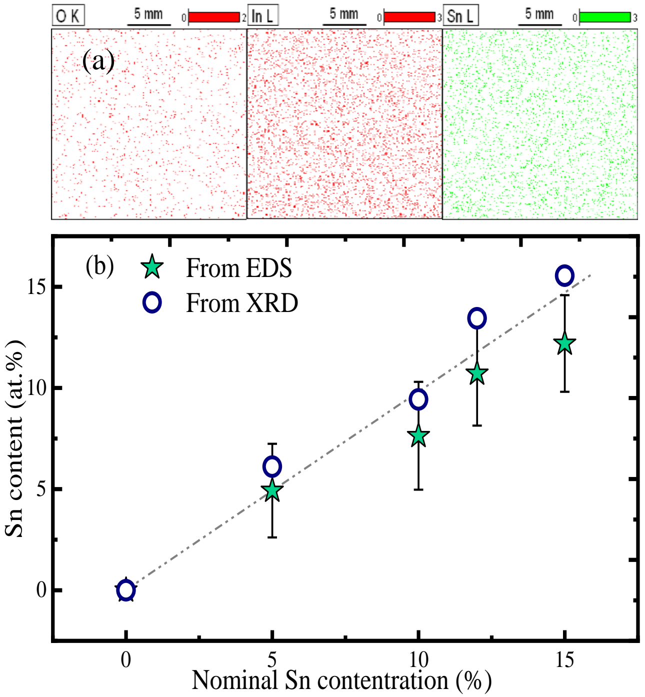

Figure 4.1.3 – (a) Atomic distribution of elements of Sn-doped In_2O_3 along the film (b) chemical composition by EDS and XRD analysis for the films with different nominal Sn concentrations (0, 5, 10, 12, 15%).

This behavior can be correlated with the enhanced crystallinity observed by XRD.

4.1.5 XPS analysis

Figure 4.1.5(a) presents the wide-range X-ray photoelectron spectroscopy (XPS) survey spectra of In_2O_3 thin films with different Sn concentrations. The spectra clearly reveal the presence of In, Sn, and O core-level peaks, in good agreement with the compositional analysis obtained from EDS measurements. In addition, weak C 1s signals are observed, which are commonly attributed to adventitious carbon species adsorbed on the film surface during exposure to ambient atmosphere prior to XPS analysis.

This carbon signal is useful for calibrating the binding energies in the high-resolution spectra of each element in the ITO films by referencing the C 1s peak at 284.8 eV (GRECZYNSKI; HULTMAN, 2022).

High-resolution XPS O 1s spectra were fitted with two components, the first component, centered at 529.3 ± 0.4 eV, is assigned to lattice (structural) oxygen (O^{Struc}), which is typically observed at lower binding energies in the range of 529–530 eV. This contribution is associated with In/Sn–O bonds in the bixbyite Sn-doped In_2O_3 structure. The second component, located at 530–532 eV, corresponds to non-structural oxygen species ($O^{\text{Non-Struc}}$). The assignment of this peak remains debated in the literature. It is frequently attributed to chemisorbed oxygen-related species at the surface, such as hydroxyl groups (OH^-), adsorbed molecular species (e.g., CO

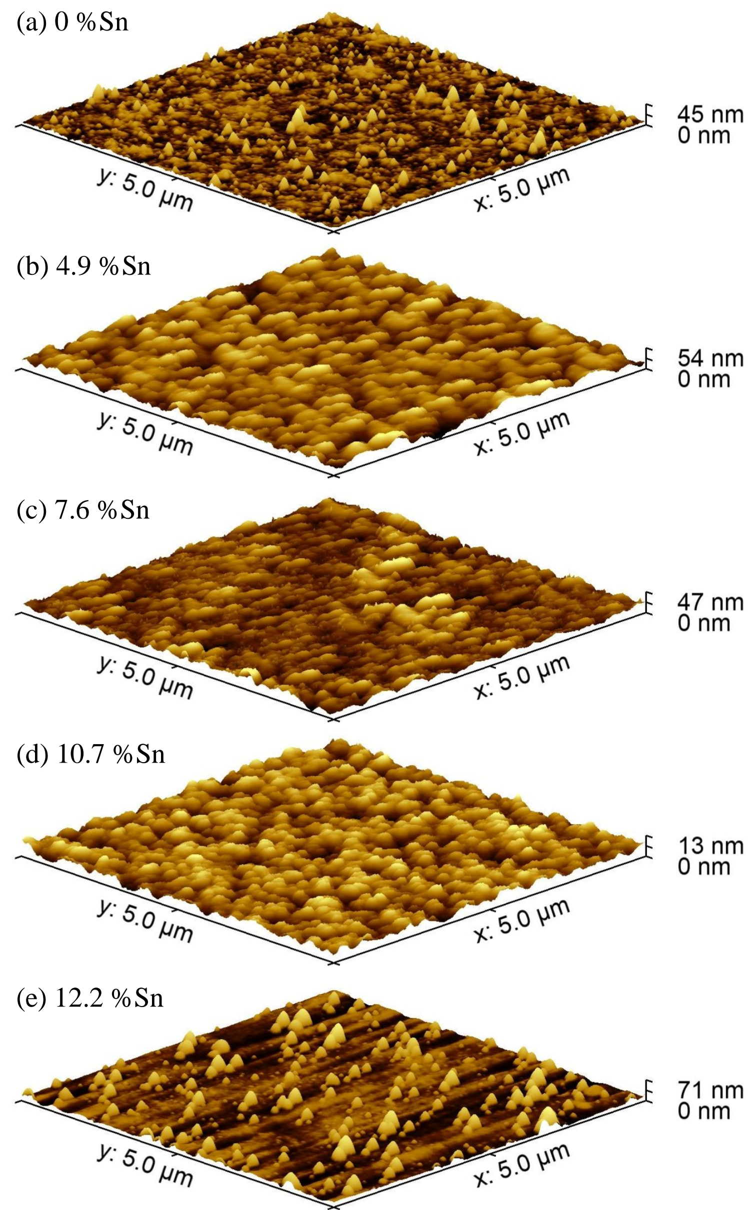

Figure 4.1.4 – AFM images of films for different concentrations of Sn (a) 0% , (b) 4.9% , (c) 7.6%, (d) 10.7%, (b) 12.2% Sn.

and CO_2) or O^{Vac} (ARAGÓN et al., 2015). According to Sahai *et al.*, the $O^{\text{Non-Struc}}$ contribution may arise from both O^{Vac} and O^{int}, with the binding energy positions following the sequence O^{Struc}<O^{Vac}< O^{int} (SAHAI; GOSWAMI, 2014). Considering that all samples were stored under similar conditions, variations in the $O^{\text{Non-Struc}}$ component are unlikely to originate solely from surface-adsorbed species such as hydroxyl groups or carbon-based radicals. Instead, these changes are more plausibly related to structural modifications within the material, consistent with the lattice distortions and phase evolution evidenced by the XRD analysis. This observation is consistent with previous reports on ITO (GöKçELI; KARATEPE, 2021; HAI-BO et al., 2007).

Figure 4.1.5(c) shows the Sn 3d core-level XPS spectra of Sn-doped In_2O_3 thin films. As the Sn concentration increases, a noticeable broadening of both the Sn $3d_{5/2}$ and Sn $3d_{3/2}$ peaks

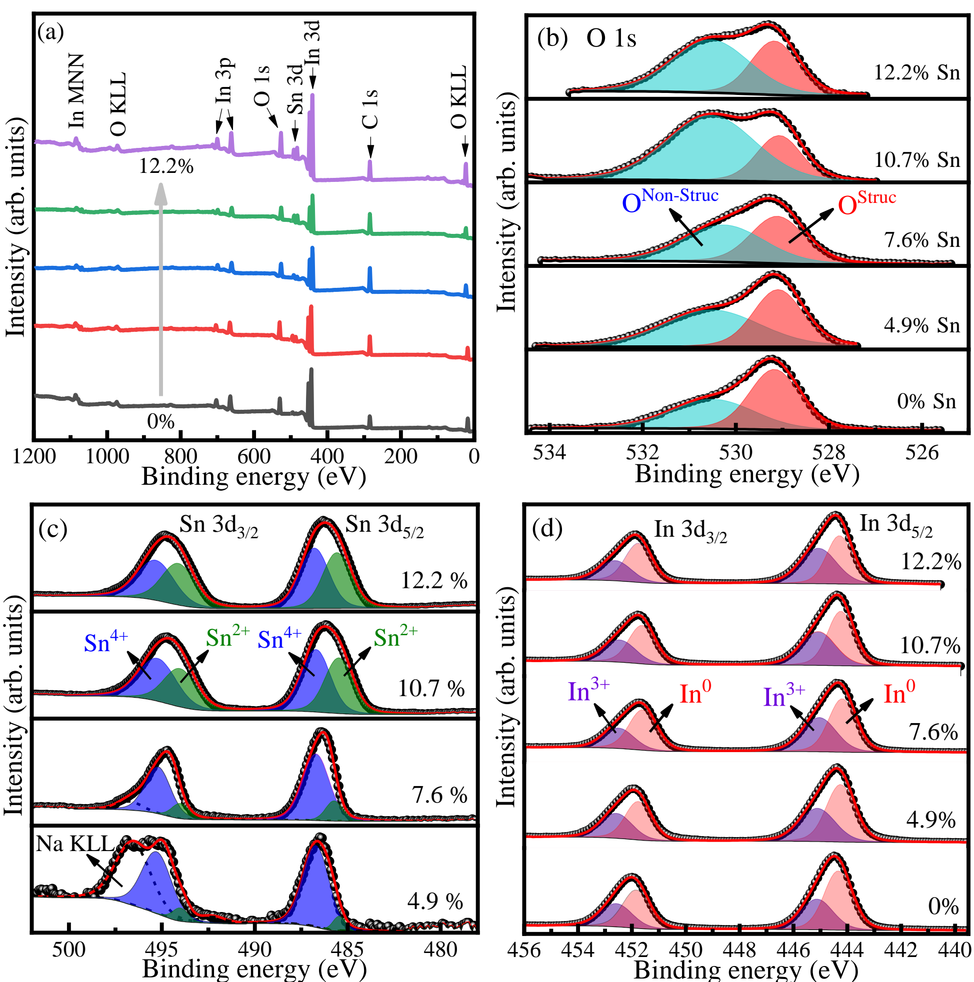

Figure 4.1.5 – XPS spectra of films for different concentrations of Sn (a) Survey, (b) O 1s orbital, (c) Tin (Sn) peaks related to $3d_{3/2}$ and $3d_{5/2}$ orbitals, (d) indium (In) peaks related to $3d_{3/2}$ and $3d_{5/2}$ orbitals.

is observed, indicating the coexistence of multiple tin oxidation states. This behavior is confirmed by peak deconvolution, which reveals two distinct components assigned to Sn^{2+} and Sn^{4+} species. For the Sn $3d_{5/2}$ orbital, these components are centered at binding energies of 485.3 ± 0.2 eV and 486.6 ± 0.2 eV, respectively, in good agreement with reported values for mixed-valence tin oxides. The relative integrated area ratio $[Sn^{2+}]/[Sn^{4+}]$, summarized in Table 4.1.1, exhibits a strong dependence on Sn concentration, increasing from 0.14 to 0.90 as the dopant level rises. This trend indicates a progressive stabilization of the Sn^{2+} oxidation state at higher doping levels. Such behavior may be related to charge-compensation mechanisms involving the formation of oxygen-related defects, such as O^{int}, potentially associated with SnO-like local environments, which help maintain charge neutrality and thermodynamic equilibrium within the lattice. An additional peak located at approximately 496.4 eV is observed in the film with 4.9 at.‰ Sn (see Figure 4.1.5(c)). This feature is likely associated with the Na KLL Auger transition (CHEN et al., 2020). Considering that the films were deposited onto glass substrates, its presence may be related to microcracks in the film, which locally expose the underlying substrate and allow the detection of sodium from the glass during the XPS measurements.

Figure 4.1.5(d) presents the high-resolution XPS spectra of the In 3d core level. The spectra exhibit the characteristic spin–orbit doublet corresponding to the In $3d_{5/2}$ and In $3d_{3/2}$ states, with a noticeable asymmetry in the high-binding-energy shoulders of both components. This asymmetry suggests the coexistence of two distinct chemical states, and accordingly the spectra were fitted using two contributions for each spin–orbit component. The dominant components, located at binding energies of 445.0 ± 0.2 eV and 452.6 ± 0.2 eV, are assigned to In^{3+} species. Additional lower-binding-energy components at 443.9 ± 0.2 eV and 451.7 ± 0.2 eV are observed for the In $3d_{5/2}$ and In $3d_{3/2}$ orbitals, respectively, and are attributed to metallic indium (In^0). The coexistence of oxidized and metallic indium is consistent with the traces of metallic In detected by XRD analysis. These results indicate that a fraction of indium is present in a reduced oxidation state, most likely localized at the film surface.

4.1.6 Electrical properties

The electrical properties of the films were evaluated at room temperature using a four-point probe system in the Van der Pauw configuration. The electrical resistivity (ρ), charge carrier concentration (N_{Hall}), and Hall mobility (μ_{Hall}) extracted from the Hall measurements are summarized in Table 4.1.2. A clear increase in the charge carrier concentration is observed for the Sn-doped films compared to the undoped In_2O_3 film. This enhancement is commonly attributed to the aliovalent substitution of In^{3+} ions by Sn^{4+} ions in the In_2O_3 lattice, which introduces additional free electrons. Nevertheless, the observed electrical behavior cannot be explained solely by a simple substitutional model. As suggested by XRD and XPS analyses, the aliovalent solid solution formed by Sn^{4+} and In^{3+} ions induces deviations from stoichiometry through the generation of oxygen-related point defects, such as O^{Vac} and O^{int}. These defects play a crucial role in the charge compensation process and strongly influence the transport properties. As a consequence, at relatively low to intermediate Sn contents, the electrical resistivity decreases markedly, reaching a minimum value of 7.4×10^{-4} Ω·cm for the film doped with 10.7% Sn (see Table 4.1.2). This value is in good agreement with the resistivity range typically reported for ITO thin films (HUAYHUA et al., 2025).

Figure 4.1.6 shows that the maximum carrier concentration correlates with the solubility limit of Sn in In_2O_3, reaching its highest N_{Hall} value at approximately 10% Sn doping, in agreement with previously reported results for ITO. On the other hand, the dashed blue line in Figure 4.1.6 represents the theoretical values assuming that each soluble Sn atom contributes one free electron ($N = 3 \times 10^{20} \cdot \mathrm{Sn}\%$). At low Sn concentrations, the experimental N_{Hall} values are close to the theoretical prediction, indicating that Sn substitutions are predominantly electrically active in this regime. However, as the Sn content increases, the N_{Hall} values progressively deviate from the theoretical ones until a critical value is reached, suggesting that a fraction of the Sn^{4+} ions becomes electrically inactive.

After the Sn solubility limit (~ 10%) is exceeded, the concentration of free electrons is

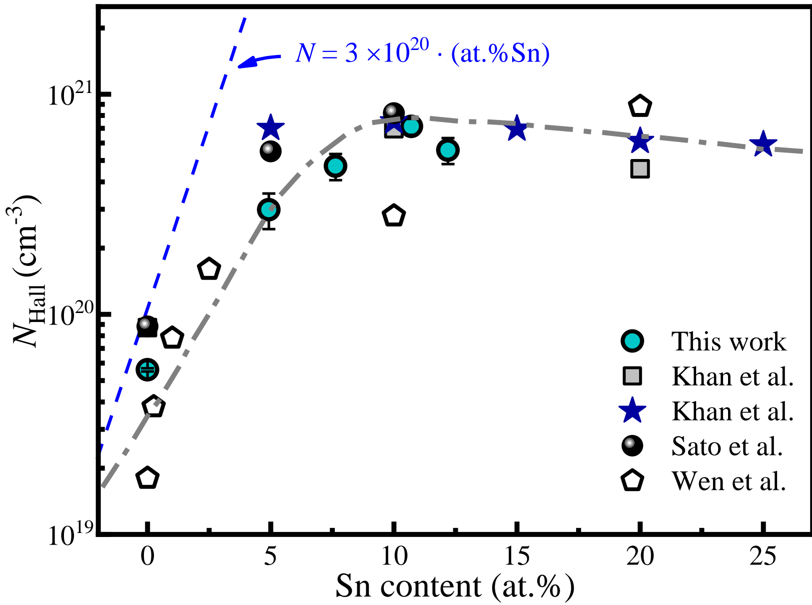

Figure 4.1.6 – Charge carrier measurements obtained by Hall effect for In_2O_3 films doped with different Sn concentrations. Experimental results were included: Khan et al. (KHAN et al., 2020), Khan et al. (KHAN et al., 2022), Sato et al. (SATO et al., 2010) Wen et al. (WEN et al., 1992).

limited by the formation of self-compensating intrinsic defects that arise to restore thermodynamic equilibrium in the presence of excess Sn. These defects act as compensating centers, thereby limiting further increases in the N_{Hall} despite continued Sn incorporation. This trend is evident in Figure 4.1.6, which also includes reference data from the literature for comparison, confirming the observed behavior (KHAN et al., 2020; KHAN et al., 2022). In light of the above discussion, this behavior can be understood in terms of the interplay between O^{Vac} and O^{int}. In particular, the formation of O^{int} is enhanced at Sn concentrations above $\sim$ 5%, where these defects may participate in the formation of Sn–O-related complexes, as suggested by previous studies (FRANK; KöSTLIN, 1982; GONZáLEZ et al., 2001). Besides, the formation of stable, nonreducible Sn–O complexes has also been proposed (FRANK; KöSTLIN, 1982). The impact of these defect complexes is evidenced by DFT calculations discussed in Sec. 4.1.9.

In addition, as show in Table 4.1.2, increasing the Sn concentration leads to a systematic enhancement of the Hall mobility (μ_{Hall}), reaching a maximum value of 11.9 cm^2 V^{-1} s^{-1} for the film doped with 10.7% Sn. This improvement is correlated with the increase in crystallite size inferred from the XRD analysis, which reduces the density of grain boundaries and, consequently, suppresses electron scattering.

4.1.7 Optical properties

Figure 4.1.7 shows the optical transmittance spectra of undoped and Sn-doped In_2O_3 thin films with different Sn concentrations measured in the UV–Vis–NIR spectral range (250-2500 nm). The undoped film exhibits high transparency in the visible region, with a slight reduction

Table 4.1.2 – Electrical resistivity (ρ), carrier concentration (N_{Hall}) and Hall mobility (μ_{Hall}) obtained by four-point probe method. Transmittance (T_{max}) and results obtained from the adjustments of the transmittance spectra using the Tauc Lorentz and the Hamberg model, thickness (t_{Opt}), carrier concentration (N_{Opt}), electron effective mass (γ).

Sn doped (at.%)	ρ ($\Omega \cdot cm$)	N_{Hall} ($\times 10^{20}$cm^{-3})	μ_{Hall} cm^2/V ·s	T_{max} (%)	t_{Opt} (nm)	N_{Opt} ($\times 10^{20}$cm^{-3})	γ
0	2.3×10^{-2}	0.56 ± 0.09	4.8 ± 0.9	77.4	336 ± 3	0.21 ± 0.09	0.293
4.9	6.1×10^{-3}	2.98 ± 0.55	4.1 ± 1.4	87.1	323 ± 3	1.51 ± 0.15	0.284
7.6	1.5×10^{-3}	4.71 ± 0.64	8.9 ± 1.1	85.7	321 ± 3	1.77 ± 0.11	0.294
10.7	7.4×10^{-4}	7.13 ± 0.59	11.9 ± 2.8	81.1	355 ± 3	3.71 ± 0.05	0.405
12.2	9.8×10^{-4}	5.57 ± 0.75	11.3 ± 2.1	73.6	307 ± 3	1.82 ± 0.15	0.233

toward the near-infrared wavelengths. As the Sn content increases, the optical transmittance exhibits two distinct effects. In the UV–Vis region, a slight increase in transmittance is observed at low Sn concentrations, followed by a decrease at higher Sn contents. Meanwhile, a pronounced and progressive reduction in transmittance is observed in the near-infrared (NIR) region, which can be attributed to enhanced free-carrier absorption (BADGUJAR et al., 2022). This latter behavior is characteristic of degenerately doped transparent conducting oxides and is consistent with the trends observed in the Hall-effect measurements. To assess further insight into the optical response, the transmittance spectra were analyzed over the UV–Vis and NIR regions using the Tauc–Lorentz and Hamberg models, respectively. These models provide a reliable description of both interband transitions and free-carrier contributions and show good agreement with the transport parameters obtained from Hall-effect measurements (HUAYHUA et al., 2025; SALES, 2022). The optical modeling was performed using SENTECH's *SpectraRay/4* software, employing an air/substrate/film/air multilayer configuration. The transmittance of the substrate was first analyzed using soda–lime glass (SLG) from the software database. Subsequently, the optical response of the ITO films was modeled by fitting the film thickness (t_{opt}), optical carrier concentration (N_{opt}), and electron effective mass ($m^* = \gamma m_e$). Finally, as shown in Figure 4.1.7, the red continuous line represents the overall fit, showing good agreement between the calculated and experimental transmittance data. The extracted parameters are summarized in Table 4.1.2.

As shown in Table 4.1.2, the t_{Opt} are in the range of 307–355 nm and do not exhibit a systematic trend as the Sn content, consistent with the some growth parameters used for the deposition of all films (see Experimental details). The optical carrier concentrations (N_{Opt}) extracted using the Hamberg model follow a trend similar to that observed in the Hall-effect measurements. However, the carrier concentrations derived from optical transmittance are systematically lower than the corresponding Hall values. This discrepancy arises because the optical model does not explicitly account for carrier scattering at grain boundaries, as discussed in the next works. The undoped In_2O_3 film exhibits γ of 0.294, which falls within the range of values reported in the literature (VILCA-HUAYHUA et al., 2025). In contrast, the film doped with 10.7% Sn shows the highest reduced effective mass (see Table 4.1.2). This increase can

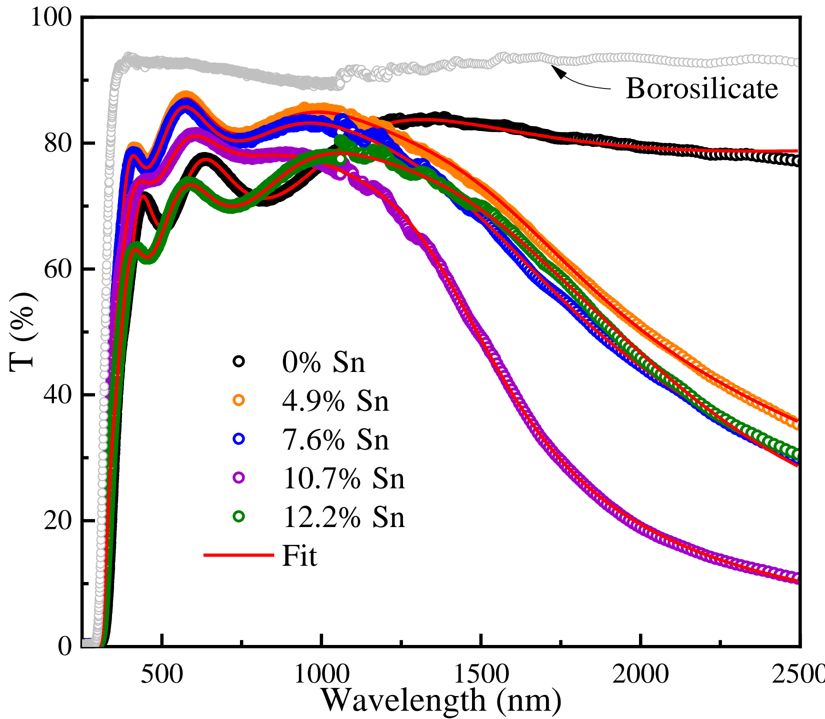

Figure 4.1.7 – UV-vis transmittance spectra obtained for Sn doped In_2O_3. A good fited transmittance spectra are represented by the solid red lines using the Tauc Lorentz and Hamberg models.

be correlated with the enhanced carrier concentration and is consistent with the nonparabolic nature of the conduction band in heavily doped In_2O_3-based materials (SHARIKA et al., 2022; VILCA-HUAYHUA et al., 2025).

The optical bandgap energy (E_g^{opt}) was determined from the absorption coefficient (α), calculated using the relation $\alpha = 4\pi k/\lambda$. Furthermore, the band fluctuation (BF) model (see Equation 49) was employed to evaluate both E_g^{opt} and the Urbach energy (E_U) for Sn-doped In_2O_3, which exhibits direct electronic transitions. A representative fit to the experimental data using the BF model is presented in Figure 4.1.8(a).

$$\alpha(h\nu) = (1/2)(A_0/h\nu)\sqrt{\pi/\beta}Li_{1/2}(e^{\beta(h\nu - E_g)}) \tag{49}$$

Here $h\nu$ is the photon energy, A_0 is a constant in units of $eV^{-1}\cdot cm^{-1}$, β is the inverse of Urbach energy, and Li_j (x) is the j-th order polylogarithm function of x.

Figure 4.1.8 (a) shows an E_g^{opt} value of 3.79 eV for undoped In_2O_3, which is in good agreement with the reported bulk bandgap of ~3.75 eV (WALSH et al., 2022b). Upon Sn doping, a progressive increase in the E_g^{opt} is observed as the Sn concentration increases, reaching a maximum at a critical Sn content of approximately 10.7%. This widening of the bandgap can be explained by the Moss–Burstein effect, arising from the increase in charge carrier concentration (see Figure 4.1.6). At higher Sn concentrations (12.2%), a reduction in the E_g^{opt} is observed.

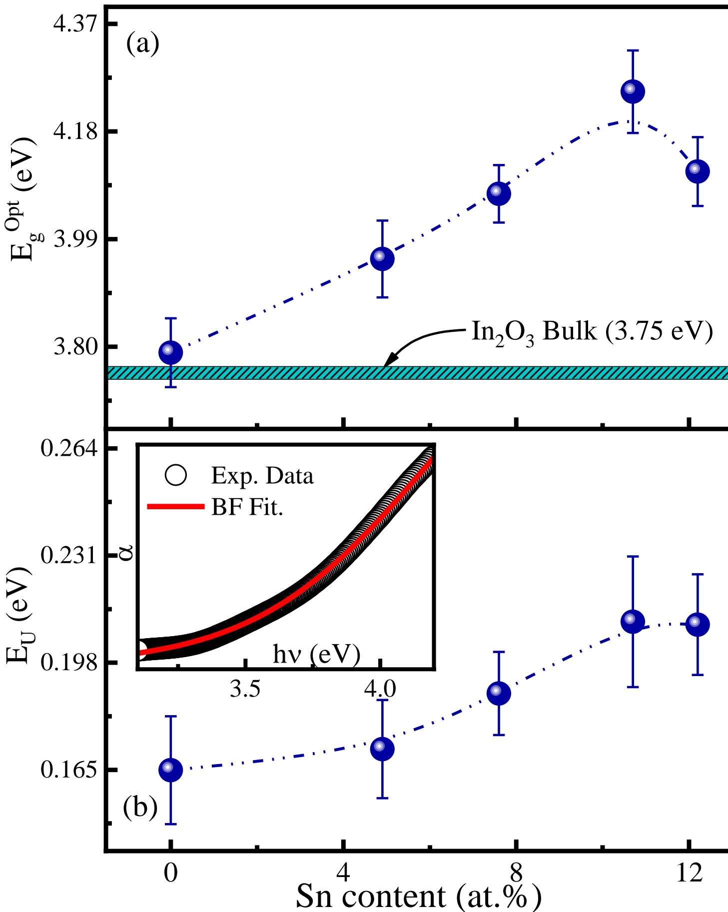

Figure 4.1.8 – (a) Bandgap, the light blue line represents the value of the bandgap bulk for In_2O_3. (b) Urbach energy for In_2O_3 and Sn doped In_2O_3 films, the red inset line shows the fit over the absorption region using the band fluctuation model.

This behavior is attributed to bandgap renormalization (BGR), which competes with the Moss–Burstein shift at high doping levels. In this regime, enhanced electron–electron interactions and increased scattering by ionized impurities lead to a net bandgap narrowing, resulting in a redshift of the optical absorption edge, as shown in Figure 4.1.8(a). This indicates that the BGR effect predominates over the Moss–Burstein shift at high Sn concentrations and increased oxygen vacancy densities. This dynamic evolution of the bandgap is consistent with the trend observed in the Urbach energy, as shown in Figure 4.1.8(b).

4.1.8 Photocurrent measurements and methane gas detection

In this section, the photocurrent response of undoped and Sn-doped In_2O_3 thin films under UV illumination is analyzed. Figure 4.1.9(a) shows a representative photocurrent response for the Sn-doped In_2O_3 film with 4.9% Sn content, measured at room temperature under an applied bias of 1.3 V using a UV-C light source. Upon UV illumination, the photocurrent increases rapidly and reaches a saturation level due to the efficient photogeneration of electron–hole pairs ($h\nu \rightarrow e^- + h^+$). When the UV light is switched off, the current initially decreases sharply

as a result of free carrier recombination, a behavior characteristic of n-type semiconductors. Subsequently, a slower decay of the photocurrent is observed, which is attributed to oxygen re-adsorption at the surface, a process mediated by surface traps and recombination centers in Sn-doped In_2O_3 films (KUMAR; SHUKLA; SRIVASTAVA, 2024).

To provide insight into the photoresponse, PR=I_{UV}/I_{dark}, mechanism as a function of Sn content, we first examine the behavior of the intrinsic In_2O_3 film, followed by the effects induced by Sn incorporation. The undoped In_2O_3 film exhibits a higher PR compared to the Sn-doped samples, as shown in the inset of Figure 4.1.9(a). This enhanced response can be attributed to the relatively lower free-electron concentration and to the presence of intrinsic donor-type defects generated during the growth process, which allow ultraviolet illumination to effectively promote electron–hole pair generation and significantly modulate the carrier population. As the Sn content increases, the photocurrent response progressively decreases. This reduction follows an inverse trend with respect to the charge carrier concentration (see Figure 4.1.6), indicating a clear correlation between these two quantities. The extracted values of photocurrent response and carrier concentration are summarized in Table 4.1.3. At higher Sn concentrations, the increased density of donor states shifts the Fermi level toward, and eventually into, the conduction band, reducing the relative change in carrier concentration induced by UV illumination and thus suppressing the overall photocurrent response.

Table 4.1.3 – Photocurrent parameters: recovery times (τ_{rec}) and response times (τ_{res}); photoresponse ($PR = I_{UV}/I_{dark}$); UV-light-saturated photocurrent (I_{UV}) and saturated dark current (I_{dark}). Parameters of the methane gas sensing response: response time (t_{res}) and recovery time (t_{rec}); gas sensor response ($GSR = R_{air}/R_{gas}$).

Sn doped	Photocurrent			Gas sensor		
(at. %)	τ_{res} (s)	τ_{rec} (s)	PR	t_{res} (s)	t_{rec} (s)	GSR
0	76.1 ± 5.1	183.1 ± 14.1	1.120	177.0 ± 19.2	163.6 ± 17.1	1.65
4.9	51.2 ± 4.4	150.9 ± 10.7	1.025	40.6 ± 5.5	42.3 ± 8.4	1.06
7.6	47.4 ± 3.7	144.5 ± 11.5	1.017	25.8 ± 7.3	25.1 ± 5.5	1.02
10.9	49.6 ± 5.9	145.8 ± 10.3	1.005	17.5 ± 4.1	22.0 ± 5.9	1.01
12.2	58.1 ± 4.8	165.3 ± 12.0	1.054	66.2 ± 11.2	71.2 ± 9.5	1.15

To analyze the photocurrent dynamics, the data were fitted using an exponential rise model Equation 50, describing electron–hole photogeneration, and an exponential decay model Equation 51, accounting for adsorption and recombination processes.

$$I(t)_{Response} = A_0 + B_0(1 - \exp(-(t + t_0)/\tau_{res})) \tag{50}$$

$$I(t)_{Recovery} = A_1 + B_1 \exp(-(t + t_0)/\tau_{rec}) \tag{51}$$

where A_0, A_1, B_0, and B_1 are fitting parameters; τ_{res} and τ_{rec} denote the response and recovery time constants, respectively; and t_0 represents the time at which the UV illumination is

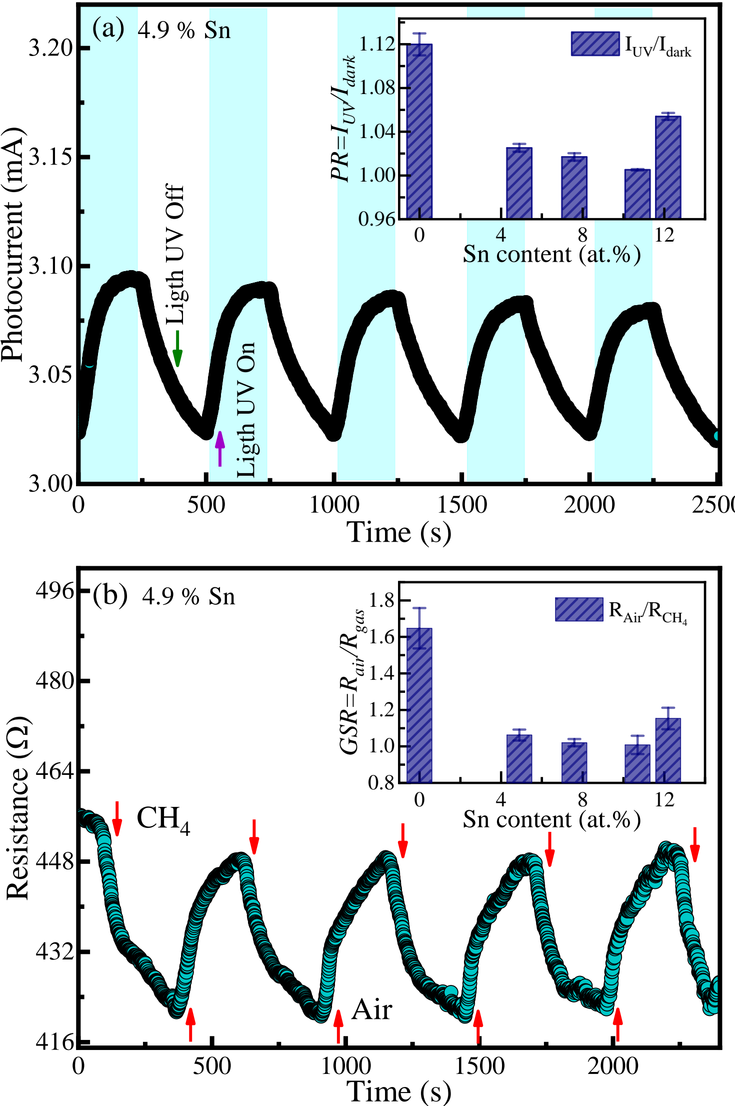

Figure 4.1.9 – (a) Photocurrent response of the 4.9% Sn-doped In_2O_3 thin film under UV illumination (light ON, sky blue). The inset shows the photoresponse (PR) extracted for all films. (b) Gas sensing response to methane (CH_4) at an operating temperature of 200 °C. The inset presents the corresponding gas sensing response (GSR) for the different films.

switched off. The extracted fitting parameters are summarized in Table 4.1.3.

The results reveal that the t_{res} is systematically shorter than the t_{rec}, indicating that electron–hole pair photogeneration occurs more rapidly than the surface-mediated recovery processes. Moreover, the evolution of t_{res} and t_{rec} with Sn concentration closely follows the trend observed for the PR, suggesting that these quantities are governed by the same physical mechanisms.

On the other hand, Figure 4.1.9 (b) shows the gas-sensing response of the 4.9% Sn-doped In_2O_3 film upon exposure to methane (CH_4), a reducing gas, at an operating temperature of 200 °C. This behavior is closely related to the fact that, at this temperature, oxygen molecules

from the ambient atmosphere are readily adsorbed onto the film surface, where they extract electrons from the conduction band and form ionized oxygen species (O_2^- and O^-, see Equation 52 and Equation 53, predominantly at the grain surfaces. The resulting electron-depletion layer increases the intergrain potential barrier, leading to an increase in the electrical resistance of the film. Upon exposure to CH_4, the reducing gas reacts with the surface-adsorbed oxygen species through redox reactions (see Equation 54 and Equation 55), releasing the trapped electrons back into the conduction band. As a result, the depletion layer narrows, the potential barrier at grain boundaries decreases, and the electrical resistance of the films is reduced. All samples exhibit a clear decrease in resistance in the presence of CH_4, followed by a recovery toward the initial resistance value once the gas is removed. This reversible behavior is consistent with the trends observed in the photocurrent measurements, highlighting the dominant role of surface-mediated charge transfer processes in both photo- and gas-sensing responses.

$$O_{2(ads)} + e^- \rightarrow O^-_{2(ads)}; (T \geq 300K) \tag{52}$$

$$O^-_{2(ads)} + e^- \rightarrow 2O^-_{ads}; (T \geq 473K) \tag{53}$$

$$2CH_4 + 4O^-_{2(ads)} \rightarrow 4H_2O + 2CO_2 + 8e^- \tag{54}$$

$$2CH_4 + 8O^-_{ads} \rightarrow 4H_2O + 2CO_2 + 8e^- \tag{55}$$

The gas-sensing response (GSR = $R_{\text{air}}/R_{\text{CH}_4}$) was evaluated for all samples and is summarized in Table 4.1.3, with a graphical representation shown in the inset of Figure 4.1.9(b). Notably, the GSR values exhibit a clear trend that closely follows the photoresponse behavior (see inset of Figure 4.1.9(a)). A similar correlation between gas-sensing response and photoresponse has been reported for ZnO thin films grown by DC magnetron sputtering under different deposition pressures (SILVA et al., 2026).

4.1.9 Ab-initio investigation of the electronic properties

To gain deeper insight into the electronic structure of Sn-doped In_2O_3 and the role of defects considered in this work, ab initio calculations were performed. Sn incorporation was modeled by substituting In atoms at the *b* crystallographic sites, as identified from the XRD analysis, while preserving the cubic bixbyite structure. Figure 4.1.10 presents schematic representations of the most representative defect configurations analyzed: (a) 9.24% Sn-doped In_2O_3; (b) 12.4% Sn-doped In_2O_3 with 2.1% O^{int}; and (c) 12.4% Sn-doped In_2O_3 with 4.2% O^{int}.

Figure 4.1.11 shows the electronic band structure along the high-symmetry path (Γ–X–M–Γ–R–X–M–Γ). At the Γ point, the minimum of the conduction band (CB) coincides with the maximum of the valence band (VB), indicating a direct band-gap transition. A

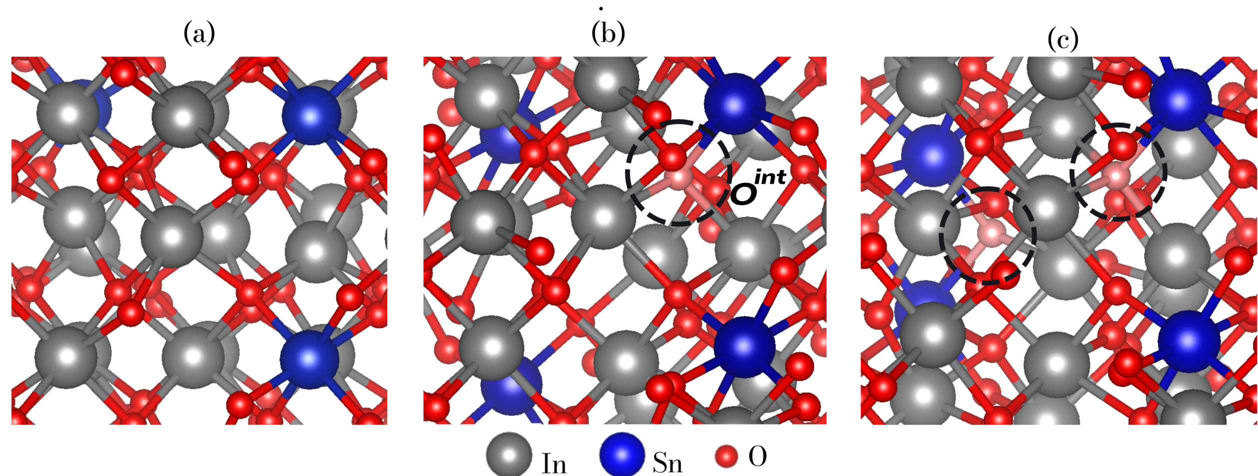

Figure 4.1.10 – (a) In_2O_3 crystal structure doped with 9.24 % Sn, (b) In_2O_3 structures doped with 12.4 % Sn, with a contribution of 2.1% O^{int}; and (c) In_2O_3 doped with 12.4 % Sn with a contribution of 4.2% O^{int} obtained by DFT.

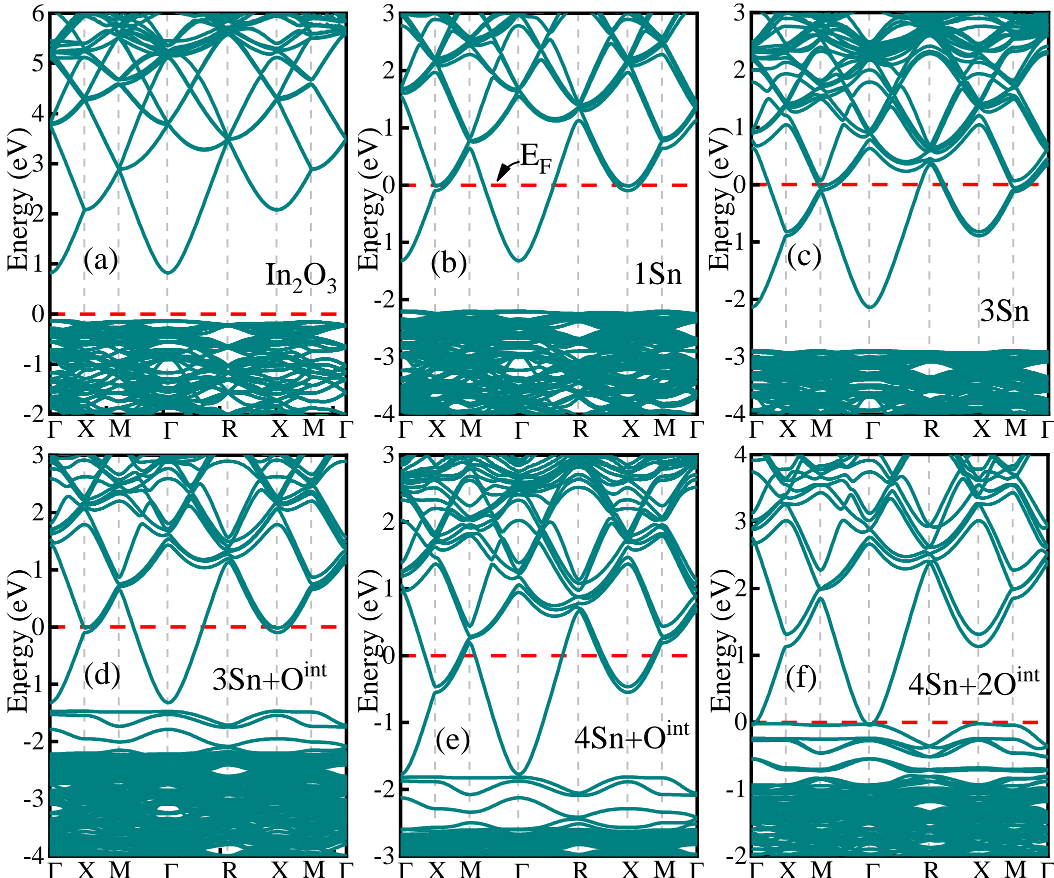

Figure 4.1.11 – Band structure for In_2O_3 with different Sn concentration (a) 0% Sn (b) 1Sn ∼ 3.1% Sn, (c) 3Sn ∼ 9.4% Sn, (d) 9.4% Sn + 2.1% O^{int}, (e) 12.5% Sn + 2.1% O^{int}, (f) 12.5% Sn + 4.2% O^{int}, the dashed red line represent the position of Fermi level.

fundamental direct bandgap of 0.92 eV is obtained for pristine In_2O_3. This value is lower than the experimental E_g^{opt} shown in Figure 4.1.8(a), a well-known underestimation inherent to standard

DFT approaches, as widely reported in the literature (APARICIO-HUACARPUMA et al., 2024; ERHART et al., 2007).

The impact of Sn incorporation on the In_2O_3 host was modeled in two distinct regimes. At low Sn concentrations ($x_{\text{Sn}} < 9.25\%$), Sn atoms occupy substitutional In sites. Above this threshold ($x_{\text{Sn}} > 9.25\%$), additional O^{int} are stabilized, which could lead to the formation of Sn–O defect complexes, according to the experimental data.

For the Sn-doped systems, we observe that the Fermi energy lies within the conduction band, as shown in Figure 4.1.11(b)–(e), which is characteristic of degenerate conducting oxides with high electron concentrations. This electronic configuration enables efficient charge transport dominated by conduction-band electrons. On the other hand, the introduction of interstitial oxygen at concentrations below 2.1% partially lowers the Fermi level while preserving the degenerate regime. As the O^{int} concentration increases to approximately 4.2%, the Fermi energy is significantly reduced and approaches the conduction band minimum, indicating enhanced band-gap renormalization effects associated with O^{int}-induced acceptor states; this behavior is consistent with the experimental electrical characterization (see Section 4.1.6). Furthermore, these defects are of the acceptor type, which introduce localized electronic states near the valence band maximum, as shown in Figure 4.1.11(d)–(f). These results are consistent with the observed increase in Urbach energy, extracted using the band-fluctuation model, reflecting enhanced structural and electronic disorder induced by oxygen-related defects (see Figure 4.1.8(b)).

Figure 4.1.12 shows the projected density of states (PDOS). For pristine In_2O_3, the valence band is dominated by O $2p$ states, with additional contributions from In $4d$ orbitals, reflecting strong In–O hybridization. In the conduction band region, oxygen-derived states remain significant, accompanied by contributions from indium states, indicating persistent metal–oxygen hybridization across the band edges. Upon Sn incorporation, pronounced deep-energy features emerge in the range of -8 to -7 eV, corresponding to a high density of states primarily associated with Sn $4d$ orbitals hybridized with O $2s$ and $2p$ states, indicative of chemically stable Sn–O environments. Importantly, the introduction of O^{int} leads to the appearance of defect-related electronic states near the valence band edge and enhanced spectral weight above the maximum of the valence band, evidencing increased energetic disorder and band tailing.

In addition, the electron effective mass, number of carriers were obtained using the Equation 56 and Equation 57 respectively (VILCA-HUAYHUA et al., 2025).

$$m^* = \gamma m_e = \hbar^2 (\frac{\partial^2 E}{\partial k^2})^{-1} \tag{56}$$

$$N_{cal} = \frac{2\sqrt{2}}{3\pi^2} (\frac{q m^*}{\hbar^2})^{3/2} (E_F - E_C)^{3/2} \tag{57}$$

The electronic transitions E_F-E_V was also calculated, the results are shown in Figure 4.1.13.

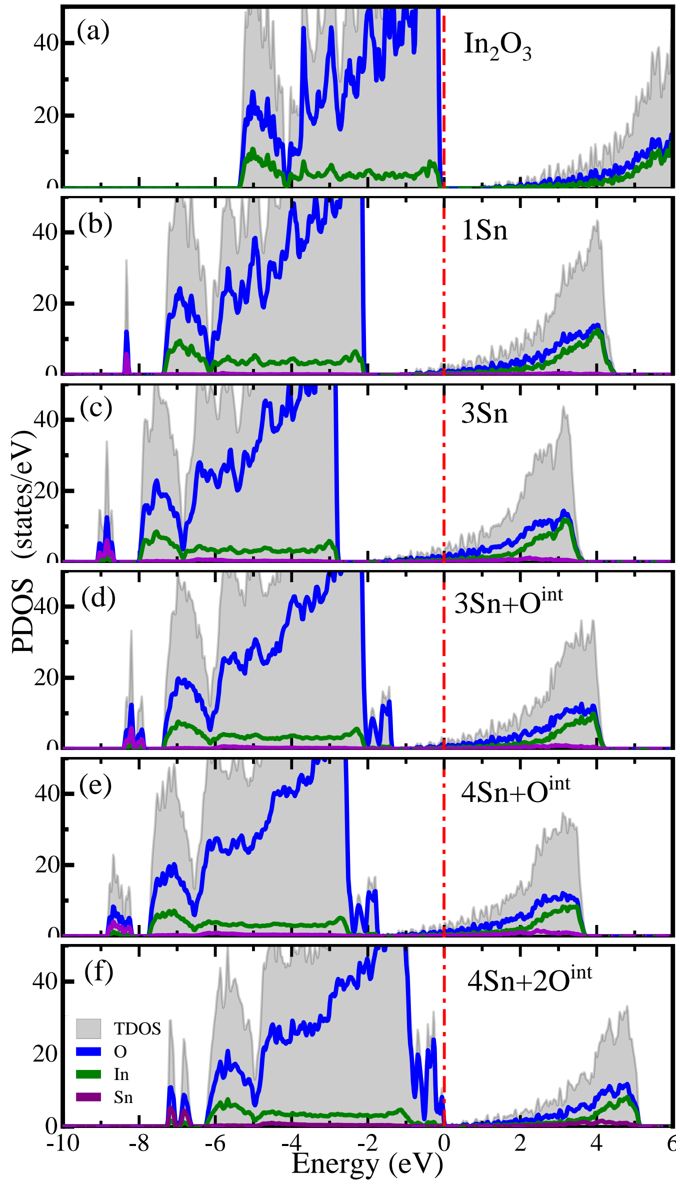

Figure 4.1.12 – Calculated Projected density of states PDOS for In_2O_3 doped (a) 0% Sn, (b) 3.1% Sn, (c) 9.4% Sn, (d) 9.4% Sn + 2.1% O^{int}, (e) 12.5% Sn + 2.1% O^{int}, (f) 12.5% Sn + 4.2% O^{int}, the dashed red line represent the position of Fermi level.

Figure 4.1.13(a) shows a systematic in $E_F - E_V$ with increasing Sn content, indicating an upward shift of the Fermi level further into the conduction band. This behavior arises from the enhanced charge carrier concentration (N_{cal}), as quantified in Figure 4.1.13(b). The observed shift is consistent with the Moss–Burstein effect, as discussed in the experimental section (sec. 4.1.7). Notably, the nonlinearity in the evolution of $E_F - E_V$ indicates the onset of carrier saturation, experimentally identified at a Sn concentration of approximately 10.7% (see Table 4.1.2). Beyond this threshold, intrinsic defects associated with O^{int} become energetically favorable. When O^{int} defects are located in the vicinity of Sn atoms (Figure 4.1.10(b)), a pronounced modification of the electronic structure occurs, manifested as a downward shift of the Fermi level and a concomitant reduction in $E_F - E_V$. At higher O^{int}concentrations (4.2%), irreducible Sn–O^{int}

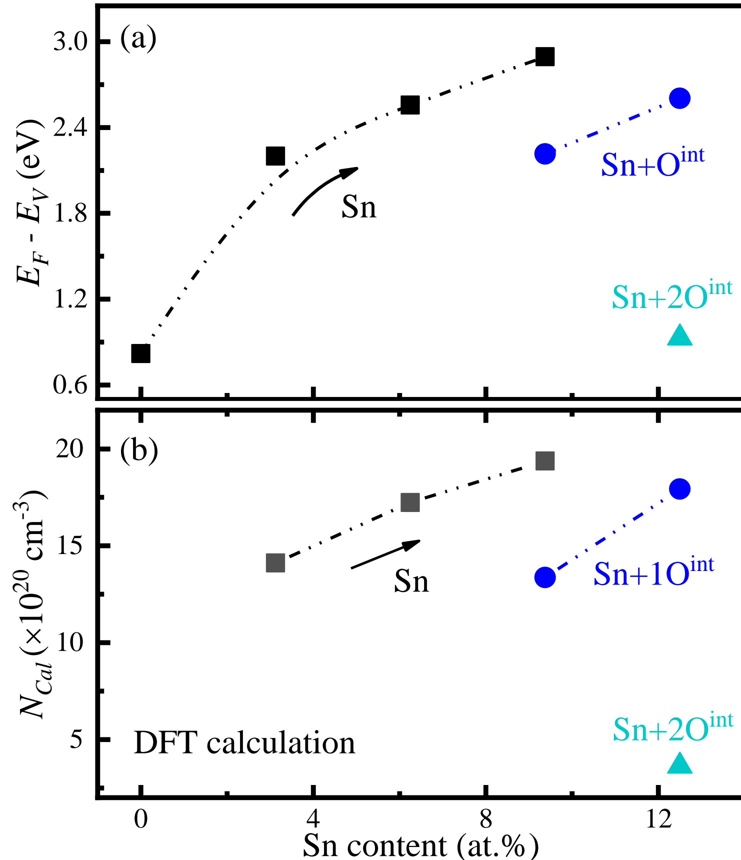

Figure 4.1.13 – (a) Electronic transition values between the valence band and the Fermi energy ($E_F - E_V$), (b) Charge carriers obtained from Equation 57 for Sn-doped In_2O_3 systems obtained by DFT calculation.

complexes are formed (Figure 4.1.10(c)), in agreement with the model proposed by Frank *et al.* (FRANK; KöSTLIN, 1982). In this regime, enhanced electron–electron and electron–ion interactions drive band-gap renormalization, leading to a sharp reduction in the free-carrier density, as evidenced in Figure 4.1.13(b). These results are consistent with the experimental observations.

4.1.10 Conclusion

In this work, we systematically investigated the effects of Sn doping concentration in In_2O_3 thin films fabricated by DC sputtering. EDS confirms that Sn atoms are homogeneously distributed throughout the films. Rietveld refinements indicate the formation of the cubic bixbyite phase of In_2O_3, with a lattice constant of 10.117 Å for the undoped film. Upon Sn incorporation, the lattice constant decreases to 10.092 Å for an Sn content of 7.6%, and increases again at higher Sn concentrations. The initial lattice contraction is attributed to the substitution of In^{3+} by the smaller Sn^{4+} ions, which simultaneously act as donor species, injecting free electrons into the conduction band and increasing the carrier density. A critical Sn concentration of approximately 10.7% is identified, at which the films exhibit a pronounced increase in the optical bandgap, in

agreement with the Moss–Burstein model and consistent with both Hall-effect measurements and optical transmission data. For Sn concentrations above this threshold, intrinsic defects, primarily associated with O^{int}, become energetically favorable, leading to a reduction in the free-carrier concentration and a consequent narrowing of the optical bandgap. These trends are well modeled by DFT calculations, which predict a critical Sn doping level beyond which defect-induced compensation dominates. Besides, photocurrent measurements revealed a clear correlation between the photocurrent and CH_4 gas-sensing responses, indicating that both phenomena are governed by the same charge-carrier modulation mechanisms at the surface.

4.2 Pos-growth thermal annealing effect on the physical properties of ITO thin films

In this work, the study of the effect of annealing temperature in air atmosphere on the structural, morphological, optical, electrical, and photocurrent properties of ITO films deposited by RF magnetron sputtering was carried out. The results show that lattice defects are modulated by the annealing temperature, leading to significant changes in the material properties. Surface analyses revealed the coexistence of defects associated with oxygen vacancies and Sn^{2+} species, which are dominant at low annealing temperatures and are correlated with an enhanced photocurrent. This behavior suggests that such defect complexes play a key role in achieving photocurrent response gain under UV illumination in ITO structures.

4.2.1 Experimental details

10% Sn In_2O_3 (ITO) thin films were grown using a In_2O_3/SnO_2 target with a purity of 99.99 %.Glass substrates of 1.0×1.0 cm dimension were used to grown the films, these one were previously cleaned in isopropyl alcohol and acetone PA in ultrasound for 15 min. The distance (target-substrates) was 6.5 cm, a vacuum of $1.06{\times}10^{-6}$ mbar was established as base pressure, then Ar/O_2 30:1 was introduced maintaining a working pressure of $1.0{\times}10^{-2}$ mbar, later we applied a power of 60 W, the growth lasted 3 hours. After the growth of the films, thermal annealing were carried out at 300, 400, 500 and 600 °C during 2h in each temperature, using a heating rate of 600 °C/h in air atmosphere. Subsequently, the films was characterized by performing X-ray diffraction (XRD) measurements using a Rigaku diffractometer with Cu-Kα radiation (λ = 1.5418 Å) in the range of $20° \leq 2\theta \leq 70°$. UV-Vis spectra were collected using a Ellipsometer, in transmittance mode in the spectra range of (250-2500 nm). Resistivity measurements were performed at room temperature using the van der Pauw configuration, and employing a current source and nanovoltimeter equipments (Keithley). AC electrical measurements at room temperature were performed using an HP 4284 A system in the 1 KHz – 100 MHz frequency range, employing a two-point probe configuration to measure their electrical properties. The photocurrent responses for UV light were obtained at room temperature, by applying a voltage of 4 V in air.

4.2.2 XPS Surface analysis

Figure 4.2.1 shows the survey XPS spectrum of the ITO films, where peaks corresponding to In, Sn, and O are observed. A C 1s peak is also detected, arising from adventitious carbon introduced during air exposure. The C 1s feature was aligned to 284.8 eV (GRECZYNSKI; HULTMAN, 2022) and used as the reference for calibrating the binding energies of the high-resolution spectra.

Figure 4.2.2(a) presents the high-resolution O 1s core-level spectra, consisting of two main components centered at 529.5 eV and 531.4 eV. These are attributed to lattice oxygen (O^{2-})

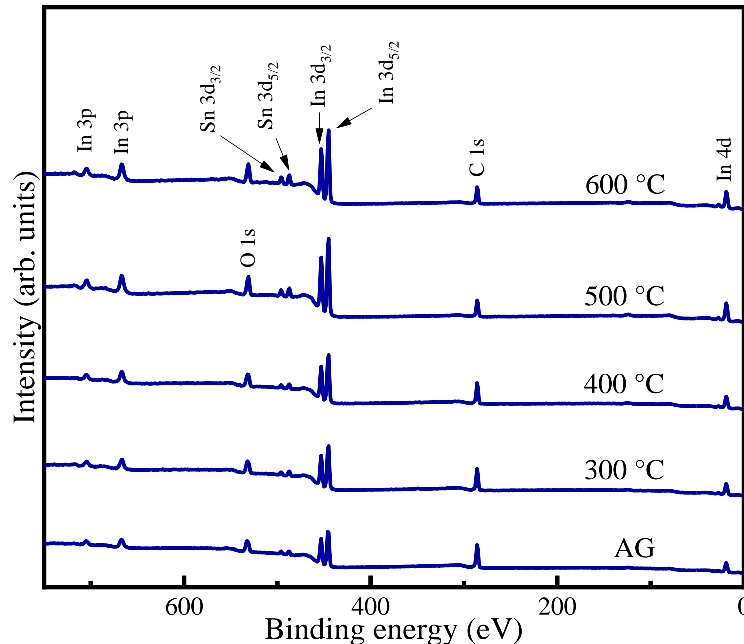

Figure 4.2.1 – XPS survey spectrum of ITO films annealed at different temperatures.

and oxygen-vacancy–related states (V_O), respectively, consistent with previous reports on ITO (ZHAO et al., 2022). As the annealing temperature increases, the crystallinity improves, which is reflected by a systematic decrease in the relative intensity of the vacancy-related component, as shown in Figure 4.2.2 (d). Figure 4.2.2(b) shows the high-resolution Sn 3d core level spectrum. The spin–orbit splitting between the 3d5/2 and 3d3/2 components is ≈ 8.4 eV, consistent with values reported in the literature (ARAGÓN et al., 2015). The $3d_{5/2}$ peak is resolved into two components at 485.6 eV (Sn^{2+}) and 486.7 eV (Sn^{4+}), confirming that both oxidation states are present in the ITO films. As the annealing temperature increases, the Sn^{4+} contribution becomes increasingly dominant. This evolution reflects the oxidation of Sn^{2+} to Sn^{4+}, which in turn enhances the donor concentration in the Sn-doped in In_2O_3. As a result, the n-type carrier density increases (see Figure 4.2.2(e)), as discussed in the next section

As reported by Zatsepin et al. (ZATSEPIN et al., 2019), stoichiometric In_2O_3 exhibits symmetric In $3d_{5/2}$ and In $3d_{3/2}$ peaks at approximately 444.1 eV and 451.7 eV, respectively, characteristic of the In^{3+} state. In contrast, the In 3d spectra of the present ITO films show a slight shift toward higher binding energies together and a marked peak asymmetry is observed (see Figure 4.2.2). This behavior suggests the coexistence of two indium environments, as reported in the literature (DONG et al., 2013). The latter originates from the screening effect induced by nearby Sn dopants, since the substitution of In^{3+} by Sn^{4+} introduces extra free electrons into the conduction band, modifying the local electronic environment and leading to the observed shift of the In 3d core level (DONG et al., 2013). From the deconvolution of the In 3d spectra, the evolution of the screened/unscreened ratio was determined, increasing monotonically from 0.42 to 1.80 by increasing the annealing temperature. This enhancement of electronic screening reflects the dopant activation improvement and is consistent with the observed increase in charge

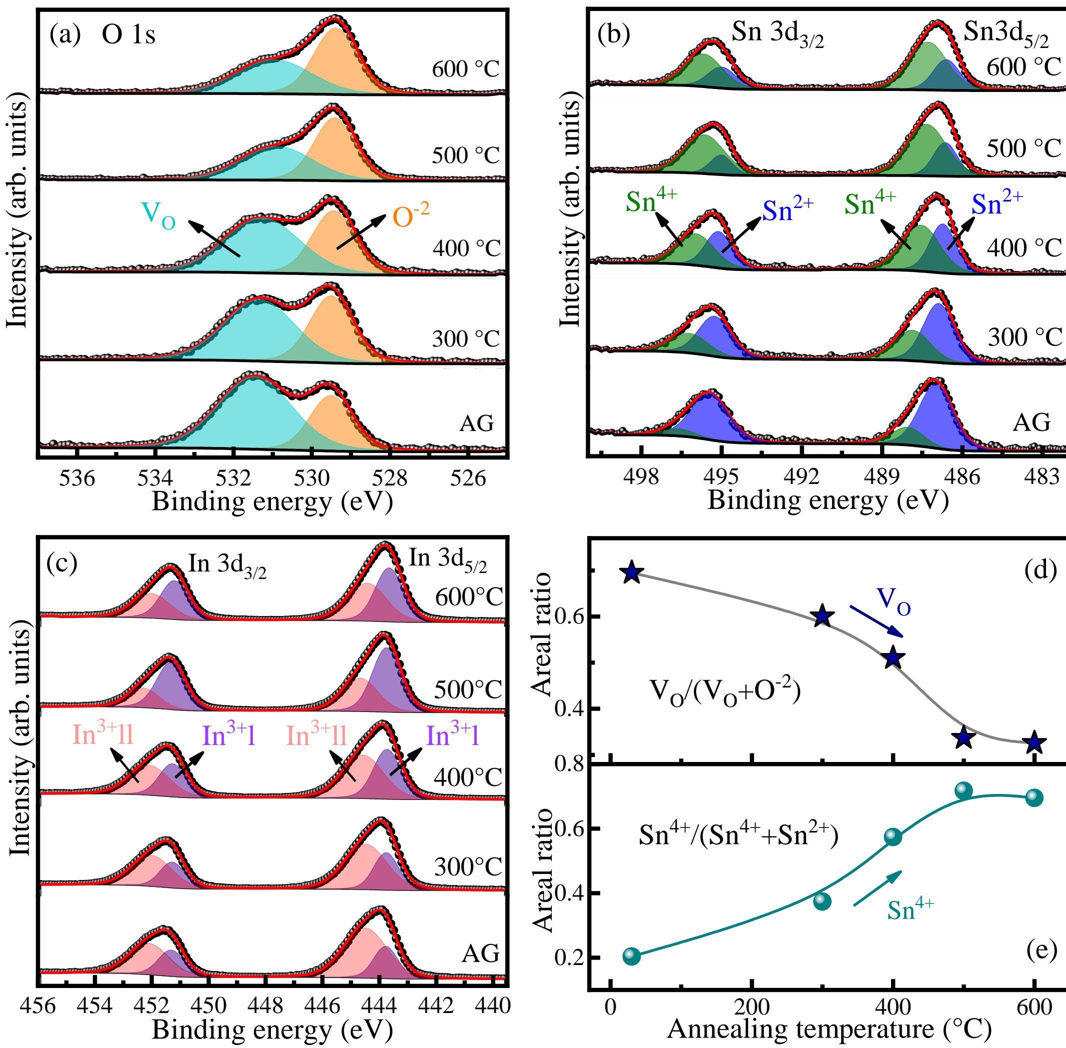

Figure 4.2.2 – (a) High-resolution for O 1s, (b) Sn 3d, (c) In 3d peak. (d) The variation of areal ratio of oxygen vacancies and (e) areal ratio of Sn^{4+} as a function of annealing temperature.

carrier concentration as discussed earlier.

4.2.3 Structural properties

Figure 4.2.3(a) shows the XRD pattern of the bixbyite-type cubic ITO films (space group *Ia*-3). The diffraction peaks exhibit good crystalline quality and correspond to the characteristic planes of the In_2O_3 matrix (211), (222), (231), (400), (332), (431), (440), and (622) with preferential orientation along the (222) and (440) directions. No extra diffraction peaks associated with SnO_2 or SnO were detected, suggesting that Sn ions are effectively incorporated into the In_2O_3 lattice. Rietveld refinements were performed using the General Structure Analysis System (GSAS) with Lorentzian peak profiles (TOBY; DREELE, 2013), yielding a good fit, as shown in Figure 4.2.3. The lattice parameter of the as-grown (AG) ITO film is approximately 2% higher than the reported value for In_2O_3, a = 10.117 Å (MAREZIO, 1966). This expansion is likely associated with the presence of mainly Sn^{2+} ions, which dominate at low annealing temperatures

as it is suggested by the XPS measurements. Sn^{2+} substituting In^{3+} expands the lattice because the ionic radius of Sn^{2+} (0.91 Å) exceeds that of In^{3+} (0.81 Å). At higher annealing temperatures, Sn^{2+} is oxidized to Sn^{4+}. Sn^{4+} ions (0.71 Å) are more stable within the ITO lattice, and their smaller radius leads to a reduction of the lattice parameter, as shown in Figure 4.2.4(a), consistent with Vegard's law.

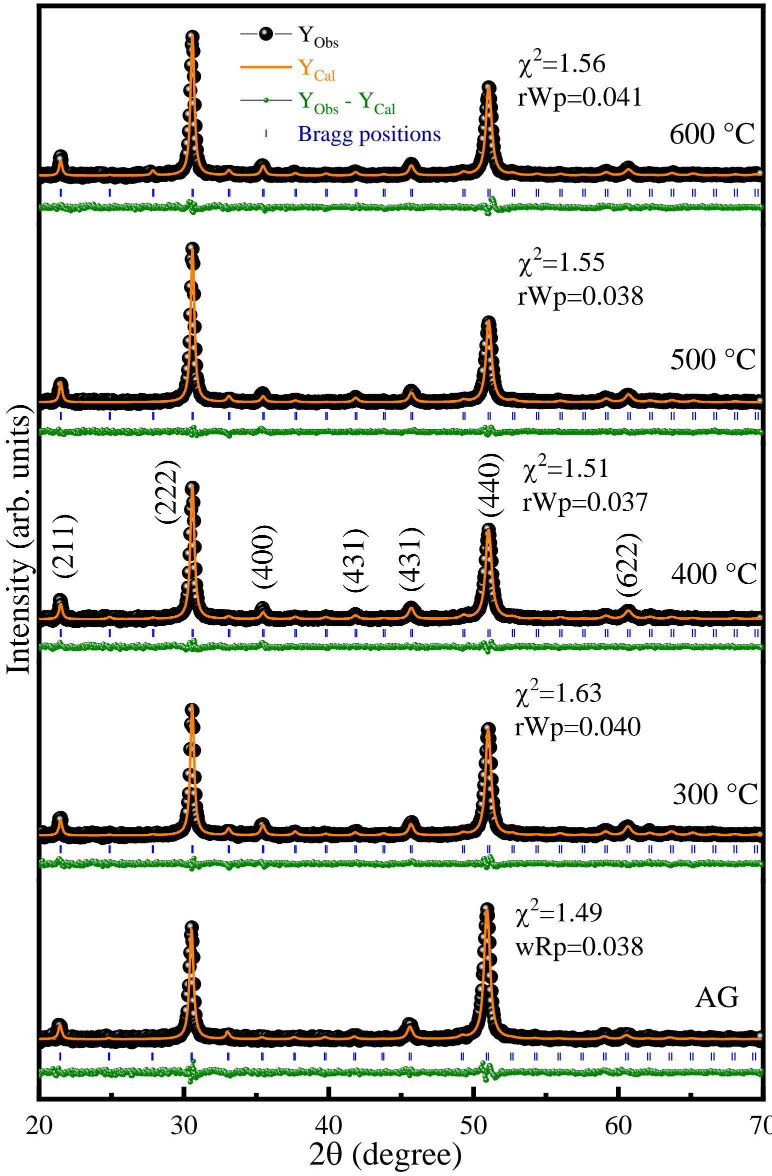

Figure 4.2.3 – (a) XRD patterns of the ITO films and their corresponding Rietveld refinements. The black spheres denote the experimental intensities (Y_{Obs}), while the orange line represents the calculated profile (Y_{Cal}). The green line represents the difference $Y_{\mathrm{Obs}} - Y_{\mathrm{Cal}}$. The blue markers indicate the Bragg positions of the cubic In_2O_3 phase.

On the other hand, the average crystallite size ($< D >$) and residual strain ($< \varepsilon >$) were estimated using the Williamson–Hall (W–H) method. This approach involves plotting $\beta \cos\theta$ versus $\sin\theta$, based on the linearized form of the Williamson–Hall.

Table 4.2.1 – Parameters obtained by XPS, ratio Sn/In, V_O/O_T and In-I/In-II. Results of structural and morphological paramenters of ITO films obtained from the XRD Rietveld refinement. The lattice parameter ($a = b = c$), average crystallite size ($< D >$),and residual strain ($< \varepsilon >$). the texture coefficient (TC) calculated using Equation 59 and goodness-of-fit (G) is also included to show the quality of the Rietveld refinement.

AT (°C)	Sn/In	V_O/O_T	In-I/In-II	$a = b = c$ (Å)	$< D >$ (nm)	$< \varepsilon >$ (%)	TC (222)	TC (440)	G
AG	0.10	0.69	0.42	10.138	52.6 ± 2	0.98	0.56	1.80	1.22
300	0.11	0.60	0.50	10.122	57.4 ± 2	0.92	0.67	1.52	1.28
400	0.11	0.57	0.75	10.119	62.7 ± 2	1.12	0.73	1.34	1.23
500	0.12	0.41	1.80	10.115	72.9 ± 2	1.05	0.82	1.21	1.24
600	0.11	0.39	1.08	10.115	74.5 ± 3	1.12	0.76	1.32	1.25

$$\beta_{Sample} \cos\theta = \frac{K\lambda}{< D >} + 4 < \varepsilon > \sin\theta \quad (58)$$

where, β_{Sample} represents the full width at half maximum (FWHM) associated with size and/or strain-induced broadening of the crystallites, after correcting from instrumental broadening ($\beta_{\text{Sample}} = \beta_{\text{Measurement}} - \beta_{\text{Inst}}$). The constant K is the Scherrer shape factor, which depends on the crystallite morphology; a value of $K \approx 0.9$ is commonly used for approximately spherical particles.

Figure 4.2.4(b) shows an increase in the crystallite size ($< D >$) from 53 nm to 75 nm as the annealing temperature rises. This improvement in $< D >$ is attributed to the reduction of defects density, primarily oxygen vacancies, which are passivated by an oxygen diffusion process occurring during the thermal annealing in air atmosphere, restructuring the ITO lattice and consequently enhancing the crystalline quality. The $< \varepsilon >$ showed a slight increase for higher annealing temperatures, likely suggesting that the difference between the thermal expansion coefficient of the substrate and the film causes internal stresses in the ITO structure.

Initially, the AG film exhibits greater texturing along the (440) plane. As the annealing temperature increases, a significant reduction in the intensity of the (440) crystallographic plane is observed. A preferential growth along the (440) direction was previously reported by Wang et al. in ITO films deposited at low temperatures using the sputtering technique (WANG et al., 2022). To quantify the degree of preferential orientation, the texture coefficient (TC) was calculated using the standard relation:

$$TC(hkl) = \frac{I_{(hkl)}/I_{0(hkl)}}{\frac{1}{N}\sum_N I_{(hkl)}/I_{0(hkl)}} \quad (59)$$

where $I_{(hkl)}$ is the measured intensity of the (hkl) diffraction peak, $I_{0(hkl)}$ is the corresponding standard intensity from the ITO (JCPDS card No. 1011258), and N denotes the number of peaks included in the analysis. Preferential orientation along the (400) plane has commonly been associated with the presence of V_O, particularly in ITO films processed under

oxygen-deficient conditions (HUAYHUA et al., 2025). However, in the AG and films annealed at low temperatures where a higher V_O density is present no preferential orientation along the (400) plane was observed. This suggests that the growth conditions play a significant role in determining the ITO structure. At the early stage of film formation on the substrate at room temperature, the surface mobility of adatoms promotes the growth of nucleation centers with different orientations. Owing to the low surface energy, crystallization may preferentially occur along the (440) plane at low temperatures. Similar findings were reported by Yanlei et al. and Shin et al., where high-temperature thermal treatment reduced the preferential orientation along the (440) plane (WANG; ZHANG; DING, 2016; SHIN et al., 1999).

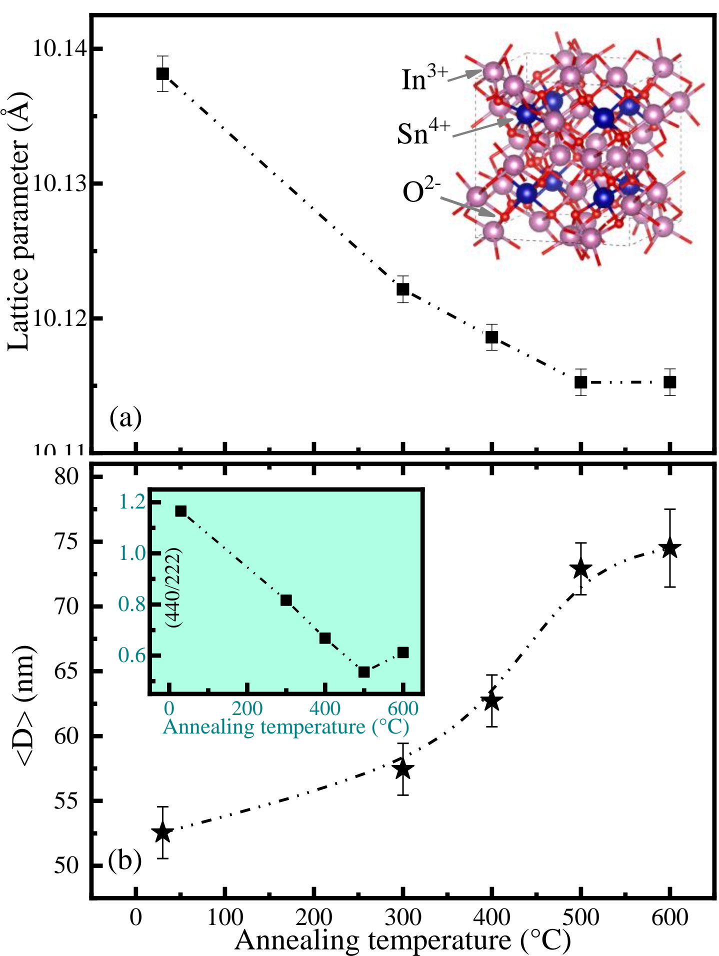

Figure 4.2.4 – (a) Lattice parameter (a) and (b) average crystallite size ($< D >$) at annealing temperature function, inset shown the ratio texture from 440/222 plane

As discussed in XPS analyzes, the annealing process carried out in air, promotes the diffusion of oxygen atoms at the surface and favors the oxidation of Sn^{2+} to Sn^{4+}, which enhances the formation of a more crystalline structure by enabling atomic rearrangement. This process ultimately results in a reduced (440) preferential orientation, as shown in the inset of Figure Figure 4.2.4(b), where the increased annealing temperature favors orientation on the (222) plane, as expected for ITO in oxygen-rich atmospheres (WANG et al., 2022). Nevertheless, the origin

of these different preferential orientations in which ITO crystallizes remains under debate, and further studies are required to achieve a deeper understanding of this phenomenon.

4.2.4 Electrical properties and Optical properties

The electrical properties of the films were evaluated using the Van der Pauw configuration (four-contact technique). The sheet resistance ($R_{\square}$) initially exhibits a high value of 10 kΩ/□, which decreases drastically with increasing annealing temperature, reaching a minimum of 66 Ω/□ for the film annealed at 500°C. This reduction is correlated with the increase in crystallite size, which in turn decreases the grain boundaries. The resistivity exhibits values of (3.2 - 450.5 $\times 10^{-3}$ Ω·cm) are slightly higher than those reported for ITO (10^{-3}–10^{-4} Ω·cm) (VILCA-HUAYHUA et al., 2025; TIEN et al., 2018), which can be attributed to the presence of Sn^{2+} in the ITO structure acting as an acceptor-type defect, thereby affecting the electrical conductivity. In Figure 4.2.5 we clearly observe that the films annealed at higher temperatures show a larger charge carriers density. This effect is attributed to the reduction of V_O-Sn^{2+} clusters due to the annealing atmosphere, oxygen atoms diffuse into the lattice, favoring the oxidation of Sn^{2+} as discussed in the XPS and structural properties sections, where the substitution of a In^{3+} ion by Sn^{4+} ion in the In_2O_3 lattice, contribute a free electron to the structure, improving the electrical conductivity. These results indicate Sn^{4+} as the primary defect contributing to the increase in carrier concentration in ITO structures.

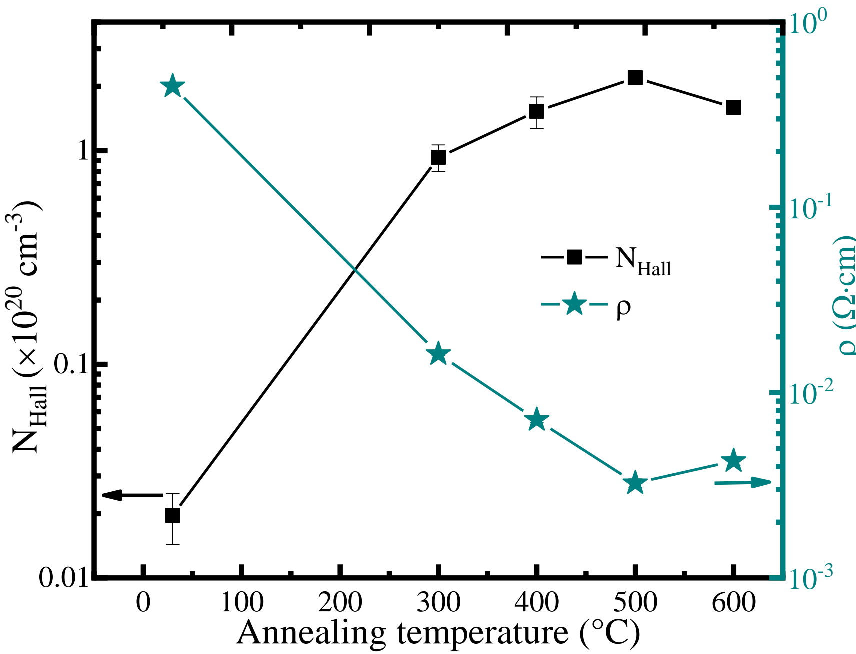

Figure 4.2.5 – Charge carrier measurements obtained by Hall (N_{Hall}) and electrical resistivity (ρ) for ITO films annealed at different temperatures.

On the other hand the increase in annealing temperature leads to an enhancement in the Hall mobility μ_{Hall} reaching a value of 9.2 cm^2/V·s for the film annealed at 600 °C. This

improvement may be linked to the increase in crystallite size as observed by XRD analysis, which reduces the number of grain boundaries and subsequently decreases electron scattering. However, for AG, the μ_{Hall} = 7 cm^2/Vs determined for the AG film is slightly higher than those ones determined for the annealed films 300 °C and 400 °C (see Table 4.2.2), this is related to the low concentration of charge carriers reducing electronic interactions or scattering.

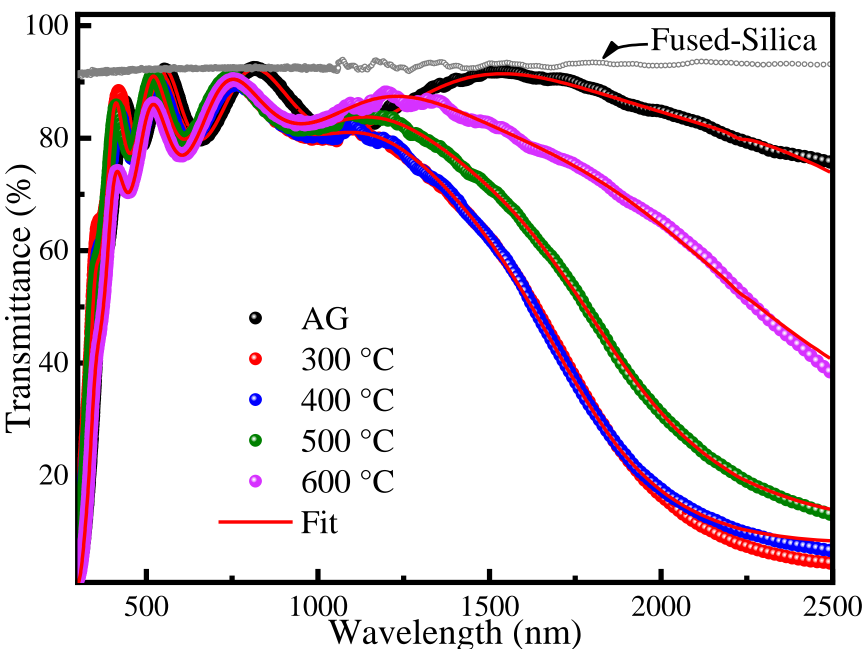

Figure 4.2.6 – UV-Vis-NIR transmittance spectra obtained for ITO; the red lines show the fit of the transmittance spectra using the Tauc-Lorentz and Hamberg models. The gray color curve represents the substrate transmittance.

The transmittance spectra for ITO films with different annealing were measured using UV-Visible-NIR spectroscopy over a range of (250-2500 nm). In the visible region, as shown in Figure 4.2.6, the ITO films exhibit a high transmittance above 86.0%, these transmission values make it suitable for various transparent conductive oxide (TCO) applications. Additionally, adjustments were made to the transmittance spectra. For the UV-Vis region, the Tauc-Lorentz oscillator model was applied, while the Hamberg model was used for the NIR region, due to the good approximations obtained with the carriers density obtained by Hall measurements. Both models are implemented in SENTECH's SpectraRay/4 software following an air/substrate/film/air layer configuration. Initially, the transmittance of the 0.5 mm thick substrate was modeled using Fused Silica (FS) as specified in the software database, subsequently the ITO films were modeled. The results allow to determine the values of thickness (t_{opt}), charge carriers density (N_{Opt}), electron effective mass (γ) of the films, as summarized in Table 4.2.2.

The thicknesses of the ITO films were reported to range between 408.9 - 440.0 nm, being slightly lower for higher annealing temperatures. This reduction can be associated with thermal densification, which is attributed to the elimination of defects within the lattice in consistency

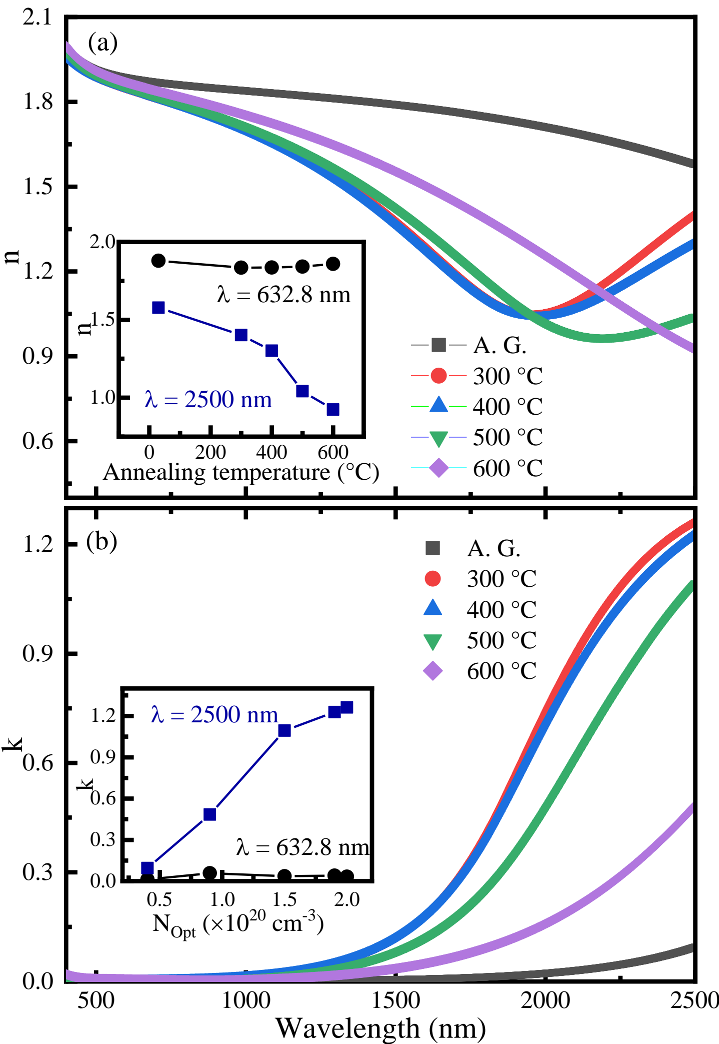

Figure 4.2.7 – Optical constants obtained from fitting the T-L/Hamberg model, (a) refractive index (n) as a function of wavelength, inset shows the dependence of n on the annealing temperature, for wavelengths of 632 and 2500nm, (b) extinction coefficient (k) as a function of wavelength, inset shows k as a function of the number of carriers.

with what was observed from the structural properties. In the NIR region the Hamberg model approximation was used where ionized impurities are considered as the main generators of conduction electrons (PFLUG et al., 2004), a reduction in transmittance is observed for the ITO films, with the highest absorption occurring for the annealing temperature 300 °C, attributed to the larger value of N_{Opt} = 2.0×10^{20} cm^{-3}. Furthermore, in the low annealing temperature region, the charge carrier concentrations obtained from transmittance spectra are slightly higher than those derived from Hall measurements. This discrepancy arises from the limitations of the Hamberg model, in which scattering effects caused by clusters and grain boundaries are not taken into account. As a result, a noticeable difference of up to one order of magnitude is observed between the N_{Hall} and N_{Opt} values. On the other hand, as the annealing temperature increases, these differences become smaller due to the reduction in defect density and grain boundaries, as shown in Table 4.2.2.

Moreover, the electron effective mass (γ) for the films showed values ranging from 0.177 to 0.310, which fall within the range reported for ITO (VILCA-HUAYHUA et al., 2025). These γ values decrease with increasing annealing temperature (see Table 4.2.2), which can be correlated to the enhancement of electron mobility, in agreement with the μ_{Hall} obtained from Hall measurements.

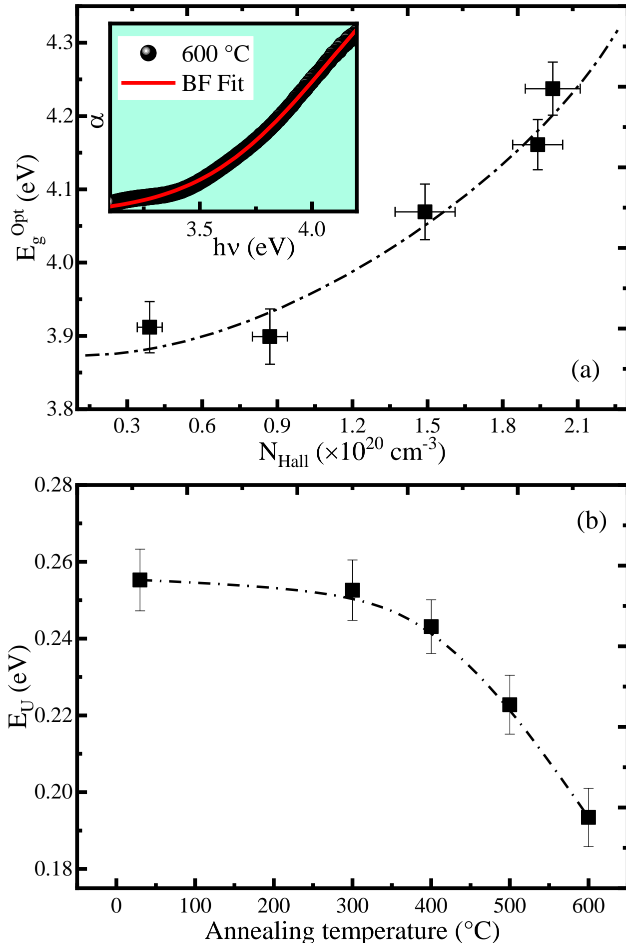

Figure 4.2.8 – (a) Optical bandgap (E_g^{Opt}) vs. N_{Hall} funtion, the inset shows the fit over the absorption region using the BF method. (b) Urbach energy (E_U) as a function of annealing temperature

Figure 4.2.7(a) shows the refractive index (n) as a function of wavelength, a reduction in n values for longer wavelengths is observed for films with different thermal annealings. In the inset of Figure 4.2.7(a) it can be seen that the n decreases for wavelengths of λ = 2500 nm in the NIR region. This shows that the interaction between photons and their propagation within the film is reduced with the decrease in defects with the annealing temperature. On the other hand, for λ = 632.8 nm in the visible region, no change in the n was observed. In contrast, the extinction coefficient (k) as a function of N_{opt} show significantly constant values throughout the visible region, where for longer wavelengths near infrared, an increase in k is observed influenced by the increase in the charge carriers density, as observed in the inset of Figure 4.2.7(b) where the effect of charge carriers makes a clear contribution to the NIR.

The optical bandgap energy can be determined from the absorption coefficient (α), which is calculated using the relation $\alpha = 4\pi k/\lambda$ over the absorption edges using the band fluctuation model represented by Equation 60 which allows us to additionally obtain the Urbach energy:

$$\alpha(h\nu) = (1/2)(A_0/h\nu)\sqrt{\pi/\beta}Li_{1/2}(e^{\beta(h\nu - E_g)}) \tag{60}$$

Here $h\nu$ is the photon energy, A_0 is a constant in units of $eV^{-}1{\cdot}cm^{-1}$, β is the inverse of Urbach energy, and Li_j (x) is the j-th order polylogarithm function of x.

A bandgap of 3.92 eV is determined for the AG film (see Figure 4.2.8(a)), which slightly higher than the bulk bandgap of 3.75 eV (WALSH et al., 2022a) A progressive bandgap increase with the optical carrier concentration (N_{Opt}) is observed. This can be explained based on the Burstein-Moss model. On the other hand, as the annealing temperature increases, oxygen diffusion on the surface compensates for the vacant sites, thereby reducing the defect density and stabilizing the lattice. Consequently, the E_U is reduced as shown in Figure 4.2.8(b).

Table 4.2.2 – Results obtained from the adjustments of the transmittance spectra using the Tauc Lorentz model and the Hamberg model, thickness (t), carrier concentration (n_{Opt}), reduced effective mass (γ), Transmittance (T) and Electrical measurement sheet resistance ($R_\square$), resistivity (ρ), carrier concentration (N_{Hall}) and Hall mobility (μ_{Hall}) using the Van der Pauw configuration.

AT (°C)	t_{Opt} (nm)	N_{Opt} ($\times 10^{20}$cm^{-3})	γ	T_{max} (%)	$R_\square$ (Ω)	ρ ($\times 10^{-3}\Omega$cm)	N_{Hall} ($\times 10^{20}$cm^{-3})	μ_{Hall} cm^2/Vs
AG	440.0	0.4 ± 0.1	0.310	92.2	10238 ± 12	450.5 ± 2.1	0.02 ± 0.01	7.1 ± 2
300	427.2	2.0 ± 0.1	0.309	91.2	378 ± 6	16.2 ± 0.3	0.93 ± 0.13	4.2 ± 1
400	427.6	1.9 ± 0.1	0.288	89.7	167 ± 5	7.1 ± 0.2	1.53 ± 0.26	5.7 ± 1
500	414.5	1.5 ± 0.1	0.233	91.0	78 ± 4	3.2 ± 0.2	2.19 ± 0.16	8.8 ± 1
600	408.9	0.9 ± 0.1	0.177	86.0	105 ± 5	4.3 ± 0.2	1.60 ± 0.11	9.2 ± 1

4.2.5 Photocurrent measurements

Figure 4.2.9 (a) depicts photocurrent measurement obtained at room temperature for the AG film. A current increase is observed during UV light irradiation (with an applied voltage of 4 V). When the irradiation light is turned off, an decrease in photocurrent response is shown. This behavior is characteristic of n-type semiconductor, and its nature is attributed to V_O and/or Sn^{4+} defect presents in the ITO films, in consistency with Hall effect measurements. These defects create energy levels be low to the conduction band, displacing the Fermi energy to higher energies. Initially, the semiconductor exhibits a depletion region dominated by electrons. Atmospheric oxygen captures these electrons, leading to the formation of ionized oxygen species at the grain boundaries. When UV light is incident on the surface of the semiconductor, electrons from the valence band, or from donor-type defect-created levels, jump to the conduction band, generating electron-hole pairs. These photoinduced holes can migrate to the grain boundaries, preventing

electron-hole recombination and interacting with the ionized oxygen species to produce an electron and oxygen molecules, thereby increasing the photogenerated electron density in the semiconductor. This results in an n-type photocurrent.

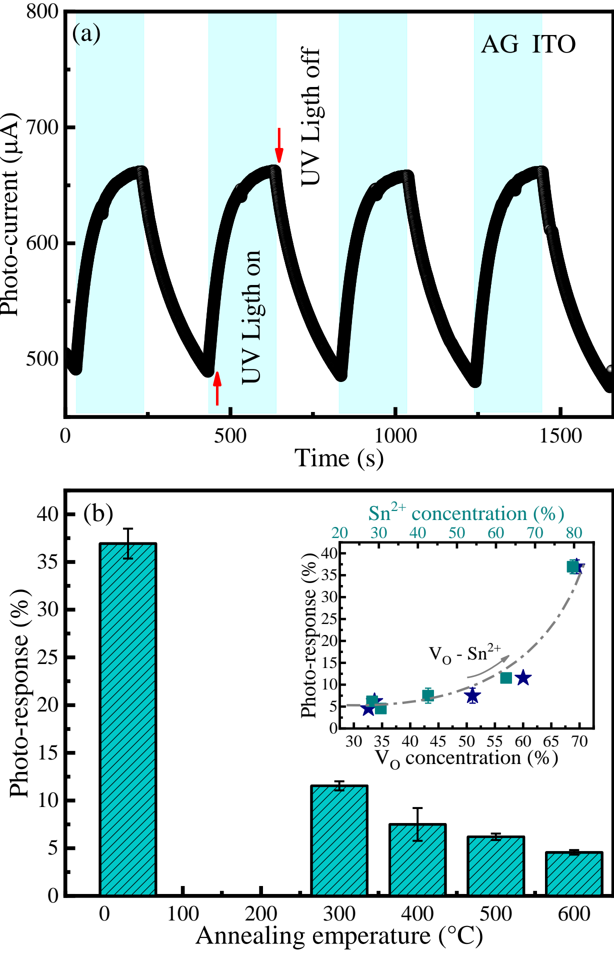

Figure 4.2.9 – Photocurrent curves as a function of time for the ITO:AG film. The shaded regions indicate the intervals during which the sample was exposed to UV light. (b) Percent photoresponse (PR) as a function of annealing temperature; the inset shows the dependence of the PR on the Sn^{2+} and V_O defects.

To calculate the photo-response (PR), the average current in dark and light conditions was utilized in accordance with:

$$PR = (I_{UV} - I_{dark}) / I_{dark} \times 100\% \quad (61)$$

where, I_{UV} and I_{dark} are the maximum and minimum photocurrent with UV light and dark conditions, respectively. Figure 4.2.9(b) shows an increase in photocurrent with decreasing temperature reaching a maximum value of around 37 % of photo-response. This result is particularly interesting because it suggests that Sn-Vo complexes play an important role in photocurrent response, oxygen vacancies can act as deep-level defects that facilitate absorption and desorption during electron–hole pair excitation (SILVA et al., 2026). Additionally, Sn^{2+}

introduces acceptor-type defects that promote hole migration toward the grain boundaries, preventing excitonic recombination, consequently favoring the photocurrent increase. The charge contribution from Sn^{4+} ion does not participate in the photoresponse, due to its electronic states being near or overlapping the conduction band, giving to the ITO material the characteristics of a degenerate semiconductor. Therefore, the dark current does not undergo significant changes when UV light is turned on, because the photoinduced electrons are negligible compared to the excess of charge carriers produced by the presence of Sn^{4+} substituting In^{3+}.

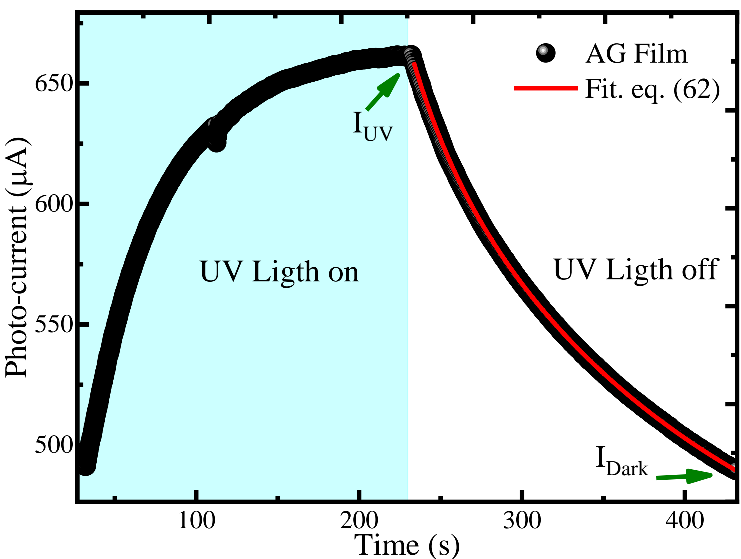

Figure 4.2.10 – The photocurrent curves show the exponential fit of the decay curve using Equation 62.

Table 4.2.3 – Results of resistance (R), inductance (L), capacitance (C), wolbur (W), obtained from the adjustments of the Nyquids curves, the error was obtained below 0.5%.

AT (°C)	$t_{response}$ (s)	τ_1 (s)	τ_2 (s)	PR (%)
AG	39.9 ± 5.4	26.8 ± 1.0	197.8 ± 15.4	36.9 ± 1.6
300	33.8 ± 6.8	24.9 ± 5.1	270.9 ± 25.7	11.5 ± 0.5
400	30.6 ± 5.0	23.8 ± 3.5	264.3 ± 31.5	7.5 ± 1.7
500	25.4 ± 2.7	21.3 ± 2.5	244.4 ± 25.8	6.2 ± 0.3
600	27.5 ± 1.1	22.2 ± 1.8	210.5 ± 6.4	4.6 ± 0.2

To assess the temporal decay time and provide a more comprehensive understanding of the photocurrent response, a bi-exponential function (Equation 62 was used to fit the experimental data. A_0, B_0, and C_0 are fitting parameters; t_0 denotes the point at which the UV illumination is switched off; and τ_1 and τ_2 denote the fast and slow recovery time constants, which are associated with carrier entrapment and recombination dynamics. In Figure 4.2.10, is depicted a representative fit for the AG film and demonstrates the high agreement between the model and the actual data.

$$I(t) = A_0 + B_0 \exp(-(t + t_0)/\tau_1) + C_0 \exp(-(t + t_0)/\tau_2) \tag{62}$$

The response time shows values ranging from 25.7 to 39.9 s, being slightly shorter for higher annealing temperatures. A similar behavior is observed for τ_1, which represents the time associated with electron–hole recombination. The electronic states related to defects act as traps within the bandgap, affecting the τ_1 and τ_2 times.

As discussed earlier, increasing the annealing temperature reduces the defect density, thereby facilitating the charge recombination and consequently the photocurrent reduction. During the recombination process, adsorption and desorption phenomena occur on the film surface. This happens because electrons trapped in defect states can be trapped by oxygen to form ionized oxygen species, while some decay to lower energy levels. This competition leads to the lasting of the τ_2 time. These results indicate that the generation and recombination of electron–hole pairs are strongly related to the defect density, which is essential for the photocurrent generation.

4.2.6 Conclusion

In this work, the effect of annealing temperature in air atmosphere on the physical properties of indium tin oxide (ITO) films was investigated. X-ray diffraction analysis indicates the formation of only the cubic bixbyite-type In_2O_3 phase. Rietveld refinements revealed that the lattice parameter decreases with increasing annealing temperature, which is attributed to the substitution of In^{3+} ions by Sn^{4+} ions, in agreement with X-ray photoelectron spectroscopy analysis. Surface analysis showed that at low annealing temperatures, the presence of Sn^{2+} ions deactivates the charge generated by oxygen vacancies via cluster formation, leading to an increase in the Urbach energy. The Annealing temperature increase promotes the oxidation of Sn^{2+} to Sn^{4+} which can generate free electrons to the conduction band of the ITO structure, thereby increasing the carrier concentration and resulting in an optical bandgap opening in accordance with the Burstein–Moss model. Photocurrent measurements under ultraviolet illumination confirm the n-type semiconductor behavior, consistent with Hall measurements. Furthermore, a higher photoresponse was observed for the as-grown film due to the higher density of V_O–Sn^{2+}-type defects, which favor the generation of photoinduced electrons.

4.3 Tailoring structural, electrical, and optical properties of ITO thin films via vacuum-pressure annealing: An experimental and theoretical study

To clarify the problems mentioned in the introduction and the ability to perform post-deposition defect engineering, in this report, we investigates the effects of thermal annealing in different vacuum levels on the properties of Sn-doped In_2O_3 films. A comprehensive analysis of the structural, electrical, and optical properties of these films have been carried out. Our findings are further supported by ab-initio theoretical calculations. This work was published in the **Journal of Alloys and Compounds** DOI: https://doi.org/10.1016/j.jallcom.2025.178909

4.3.1 Experimental details

Indium tin oxide (ITO) thin films were deposited using a direct current (DC) sputtering method. The films were grown from a metallic target composed of 90% indium (In) and 10% tin (Sn) with a purity of 99.99%. The deposition was carried out on borosilicate substrates, (0.5 cm × 0.5 cm), which were pre-cleaned in an ultrasound bath with acetone for 15 minutes. Sputtering was performed at a working pressure of 2.2×10^{-2} mbar, in high purity argon gas atmosphere, which an applied potential difference of 1600 V. The distance between the target and the substrates was 12 mm. The growth process was conducted over 4 hours. Post-growth thermal annealing was conducted at 600 °C for 2 hours under varying vacuum pressures of 1×10^{0} mbar, 2.3×10^{-1} mbar, 2.3×10^{-2} mbar, 5.0×10^{-5} mbar, and 2.3×10^{-6} mbar.

4.3.2 Theoretical Approach

Theoretical-computational calculations were conducted using Perdew-Burke-Ernzerhof (PBE) exchange-correlation functional (PERDEW; BURKE; ERNZERHOF, 1996) under the Quantum Espresso code (GIANNOZZI et al., 2009), with the valence atomic configurations $5s^2\ 5p^1\ 4d^{10}$, $2s^2 2p^4$, and $5s^2\ 5p^2\ 4d^{10}$ for In, O and Sn atomic species, respectively (CORSO, 2014). Initially, the structure of Sn-doped In_2O_3 cubic phase with 80 atoms was optimized by replacing three In atoms with Sn atoms, resulting in a doping concentration of approximately 9.4% ($In_{29}Sn_3O_{48}$) achieving a lattice parameter of 10.324 Å, consistent with other works using DFT(CHEN et al., 2015). Subsequently, oxygen vacancies were introduced, yielding structures with varying stoichiometries: $In_{29}Sn_3O_{47}$, $In_{29}Sn_3O_{46}$, $In_{29}Sn_3O_{45}$ and finally a structure with interstitial oxygen defects $In_{29}Sn_3O_{49}$. For these calculations, a cutoff energy of 600 Ry and a k-point mesh of $4\times4\times4$ were employed to optimize our structures until the forces acting on ions became smaller than 0.02 eV/Å to minimize the total energy. The results were analyzed through the density of states (DOS), projected density of states (PDOS), and the band structure, following the high-symmetry points Γ, N, P, Γ, H, and A. The aim of this study was to address

the electronic properties of the ITO samples.

4.3.3 Morphological characterization

Scanning electron microscopy (SEM) images of the film cross-section were used to estimate the thickness of the Sn-doped In_2O_3 layers thermally treated at different vacuum pressures (1×10^0 mbar, 2.3×10^{-1} mbar, 2.3×10^{-2} mbar, 5.0×10^{-5} mbar, and 2.3×10^{-6} mbar), where the thin film thermal treated at air atmosphere was included for comparison, as shown in Figure 4.3.1 (a)-(f). The cross-sectional SEM images reveal thin films with measured thicknesses ranging from 517 nm to 542 nm. The films are uniformly deposited over the substrate, exhibiting smooth and continuous surfaces without significant irregularities. The film-substrate interface is well-defined and sharp, indicating strong adhesion between the film and the substrate. The thickness values derived from SEM images are provided in Table 4.3.1. For comparison, thickness estimates based on transmittance measurements are also included, and these will be discussed in detail later.

Table 4.3.1 – Structural parameters, including lattice constants and crystallite size, are obtained from XRD analysis. Thickness measurements are assessed using cross-sectional SEM images and transmittance data, under vacuum conditions ranges from room atmosphere to 2.3×10^{-6} mbar, as described in the text.

Vacuum Pressure mbar	$a = b = c$ (Å)	$< D >$ (nm)	SEM (nm)	Transmittance (%)
Room air	10.1060	85 ± 1	528 ± 32	492 ± 2
1.0×10^0	10.1009	70 ± 1	517 ± 20	566 ± 2
2.3×10^{-1}	10.1025	75 ± 1	535 ± 11	497 ± 2
2.3×10^{-2}	10.1040	78 ± 1	540 ± 36	582 ± 2
5.0×10^{-5}	10.1124	89 ± 1	542 ± 18	491 ± 2
2.3×10^{-6}	10.1126	93 ± 1	529 ± 32	548 ± 2

Figure 4.3.2 presents a set of 3D atomic force microscopy (AFM) images that illustrate the surface topography of Sn-doped In_2O_3 thin films annealed under varying pressures. Notably, the film is thermally treated in an air atmosphere (see Figure 4.3.2 (a)), which shows a root mean square (RMS) surface roughness of ~ 25.7 nm and exhibits larger grain sizes. At this stage, under atmospheric pressure, oxidation prevails, causing substantial particle agglomeration and increased surface roughness. As the vacuum is increased the surface morphology of the Sn-doped In_2O_3 films becomes smoother, reaching a RMS surface roughness of 2.3 nm for the film annealed at 2.3×10^{-6} mbar of vacuum pressure. This smoothing is likely driven by the minimization of interfacial energy between grains, which promotes more uniform grain growth. A similar phenomenon is observed in thin films of ZnO, where low-pressure, high-vacuum annealing ($\sim1.0\times10^{-6}$ mbar) reduces grain boundary formation and improves surface homogeneity, as reported by Paz-Corrales et al. (2022) (PAZ-CORRALES et al., 2022). This effect is analogous

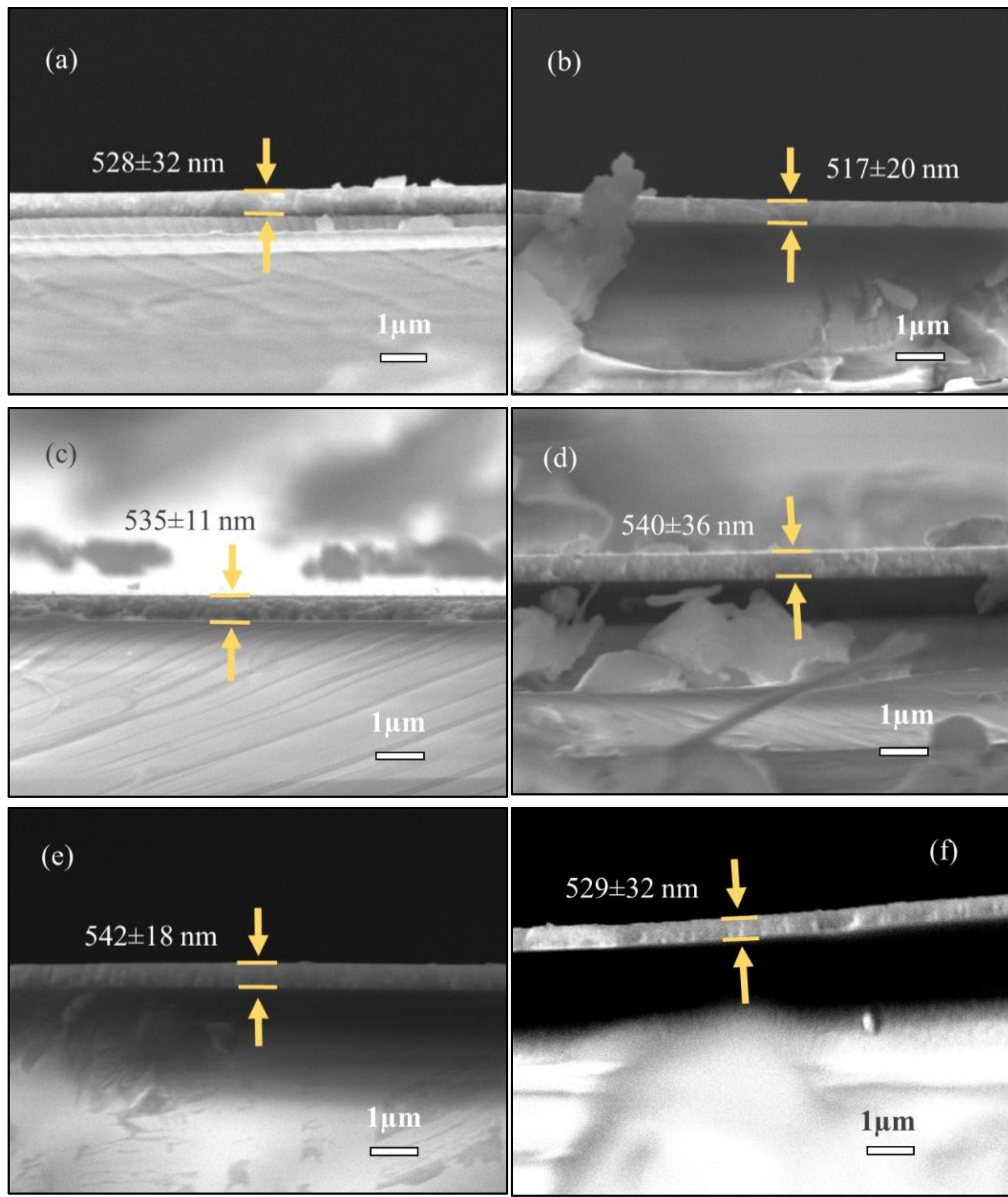

Figure 4.3.1 – Scanning electron microscopy (SEM) images of the cross-sections of Sn-doped In_2O_3 films annealed at different vacuum pressures at 600° for 2 hours, as shown in (a) air atmosphere, (b) 1×10^{0} mbar, (c) 2.3×10^{-1} mbar, (d) 2.3×10^{-2} mbar, (e) 5.0×10^{-5} mbar, and (f) 2.3×10^{-6} mbar.

to increasing the annealing temperature, which enhances the atom mobility and promotes grain growth, ultimately leading to a smoother surface.

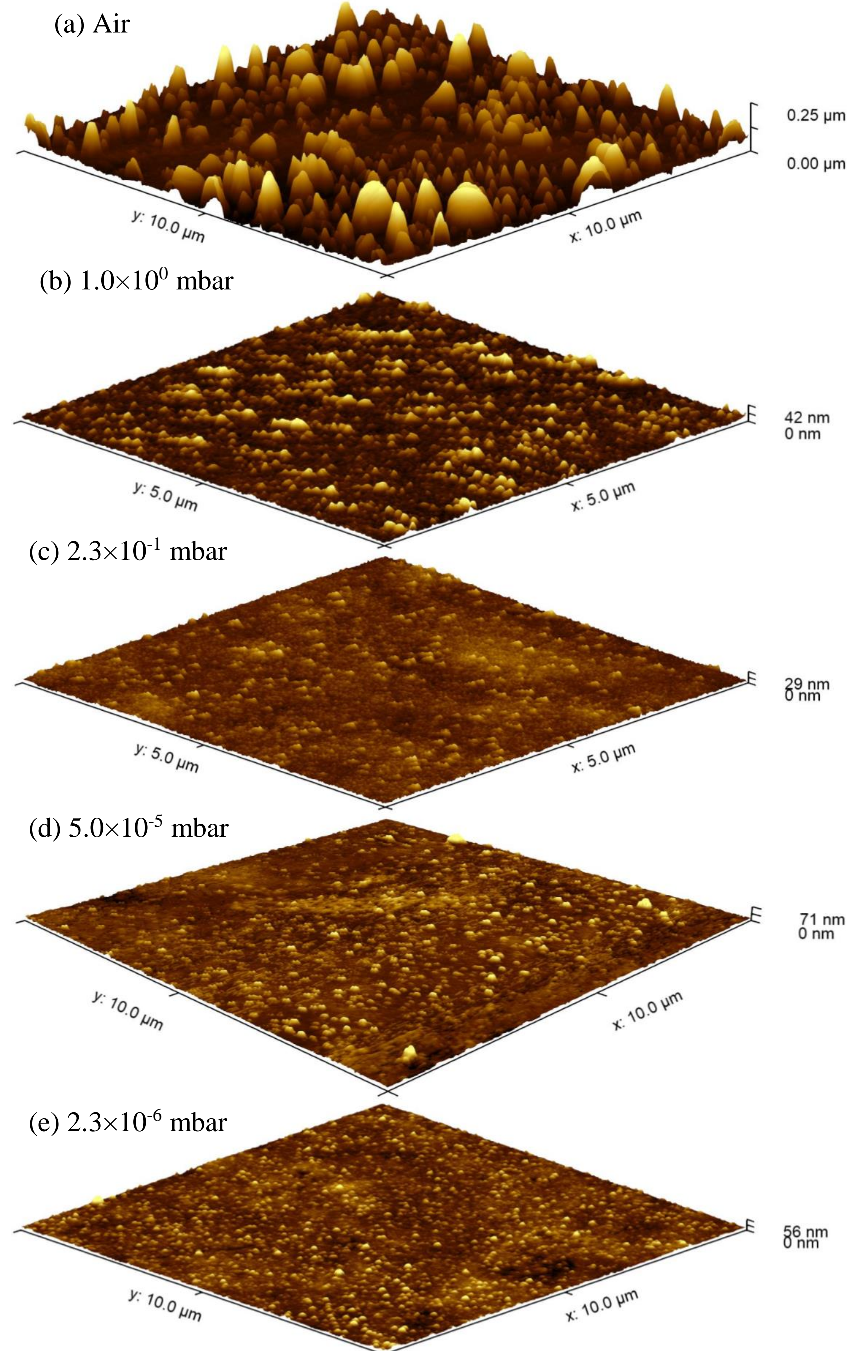

Figure 4.3.2 – 3D AFM images of Sn doped In_2O_3 films annealed at different pressures (a) air atmosphere, (b) 1×10^{0} mbar, (c) 2.3×10^{-1} mbar, (d) 5.0×10^{-5} mbar, and (e) 2.3×10^{-6} mbar.

4.3.4 Structural Characterization

Figure 4.3.3 (a) shows the XRD spectra for the thermally annealed (TA) ITO thin films, revealing the characteristic crystal planes of the In_2O_3 crystalline phase, specifically the (211), (222), (400), (440), and (622) planes. Notably, the as-grown films exhibit an amorphous phase, as indicated by their XRD patterns (not shown here). The preferential orientation in the (222) plane is significant and can be attributed to the specific conditions and parameters of the deposition

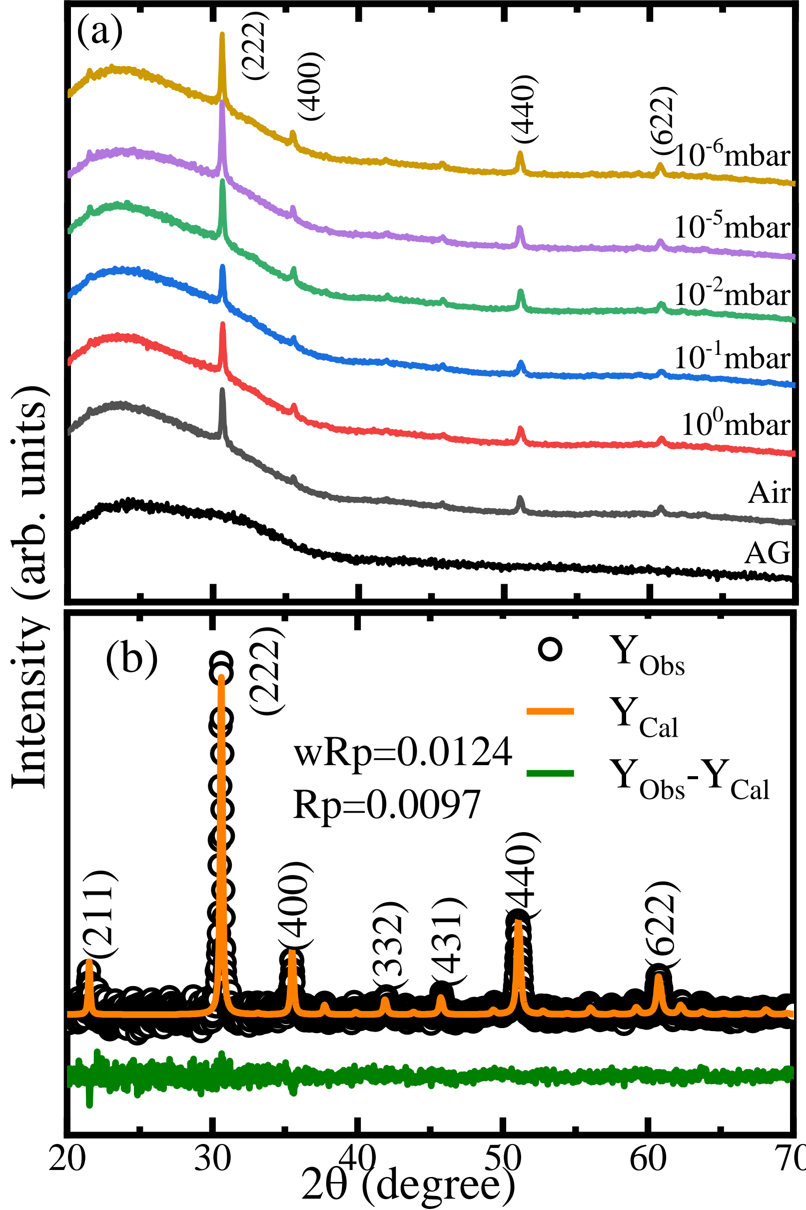

Figure 4.3.3 – (a) X-ray diffraction patterns of Sn-doped In_2O_3 films annealed at various pressures. The as-grown (AG) XRD pattern is included for comparison. (b) Rietveld refinement of the sample annealed at 10^{-6} mbar.

process. The absence of diffraction peaks corresponding to tin oxide secondary phases suggests that Sn^{4+} ions have been successfully incorporated into the In_2O_3 lattice, substituting In^{3+} ions without forming separate tin oxide phases. Figure 4.3.3 (b) illustrates a typical Rietveld refinement analysis for a sample thermally annealed at 10^{-6} mbar, conducted using GSAS software (TOBY; DREELE, 2013). In the approach that the broadening of the diffraction peaks is primarily due to the finite crystallite size, the mean crystallite size, $< D >$, can be determined using the Scherrer equation, $< D >= k\lambda/\beta_{size} \cdot cos\theta$, in this equation, λ =1.542 Å is the x-ray wavelength of Cu-Kα radiation, k = 0.9 is the Scherrer constant for spherical-like crystals, The shape of the diffraction peaks was modeled using Lorentzian profile function implemented in the GSAS

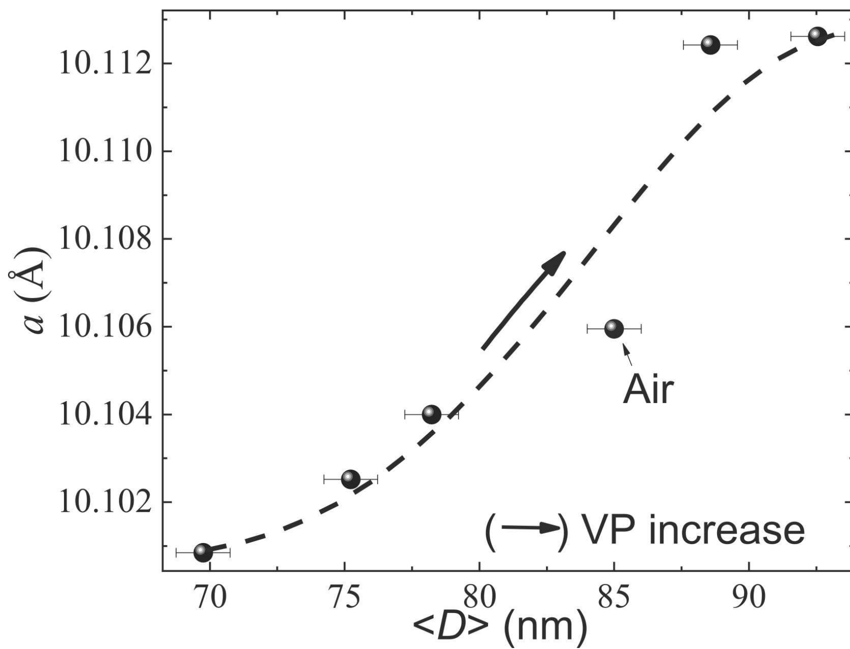

Figure 4.3.4 – Dependence of mean crystallite size on lattice parameters, with the arrow indicating an increase in the vacuum pressure (VP).

software. This approach allowed for the removal of the instrumental broadening contribution (β_{inst}) from the experimentally measured FWHM, peak broadening (β_{meas}), to determine the size broadening contribution, $\beta_{size} = \beta_{meas} - \beta_{inst}$. The angle θ correspond to the Bragg angle. Table 4.3.1 illustrates the dependence of crystallite size on vacuum annealing pressure. The results show that crystallite size increases as the vacuum is raised. This trend can be explained by the fact that lower pressures (higher vacuum enhance the atomic mobility, which increases the diffusion coefficient. According to the Ostwald ripening model, this leads to a transference of atoms from smaller grains to larger grains, which have higher surface energy, promoting grain growth (PACHECO-SALAZAR et al., 2020), also Table 4.3.1 illustrates the lattice parameter $a = b = c$ with vacuum pressure dependence for ITO films, which are observed to be smaller than that of bulk In_2O_3 (10.117 Å) (MAREZIO, 1966). The reduction in the lattice parameter can be attributed to the formation of a solid solution between tin and indium atoms. The difference in their ionic radii (Sn^{4+} = 0.69 Å and In^{3+} = 0.80 Å) (SHANNON, 1976) leads to a contraction of the lattice parameter. Additionally, as the VPs increased, the lattice parameter further increased. This phenomenon can be explained by size effects (see Figure 4.3.4) where smaller crystallites exhibit larger strain due to the presence of strained regions within the films, particularly at the surfaces of the nanocrystals. As the crystallite size decreases, the strain becomes more pronounced, which is consistent with the strain effects predicted by the Volmer–Weber growth model(KOCH, 1994), A similar trend has been previously reported for Fe-doped SnO_2 films deposited by DC sputtering (GUILLEN-BACA et al., 2019). It is interesting to note that the texture coefficient (TC) for the (222) and (400) planes was determined. A slight increase in the intensity of the (222) peak relative to the (400) peak was observed, which, according to the reference (THIRUMOORTHI; PRAKASH, 2016), could be attributed to the occupation of

additional indium vacancy sites by tin atoms that were previously unoccupied.

4.3.5 Optical and DC electrical properties

Figure 4.3.5 presents the transmittance spectra of ITO thin films, measured from 200 nm to 1000 nm, as a function of vacuum pressure thermal annealing. Besides, for comparison, the transmittance spectrum of the borosilicate substrate is also included (black curve). All spectra show maximum transmittance values between 65% to 80% in the visible range, with clear oscillations appearing above approximately 380 nm. To simulate the transmittance spectra from the ultraviolet to near-infrared regions, an optical model has been employed that integrates layers of air/film/substrate/air. This simulation is conducted using the SpectraRay/4 software from SENTECH. Initially, the substrate transmittance, 1 mm in thick, was modeled using soda-lime float glass (SLG) with tin impurities, as specified in the software's database. In the air/film/substrate/air model, the contribution of the substrate was maintained as a constant, while the film's properties were represented through a combination of Tauc–Lorentz oscillators (TLOs) and Drude oscillators. The inset of Figure 4.3.5 shows the near-infrared region with a wavelength from 1000 to 2400 nm, which displays a monotonic decreasing drop as the vacuum increases, this observation provides compelling evidence of a sustained increase in the charge carrier concentration. The thickness of the films was evaluated based on the analyses, and the results are shown in Table 4.3.1. These results are compared with the results obtained from cross-section measurements, showing good agreement between the two techniques.

The absorption edges in the wavelength (λ) range of 200 nm to 400 nm (see Figure 4.3.5) are associated with the optical bandgap energy (E_g). The optical bandgap energy can be determined from the absorption coefficient (α), which is calculated using the relation $\alpha = 4\pi k/\lambda$. To estimate E_g, the band-fluctuation (BF) model was employed (GUERRA et al., 2019), this method well effectively used to determine the E_g and Urbach energy (E_U) for Tb-doped ITO (LLONTOP et al., 2022) and Cu_2S p-type semiconductor thin films (VELASQUEZ-ORDOñEZ et al., 2024).

$$\alpha(h\nu) = (1/2)(A_0/h\nu)\sqrt{\pi/\beta}Li_{1/2}(-e^{\beta(h\nu-E_g)}) \tag{63}$$

Here $h\nu$ is the photon energy, A_0 is a constant in units of $eV^{-1} \cdot \mathrm{cm}^{-1}$, β is the inverse of E_U, and $\mathrm{Li}_j(x)$ is the j-th order polylogarithm function of x. The inset of Figure 4.3.6 (a) demonstrates a strong correlation between the model and the absorbance data. Additionally, as shown in Figure Figure 4.3.6 (a), the bandgap energy displays a slightly increasing tendency as the vacuum pressures, which lies between 3.8 and 4.1 eV. These values are higher than the bandgap of bulk In_2O_3 (~ 3.6 eV (KHAN et al., 2012)), which is consistent with the Burstein–Moss effect reported in the literature (BURSTEIN, 1954). This effect suggests that increased free carrier concentrations lead to higher bandgap values. However, the Urbach energy decreases with the

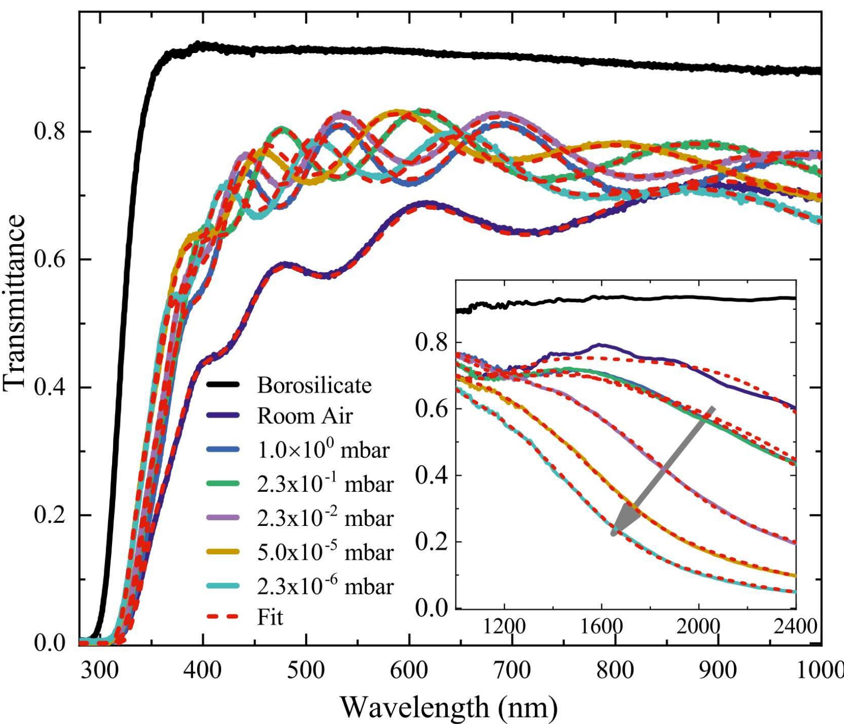

Figure 4.3.5 – UV-visible transmittance measurements of ITO thin films subjected to various vacuum pressures during thermal treatment. The inset displays the main near-infrared region with wavelength from 1000 to 2400 nm spectra.

increase of the vacuum during the annealing (see Figure 4.3.6 (b)). This trend correlates with the crystal improvement trend determined from XRD data analyses, indicating the density of defects and structural disorder reduction provoked by the thermal annealing.

Although vacuum annealing could generate oxygen vacancies due to the oxygen-deficient atmosphere, it can also induce the migration of oxygen ions from interstitial sites (GONZáLEZ et al., 2001). This can explain the progressive crystal improvement and the Urbach energy reduction with the vacuum. Moreover, the likely formation of oxygen vacancy-Sn interstitial complexes can also enhance crystallinity as reported by Li et al (LI et al., 2015) Although these effects can explain the experimental results, further investigations are necessary to confirm these hypotheses. Additionally, the model proposed by Dolgonos and Hamberg (DOLGONOS; MASON; POEPPELMEIER, 2016; HAMBERG et al., 1984) was also used, $\alpha \propto 1 - \frac{2}{\pi}\arctan(\frac{E_g - h\nu}{\Gamma})$ and the results provided bandgap values consistent with the Band fluctuation model.

Figure 4.3.7 (a) presents the electrical resistivity measured using the four-point method as a function of the vacuum during the annealing, ranging from 33.6 to 1.4×10^{-3} Ω·cm as the vacuum is increased. A significant reduction in electrical resistivity with increasing vacuum pressure is observed (see Figure 4.3.7 (a)). This can be associated with the thermal induce tunning of defects, enhanced by the vacuum pressure during the thermal annealing. Defects such as V_O which contribute with free carriers can be generated during the vacuum thermal annealing, thereby reducing resistivity (REN et al., 2022). Moreover, interstitial oxygens forming neutral

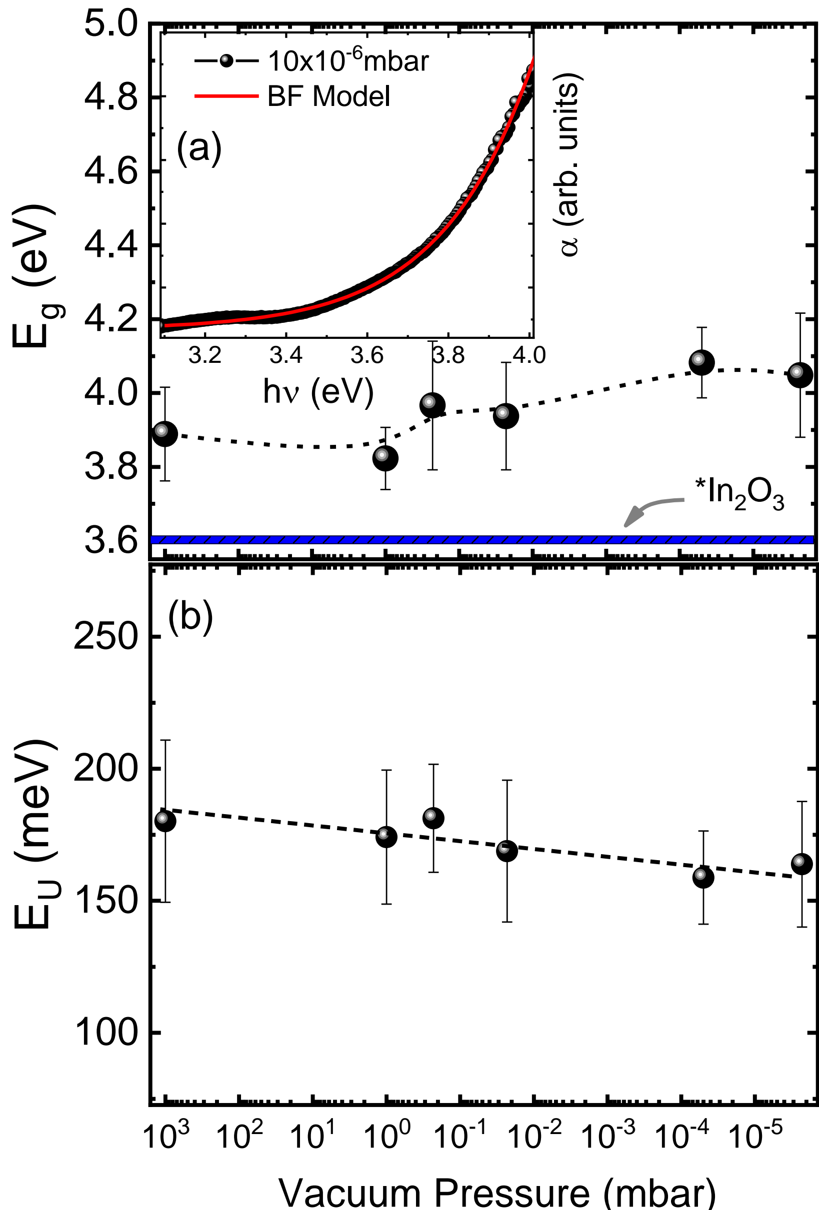

Figure 4.3.6 – (a) Dependence of bandgap energy on increasing vacuum pressures, compared with the bandgap of In_2O_3 (~3.6 eV (KHAN et al., 2012)), showing higher values for ITO films. The inset illustrates the band fluctuation model for a vacuum of 10^{-6} mbar. (b) Urbach energy variation as a function of vacuum pressure. The error bars were derived from analyses of approximately 10 different regions in the absorption spectrum.

complexes with two nonadjacent Sn^{4+} ions (FRANK; KöSTLIN, 1982) can also be removed by the vacuum annealing condition, leading to the increase of carrier density and resistivity reduction. Besides, the vacuum thermal annealing can favor the migration of interstitial tin to V_O sites, further reducing the scattering centers and enhancing the carrier mobility (REN et al., 2022). The increase in carrier concentration suggests an increase in the effective mass. In systems like ITO, where carrier concentration is high, the density of states may transition from a parabolic to a non-parabolic shape, leading to an increase in the reduced mass (SHARIKA et al.,

2022). In this context, analyzing the near-infrared region (see inset in Figure Figure 4.3.5) allows us to determine the free carrier density (n) and carrier mobility (μ_{Opt}) from the optical analysis. These parameters are derived from the plasma frequencies (ω_p) and damping frequencies (ω_τ) using Equation 64 and Equation 66, respectively (LLONTOP et al., 2022).

$$\omega_p = \sqrt{\frac{ne^2}{\epsilon_0 m^*}} \tag{64}$$

Equation 64, can be rewritten as,

$$\gamma = \frac{n_{Hall} e^2}{\omega_p^2 \epsilon_0 m_e} \tag{65}$$

and

$$\omega_\tau = \frac{e}{\mu_{Opt} m^*} \tag{66}$$

Here, ϵ_0 denotes the permittivity of free space, $m^* = \gamma m_e$ is the effective mass of the carriers (reported in the literature for the γ parameter is between 0.1-0.6 m_e (HAMBERG et al., 1984; SHARIKA et al., 2022)), and e represents the electron charge.

Here we use, Equation (3) to calculate the γ parameter, using carrier concentration (n_{Hall}), and ω_p^2, derived from Hall effect and from optical measurements, respectively.

The γ parameter, whose values are presented in Figure 4.3.7 (b), shows a clear increasing trend as VP is increased. The obtained values fall within the range reported in the literature (HAMBERG et al., 1984; SHARIKA et al., 2022). Using the values obtained from γ, the determination of the charge carrier mobility based on damping frequency yielded results ranging from 24 to 10 cm^2/V$\cdot s$ as the vacuum is increased. Furthermore, the observed decrease in optical mobility with increasing vacuum (see Table 4.3.2) may be attributed to the reduction of impurities and defects within the film structure, which aligns with the obtained Urbach energy. This reduction facilitates more effective carrier transport. Additionally, at high vacuum, improved crystallinity further minimizes scattering mechanisms that can hinder carrier movement. On the other hand, the optical mobility values were significantly greater than those obtained by Hall effect measurements, especially after annealing at lower VP, as shown in Table 4.3.2. To highlight this difference, in the inset of Figure 4.3.7 (b) depicts the μ_{Opt}/μ_{Hall} ratio as a function of the charge carrier concentration. It is remarkable that at high carrier concentrations, here around ∽ 4.5×10^{20} cm^{-3} the ratio is near to one, in agreement with the enhanced crystallinity. However, for carrier concentrations below this value, the ratio reaches values greater than one. This results can be explained according to Matthiessen's rule, which states that Hall mobility, μ_{Hall}, is the result of a superposition of optical mobility, μ_{Opt}, and grain boundaries (BND) scattering, μ_{BND}. This relationship is given by the equation μ_{Hall}^{-1}=μ_{Opt}^{-1}+μ_{BND}^{-1} (GHOSH; BASAK, 2019). For lower carrier concentrations, grain boundary scattering becomes more significant. This also illustrates that μ_{Opt} is mainly influenced by in-grain scattering, which leads to a pronounced

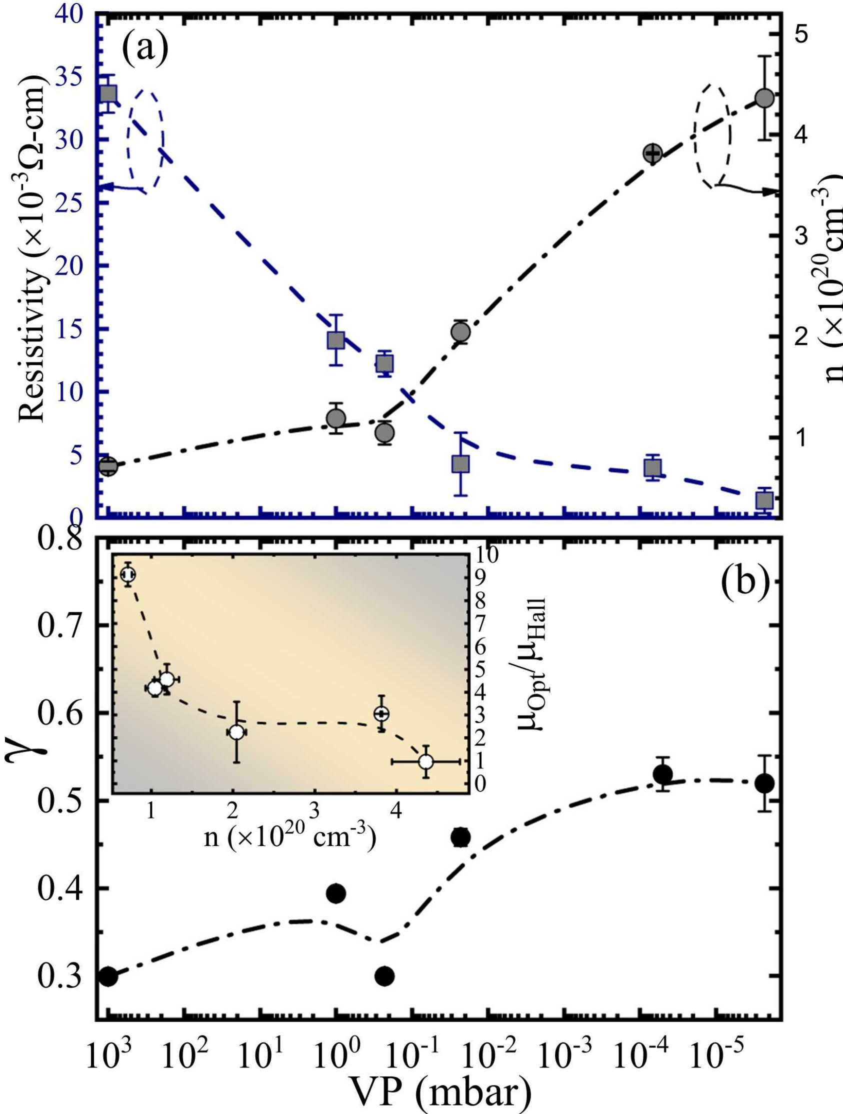

Figure 4.3.7 – (a) Variation in resistivity and carrier concentration (n) based on electrical measurements as a function of the vacuum pressure. (b) γ parameters versus VP assessed via equation 3. The mobility (μ) obtained from optical and Hall effect measurements is displayed in the inset. The dashed lines are shown only as a guide to the eye.

divergence, from the Hall mobility, specially for small particles where grain boundary scattering is the dominant one. This divergence is attributed to the short path length of free electrons as they interact with the high-frequency electric field of light. Furthermore, our results align well with that reported by Ruske et al.(RUSKE et al., 2009) for Al-doped ZnO.

To determine the photocurrent response of the ITO films under UV illumination at room temperature, the films were exposed to UV light with an applied voltage of 2.0 V in air. The changes in current were recorded as the UV light was alternately turned on and off, as shown in Figure 4.3.8.

The observed variation in photocurrent can be attributed to the photoabsorption mechanism. When the semiconductor is exposed to light with energy equal to or greater than its bandgap,

Table 4.3.2 – Resistivity, carrier concentration (n_{Hall}), and mobility (μ) values for ITO thin films were measured using the van der Pauw method. Additionally, the parameter γ was determined from both transmittance and Hall effect measurements.

Vacuum Pressure mbar	ρ $\times 10^{-3}$ Ω·cm	n_{Hall} $\times 10^{20}$cm^{-3}	μ_{Hall} cm^2/V· s	γ	μ_{Opt} cm^2/V· s
Air	33.6 ± 1.5	0.71 ± 0.05	2.6 ± 0.1	0.299 ± 0.005	23.8 ± 0.8
1.0×10^{0}	14.1 ± 2.0	1.19 ± 0.15	3.7 ± 0.5	0.394 ± 0.007	17.0 ± 0.4
2.3×10^{-1}	12.2 ± 1.0	1.05 ± 0.11	4.9 ± 0.4	0.300 ± 0.005	20.4 ± 0.5
2.3×10^{-2}	4.3 ± 2.5	2.05 ± 0.11	7.2 ± 4.2	0.458 ± 0.010	16.2 ± 0.4
5.0×10^{-5}	4.0 ± 1.0	3.82 ± 0.01	4.1 ± 1.0	0.530 ± 0.019	12.6 ± 0.6
2.3×10^{-6}	1.4 ± 1.0	4.36 ± 0.42	10.5 ±7.6	0.520 ± 0.032	10.0 ± 0.6

photons are absorbed, exciting electrons from the valence band to the conduction band, thereby generating electron-hole pairs. The excited electrons move to the conduction band, increasing the current in the circuit, when the light is turned off, the photocurrent decreases, showing the absence of photoexcitation, the homogenized cycles demonstrate the reversible nature of the photocurrent, which is driven by light exposure. Figure 4.3.8 (a) inset depicts the photosensitivity (PS=I_{Light}/I_{Dark}) for films annealed at different vacuum pressures revealing that as the vacuum increases, the photosensitivity decreases. These results suggest that the defects play a significant role in the photocurrent process. Defect centers can localize photogenerated charge, reducing the electron-hole recombination process and, therefore, enhancing the resulting photocurrent. Furthermore, the influence of the size effect cannot be ruled out, as smaller crystallites can provide more active sites for the charge separation process, as observed in Figure 4.3.8 (b) where smaller crystallites exhibit enhanced photocurrent responses.

4.3.6 AC electrical properties

Electrical impedance measurements were performed to understand the effects of thermal annealing in different vacuum pressures on the electrical properties of the ITO films. For this purpose, the Bode plots at different vacuum pressures are presented with their respective equivalent circuits, used to fit these curves as shown in Figure 4.3.9 (a)-(e).

Table 4.3.3 – Values obtained from the impedance measurements, where the equivalent circuit is showing and all electrical components of each of the equivalent circuits.

Vacuum Pressures mbar	L_1 $\times10^{-7}$H	R_1 Ω	C_1 pF	R_2 Ω	L_2 $\times10^{-7}$H	W
1.0×10^{0}	46.10	121.22	25.1	411.1	-	-
2.3×10^{-1}	40.40	104.22	26.6	370.5	-	-
2.3×10^{-2}	2.83	0.56	102.0	145.5	26.3	-
5.0×10^{-5}	2.42	0.56	120.0	121.1	22.2	2.17
2.3×10^{-6}	2.28	0.60	262.0	47.5	10.6	1.20

The values of all electrical components of each of the equivalent circuits are shown in

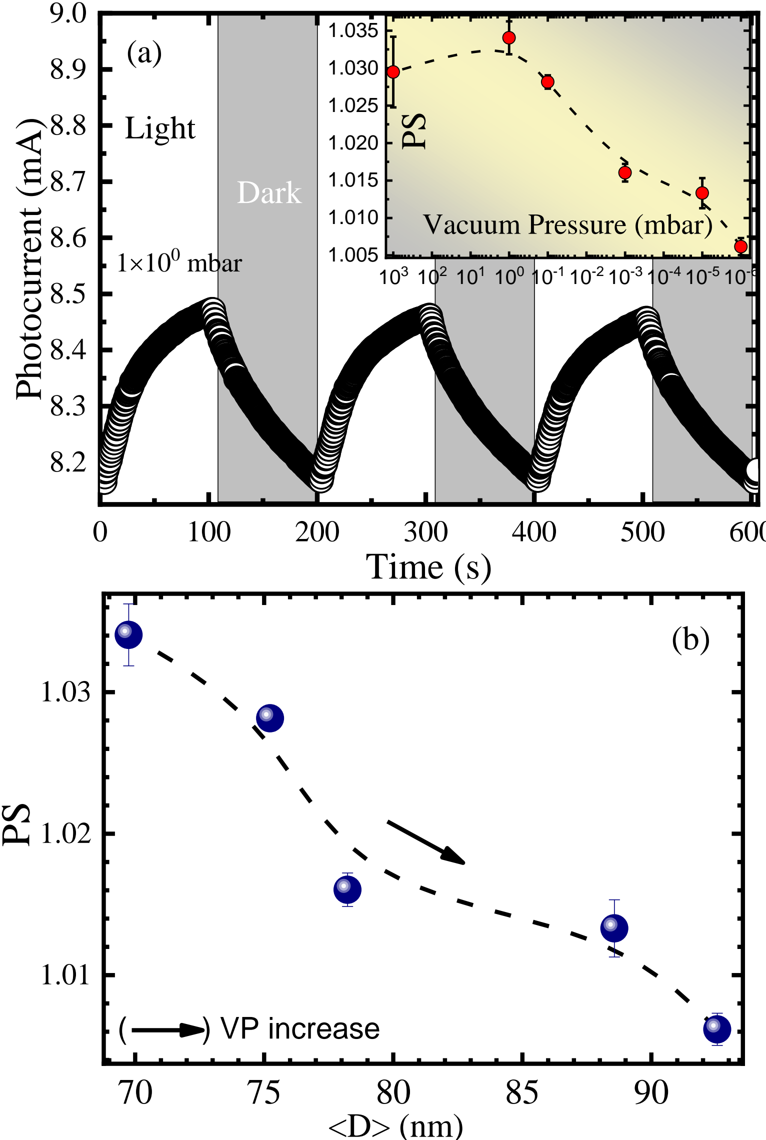

Figure 4.3.8 – (a) Photocurrent as a function of time under alternating light and dark conditions for the sample annealed at a vacuum of 1.0×10^{-2} mbar. (b) Photosensitivity ($PS = I_{Light}/I_{Dark}$) as a function of crystallite size, showing a decrease in PS with increasing crystallite size. The inset shows the PS response as a function of the vacuum pressure, indicating the influence of environmental conditions on the photocurrent response. The dashed lines are provided only as a guide for the eyes.

Table 4.3.3. As shown in Figure 4.3.9 (f), for a better understanding, component groups are defined as follows: group 1 (G_1) is formed by an inductor (L_1) and a resistor (R_1) in parallel, group 2 (G_2) is formed by a capacitor (C_1) and a resistor (R_2) in parallel, group 3 (G_3) is formed by an inductor (L_2) and a resistor (R_2) in series, both in parallel with the capacitor (C_1) and finally group 4 (G_4) formed by the Warburg component. The R_C value would be a contact resistance, which is why it was not considered within the groups. From data shown in Table 4.3.3 the following can be observed. More accurate modeling of the impedance as a function of frequency curves is achieved in films subjected to VPs higher than $2.3{\times}10^{-1}$ mbar using the G_3 component as it is observed in Figure 4.3.9. Moreover, as the vacuum is changed from 1.0×10^{0} to

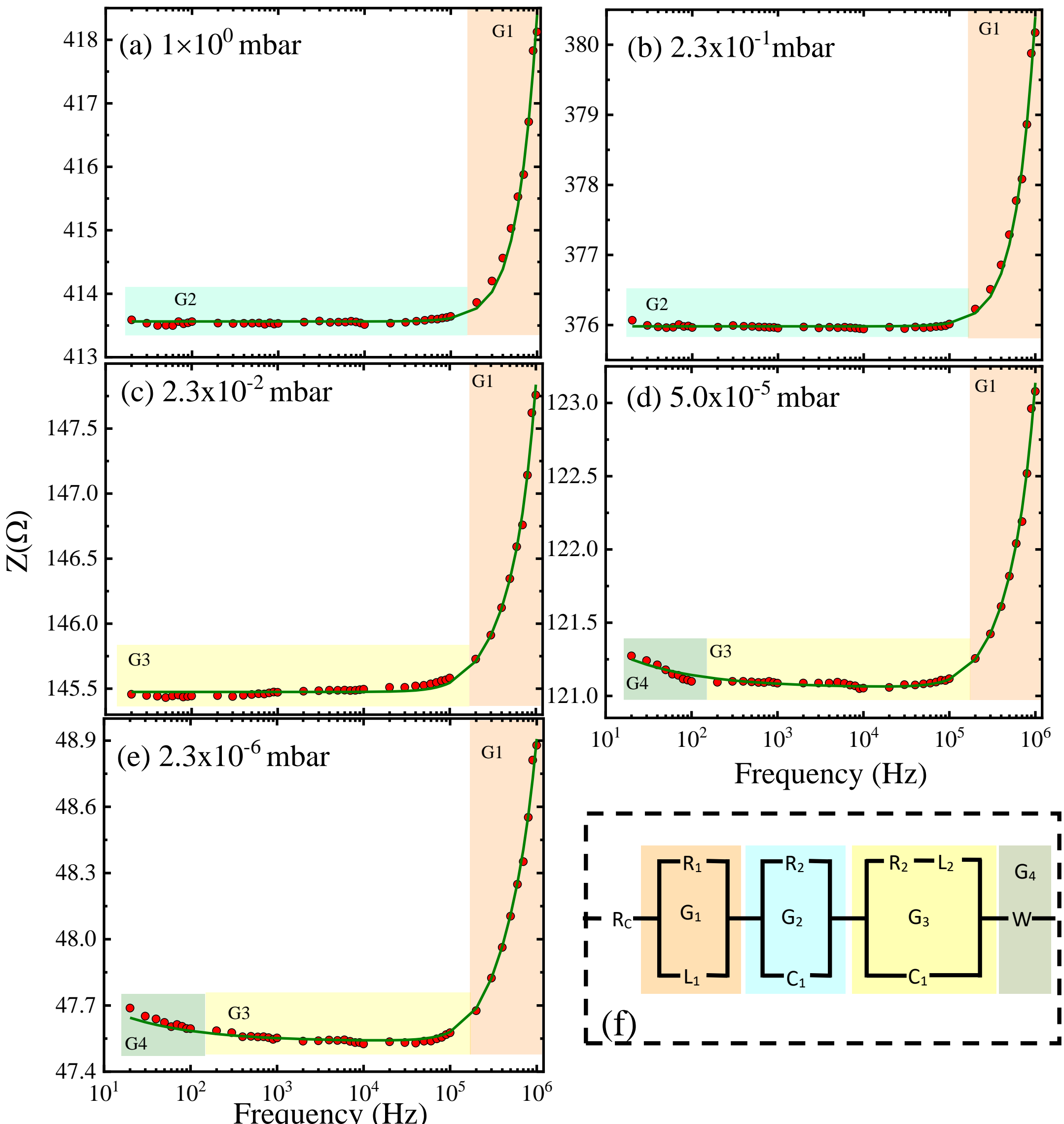

Figure 4.3.9 – (a)-(e) Bode plots at different vacuum pressures and their respective equivalent circuits. The red dots are the experimental data and the solid green line is the fit. The letters present the following: resistance (R), inductance (L), capacitance (C), and Warburg component (W). (f) The mounted circuit was divided into four component groups: group 1 (G_1), group 2 (G_2), group 3 (G_3), and group 4 (G_4).

2.3×10^{-1} mbar, the capacitance C_1 increases by approximately 6%. Concurrently, the resistance R_1 decreases dramatically from 121 Ω to 0.60 Ω, reflecting a reduction of about 99.7%. Similarly, the resistance R_2 of G_2 group also shows a significant decrease of around 10%. At vacuum higher than 2.3×10^{-1} mbar, C_1 continues to rise, while R_2 continues to decrease. The reduction in the resistance aligns well with the observed decrease in the DC resistivity as is shown in Figure 4.3.7 (a). Additionally, with the increase of the carrier concentration, an increase in capacitance C at the grain boundaries is expected, as evidenced by our data.

For all VPs used to anneal the films, the inductance of the G_1 components show a decrease from $46.1{\times}10^{-7}$ H to $2.28\ {\times}10^{-7}$ H for L1 (~95% less) and for the G_3 from 26.3 to $10.6\ {\times}10^{-7}$

H. According to the optical measurements, this implies that the local mobility for ITO films diminishes as the vacuum of the post-thermal annealing process rises. This decrease is attributed to the annihilation of defects within the film structure, likely due to the improved crystallinity. Specifically, regulating these defects may alter the local magnetic field as they respond to alternating current excitation. It is important to note that the inductance component is primarily observed at high frequencies, around 1×10^6 Hz. In this range, ionic conduction becomes the dominant mechanism (HAUFF, 2019), as ions move in response to the high-frequency alternating field. The latter can explain the observed reduction in the inductive (L_1, and L_2) components

Finally, at a vacuum pressure above 5.0×10^{-5} mbar, the Warburg component becomes apparent. This is evidenced by the increase in impedance at lower frequencies, as it is inversely proportional to $\sqrt{\omega}$ (TAYLOR; GILEADI, 1995).

4.3.7 Theoretical Results and Discussions

The $In_{29}Sn_3O_{48}$, corresponding to a 9.4% tin doping concentration, was produced to represent optimized ITO structures. In this ITO framework, defects such as oxygen (V_O) vacancy and interstitial oxygen (O_i) were introduced. Next, the band structure was calculated to improve understanding of the material's electrical and optical properties.

Figure 4.3.10 (a) shows the band structure of $In_{29}Sn_3O_{48}$. The Fermi level is aligned with the conduction band, a hallmark of highly degenerate transparent conducting oxides. The calculated energy gap from the maximum valence band to the Fermi level is 2.75 eV, which is lower than the experimental value (see Figure 4.3.6 (a)). This underestimation is a known limitation of the PBE pseudopotentials used in various density functional theory (CHEN et al., 2015). In the PDOS figures, we observe that the In(s) and Sn(p) orbitals make the most significant contributions to the conduction band of ITO with minor contributions from the In(p) and Sn(p) orbitals, in the case of O(p) orbitals they dominate in the valence band, with a slight contribution in the conduction band. As shown in Figure 4.3.10 (b)-(d), introducing oxygen vacancies in the $In_{29}Sn_3O_{48}$ structure leads to noticeable changes in the band structure, with the appearance of new bands between the valence band maximum (E_V) and below the Fermi level (E_F) related to the O(p) orbitals. Furthermore, when we increase the number of oxygen vacancies, the electronic states associated with those defects start to localize. These changes can be attributed to the hybridization of In and Sn electronic orbitals, which may also explain the observed increase in the transmittance of ITO films, as suggested in the literature (CHEN et al., 2014).

The projected density of states (PDOS) shown in Figure 4.3.10 reveals that the In(s) and Sn(p) orbitals still contribute to the ITO conduction band. However, in the band structure of Figure 10 (e), we observe that interstitial oxygen produces shifts near the valence band with an upward splitting increasing the density of the O(p) orbitals, it is important to highlight that these defects (V_O and O_i) cause significant changes in the electrical properties of ITO.

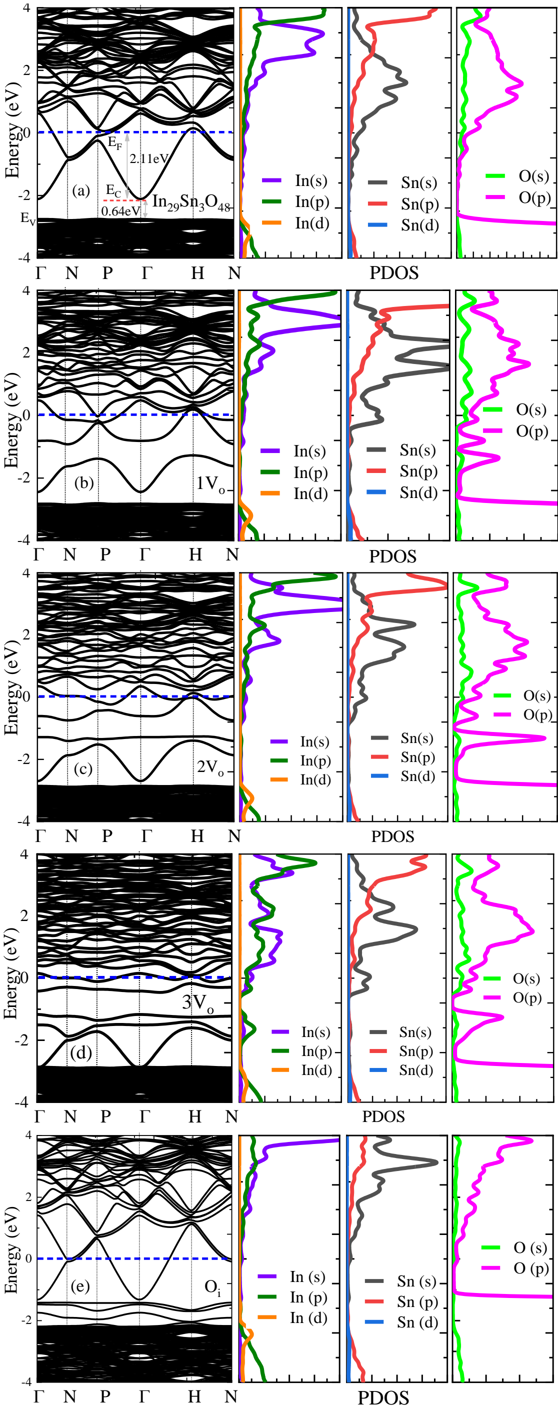

Figure 4.3.10 – Band structures calculated via DFT for (a) pristine ITO, (b) ITO with 1 oxygen vacancy, (c) 2 oxygen vacancies, (d) 3 oxygen vacancies, and (e) 1 oxygen interstitial. The projected density of states (PDOS) for In, Sn, and O orbitals is also shown. The blue line indicates the Fermi energy level.

The Fermi level overlaps with the conduction band, indicating that oxygen vacancies enhance the conductivity of Indium tin oxide (ITO). This enhancement occurs because oxygen can contribute up to two electrons to the conduction process. Additionally, charge carrier calculations obtained through density functional theory (DFT) confirm this improvement in conductivity as discussed above. To calculate the charge carriers, it is necessary first to make an adjustment to

the parabola formed in the conduction band at the Γ point, to obtain the effective mass of the electron (m^*), using this equation:

$$m^* = \gamma m_e = \hbar^2 (\frac{\partial^2 E}{\partial k^2})^{-1} \tag{67}$$

The charge carriers for highly degenerate n-type doped systems, (where $E_F > E_C$), may be calculated using the following expression, which takes the values of the Fermi energy (E_F) and the conduction band energy (E_C) (ZEGHBROECK, 2011).

$$n_{cal} = \frac{2\sqrt{2}}{3\pi^2} (\frac{qm^*}{\hbar^2})^{3/2} (E_F - E_C)^{3/2} \tag{68}$$

The parameter γ of the effective mass can be found by fitting the electronic band structure to a parabolic function, as demonstrated by Equation (5). The result of the fit is shown in Table 4.3.4, which indicates a slight increase as more oxygen vacancies are generated, which could be interpreted with a flattening of the parabolas around the high Γ symmetry point, inducing low electron mobility (see Figure 4.3.10). In contrast, in the system containing interstitial oxygen, the effective mass increases by 0.2% compared to the pristine $In_{29}Sn_3O_{48}$ structure, rather than decreasing. However, n_{cal} display an overestimation, a fact already reported by DFT calculations, because dispersion effects are not considered (BREWER; F, 2004).

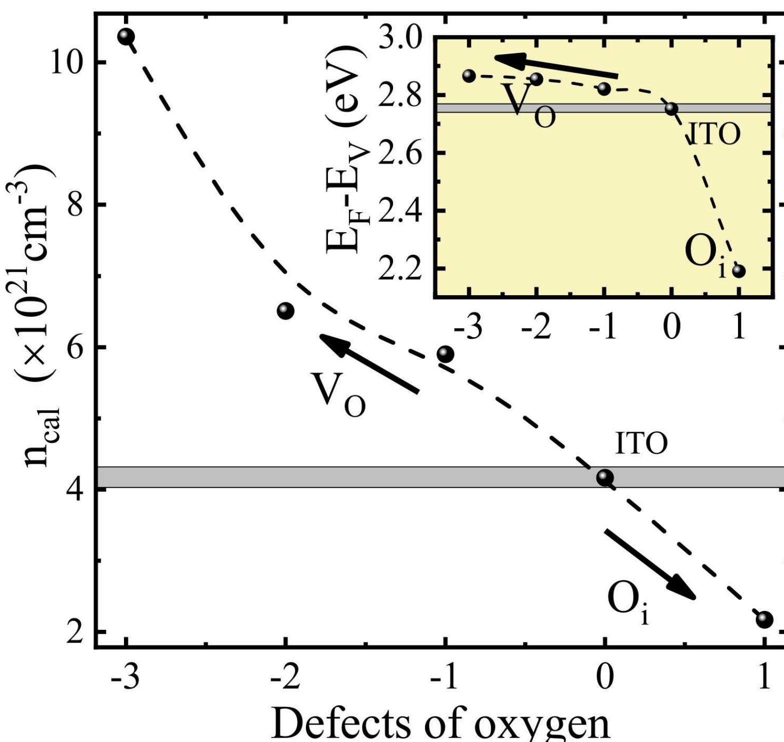

Figure 4.3.11 – Carrier concentration as a function of oxygen vacancies, calculated via DFT. The inset shows the observed shift between the Fermi energy (E_F) and the valence band maximum (E_V) due to oxygen defects. Dashed lines are included as a visual guide.

Furthermore, the charge carrier concentration, calculated using Equation 6, is presented in Figure 4.3.11, which shows an increase with the rise in oxygen vacancies. This observation is consistent with the existing literature, indicating that oxygen vacancies effectively enhance the carrier concentration in ITO (REN et al., 2022). In contrast, oxygen interstitials exert an opposing effect by decreasing the calculated carrier concentration (n_{cal}), likely due to the interstitial atoms serving as sources of carrier scattering (LI et al., 2015). Films subjected to thermal annealing in air atmospheres (1.0×10^3 mbar) exhibit a significantly higher density of scattering centers compared to those annealed in vacuum. Furthermore, the calculated values of n_{cal} tend to be overestimated, as has been previously observed in DFT calculations, likely due to the lack of dispersion effects (BREWER; F, 2004).

In the inset of Figure 4.3.11, the observed difference between the Fermi energy (E_F) and the maximum of the valence band energy (E_V), associated with the bandgap, is displayed as a function of oxygen defects in the structure. The presence of intestitial oxygen atoms in the structure results in a lower Fermi energy compared to ITO. However, when oxygen vacancies are introduced, a shift to higher Fermi energy values is observed, consistent with the Moss-Burstein effect.

Table 4.3.4 – Effective mass of free electrons, transition between E_F-E_V and charge carriers, calculated for indium tin oxide with different defects by DFT.

Defect	γ	$(E_F - E_V)$ (eV)	n_{cal} ($\times 10^{21}$ cm^{-3})
1 O_i	0.46	2.19	2.17
$In_{29}Sn_3O_{48}$	0.45	2.75	4.16
1 V_O	0.46	2.82	5.90
2 V_O	0.47	2.85	6.51
3 V_O	0.61	2.87	10.4

4.3.8 Conclusions

In this work, we study the effect of thermal annealing under different vacuum pressures on the properties of ITO thin films. Results indicate that the increase of the vacuum pressure during the annealing significantly improves the surface morphology, with a surface roughness decrease. The crystallite size becomes larger as the vacuum of the annealing is increased. This was assigned to the progressive enhancement of the atomic diffusion, in consistency with the Ostwald ripening model. Optical results revealed that the bandgap energy increases with the vacuum of annealing, meanwhile, the Urbach energy showed a decreasing trend, suggesting the reduction of structural defects and the crystalline improvement. The observed increase in carrier concentration aligns with the electrical resistivity reduction and these results are assigned to the generation of oxygen vacancies favored by the vacuum during the annealing. The photocurrent measurements show that smaller crystallite size resulting from the annealing in lower vacuum pressures, boosting the photocurrent generation, due to the larger surface. DFT calculations corroborate that the oxygen

vacancies lead to the increase of the carrier concentration and electrical conductivity, while the presence of interstitial oxygen have a less significant impact. The calculated charge carriers density shows a tendency to increase with the increase of the oxygen vacancies in consistency with the experimental results.

4.4 Tuning the structural, electrical, and optical properties of ITO thin films via thickness control and vacuum annealing

In this work, we present an experimental investigation of the effect of the film's thickness on the structural, morphological, optical, and electrical properties of ITO films deposited by DC sputtering. We evaluated the impact of film thickness on the metal-insulator transition observed at low temperatures and modeled by the weak localization corrections model.. In addition, we employ first-principles calculations on the structure with intrinsic defects associated with O_i and V_O using Density Functional Theory (DFT) to deepen our understanding of the structural and optoelectronic properties of the ITO structure. This work was published in the journal **Materials Today Communications**, DOI: https://doi.org/10.1016/j.mtcomm.2025.113605

4.4.1 Experimental details

Sn-doped In_2O_3 thin films were deposited onto borosilicate glass substrates via DC sputtering. The working pressure was maintained at $\sim 4.0 \times 10^{-2}$ mbar during the deposition process. Films of varying thicknesses were obtained by arranging the substrates side by side, as illustrated in Figure 4.4.1, with a 5 mm separation between them. A metallic target composed of 90 wt.% In and 10 wt.%Sn (99.99% purity) was used for the deposition. During the sputtering process, the substrates were kept at room temperature and positioned ~15 mm from the cathode (target). Throughout the deposition, a constant voltage of approximately ~ 1400 V was applied.

Thermal oxidation was carried out by annealing the samples in a tubular furnace under high vacuum ($\sim 2.0 \times 10^{-6}$ mbar) at 500 °C for 2 hours, with a heating rate of 10 °C/min. X-ray diffraction (XRD) measurements were performed using a Rigaku model diffractometer with a CuKα copper anode (1.540558 Å) with a step of 0.025° and a speed of 2.0 °/min in range from $20^\circ \leq 2\theta \leq 70^\circ$. To estimate the structural parameter, the Rietveld refinement was performed utilizing the general structure analysis system (GSAS) using the EXPGUI graphical user interface for GSAS (TOBY; DREELE, 2013). UV-Vis spectra were collected using the SENTECH SENresearh 4.0 equipment, in transmittance mode in the spectrum range of 250 - 2500 nm. Electrical resistivity, charge carrier concentration, and mobility of the films were measured at room temperature (RT) using the Hall system, in a four probe, van der Pauw configuration, with an applied magnetic field of 0.35 T. Temperature dependent measurement, were placed nitrogen commercial cryostat (Janis Inc.), measurement were made at low temperature (80 K). Data was collected using a Keithley 6220 current source and a Keilhley 2182A voltmeter, and temperature was measured using a Lakeshore DRC-91CA temperature controller.

4.4.2 Theoretical Approach

Density functional theory (DFT) (HOHENBERG; KOHN, 1964; KOHN; SHAM, 1965) calculations were performed, using the Vienna Ab initio Simulation Package (VASP) (KRESSE;

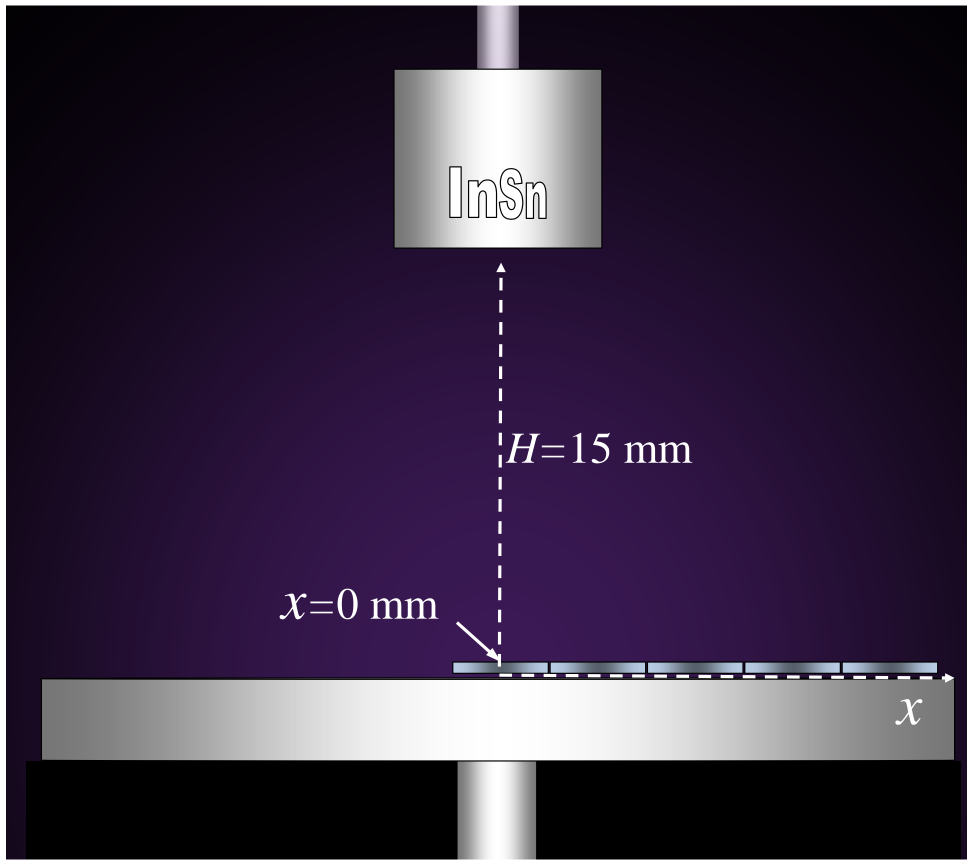

Figure 4.4.1 – Schematic representation of the substrate arrangement during the DC sputtering process. The substrates are positioned at different distances (x) from the center of the metallic In–Sn target, which is located 15 mm above the substrate plane. Using this configuration one can obtain films which thickness depends on the x position.

FURTHMüLLER, 1996) and the Quantum ESPRESSO package under the GNU General Public License (GIANNOZZI et al., 2009). The study focused on indium oxide ($In_{32}O_{48}$), where three In atoms were substituted with Sn atoms, yielding a doping concentration of approximately 9.4 % ($In_{29}Sn_3O_{48}$). Additionally, various intrinsic defects were introduced into the indium tin oxide unit cell, resulting in configurations such as $In_{29}Sn_3O_{47}$, $In_{29}Sn_3O_{49}$, and $In_{29}Sn_3O_{50}$. The Kohn-Sham (KS) equations were solved using the projector-augmented wave (PAW) method (BLöCHL, 1994), with the KS states expanded by using plane waves. The electronic and structural properties were described through the Perdew Burke Ernzerhof (PBE) Exchange correlation functional (PERDEW; BURKE; ERNZERHOF, 1996). For Brillouin zone (BZ) integration, a Γ-centered k-mesh of $4 \times 4 \times 4$ was used for the optimization process, and $8 \times 8 \times 8$ for electronic properties (density of states and bands structure). During structural optimization, the self-consistent cycle converged with a total energy criterion of 10^{-6} eV, and atomic forces were minimized to less than 0.01 eV Å^{-1}. A plane-wave energy cutoff of 600 eV was applied in all simulations. Visualization and structural analyses were carried out using VESTA software (MOMMA; IZUMI, 2008). The post processing were performed using the VASP+ Phonopy package (TOGO; TANAKA, 2015).

4.4.3 Structural characterization

Figure 4.4.2 shows the XRD patterns of the ITO films deposited at different substrate positions, as shown in Figure 4.4.1. The diffraction peaks observed at (211), (222), (321), (400), (411), (431) (440) and (622) are consistent with the cubic bixbyite structure of indium oxide (In_2O_3), in accordance with the JCPDS reference card no. 71-2194. No secondary phases were detected within the detection limits of the technique, indicating that Sn is likely incorporated into the In_2O_3 lattice without forming separate phases. Rietveld refinement was performed using Lorentzian-shaped peak functions, as implemented in the GSAS software package (TOBY; DREELE, 2013). Refinement results are shown in Figure 4.4.2, where the orange solid line represents the calculated diffraction pattern. The difference between the observed and calculated patterns is also plotted, highlighting the quality of the fit. The refined structural parameters are summarized in Table 4.4.1.

Figure 4.4.3(a) shows the variation of the lattice parameter for samples deposited at different positions, ranging from the center (x= 0 mm) to x= 20 mm. The measured lattice constant is slightly lower than the bulk value reported for cubic In_2O_3 (10.117 Å (MAREZIO, 1966)), with the sample exhibiting a value below 10.106 Å. This corresponds to a reduction of approximately 0.11% in the unit cell volume. The observed lattice contraction is attributed to the partial substitution of In^{3+} ions (ionic radius = 0.81 Å) by smaller Sn^{4+} ions (ionic radius = 0.71 Å), which induces local compressive strain within the crystal lattice. Such distortion is consistent with Vegard's law, which predicts a linear variation of the lattice parameter with composition in a solid solution. The absence of phase segregation and the monotonic trend in lattice shrinkage further support the incorporation of Sn into the In_2O_3 matrix without the formation of secondary phases.

Table 4.4.1 – Structural parameters obtained from X-ray diffraction analysis for Sn-doped In_2O_3 thin films deposited at different substrate positions. Parameters include the lattice constant ($a = b = c$), average full width at half maximum ($\langle$FWHM$\rangle$), texture coefficients (TC) for the (222) and (400) planes, and the S-factor (S = WRp/Rp) indicating the quality of the Rietveld refinement. Film thickness (t_{XRD}) was estimated using the absorption-based method described in the text, with an uncertainty of approximately 12% which does not affect the uncertainty of the resistivity and carrier concentration

Position (mm)	$a = b = c$ (Å)	⟨FWHM⟩ (°)	TC (222)	TC (400)	S	t_{XRD} (nm)
0	10.1047	0.1789	1.81	0.72	1.31	552
5	10.1044	0.1915	1.21	0.91	1.30	333
10	10.1035	0.1723	1.18	1.11	1.28	298
15	10.0020	0.1705	1.16	1.30	1.33	215
20	10.1015	0.1650	1.25	1.28	1.26	199

.

Moreover, a systematic variation in the lattice parameter is observed, which values depend on x position. Films deposited closer to the center, where the deposition rate is higher,

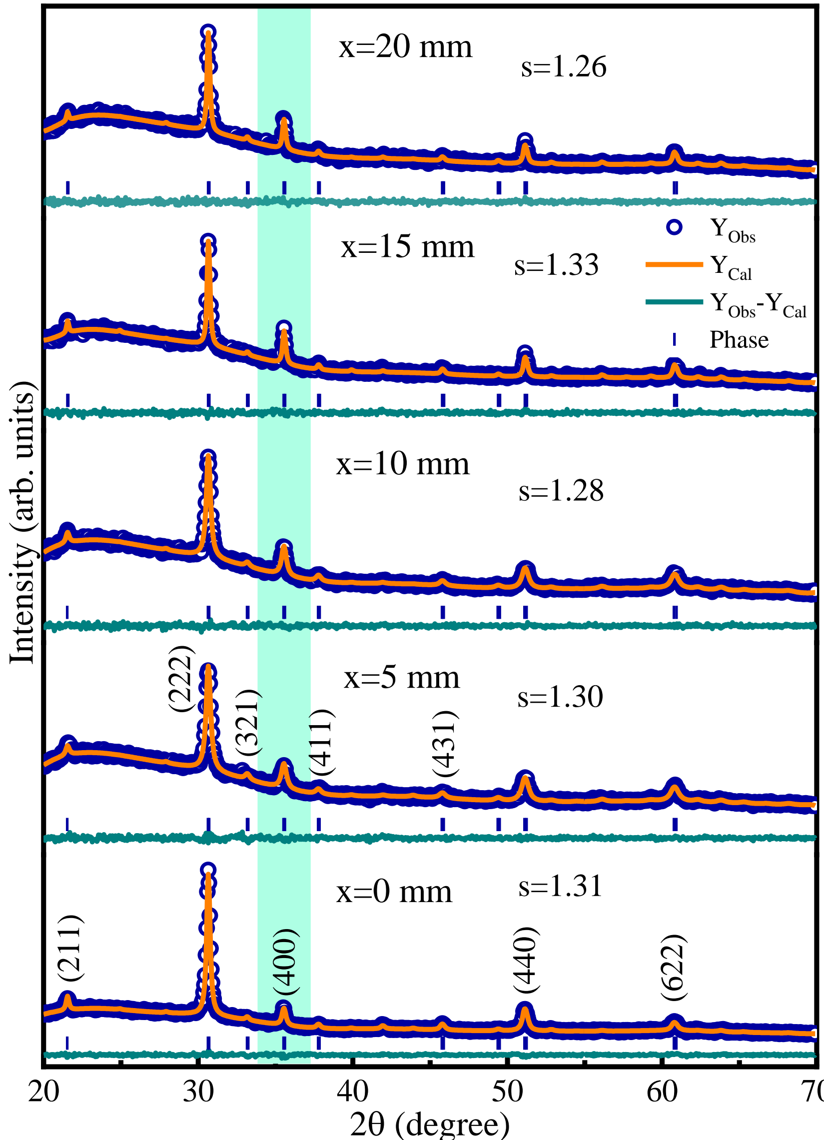

Figure 4.4.2 – XRD patterns of Sn-doped In_2O_3 thin films annealed under high vacuum at different substrate positions (x= 0 – 20 mm). The blue circles represent the experimental data (Y_{Obs}), and the orange lines correspond to the calculated diffraction patterns from Rietveld refinement (Y_{Cal}). The green lines show the difference curves ($Y_{\mathrm{Obs}} - Y_{\mathrm{Cal}}$), while the vertical bars mark the expected Bragg peak positions for the cubic bixbyite phase. Major diffraction peaks are indexed. The S-factor (S = WRp/Rp) is provided for each refinement, indicating the fit quality.

exhibit a smaller difference in the lattice constant with respect to the value of bulk compound (see Figure 4.4.3(a)). To understand this behavior, it is important to first note that as-deposited samples are typically amorphous, as previously reported (VILCA-HUAYHUA et al., 2025). This amorphous structure tends to exhibit a high density of intrinsic defects, such as interstitial oxygen (O_i) and oxygen vacancies (V_O). The interstitial oxygen atoms can form neutral complexes with two nonadjacent Sn^{4+} ions in the ITO lattice (FRANK; KöSTLIN, 1982). During thermal annealing, migration processes are activated, facilitating the removal of O_i and the formation of V_O. In this context, spatial variations in film thickness can significantly influence the effectiveness

of thermal annealing in a vacuum atmosphere. In thinner films, the vacuum annealing effect is more effective, as it is concentrated at the surface, whereas in thicker films, the effect is less significant since the vacuum primarily influences only some surface layers. This phenomenon contributes to the observed reduction in the lattice parameter, a behavior consistent with previous reports in the literature (VILCA-HUAYHUA et al., 2025).

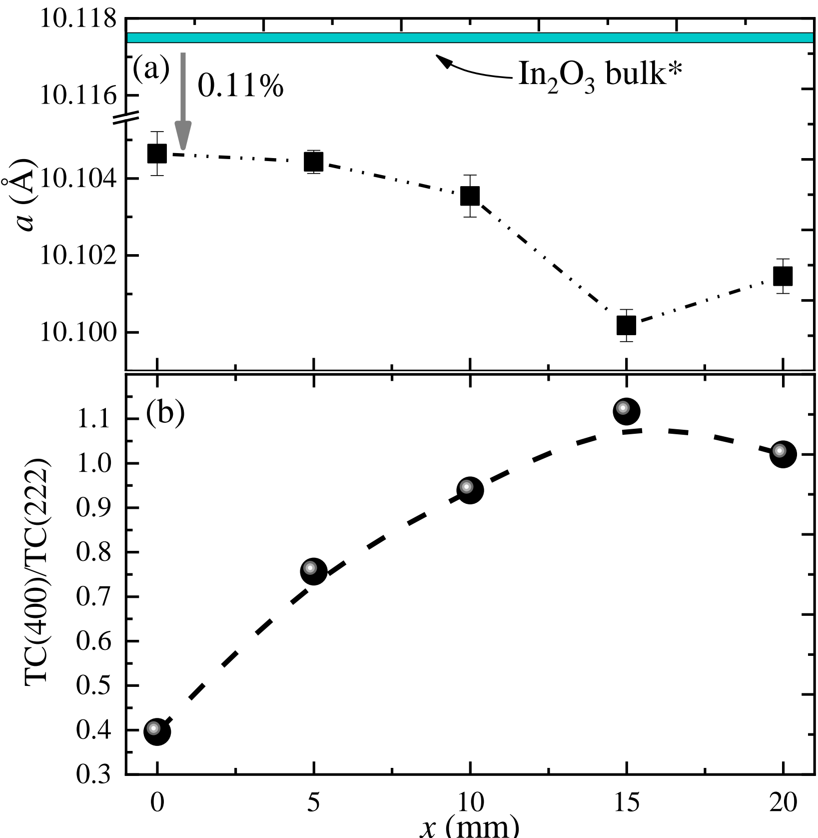

Figure 4.4.3 – (a) Lattice parameter as a function of the (x) position. The green line represents the bulk lattice parameter of In_2O_3. (b) Texture coefficients (TC) for the (222) and (400) crystallographic planes, showing the TC ratio (400)/(222) as a function of the substrate position.

X-ray diffraction patterns reveal a dominant (222) orientation in all samples, indicative of the preferred growth direction in the bixbyite structure of In_2O_3. However, a closer examination of the diffraction profiles shows that as (x) increases (film thickness decreases), the relative intensity of the (400) reflection becomes increasingly pronounced (see the marked region in Figure 4.4.2). This trend, is consistent with previous observations (GHEIDARI et al., 2007; NAJWA et al., 2019), and suggests a structural modulation linked to the oxygen stoichiometry. Specifically, a stronger (400) reflection is associated with a lower oxygen content, pointing toward the increase of V_O as the film thickness decreases. This observation is consistent with the earlier analysis of lattice parameter reduction, where thinner films exhibited greater unit cell contraction.

The texture coefficient (TC) can be calculated using the standard relation:

$$TC(hkl) = \frac{I_{(hkl)}/I_{0(hkl)}}{\frac{1}{N}\sum_N I_{(hkl)}/I_{0(hkl)}} \tag{69}$$

where $I_{(hkl)}$ is the measured intensity of the (hkl) diffraction peak, $I_{0(hkl)}$ is the corresponding standard intensity from the JCPDS card No. 71-2194, and N denotes the number of peaks included in the analysis.

As shown in Figure 4.4.3(b), the higher TC values observed for the (400) plane in samples located far away from the central point (larger x), where the films are expected to be thinner, provide additional evidence for the increase of V_O that favors this specific crystallographic orientation.

To estimate the film thickness (t_{XRD}), the diffractograms obtained by X-ray diffraction were analyzed by the reduction in the intensity of the substrate diffraction peak, which correlates directly with the thickness of the deposited layer (VELASQUEZ-ORDOñEZ et al., 2024). In this approach, the film thickness t_{XRD} of the ITO layers is determined by comparing the integrated intensity of the substrate diffraction peak before (A_s) and after (A_{ITO}) film deposition. The relationship is given by:

$$t_{\text{XRD}} = \frac{1}{2\mu_{\text{ITO}}\csc\theta}\ln\left(\frac{A_s}{A_{\text{ITO}}}\right) \tag{70}$$

where μ_{ITO} is the linear absorption coefficient of ITO (1457.4 cm^{-1}) (STEIN, 2019), and θ is the Bragg angle of the (222) reflection used for the analysis. The factor $\csc\theta$ accounts for the geometry of X-ray incidence and diffraction with respect to the sample surface. The t_{XRD} derived from this method are presented in Table 4.4.1, and show good agreement with those obtained through optical measurements, as detailed in the optical characterization section. Additional details concerning the thickness determination via XRD data analysis can be found elsewhere (SRINIVASAN et al., 1979).

4.4.4 Electrical properties

To determine the sheet resistance, resistivity, charge carrier concentration, and mobility, measurements were performed using the four probe method in Van der Pauw configuration. Table 4.4.2 shows that the sheet resistance ($R_\square$) increases, suggesting a reduction in film thickness. This result is consistent with XRD data analysis (see Table 4.4.1) and it will be also corroborated by optical measurements presented later in the optical characterization section. Using the measured thickness values, the resistivity (ρ) was calculated, yielding values in the range of $(4.9 - 7.1) \times 10^{-4}\ \Omega \cdot \text{cm}$. These resistivity values are consistent with reported resistivities for indium tin oxide (ITO) films deposited via DC sputtering, which typically range from 10^{-4} to $10^{-3}\ \Omega \cdot \text{cm}$, depending on deposition conditions such as oxygen partial pressure, substrate temperature, and post-deposition annealing (VILCA-HUAYHUA et al., 2025; TIEN et al., 2018).

However, no clear trend in resistivity is observed as the thickness decreases, suggesting that factors beyond thickness, such as variations in film microstructure or stoichiometry, also influence the electrical properties.

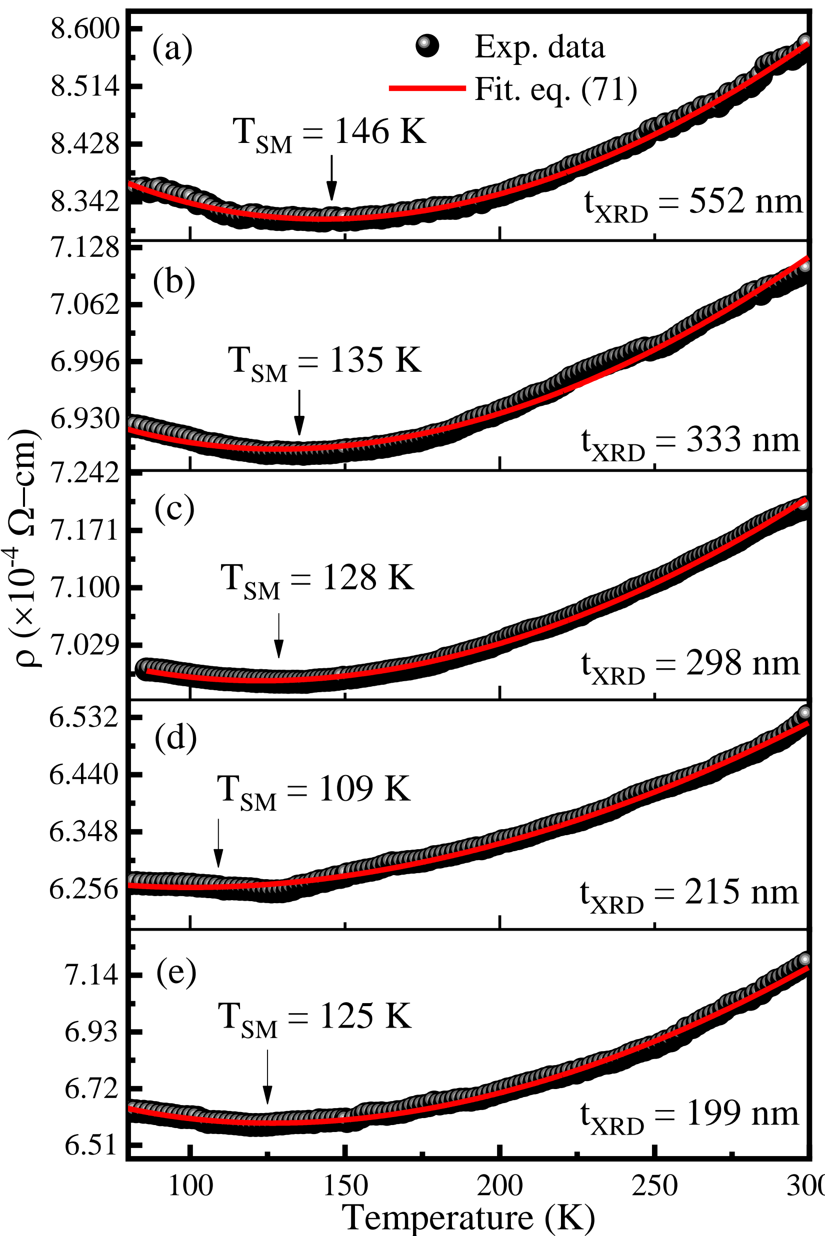

Figure 4.4.4 – (a)–(e) Resistivity vs. temperature curves measured from 80 K to 300 K for Sn-doped In_2O_3 (ITO) thin films with different thicknesses (t_{XRD}). The experimental data are shown as black symbols, while the red lines represent the fits using (Equation 71). The semiconductor-to-metal transition temperature (T_{SM}) is indicated for each film.

As shown in Table 4.4.2, the carrier concentration exhibits a slight increasing trend, while the mobility tends to decrease as the thickness decreases, particularly in regions where the lattice parameter is smaller (see Figure 4.4.3 (a)). The observed trends can be attributed to the influence of thermal annealing in vacuum, which alters the defect density of the films.

Table 4.4.2 – Electrical properties of the ITO films measured at different sample positions (x), including the sheet resistance ($R_{\square}$), resistivity (ρ), carrier concentration (N_{Hall}), and mobility (μ_{Hall}). Also reported the extrapolated resistivity (ρ_0) at $T = 0$ K, and the fitting parameters m and K, obtained from temperature-dependent resistivity measurements.

SP (mm)	$R_{\square}$ (Ω)	ρ ($10^{-4}\Omega$cm)	N_{Hall} (10^{20}cm^{-3})	μ_{Hall} (cm^2/Vs)	ρ_0 ($10^{-4}\Omega$ cm)	m (1/Ω cm $K^{1/2}$)	K ($10^{-10}\Omega$ cm K^{-2})
0	11.9±2.3	6.6 ± 2.1	3.8 ± 0.4	25 ± 9	8.36	8.3 ± 0.1	7.28 ± 0.05
5	21.4±0.1	7.1 ± 0.9	7.0 ± 0.6	13 ± 3	8.56	6.0 ± 0.2	6.70 ± 0.11
10	23.0±4.3	6.9 ± 2.1	6.9 ± 0.6	13 ± 5	8.66	5.2 ± 0.1	6.48 ± 0.05
15	22.7±1.1	4.9 ± 0.8	11.0 ± 1.0	12 ± 3	6.78	5.1 ± 0.2	5.46 ± 0.07
20	28.9±0.3	5.7 ± 0.7	9.0 ± 0.8	12± 3	8.26	17.4 ± 0.3	15.4 ± 0.13

In agreement with XRD data analysis, the vacuum annealing seems to increase V_O, which act as donor defects and contribute the free carrier generation, resulting in increased carrier concentration and reduced resistivity (REN et al., 2022; EFFECT. . . , 2022). Simultaneously, O_i, typically associated with carrier trapping and scattering, can be removed, further enhancing electrical conductivity (VILCA-HUAYHUA et al., 2025). These experimental observations align well with the charge transport behavior predicted by density functional theory (DFT) calculations, which will be discussed in the following sections.

Temperature-dependent resistivity measurements were conducted to investigate charge transport mechanisms. Figure 4.4.4 depicts the resistivity variation in the 80–300 K range for films with different thicknesses. As observed, all ITO films exhibit a minimum resistivity value, indicating a semiconductor-to-metal transition onset, a phenomenon that has been previously reported in the literature for ITO (KAUSHIK; KUMAR; SUBRAHMANYAM, 2017a; GUO et al., 2011; LIN et al., 2010). To model the thermal dependence of the resistivity, the weak localization effect (WLE) is taken into account, by Equation 71, as previously proposed in the literature (KAUSHIK; KUMAR; SUBRAHMANYAM, 2017a; HERRANZ et al., 2004).

$$\rho = \frac{1}{\rho_0^{-1} + mT^{1/2}} + KT^2 \tag{71}$$

Here, ρ_0 is the Boltzmann resistivity (residual resistivity) in the absence of thermal dependent scattering mechanisms. The $(mT)^{1/2}$ term arises from quantum corrections, WLE, whereas the KT^2 contribution accounts for electron scattering typically observed at higher temperatures in metallic regimes.

As shown in Figure 4.4.4(a)–(e), Equation 71 models well the experimental data. The extracted fitting parameters are summarized in Table 4.4.2. The semiconductor-to-metal transition temperature (T_{SM}) was determined from the condition $d\rho/dT = 0$, as defined in (Equation 71), using the values extracted from the fitted resistivity curves (see Figure 4.4.5).

As reported in the literature, the columnar growth of ITO induces different grain sizes

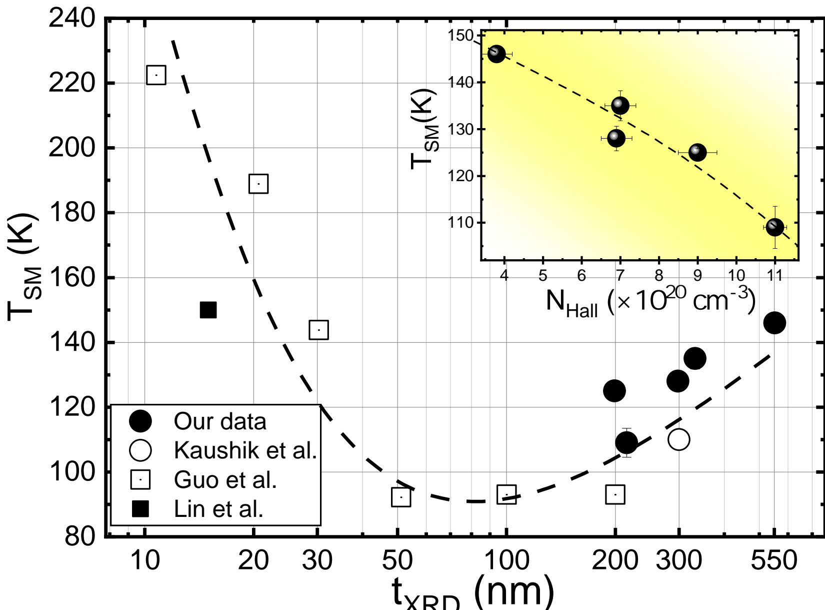

Figure 4.4.5 – Semiconductor-to-metal transition temperature (T_{SM}) as a function of film thickness (t_{XRD}) for Sn-doped In_2O_3 (ITO) thin films. This figure includes data from this work (black circles) and previously reported values by Kaushik et al. (KAUSHIK; KUMAR; SUBRAHMANYAM, 2017a), Guo et al. (GUO et al., 2011), and Lin et al. (LIN et al., 2010). The inset shows the correlation between T_{SM} and the Hall carrier concentration (N_{Hall}), highlighting the influence of charge density on the transition temperature.

and defect densities at different depths (NEUBERT et al., 2006). Therefore, carrier density and mobility are intrinsically related to film thickness, having an impact on the T_{SM}. Figure 4.4.5 depicts the T_{SM} versus t_{XRD}, along with data from Kaushik et al. (KAUSHIK; KUMAR; SUBRAHMANYAM, 2017b), Guo et al. (GUO et al., 2011), and Lin et al. (LIN et al., 2010) were included for comparison purposes. Figure 4.4.5 reveals two regions, for thicker films (above ~ 100 nm) T_{SM} decreases with decreasing thickness, in agreement with the increase in carrier concentration, as confirmed by Hall effect measurements (see inset of Figure 4.4.5). This finding indicates that a high carrier density induced Coulomb screening reduces carrier localization, thus promoting metallic conduction shifting T_{SM} to lower temperatures.

On the contrary, for thinner films (below ~ 100 nm), T_{SM} increases sharply. This inverted behavior can be traced back to effects, increased density of structural defects, higher surface-to-volume ratio, and significant internal stresses. These factors destabilize the metallic phase and make it energetically less favorable, requiring higher thermal energy (higher temperatures) to drive the transition from semiconductor to metal.

The m and K obtained from the quantum correction model Equation 71, are listed in Table 4.4.2. From the quantum correction term m, and the Boltzmann conductivity $\sigma_0 = 1/\rho_0$, the Fermi wavelength λ_F can be estimated using Equation 72(HERRANZ et al., 2004):

$$m = \lambda_F^4 \left(\frac{ne^2}{h}\right)^{3/2} \left(\frac{2m^* k_B}{h}\right)^{1/2} \sigma_0^{-1/2}. \quad (72)$$

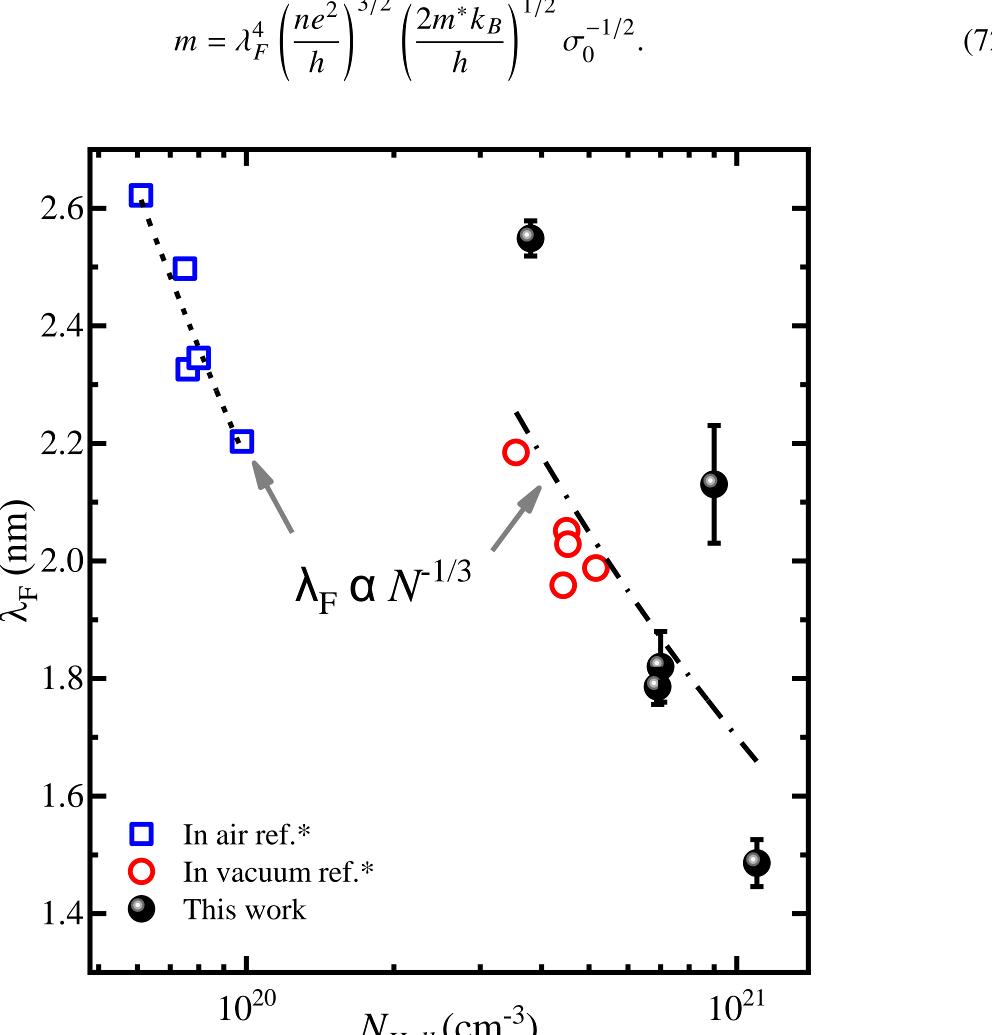

Figure 4.4.6 – Fermi wavelength (λ_F) as a function of carrier concentration for ITO films. Blue squares correspond to samples thermal annealing (TA) in air, red circles to vacuum-annealed samples ref.* (HUAYHUA, 2022), and black spheres to samples studied in this work. The dashed line is a guide to the eye.

As shown in 4.4.2, the calculated Fermi wavelength values (λ_F) are consistent with those reported by Khan *et al.* (2.23 – 2.41 nm) (KHAN et al., 2020), supporting the current of our analysis.

Figure 4.4.6 shows λ_F versus the carrier density. Here we have included values obtained also for films annealed in air, reported elsewhere (HUAYHUA, 2022), where an electron effective mass of $m^* = 0.31m_e$ (CHAUHAN; ANAND; KUMAR, 2014) were employed. Two features can be retrieved from this figure. First, λ_F decreases with increasing carrier concentration. Second, λ_F behavior with the carrier density is shifted toward lower carrier density region for samples annealed in air suggesting an oxygen vacancies passivation. In the latter case, the T_{SM} takes place at considerably higher temperatures, around room temperature (HUAYHUA, 2022). This shift could be associated with the different residual resistivity in air (625 - 63 $\times 10^{-4} \Omega \cdot cm$) and vacuum (18 - 1 $\times 10^{-4} \Omega \cdot cm$). At zero K, where thermal scattering becomes negligible, the

remaining contribution to resistivity arises primarily from defects, impurities, and structural imperfections induced by variations in the thermal annealing process.

4.4.5 Optical properties

The transmittance spectra of ITO films with varying thicknesses were measured in the wavelength range from 300 – 2500 nm, as shown in Figure 4.4.7. In the visible region, all films exhibit transmittance values of approximately 80 %. In the near-infrared (NIR), variations in transmittance are attributed to changes in free carrier absorption, consistent with Drude-like behavior.

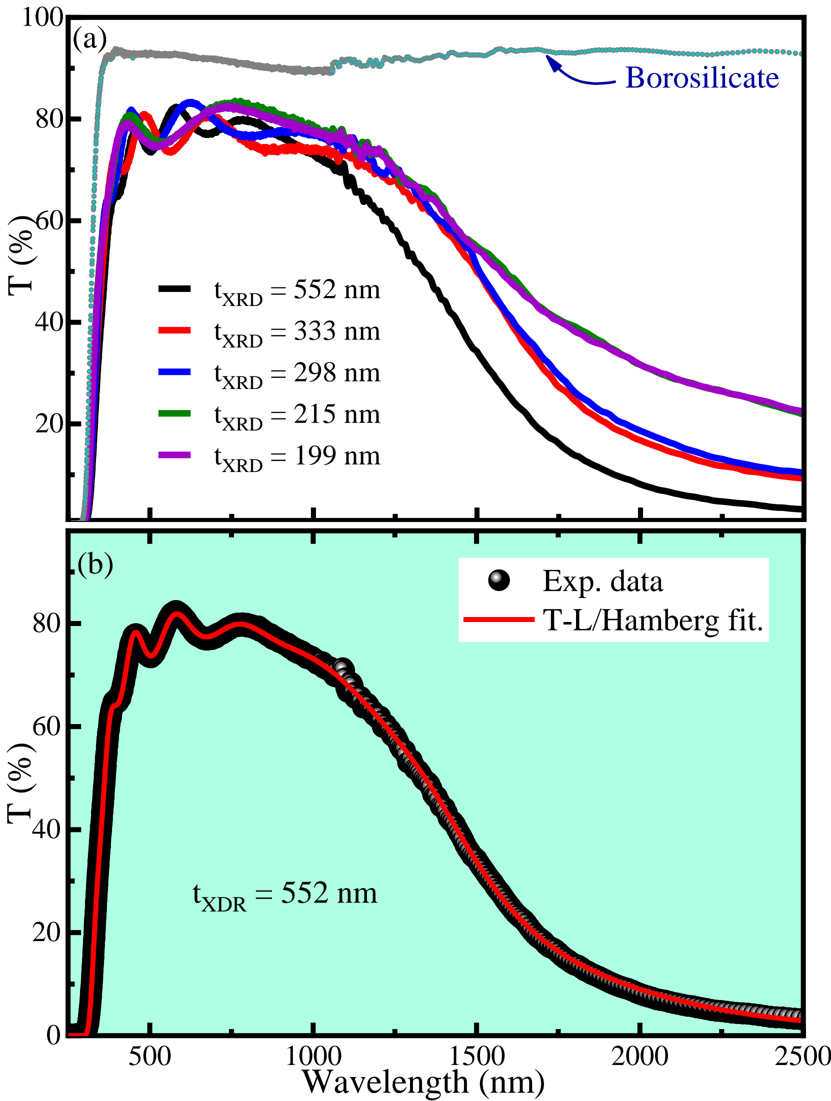

Figure 4.4.7 – (a) UV–Visible transmittance spectra of ITO thin films with varying thicknesses (t_{XRD} = 199–552 nm), measured in the range of 300–2500 nm. Thinner films exhibit fewer interference fringes and stronger free-carrier absorption in the near-infrared (NIR) region. The gray curve corresponds to the borosilicate glass substrate. (b) Transmittance spectrum and corresponding fit for the t_{XRD} = 552 nm sample using the combined Tauc–Lorentz and Hamberg (T–L/Hamberg) models (PFLUG et al., 2004).

The optical transmittance of the ITO films was analyzed using the combined Tauc–Lorentz + Hamberg model (PFLUG et al., 2004; ENRIQUE et al., 2025), implemented in the SpectraRay/4 software by SENTECH. This approach extends the classical Drude model by incorporating advanced dispersion theories developed by Hamberg and Sernelius (PFLUG et al., 2004), making it particularly well-suited for accurately describing the complex optical behavior of transparent conducting oxides such as ITO. Moreover, this model enables the extraction of key optical and electronic parameters by fitting the measured transmittance spectra across the visible to near-infrared range. The film was modeled as a multilayer structure (air/film/substrate/air). Substrate properties were characterized beforehand, and its dielectric function was held constant during the fitting procedure of the film properties. As shown in Figure 4.4.7(b), the transmittance spectra modeled using the Tauc-Lorentz/Hamberg approach exhibit good agreement with the experimental data. From the fits, we extracted the film thickness (t_{opt}), refractive index $n(\lambda)$, extinction coefficient $k(\lambda)$, free carrier concentration N_{Opt}, and effective mass (m^*). As summarized in Table 4.4.3, t_{opt} increases with radial distance from the substrate center is in good agreement with the thickness values obtained from XRD (t_{XRD}) analysis.

Figure 4.4.8(a) present the spectral dependence of the refractive index n, which decreases with increasing wavelength, exhibiting the typical dispersion behavior of ITO films (AHMED et al., 2021). Notably, the refractive index values at 632.8 nm remain almost constant around n = 1.77 across samples with varying thicknesses, indicating that n is almost the same for films at this specific wavelength. In contrast, the extinction coefficient varies from 0.011 to 0.022 with decreasing thickness, which is associated with changes in free absorption. This variation can be linked to changes in carrier concentration for the different samples.

Additionally, the DFT-calculated values of n and k for the pristine ITO structure are presented in Figure 4.4.8(a). These curves exhibit a spectral shape similar to the experimental results, but with a noticeable shift in the inflection point, particularly around 800 nm. In this context, it is important to emphasize that the DFT calculations were performed on an ideal, undoped ITO structure, without explicitly accounting for the high carrier concentrations present in the experimental samples. This omission likely contributes to the observed discrepancies, especially the shift in the optical response.

To extract the optoelectronic parameters from optical transmittance data, the analysis was carried out using the Hamberg model. In this framework, the dielectric function $\varepsilon(\mathbf{k}, \omega)$, which depends on both frequency and wavevector, is derived from the Lindhard function with an added Hubbard correction. From this formulation, a frequency-dependent dynamic resistivity $\rho(\omega)$ and the corresponding dielectric function $\varepsilon(\omega) = \varepsilon_\infty + \varepsilon_{IR}$ are obtained, as shown in (Equation 73).

$$\varepsilon_{IR}(\omega) = \frac{i}{\varepsilon_0(\omega)\left(\rho(\omega) - \frac{i\omega}{\varepsilon_0\omega_p^2}\right)}, \tag{73}$$

where ω_p is the plasma frequency, given by,

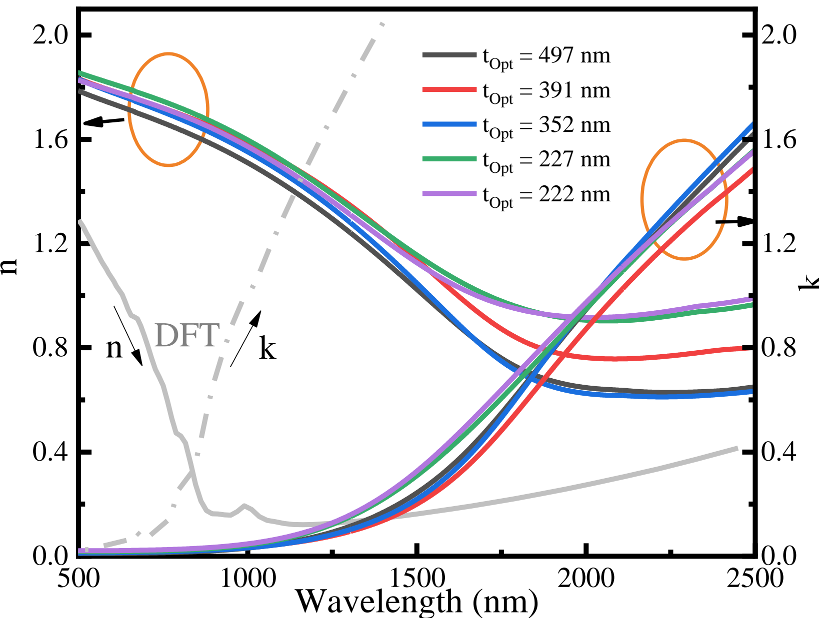

Figure 4.4.8 – Refractive index (n) and extinction coefficient (k) of Sn-doped In_2O_3 thin films, extracted using the Tauc–Lorentz/Hamberg model across the 500–2500 nm spectral range. Curves are shown for different film thicknesses (t_{opt}), along with DFT-calculated values for pristine ITO.

$$\omega_p = \sqrt{\frac{N_e e^2}{\epsilon_0 m^*}}, \tag{74}$$

with the dynamic resistivity is expressed as:

$$\rho(\omega) = i\frac{Z^2 n_i}{6\pi\varepsilon_0 n_e^2 \omega}\int_0^{\infty} k^2 \left[\frac{1}{\varepsilon(k,\omega)} - \frac{1}{\varepsilon(k,0)}\right] dk, \tag{75}$$

The above analysis allows the estimation of the free carrier concentration by optical means N_{opt}, the γ coefficient of the effective mass ($m^* = \gamma m_e$) and the optical mobility μ_{opt}. Subsequently, the plasma frequency ω_p was obtained, as summarized in Table 4.4.3.

Furthermore, as shown in Table 4.4.3, we observe that N_{opt} increases with decreasing film thickness, in good agreement with the values obtained from Hall measurements (see Table 4.4.2). Moreover, although both Hall mobility μ_{Hall} and the mobility obtained by optical means μ_{opt} exhibit a decreasing trend, the values of μ_{opt} are consistently higher than those obtained from electrical measurements. This feature can be traced to significantly higher values of dynamic resistivity compared to those measured using the four-point probe method, which in turn leads to higher values of μ_{opt}. Similar results have also been reported in the literature (SALES, 2022). This discrepancy can be attributed to the influence of additional scattering mechanisms, particularly grain boundary (BND) scattering which have a larger impact in μ_{Hall} than μ_{opt} due to the different carrier paths in both experiments. Thus, μ_{Hall} as a combination of the μ_{opt} and the mobility

limited by grain boundaries, i.e., $\mu_{\mathrm{Hall}}^{-1} = \mu_{\mathrm{opt}}^{-1} + \mu_{\mathrm{BND}}^{-1}$ (VILCA-HUAYHUA et al., 2025). In contrast, optical mobility is mainly sensitive to intragrain transport.

Table 4.4.3 – Parameters of the fits of the transmittance spectra using the Tauc–Lorentz/ Hamberg models, thickness (t_{Opt}), carrier concentration (N_{Opt}), plasma frequency (ω_P), dynamical resistivity (ρ_{Dyn}), optical mobility (μ_{Opt}) and reduce effective mass (γ). The results are shown for different sample positions.

Position (mm)	t_{Opt} (nm)	ω_P ($\times 10^3 cm^{-1}$)	N_{Opt} ($\times 10^{20}$cm^{-3})	ρ_{Dyn} ($\times 10^{-5}$ Ω· cm)	μ_{Opt} ($cm^2/V \cdot s$)	γ
0	497± 0.1	60.9	2.65 ± 0.02	7.80 ± 0.2	302 ± 80	0.252 ± 0.012
5	391± 0.2	57.6	2.81 ± 0.01	9.01 ± 0.2	247 ± 56	0.299 ± 0.001
10	352± 0.1	59.4	2.71 ± 0.01	7.20 ± 0.3	320 ± 90	0.271 ± 0.001
15	227± 0.3	59.4	3.75 ± 0.03	8.10 ± 0.2	206 ± 52	0.375 ± 0.003
20	222± 0.2	59.4	3.52 ± 0.01	9.00 ± 0.2	197 ± 44	0.352 ± 0.001

From the absorption coefficient retrieved after the optical transmittance spectra fit, the optical bandgap energy (E_g) and the Urbach energy (E_U) were determined. To extract these parameters, two models suitable for direct allowed transitions were employed: the Dolgonos–Hamberg (DH) method and the Band Fluctuations (BF) model (see inset Figure 4.4.9(b)). These approaches provide a more accurate estimation of the bandgap in degenerate semiconductors, as they account for effects such as band tailing and carrier-induced band structure modifications, thereby correcting the underestimation typically observed with conventional methods, such as the Tauc-plot method. The DH was used to estimate the optical bandgap and absorption edge broadening Γ by (Equation 77)(DOLGONOS; MASON; POEPPELMEIER, 2016), while the optical bandgap and Urbach energy was obtained from the exponential tail analysis using the BF approach, as described by (Equation 76) (GUERRA et al., 2019).

$$\alpha(h\nu) = (1/2)(A_0/h\nu)\sqrt{\pi/\beta}Li_{1/2}(-e^{\beta(h\nu-E_g)}), \tag{76}$$

Here $h\upsilon$ is the photon energy, A_0 is a constant in units of eV^{-1}·cm^{-1}, β is the inverse of Urbach energy, and Li_j (x) is the $j-th$ order polylogarithm function of x. The DH model is represented by:

$$\alpha(h\nu) \propto 1 - \frac{2}{\pi}\arctan\left(\frac{E_g - h\nu}{\Gamma}\right), \tag{77}$$

where Γ parameter is the width of the electronic transition.

Figure 4.4.9(a) presents the optical bandgap values for ITO as a function of N_{Hall}, derived from both the BF and DH models. The results from both models show good agreement, with the ITO films exhibiting higher bandgap values compared to bulk In_2O_3 (3.75 eV) (WALSH et al., 2022b). This increase in the bandgap is observed after a critical free carrier concentration is reached, in agreement with the Burstein-Moss effect.

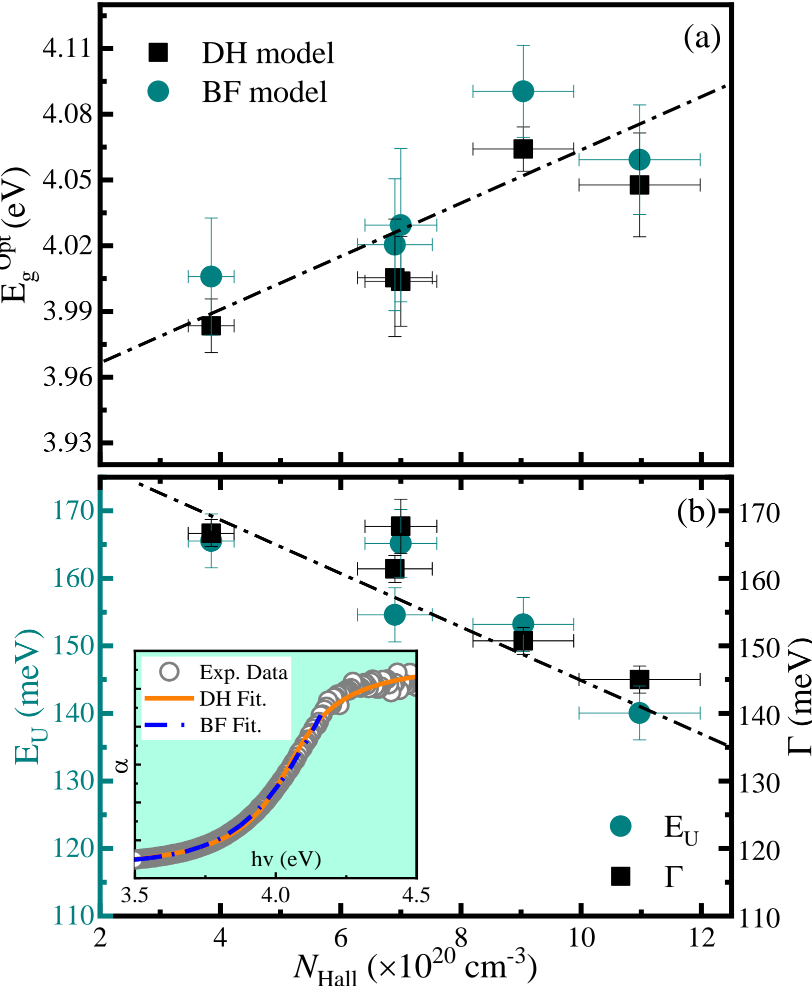

Figure 4.4.9 – (a) Optical bandgap energy (E_g^{opt}) as a function of carrier concentration (N_{Hall}), determined using the Dolgonos–Hamberg (DH) and Band Fluctuation (BF) models. (b) Urbach energy (E_U) derived from exponential tail fitting and broadening parameter (Γ) as functions of N_{Hall}. Inset: fitting curves for the optical absorption edge using both models.

Figure 4.4.9(b) shows the Urbach energy (E_U) values obtained from Equation 76. The observed decrease in E_U with the increase of N_{Hall} is closely linked to the remotion of O_i in the ITO as discussed above. Theoretical DFT calculations, as discussed in the theoretical section, reveal the existence of electronic states above the valence band associated with O_i, as well as energy states within the conduction band related to oxygen vacancies. These findings suggest that the removal of interstitial oxygen plays a key role in the decreasing the Urbach energy as the N_{Hall} increases. In thinner films, vacuum thermal treatment reduces interstitial oxygen, resulting in a decrease in the Urbach energy E_U and enhanced crystallinity of the ITO layers. Interestingly, the parameter Γ in Equation 77 follows a similar trend to E_U. While no direct correlation between E_U and Γ has been established in the literature, both quantities are linked to structural disorder. Defect-induced lattice distortions lead to electronic disorder, which manifests as spectral broadening observable through Urbach tails. This observation supports the interpretation of Γ as a disorder-related parameter, in consistent with the defect-mediated

broadening commonly observed in degenerate semiconductors.

4.4.6 Theoretical Results

According to the experimental results, our data suggest that ITO films contain structural defects such as O_i and V_O. These defects can be effectively modified through vacuum thermal treatment. In particular, the treatment promotes the reduction of O_i and the enhancement of V_O, leading to improved electrical conductivity. This effect is more pronounced in thinner films, where the reduced atmosphere created by the vacuum can diffuse more deeply, promoting enhanced defect modification throughout the entire film thickness. Within this framework, first-principles calculations were carried out by optimizing the crystal structure of Sn-doped In_2O_3 ($In_{29}Sn_3O_{48}$), corresponding to a tin concentration of 9.4%. This structure represents pristine ITO films, into which the O_i and V_O defects were explicitly introduced.

Figure 4.4.10 displays the electronic band structures with varying concentrations of O_i and V_O, alongside pristine ITO. In the pristine structure (see Figure 4.4.10(c)), the Fermi level (red dashed line) lies well within the conduction band, characteristic of degenerate semiconductor behavior with metallic-like conductivity. When O_i defects are introduced at concentrations of 2.1% (Figure 4.4.10(b)) and 4.2% (Figure 4.4.10(a)), the Fermi level progressively shifts closer to the conduction band edge, indicating a reduction in the free carrier concentration. This suggests that interstitial oxygen acts as a compensating donor or trap state, reducing the number of conduction electrons and thus lowering the electrical conductivity.

In contrast, the introduction of 2 % oxygen vacancies (see Figure 4.4.10(d)) further shifts the Fermi level into the conduction band, enhancing the metallic character. This behavior is consistent with the known role of oxygen vacancies as effective electron donors in ITO, enhancing electrical conductivity. It is worth, highlighting that in the experimental results suggest then thicker films (e.g., ~ 552 nm and ~ 333 nm) tend to retain more O_i, whereas thinner films (e.g., ~ 199 nm) favor the formation of V_O due to enhanced reduction effects from vacuum annealing. These findings bridge the experimental observations with the theoretical DFT predictions, confirming the critical role of defect engineering in tuning the optoelectronic properties of ITO thin films.

Figure 4.4.11(a) displays the projected density of states (PDOS) for the pristine ITO structure. The valence band, located below –3 eV, is dominated by O 2p states, consistent with the electronic structure of In_2O_3. A distinct feature appears between –9 and –10 eV, associated with hybridized Sn–O states; this spectral signature is absent in both In_2O_3 and SnO_2 (KARAZHANOV et al., 2007; ARAGóN et al., 2017), confirming its origin in Sn doping. The conduction band arises primarily from In 5s and O 2p states, with additional contributions from Sn-induced states. The substitution of In by Sn introduces donor levels that hybridize with the host conduction band, enhancing the carrier density. This hybridization could be the directly responsible for the degenerate n-type behavior characteristic of ITO, as reflected in the delocalized states near the Fermi level.

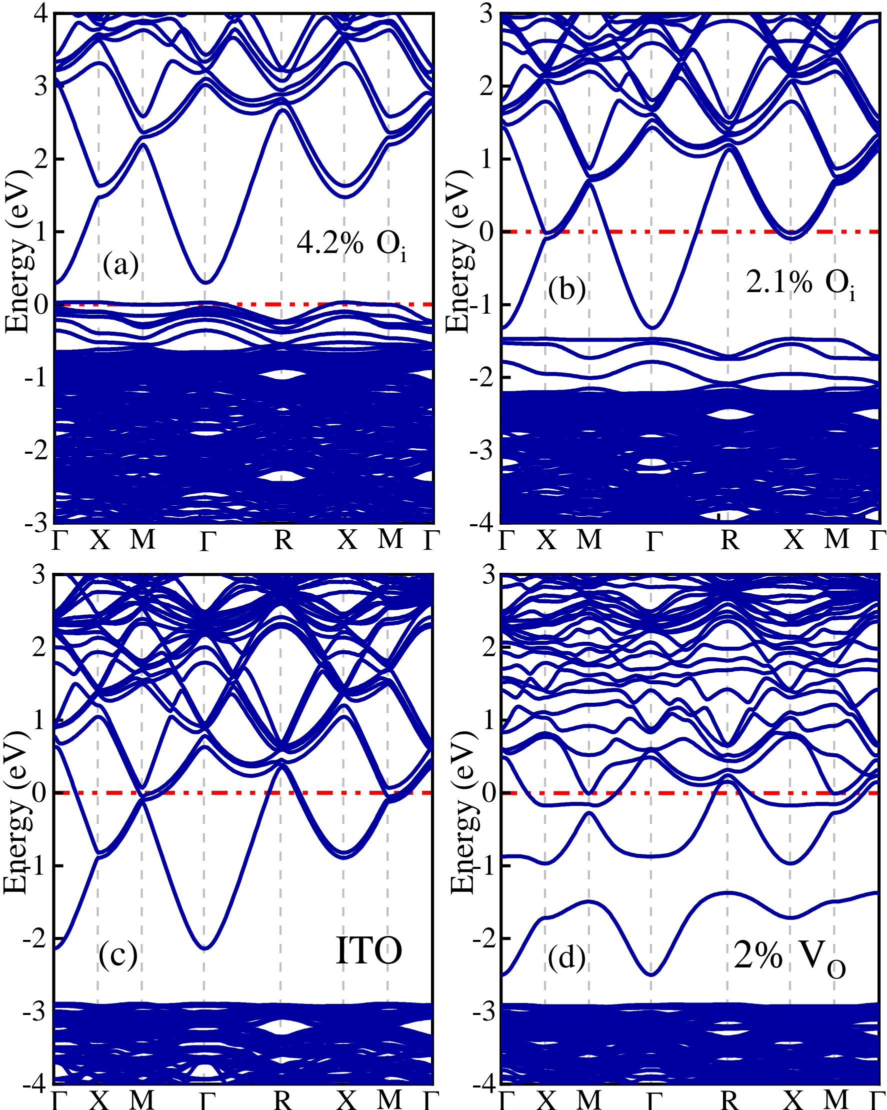

Figure 4.4.10 – Electronic band structures calculated via DFT for ITO with different defect configurations: (a) 4.2% interstitial oxygen (O_i), (b) 2.1% interstitial oxygen, (c) pristine ITO, and (d) 2% oxygen vacancies (V_O). The red dashed line indicates the Fermi level.

On the other hand, for structures containing 2.1% and 4.2% of O_i, the PDOS reveals a noticeable upward shift of the valence band maximum (VBM), accompanied by the emergence of localized states near the top of the valence band (see Figure 4.4.11(c) and (d)). These features are characteristic of acceptor-like behavior, consistent with the role of O_i as a defect introducing partially filled or empty states close to the VBM. The presence of such states can significantly alter the electronic structure by reducing the effective bandgap and promoting hole trapping, which may impact the conductivity and optical absorption. In contrast, the formation of V_O introduces donor-like states that appear within the bandgap or near the edge of the conduction band (see Figure 4.4.11 (b)). These defect-induced states exhibit a strong degree of localization, as indicated by their narrow distribution in the PDOS. This behavior is attributed to the breaking of local bonding symmetry and the associated reorganization of the electronic density, primarily

involving In 5s and Sn 5s orbitals. The hybridization of these orbitals, as supported by prior theoretical studies (CHEN et al., 2014), contributes to the partial delocalization of the defect states and is crucial for understanding the n-type conductivity observed in ITO. Furthermore, the presence and distribution of these localized states may act as scattering centers, influencing charge transport and carrier mobility.

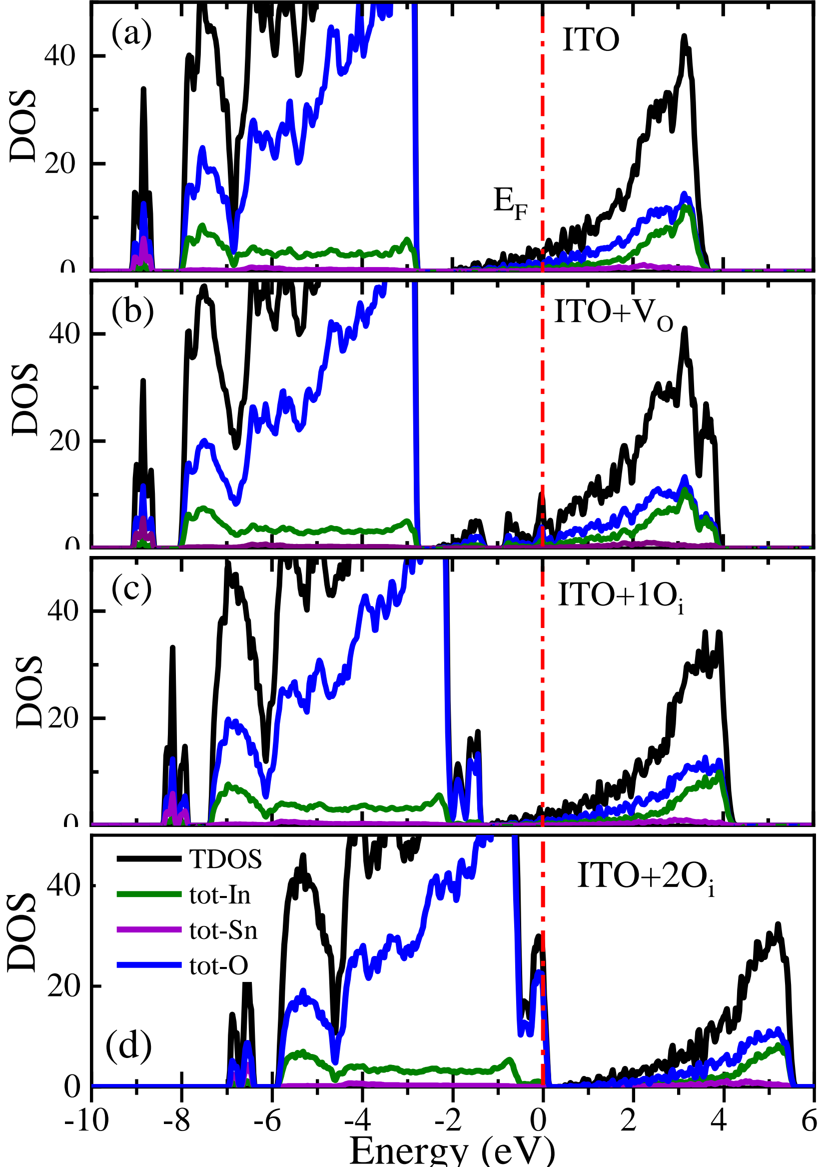

Figure 4.4.11 – Projected density of states (PDOS) calculated via VASP for In, Sn, and O orbitals in Sn-doped In_2O_3 (ITO) with different defect configurations: (a) pristine ITO ($In_{29}Sn_3O_{48}$), (b) ITO with 2% oxygen vacancies (V_O), (c) ITO with 2.1% interstitial oxygen (O_i), and (d) ITO with 4.2% O_i. The red vertical dashed line indicates the Fermi level.

The effective electron mass, m^*, was determined by fitting the parabolic region of the conduction band minimum near the high-symmetry point Γ, as described in Equation 78. This value was subsequently used to calculate the theoretical charge carrier concentration (N_{DFT}) and plasma frequency ($\omega_p(DFT)$), according to Equation 79 and Equation 74, respectively. The

corresponding results, obtained using both VASP and Quantum Espresso, are summarized in Table 4.4.4. As shown in the latter table, a clear numerical trend emerges $N_{DFT}(\text{ITO} + V_{\text{O}}) > N_{DFT}(\text{ITO}) > N_{DFT}(\text{ITO} + O_i)$, in agreement with the defect behavior discussed throughout this work. Notably, although the absolute values obtained from both DFT packages exhibit some numerical differences primarily arising from variations in the underlying approaches, such as the choice of exchange–correlation functionals, pseudopotentials, and other implementation-specific parameters both codes consistently reproduce the same qualitative trends. Furthermore, the effective masses reported in previous studies, such as those by DMo13 Scott et al. (BREWER; F, 2004) and VASP Chem et al. (CHEN et al., 2015), fall within the same range as those calculated in the present work, further supporting the reliability and robustness of the DFT-based methodology employed here.

$$m^* = \gamma m_e = \hbar^2 (\frac{\partial^2 E}{\partial k^2})^{-1} \tag{78}$$

and for the charge carriers for highly degenerate n-type doped systems is obtained using the following equation (ZEGHBROECK, 2011; VILCA-HUAYHUA et al., 2025).

$$N_{DFT} = \frac{2\sqrt{2}}{3\pi^2} (\frac{q m^*}{\hbar^2})^{3/2} (E_F - E_C)^{3/2} \tag{79}$$

Table 4.4.4 – DFT-calculated effective mass (γ_{DFT}), energy difference between the Fermi level and the valence band maximum ($E_F - E_V$), theoretical carrier concentration (N_{DFT}), e plasma frequency (ω_p(DFT)) for Sn-doped In_2O_3 (ITO) with different defect types, obtained using both VASP and Quantum ESPRESSO. Literature values from DMo13 Scott et al. (BREWER; F, 2004) and VASP Chem et al. (CHEN et al., 2015) are included for comparison.

Defect	γ_{DFT}	$(E_F - E_V)$ (eV)	N_{DFT} ($\times 10^{21}$ cm^{-3})	$\omega_P(DFT)$ (cm$^{-1} \times 10^3$)
VASP				
1 V_O	0.215	2.91	2.24	192.2
$In_{29}Sn_3O_{48}$	0.196	2.89	1.94	186.8
1 O_i	0.200	2.22	1.33	116.2
2 O_i	0.190	0.30	0.06	34.2
Quantum Espresso				
1 V_O	0.463	2.82	5.90	212.1
$In_{29}Sn_3O_{48}$	0.451	2.75	4.16	178.1
1 O_i	0.463	2.19	2.17	128.6
2 O_i	0.530	0.25	0.22	38.0
DMol3 Scott et al(BREWER; F, 2004)	0.30	-	1.50	24.0
VASP Chem et al(CHEN et al., 2015)	0.19	2.56	-	-

4.4.7 Conclusions

In summary, our results demonstrate that the optoelectronic and structural properties of indium tin oxide (ITO) thin films grown by DC sputtering are strongly influenced by film thickness and can be tailored during the deposition process and after vacuum thermal annealing. The primary mechanism driving this influence is the effect of the vacuum annealing. which promotes crystal texturization along the (400) plane, particularly in thinner films, which was found to be related the concentration of oxygen vacancies, V_O. These structural changes are consistent with variations in optical parameters such as effective mass, carrier concentration, and mobility, and align well with electrical transport measurements, including resistivity and Hall effect. The differences observed between optical and electrical responses are attributed to grain boundary scattering, which predominantly affects electrical conduction. An increase in the optical bandgap with film thickness, consistent with the Burstein-Moss effect, further reflects the rise in carrier density. It is worth highlighting that low-temperature resistivity measurements indicate that the dominant transport mechanism in ITO films is governed by the weak localization effect (WLE). It was found that the semiconductor-to-metal transition temperature strongly depends on the carrier concentration, since higher concentration shifts the transition to lower temperature. These trends are supported by DFT calculations, which show that the removal of interstitial oxygen and the formation of oxygen vacancies lead to modifications in the electronic and structural properties of ITO compound, consistent with the effects observed experimentally under vacuum annealing.

4.5 Room-Temperature Ferromagnetism and Anomalous Transport in Vacuum-Annealed Fe-Doped ITO Thin Films

The present work addresses the role of defects in mediating magnetic interactions with transition-metal ions in Fe-doped ITO. To this end, the influence of post-deposition thermal annealing under high vacuum on the structural, electrical, optical, and magnetic properties of Fe-doped ITO thin films was systematically investigated. Particular attention is given to elucidating how the interplay between magnetic impurities and intrinsic defects, such as oxygen vacancies, governs the low-temperature resistivity behavior, optical transmittance, and the emergence of room-temperature ferromagnetism. This work was submitted to the **Journal of Physics D: Applied Physics**, number manuscript JPhysD-142255.

4.5.1 Experimental details

Fe-doped ITO thin films were deposited on fused-silica (FS) substrates by RF magnetron co-sputtering. Prior to deposition, the substrates were ultrasonically cleaned in acetone for 10 min. The sputtering process was performed using a commercial ITO target (90% In_2O_3 and 10% SnO_2) and a metallic Fe target, both with 99.99% purity. The target–substrate distance was fixed at 7.5 cm. The base pressure before deposition was 1.06×10^{-6} mbar, while the working pressure was adjusted to 1.06×10^{-2} mbar by introducing ultra high purity Ar gas (35 sccm). During growth, the ITO and Fe targets were powered at 60 W and 150 W, respectively, while the substrate was cooled to 15 °C and rotated at 50 rpm to ensure film homogeneity; the deposition time was set to 3 h. Post deposition annealing was carried out in a vacuum atmosphere (2.0×10^{-6} mbar) at temperatures ranging from 400 to 700°C for 2 h with a heating rate of 10 °C/min. Structural characterization was carried out by X-ray diffraction (XRD) using a Rigaku diffractometer with Cu-Kα radiation (λ = 1.5418 Å) over the range $20° \leq 2\theta \leq 80°$ with a step of 0.05°. Optical properties were investigated through transmittance measurements in the UV–Vis–NIR range (400–2500 nm) using a SenResearch 4.0 ellipsometer from SENTECH, due to the samples size 5mm × 5mm only transmittance measurements were feasible. The electrical resistivity, charge carrier concentration and mobility of the films were measured at room temperature (RT) using the Hall system in the van der Pauw configuration. Charge carrier measurements were performed with, a magnetic field of 0.515 T. Resistivity versus temperature was recorded from 80 K to 300 K employing a commercial nitrogen cryostat (Janis Inc.). Photocurrent responses under UV illumination were studied at room temperature with an applied bias of 1.5 V in air. Magnetic properties were investigated using a vibrating sample magnetometer (VSM, Quantum Design SQUID) under fields up to ±70 kOe at both 2 K and 300 K.

4.5.2 Structural properties

Figure 4.5.1(a) shows the XRD patterns of the Fe-doped ITO films annealed at different temperatures (400–700 °C). The patterns display the (211), (222), (400), (440), and (622) planes corresponding to the cubic bixbyite structure of In_2O_3 (CPDS card no. 6–0416, space group Ia3). Within the detection limits of the XRD equipment, no secondary phases related to Fe or its oxides, such as Fe_2O_3, Fe_3O_4, or FeO, were determined. Analysis of the diffraction patterns indicated a preferential orientation along the (222) plane, consistent with that expected for poycrystalline ITO structure. To provide more detailed information, the XRD patterns were analyzed using the Rietveld method, where the shape of the peaks was modeled using Lorentzian functions implemented in the GSAS software (TOBY; DREELE, 2013).

As shown in Figure 4.5.1, Rietveld refinements of the samples exhibit good agreement between the calculated and experimental data. The quality of the refinements was evaluated using the χ parameter, defined as $\chi^2 = (R_{wp}/R_{exp})^2$, with χ also reported as the goodness-of-fit (G) (TOBY, 2006), as listed in Figure 4.5.1.
Table 4.5.1 shows that the as-grown (AG) film exhibits a larger lattice parameter of 10.116 Å, likely due to structural disorder. After vacuum annealing 400 °C, the lattice constant abruptly decreases to 10.052 Å. The latter can be attributed to a thermal-induced relaxation effect, reducing structural distortions and disorder. For higher annealing temperatures, the lattice parameter continues to decrease more gradually. This trend can be plausibly explained by the evolution of defects within the film as a function of the annealing temperature. Below 400°C, oxygen vacancies are partially reduced, coexisting with the formation of Sn-cluster complexes. At temperatures above 400 °C, the formation of isolated Sn-vacancy complexes is likely to become more favorable, as reported by Qichao Li et al. (LI et al., 2015). These defect-related processes enhance the degree of crystallinity, which is reflected in the reduction of the average full width at half maximum ($\langle FWHM \rangle$) obtained after the Rietveld analysis, in line with the structural results summarized in Table 4.5.1.

Table 4.5.1 – Structural parameters obtained from the Rietveld refinement: lattice parameter ($a = b = c$), average ⟨FWHM⟩, goodness-of-fit (G), and texture coefficients (TC) for the (222) and (400) reflections. Atomic concentrations per formula unit of In, Sn, Fe, O, fraction of Fe atoms per cation (At. Fe) were determined by EDS, with an estimated uncertainty below 14%.

AT (°C)	$a = b = c$ (Å)	$< FWHM >$ (°)	G	TC (222)	TC (400)	In (%)	Sn (%)	Fe (%)	O (%)	At. Fe
AG	10.116	0.286	1.02	-	-	33.0	3.2	0.8	63.0	0.022
400	10.052	0.156	1.22	0.68	0.85	34.7	3.4	0.9	61.0	0.023
500	10.050	0.142	1.23	0.73	0.82	34.9	3.2	0.9	61.0	0.023
600	10.051	0.123	1.10	0.62	0.76	35.4	2.6	0.9	61.1	0.023
700	10.046	0.106	1.21	0.72	0.76	35.4	2.6	0.8	61.2	0.021

On the other hand, the degree of crystallographic orientation was quantified by calculating

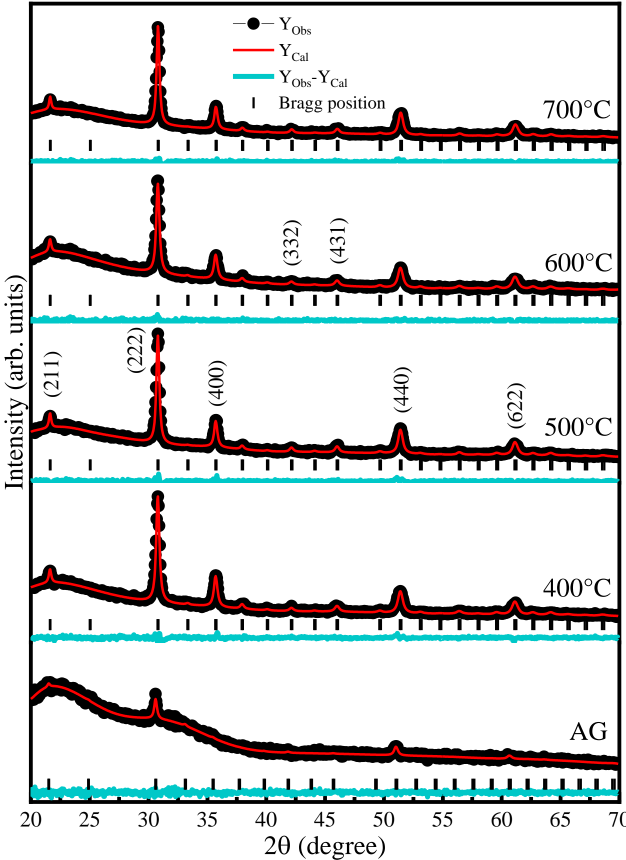

Figure 4.5.1 – XRD patterns of Fe-doped ITO films at different AT, refined using Rietveld method. Black circles represent the experimental data (Y_{Obs}), the red line corresponds to the calculated fit (Y_{Cal}), the sky-blue line shows the difference between Y_{Obs} and Y_{Cal}, and the black vertical lines indicate the peak positions of the phase.

the texture coefficient (TC) using Equation 80.

$$TC(hkl) = \frac{I_{(hkl)}/I_{0(hkl)}}{\frac{1}{N}\sum_N I_{(hkl)}/I_{0(hkl)}}, \tag{80}$$

where $I_{(hkl)}$ is the measured intensity of the (hkl) diffraction peak, $I_{0(hkl)}$ is the corresponding standard intensity of the JCPDS card No. 71-2194, and N denotes the number of peaks included in the analysis. The structural results summarized in Table 4.5.1, show that the Fe-doped ITO films exhibit a slight preferential orientation along the (400) plane after annealing at 400 °C. This preferential orientation is more pronounced at lower annealing temperatures, suggesting oxygen vacancies are more abundant in this temperature. Subsequently, it decreases progressively as the annealing temperature increases, suggesting the annihilation of V_O, resulting in a more ordered crystallographic structure. The observed correlation between (400) orientation and oxygen vacancies is consistent with the findings of Kim et al. (KIM et al., 2007), who reported that the (400) diffraction peak intensity in ITO films increases under oxygen-poor conditions and decreases in oxygen-rich environments; a similar trend was also observed in Ref. (HUAYHUA et al., 2025). In contrast, the (222) plane shows consistently lower texture coefficient values

(0.62–0.73), indicating that this orientation is under-represented and less favored throughout the thermal treatment temperature range. The AG sample was excluded from this analysis due to its low crystallinity and significant amorphous content, which limits reliable interpretation of our diffraction data. Therefore, these results indicate that lower annealing temperatures favor the preferential orientation along the (400) plane, whereas the (222) orientation remains invariant across all treatments.

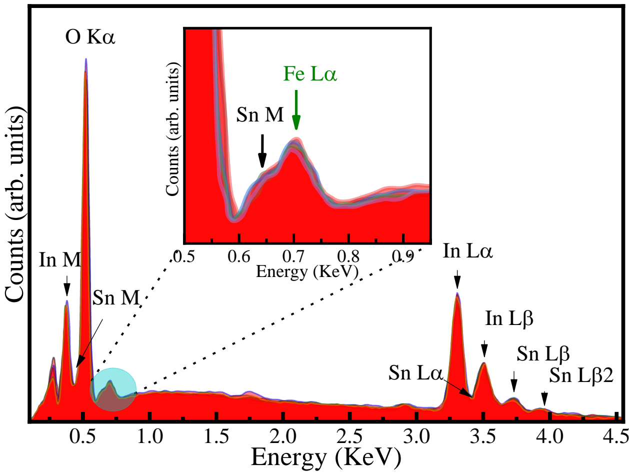

Figure 4.5.2 – Representative EDS spectrum of Fe-doped ITO thin films. The characteristic emission lines of O (K_α at 0.52 keV), Fe (L_α at 0.704 keV), In (M_α at 0.45 keV, L_α at 3.29 keV, L_β at 3.45 keV), and Sn (M_α at 0.49 keV, L_α at 3.44 keV, L_β at 3.66 keV, $L_{\beta 2}$ at 3.93 keV) are indicated. The inset highlights the low-energy region, where the Fe–L_α peak is resolved from the nearby Sn–M line.

The chemical composition of the Fe-doped ITO films was analyzed by energy-dispersive X-ray spectroscopy (EDS). A representative spectrum is shown in Figure 4.5.2, in which the characteristic peaks of O (K_α at 0.52 keV), Fe (L_α at 0.704 keV), In (M_α at 0.45 keV, L_α at 3.29 keV, L_β at 3.45 keV), and Sn (M_α at 0.49 keV, L_α at 3.44 keV, L_β at 3.66 keV, $L_{\beta 2}$ at 3.93 keV) are clearly identified. The inset in Figure 4.5.2 emphasizes the low-energy region, evidencing the Fe–L_α signal superimposed on the Sn–M contribution. Quantitative analyses are summarized in Table 4.5.1. The consistency of these values across different regions confirms the homogeneous distribution of the cations in the films. Notably, the Fe concentration obtained by EDS is in line with the values inferred from magnetic measurements, as discussed below.

4.5.3 Optical properties

Transmittance spectra of Fe-doped ITO films subjected to thermal annealing in vacuum at different temperatures, measured in the wavelength range 250–2500 nm, are shown in Figure 4.5.3(a). For comparison, the transmittance of the substrate was also measured and included in the analysis model. The AG film exhibits the lowest transmittance among the samples, consistent with its poor crystallinity, as determined from XRD data analysis. As the annealing temperature increases, a progressive increase in transmittance is observed, in good agreement

with the continuous improvement of crystallinity due to defect evolution, reaching nearly to 80% at telecommunications wavelength 1550 nm after 600 °C thermal treatment. As shown in Figure 4.5.3. The transmittance spectra were modeled using two Tauc-Lorentz oscillators, the second oscillator was included to emulate the fundamental absorption, which more realistically reproduces the absorption edge caused by defects, and the Hamberg model for the free carrier IR absorption (PFLUG et al., 2004; ENRIQUE et al., 2025), the Hamberg model provides good agreement between the estimated charge carrier concentration obtained from the NIR region of the transmittance and the experimental values obtained from Hall effect measurements, as well as for the electron effective mass (HUAYHUA et al., 2025), for this, we assume an FS/ITO/Air layer configuration. The modeling was performed with the SpectraRay/4 software by SENTECH, as described in previous works (VILCA-HUAYHUA et al., 2025). The resulting fit, represented by the red dotted line, shows good agreement with the experimental data. From the fits, film thickness (t_{Opt}), free carrier concentration (N_{Opt}), and electron effective mass (m_e^*) were retrieved. As summarized in Table 4.5.2, the thickness of the films, as expected, remained nearly constant between ~761-798 nm.
N_{Opt} displays values ranging from 6.5×10^{19} to 2.15×10^{20} cm^{-3}, which are of the same order as those reported for undoped ITO thin films. For instance, Zheng *et al.* (ZHENG et al., 2024) reported a wide range from 2.2×10^{19} to 7.7×10^{20} cm^{-3}. However, these values are lower than those obtained in previous studies as will be discussed later , where ITO films were grown by the DC sputtering method (3.8–11 $\times 10^{20}$ cm^{-3}), as determined from Hall effect measurements (VILCA-HUAYHUA et al., 2025).

Moreover, a slight increase in N_{Opt} is observed up to 500 °C, followed by a decrease at higher annealing temperatures (see Table 4.5.2). This behavior could be attributed to the competing effects of enhanced crystallinity and oxygen desorption from the film surface during vacuum annealing, which may promote the formation of oxygen vacancies that act as surface donor states and consequently increase the free carrier density at intermediate annealing temperatures. Moreover, it cannot be excluded that at high annealing temperatures, enhanced Fe diffusivity promotes ion clustering or partial phase segregation, while concurrent oxygen depletion increases the likelihood of forming deep-level defect states within the bandgap, which can act as efficient carrier-trapping centers, thereby reducing the optically active carrier concentration (N_{Opt}). In parallel, the electron effective mass ($\gamma = m_e^*/m_0$), as determined from the Hamberg model, shows a lower value for the AG sample, followed by an increasing trend with the annealing temperature, except for the sample annealed at 500 °C, which exhibits a higher carrier concentration. Typical values of γ are reported between 0.3 and 0.6 (BLAIR et al., 2023). Here, as the annealing temperature increases, the electron effective mass retrieved from the Hamberg model approaches those reported in the literature for undoped ITO samples, reflecting improved crystal quality and reduced electron scattering. Furthermore, the oxygen-poor environment at the film surface can generate surface oxygen vacancies, which further influence the carrier density and local electronic structure. These combined effects are in good agreement with previous studies on

ITO and Fe-doped ITO films (VILCA-HUAYHUA et al., 2025; OHNO et al., 2007), confirming that vacuum annealing not only enhances crystallinity and defect migrations, but enables the capability to tune both bulk and surface electronic transport properties.

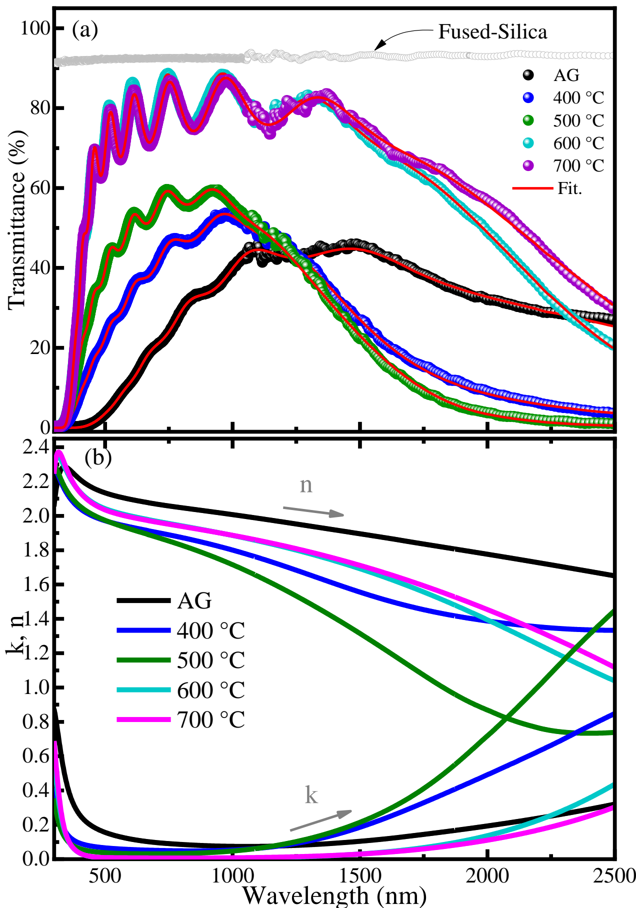

Figure 4.5.3 – (a) UV–Visible transmittance spectra of Fe doped ITO thin films with varying annealing temperature (400-700°C), measured in the range of 300–2500 nm. The red line represents the fit T-L/Hamberg model, (b) optical constants, refraction index (n) and extinction coefficient (k) obtained from fitting T-L/Hamberg model.

Table 4.5.2 – Results obtained from the adjustments of the transmittance spectra using the Tauc Lorentz and the Hamberg model, thickness (t), carrier concentration (N_{Opt}), effective mass (γ), Transmittance (T_{max}), refraction index (n) and extinction coefficient (k) at λ = 632.8 nm. (* Ref (POLYANSKIY, 2024))

AT (°C)	Thickness (nm)	N_{Opt} ($\times 10^{20}$cm^{-3})	γ	T_{max} (%)	n	k
AG	797 ± 3	0.65 ± 0.03	0.177 ± 0.031	24.0	2.09	0.109
400	792 ± 3	1.93 ± 0.09	0.222 ± 0.012	46.0	1.92	0.054
500	793 ± 3	2.15 ± 0.10	0.203 ± 0.023	59.1	1.91	0.032
600	761 ± 3	1.34 ± 0.10	0.278 ± 0.020	88.4	1.99	0.005
700	770 ± 3	1.16 ± 0.09	0.277 ± 0.021	86.2	1.98	0.008
ITO*	-	-	-	-	1.37	0.002

Figure 4.5.3(b) shows the spectral curves of the refractive index (n) and the extinction

coefficient (k). The refractive index n decreases with increasing wavelength, whereas the extinction coefficient k exhibits the opposite trend, increasing at longer wavelengths, this is because free electrons absorb radiation that increases sharply in the infrared region of the electromagnetic spectrum, typical of ITO films. Furthermore, the values of n and k at λ = 632.8 nm show a slight tendency to decrease, approaching those reported for bulk ITO (POLYANSKIY, 2024), as summarized in Table 4.5.2. This trend can be associated with a reduction of impurities, which decreases photon absorption as the thermal annealing is increased.

The optical bandgap energy (E_g^{Opt}) can be determined from the absorption coefficient (α), which is calculated using the relation $\alpha = 4\pi k/\lambda$. Therefore, it is necessary to carefully consider the physics underlying the determination of the bandgap. However, in heavily doped systems, defect states are created near the edges of the conduction or valence bands, or even deep-level defects within the bandgap. This results in a shift of the absorption onset toward lower energies, as observed in Figure 4.5.4(a). Consequently, the application of the Tauc method to systems such as Fe-doped ITO is limited by the overlap of different interband transitions, as well as by their superposition with optical transitions, commonly referred to as many-body effects (KLEIN et al., 2023). Here we use a recently developed fundamental absorption model incorporating the presence of tail states to accurately determine the optical bandgap and Urbach energies of direct electronic transitions materials, based on the Band Fluctuations approach (BF) (GUERRA et al., 2019), according to Equation 81.

$$\alpha(h\nu) = (1/2)(A_0/h\nu)\sqrt{\pi/\beta}Li_{1/2}(-e^{\beta(h\nu - E_g)}) \tag{81}$$

Here $h\nu$ is the photon energy, A_0 is a constant in units of $eV^{-1}\cdot cm^{-1}$, β is the inverse of Urbach energy, and Li_j (x) is the $j-th$ order polylogarithm function of x.

For the AG film, a bandgap value of 2.9 eV is observed. This is lower than the typical values reported for ITO (3.5–4.3 eV) (YU et al., 2016), indicating the influence of Fe atoms within the matrix. Similar bandgap narrowing has been experimentally reported in other oxide systems, such as Fe-doped CeO_2, where the bandgap decreases from 3.11 eV to about 2.80 eV with increasing Fe concentration (EL Gana et al., 2025). To explain this, it should be noted that iron can act as electron capture centers or surface trap centers located just below the conduction band or above the valence band (CHAKRABORTY et al., 2020b), creating localized states that shift the optical absorption edge toward lower energies. However, the effect of Fe on the bandgap is complex since Fe incorporation can modify the concentration and distribution of oxygen vacancies, which further perturbs the electronic structure. These combined effects not only modifies the optical response but can also affect the electrical properties by changing the carrier density (ARAGóN et al., 2021). Additionally, since Fe doped ITO is a degenerate semiconductor, several physical phenomena influence the dependence of the E_g^{Opt} on the carrier concentration. These include the Burstein-Moss effect (MB), which causes a blue shift of the optical bandgap with increasing charge carrier density, and bandgap contraction or bandgap

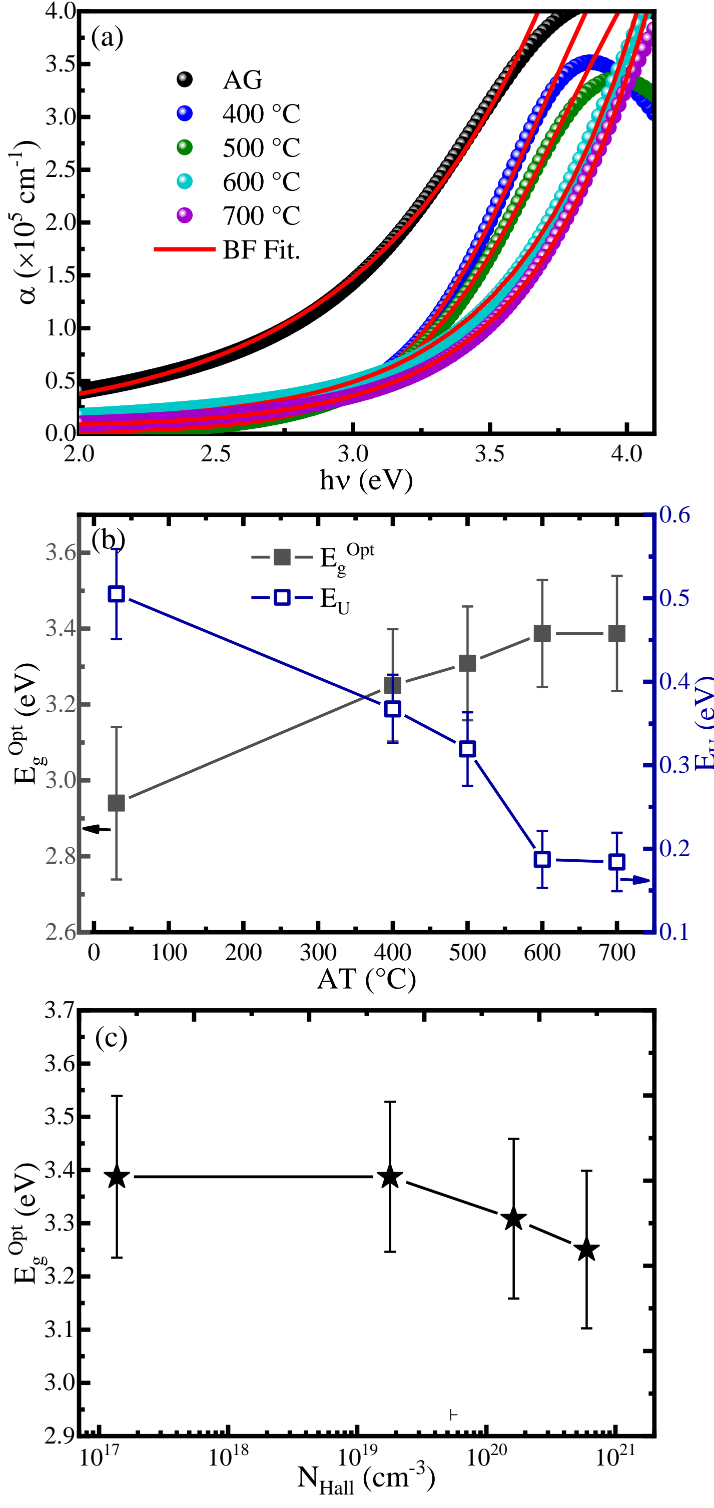

Figure 4.5.4 – (a) Fit over the absorption region using the band fluctuation model (BF), (b) Optical bandgap (E_g^{Opt}) and Urbach energy for Fe-doped ITO films at different annealing temperatures, (c) E_g^{Opt} at Hall carrier concentration function.

narrowing (BGN) arising from electron–electron interactions and scattering by ionized impurities. These effects compete with each other. An increase V_O leads to a higher defects density, which in turn increase the carrier concentration and enhances interactions among electrons as well

as between electron and Fe ions. As a consequence, a red shift of the bandgap is observed, as shown in Figure 4.5.4(c), suggesting that BGN dominates over the BM effect. On the other hand, thermal annealing increases the bandgap of the AG film, which is in line with the improvement in crystallinity and the partial annihilation of defects, such as oxygen vacancies, during the annealing process. That annihilation decreases the density of localized states within the bandgap, leading to a blueshift of the optical absorption edge. This result is supported by XRD characterization, which shows sharper diffraction peaks and improved lattice order after annealing, indicating a reduction of defect-induced distortions.

Regarding the Urbach energy, it decreases progressively with increasing annealing temperature, as shown in Figure 4.5.4(b). This reduction reflects a lower density of defects within the film. These structural improvements are directly correlated with the widening of the bandgap, as the reduction of defect-related localized states and disorder minimizes sub-bandgap absorption, shifting the optical absorption edge to higher energies.

4.5.4 Electrical properties

To investigate the influence of Fe incorporation on the transport properties of the ITO host matrix, the sheet resistance ($R_\square$), electrical resistivity (ρ), carrier concentration (N_{Hall}), and Hall mobility (μ_{Hall}) were measured at room temperature using the van der Pauw configuration with a standard four-point probe setup. The results are summarized in Table 4.5.3. The AG film exhibits a sheet resistance of 834.2 $\Omega/\square$. Upon annealing at 400 °C, $R_\square$ decreases markedly to 60.2 $\Omega/\square$, indicating a significant enhancement in electrical conduction. However, further increasing the annealing temperature leads to a progressive rise in $R_\square$, reaching a maximum of ~51 K$\Omega/\square$ at 700 °C. These variations suggest that the observed behavior originates from intrinsic changes in the resistivity of the films, likely associated with thermally induced modifications in defect structure or carrier scattering mechanisms.
After calculating the resistivity using $\rho = R_\square \times t$, a pronounced decrease in ρ was observed after the first annealing step, reaching $(4.8 \pm 0.8) \times 10^{-3}$ $\Omega \cdot$ cm. This reduction in resistivity can be attributed to the structural improvements induced by thermal treatment, which enhance the crystallinity. The observed value lies within the typical range reported for ITO thin films. This behavior is consistent with the XRD results, which revealed an increase in the intensity and sharpness of the diffraction peaks, indicating improved crystallinity. Beyond this temperature, ρ exhibits a monotonic increase, along with a progressive reduction in carrier concentration driven by the diminished density of oxygen vacancies, as indicated by the structural characterization. Nevertheless, the contribution of Fe ions cannot be disregarded, as their diffusion during annealing may promote the formation of Fe-rich clusters, further influencing the transport properties. The carrier density exhibits a value of N_{Hall}=5.86×$10^{20}cm^{-3}$ after 400 °C, within the range of that obtained for the ITO (HUAYHUA et al., 2025). However, the carrier concentration gradually decreases with increasing annealing temperature (see Figure 4.5.5). This behavior can be attributed

to the reduction of oxygen vacancies (V_O) and the limited diffusivity of Fe ions, as previously discussed in this section and in the optical properties. The discrepancy between these Hall-derived carrier concentrations and the N_{Opt} values obtained from the transmittance fitting (Table 4.5.2) can be explained by the fact that optical measurements probe the bulk optical response and in the Hamberg model, carrier density information is provided for ionized centers and not for complexes; therefore, the coexistence of multiple scattering mechanisms is not considered. or trapping at grain boundaries. These dispersion mechanisms are evidenced in low temperature resistivity measurements as will be discussed later. In contrast, the Hall effect measurements are strongly influenced by such structural inhomogeneities, which may limit carrier mobility and alter the effective carrier density.

Furthermore, as the defect density decreases with increasing annealing temperature, the number of scattering and trapping centers is also reduced. Notably, the latter leads to a significant enhancement in the Hall mobility (μ_{Hall}), as shown in Figure 4.5.5. The improved mobility therefore reflects not only a reduction in charged defect scattering but also the progressive crystal improvement and grain growth that facilitate more efficient charge transport.

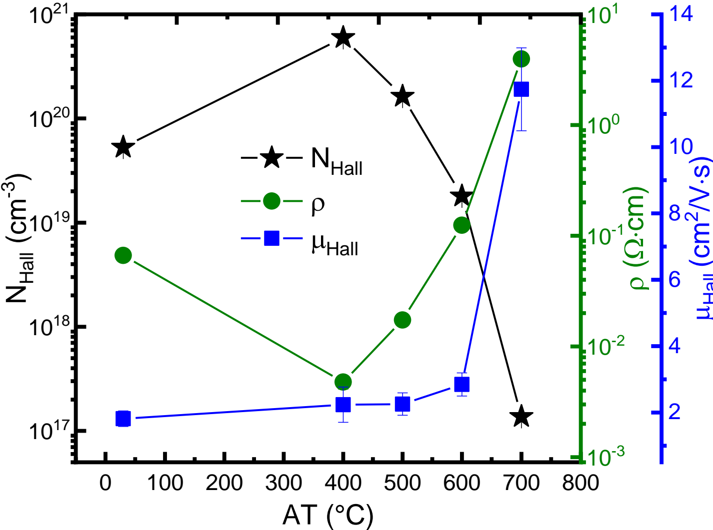

Figure 4.5.5 – Hall carrier concentration (N_{Hall}), electrical resistivity (ρ), and Hall mobility (μ_{Hall}) measured for Fe-doped ITO films as a function of the annealing temperature.

Table 4.5.3 – Electrical characterization at room temperature using the four-point probe method, showing the sheet resistance ($R_{\square}$), electrical resistivity (ρ), carrier concentration (N_{Hall}), and Hall mobility (μ_{Hall}) for the Fe-doped ITO films.

AT (°C)	$R_{\square}$ ($\Omega/\square$)	N_{Hall} (cm^{-3})	ρ ($\times10^{-3}\Omega \cdot cm$)	μ_{Hall} (cm^2/V·s)
AG	834.2 ± 21.1	5.19 $\times10^{19}$	66.5 ± 1.9	1.8 ± 0.2
400	60.2 ± 9.8	5.86 $\times10^{20}$	4.8 ± 0.8	2.2 ± 0.5
500	218.9 ± 10.1	1.60 $\times10^{20}$	17.4 ± 0.9	2.3 ± 0.3
600	1636.7 ± 28.8	1.78 $\times10^{19}$	124.6 ± 2.7	2.8 ± 0.3
700	51305.7 ± 52.9	1.35 $\times10^{17}$	3952.7 ± 20.5	11.7 ± 1.2

Temperature dependence of the electrical resistivity was measured for all samples. As shown in Figure 4.5.6(a), the AG Fe-doped ITO film exhibits semiconducting behavior, with the resistivity decreasing monotonically as the temperature increases. Interestingly, no semiconductor-to-metal transition (T_{SM}) was observed within the analyzed temperature range (80-300 K), which is expected for undoped ITO films (VILCA-HUAYHUA et al., 2025). This suppression of T_{SM} can be attributed to the introduction of localized states associated with Fe ions and to additional scattering centers, which modify the Burstein–Moss effect. This effect is closely associated with the metallic behavior of ITO films, where high carrier concentrations shift the optical absorption edge (KIM et al., 2014). Fe-related defects, together with oxygen vacancies stabilized by the deposition and annealing conditions, may inhibit the delocalization of electrons that typically drives the semiconductor–metal transition. Additionally, the relatively low carrier concentration and altered effective mass in these Fe-doped films, as discussed earlier, reduce the likelihood of achieving the critical carrier density necessary for metallic conduction at moderate temperatures. Therefore, we believe that the combined effects of Fe doping, defect distribution, and oxygen-poor conditions likely stabilize the semiconducting behavior over the measured temperature range.

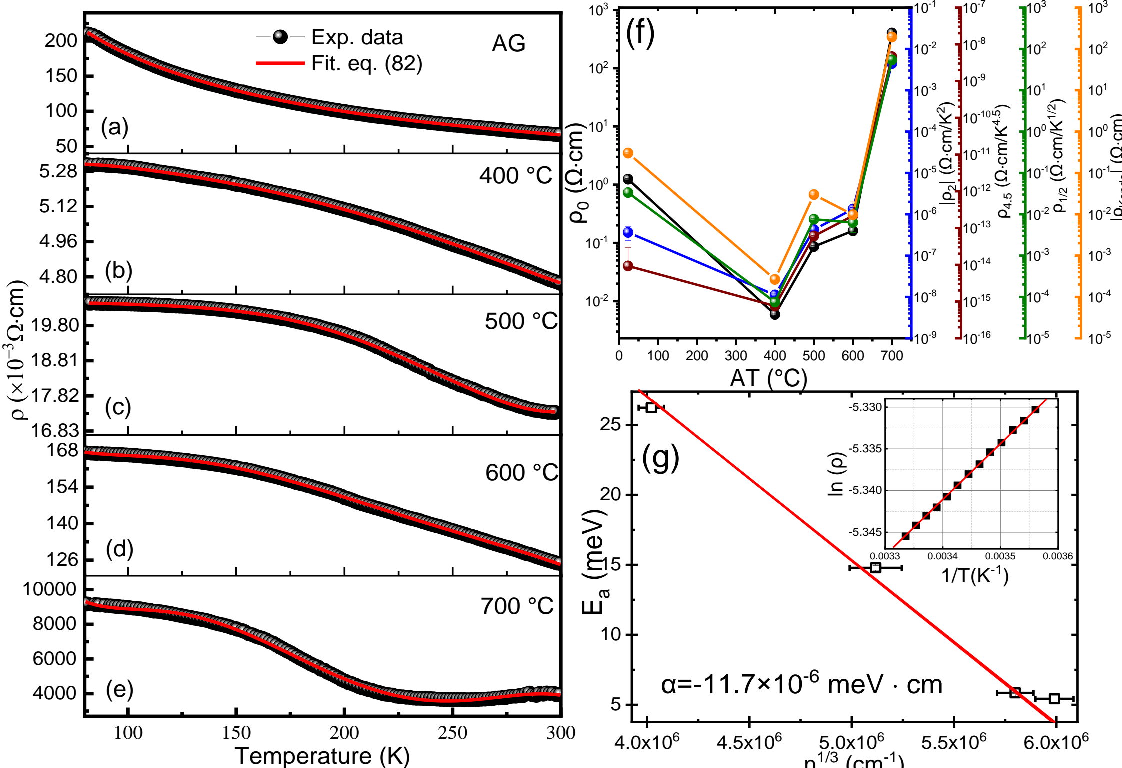

Figure 4.5.6 – (a)-(e) Resistivity vs. temperature curves measured from 80 K to 300 K for Fe doped ITO thin films with different anneling temperatures. The experimental data are shown as black symbols, while the red lines represent the fits using (Equation 82). (f) Correction resistivity parameters a function of the annealing temperature, (g) Activation energy (E_a) vs. carrier concentration ($n^{1/3}$), inset: Resistivity ln ρ vs. 1/T.

For films annealed in vacuum above 400 °C an anomalous low-temperature behavior is

observed, as evidenced by the change in the resistivity curvature shown in Figure 4.5.6(b)–(e). A similar trend has been reported in Fe-doped InSb films (AGRAWAL; SARKAR; GANESAN, 2019). Such anomalies are commonly attributed to the presence of Fe-content. The film annealed at 700°C (see Figure 4.5.6(e)) exhibits a resistivity minimum at $T_{SM} \sim 250$K. At temperatures above T_{SM}, the resistivity also increases, displaying a metallic-like response, meanwhile below T_{SM}, the resistivity shows an increase as the temperature decreases and shows an unusual behavior. It suggests the coexistence of multiple scattering mechanisms, including grain boundary scattering (ρ_0), electron–electron interactions ($\rho_{1/2}T^{1/2}$ and the $\rho_2 T^2$ for different range temperatures), two-magnon scattering ($\rho_{4.5}T^{4.5}$), and Kondo-like spin-dependent scattering ($\rho_s \ln T$), as suggested by Agrawal *et al.* (AGRAWAL; SARKAR; GANESAN, 2019). To quantitatively describe this behavior, Equation 82 was employed to fit the experimental data.

$$\rho(T) = \rho_0 + \rho_{1/2}T^{1/2} + \rho_s lnT + \rho_2 T^2 + \rho_{4.5}T^{4.5} \tag{82}$$

The resistivity coefficients obtained from the fit of Equation 82 are listed in Table 4.5.4 and shown graphically in Figure 4.5.6(f). All parameters exhibit a similar trend (ρ_2 and ρ_s are considered in absolute terms). This correlation among the parameters indicates that the annealing at temperatures below 400 °C leads to a decrease in resistivity, suggesting an improvement in electrical conductivity, likely due to enhanced crystallinity. However, as the annealing temperature further increases, the possible formation of extended defects or Fe clusters, as well as oxygen loss, may introduce additional disorder and scattering centers, thereby reducing conductivity. For the film thermally treated at 700 °C, an additional electron–phonon interaction term ($\rho_5 T^5$) was included, which was necessary to achieve a satisfactory fit.

Table 4.5.4 – Parameters obtained from the fits of the low temperature resistivity curves employed Equation 82.

AT (°C)	ρ_0 ($\Omega \cdot$cm)	$\rho_{1/2}$ ($\Omega \cdot$cm$\cdot$K$^{1/2}$)	ρ_s ($\Omega \cdot$cm)	ρ_2 ($\Omega \cdot$cm$\cdot$K^2)	$\rho_{4.5}$ ($\Omega \cdot$cm$\cdot$K$^{4.5}$)	ρ_p ($\Omega \cdot$cm$\cdot$K^5)
AG	1.24	3.34×10^{-2}	-3.01×10^{-1}	-3.64×10^{-7}	9.31×10^{-15}	-
400	5.88×10^{-3}	7.53×10^{-5}	-2.66×10^{-4}	-1.12×10^{-8}	7.57×10^{-16}	-
500	8.65×10^{-2}	7.56×10^{-3}	-2.99×10^{-2}	-4.27×10^{-7}	6.08×10^{-14}	-
600	1.62×10^{-1}	6.27×10^{-3}	-9.71×10^{-3}	-1.34×10^{-6}	2.16×10^{-13}	-
700	4.01×10^{2}	5.40×10^{1}	-1.93×10^{2}	-4.40×10^{-3}	4.61×10^{-9}	-1.98×10^{-10}

At higher temperatures (above 280 K), the activation energy (E_a) can be extracted by applying the Arrhenius relation, which describes the thermally activated conduction process as $\ln \rho = \ln \rho_0 + E_a/k_B T$, where k_B is the Boltzmann constant. The activation energy is obtained from the slope of the linear region in the $\ln \rho$ versus $1/T$ plot, as shown in inset Figure 4.5.6(g) for the sample thermally treated at 400 °C. Assuming charge neutrality, the effective donor concentration satisfies $N_D^+ - N_A^- = n$, where N_D^+ and N_A^- denote the ionized donor and acceptor concentrations, respectively, and n is the free carrier concentration. Accordingly, the activation

energy can be expressed as $E_a(N_D^+) = E_a(0) - \alpha(N_D^+)^{1/3}$, where $E_a(0)$ represents the activation energy at very low doping levels, and α is a proportionality constant quantifying the reduction of E_a with increasing donor density (KUMAR et al., 2012). This dependence arises from the progressive overlap of donor wavefunctions, which lowers the potential barrier as the doping level increases. In the regime where $n > N_D^+$, this expression simplifies to the empirical relation $E_a = E_a(0) - \alpha n^{1/3}$, consistent with the experimental trend shown in Figure 4.5.6(g).

4.5.5 Magnetic properties

In Figure 4.5.7(a)-(b), the magnetization (M) versus applied magnetic field (H) curves of the Fe-doped ITO thin films measured at 2 K and 300 K are presented. As shown in Figure 4.5.7(b), the curves at 300K shows the coexistance of paramagnetism (linear behavior at the high-field region) and ferromagnetic-like contribution. In order to assess parameters of the paramagnetic phase, curves at 2K were first analyzed, since at low temperature the paramagnetism is the dominant contribution. The magnetization of the paramagnetic contribution is given by the Brillouin function, Equation 84.

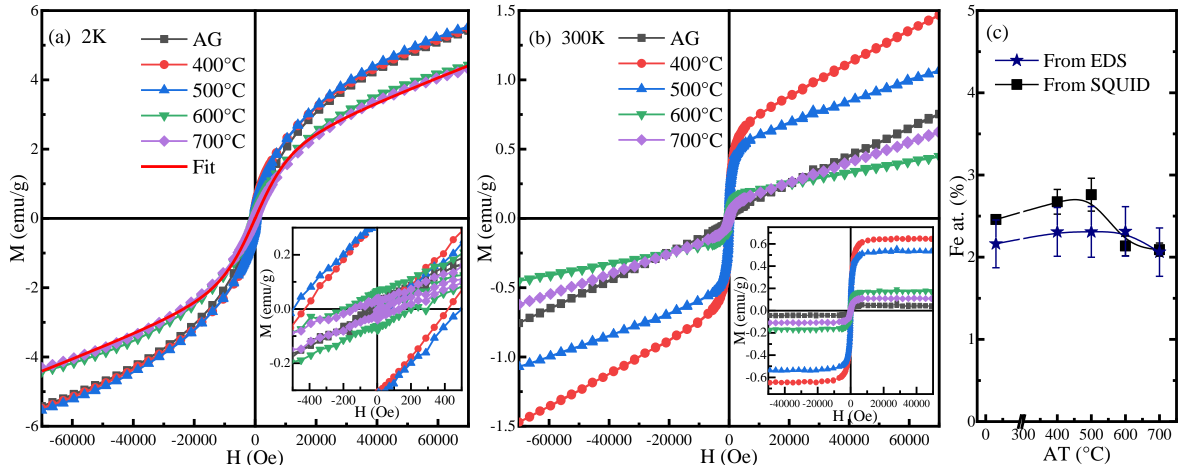

Figure 4.5.7 – Magnetization as a function of the applied external magnetic field (H) for Fe-doped ITO films, (a) M vs H at 2 K, inset coercive field, (b) M vs H at 300K, inset ferromagnetic contribution curves at room temperature, (c) Fe atomic concentration estimated from SQUID measurements and EDS.

$$M(H,T) = M_S\, B_S(y) + \chi_0\, H \tag{83}$$

$$B_S(y) = \frac{2S+1}{2S}\coth\left(\frac{2S+1}{2S}y\right) - \frac{1}{2S}\coth\left(\frac{y}{2S}\right) \tag{84}$$

$$y = \frac{g\,\mu_B\, S\,\mu_0 H}{k_B\,(T-T_0)} \tag{85}$$

where M_S is the saturation magnetization, which defines the maximum contribution of the localized Fe magnetic moments to the total magnetization. $B_S(y)$ is the Brillouin function S, describing the spin angular moment of the iron-ions. The argument y is a dimensionless parameter that incorporates the Landé g-factor, the Bohr magneton μ_B, the applied magnetic field H, and the thermal energy $k_B(T - T_0)$, where T_0 is a phenomenological parameter. The inclusion of T_0 allows the model to account for short range magnetic correlations, with positive (negative) values suggesting predominant ferromagnetic (antiferromagnetic) correlations. The χ_0, represents the temperature-independent susceptibility contribution, as in the case of Pauli

or Van Vleck paramagnetism (MUGIRANEZA; HALLAS, 2022). In Figure 4.5.7(a), the red continuous line represents the fit obtained using Equation 83. The results of the fit are presented in Table 4.5.5.

Table 4.5.5 – Parameters obtained from the fit of magnetization vs. magnetic field curves to the Brilloiun function, M_S (2K) is the saturation magnetization at 2K, spin angular moment (S), fraction paramagnetic of Fe (x_{PM}), temperature independent susceptibility (χ_0), interaction temperature (T_0), coercive field (H_C), M_S (300K) is the saturation magnetization at 300K, fraction ferromagnetic of Fe (x_{FM}), $x_{Tot} = x_{PM} + x_{FM}$ for the Fe-doped ITO films.

AT (°C)	M_S (2K) (emu/g)	S	T_0 (K)	x_{PM} ($\times10^{-2}$)	H_C Oe	M_S (300K) (emu/g)	x_{FM} ($\times10^{-3}$)	x_{Tot} (%)
AG	2.54 ± 0.02	2.52 ± 0.04	0.30	2.41±0.02	60	0.05 ± 0.01	0.48 ± 0.01	2.46 ± 0.03
400	6.44 ± 0.05	2.56 ± 0.13	1.00	2.04±0.05	326	0.64 ± 0.04	6.28 ± 0.11	2.67 ± 0.15
500	5.38 ± 0.10	2.58 ± 0.21	0.90	2.23±0.10	324	0.54 ± 0.03	5.25 ± 0.10	2.76 ± 0.20
600	1.70 ± 0.04	2.53 ± 0.09	0.20	1.97±0.04	257	0.17 ± 0.02	1.65 ± 0.08	2.14 ± 0.12
700	1.14 ± 0.03	2.52 ± 0.07	0.08	1.89±0.03	103	0.11 ± 0.02	1.11 ± 0.05	2.09 ± 0.08

As the S value determined from the fits is near to $S = 5/2$, it strongly suggests that the Fe ions are in valence state 3+ (see Table 4.5.5). Based on this, the concentration of Fe^{3+} incorporated in $In_{2-y-x}Sn_yFe_xO_3$ was estimated from the M_S. The experimental magnetic moment per formula unit was calculated as $\mu_{f.u.}(\mu_B/f.u.) = M_S M_{mol}/N_A\mu_B$, where N_A is Avogadro's number, μ_B the Bohr magneton, and M_{mol} the molar mass of the compound. Assuming that the magnetization arises only from Fe ions substituting In sites, each one contributing with a theoretical moment of $\mu_{Fe}^{theor} = 5\mu_B$, the paramagnetic fraction of Fe was estimated as $x_{PM} \approx \mu_{\text{f.u.}}/\mu_{Fe}^{theor}$, (see Table 4.5.5). The positive values of T_0 indicate the occurrence of short-ranged ferromagnetic correlation among Fe ions, reaching their maximum in the samples annealed at 400 and 500 °C.

Although at 2K the paramagnetic contribution is the dominant one, the presence of a ferromagnetic contribution is evidenced by a coercive field in the central region of the M vs H curves, as shown in the inset of Figure 4.5.7(a). As listed in Table 4.5.5, the larger coercive field is determined for samples annealed at 400 and 500 °C. The presence of ferromagnetic contributions is better resolved in M vs H curves obtained at 300K where due to the thermal effect, the paramagnetic contribution is represented by the linear trend at the high-field region, as shown in Figure 4.5.7(b). In order to assess the amount of Fe ions contributing to the ferromagnetic part (x_{FM}), the linear trend that represents paramagnetic contribution was subtracted from the curves as shown in the inset of Figure 4.5.7(b). The x_{FM} was estimated from the above relation: $x_{FM} = M_S M_{mol}/N_a\mu_B\mu^{Fe}$ and values are listed in Table 4.5.5. As observed, the Fe concentrations determined from magnetic measurements is similar in comparison to values determined from EDS analysis (see Figure 4.5.7(c)).

The strongest FM contribution was observed in the sample annealed at 400 °C, and the rapid increase relative to the AG film is an intriguing feature. It is important to note that a

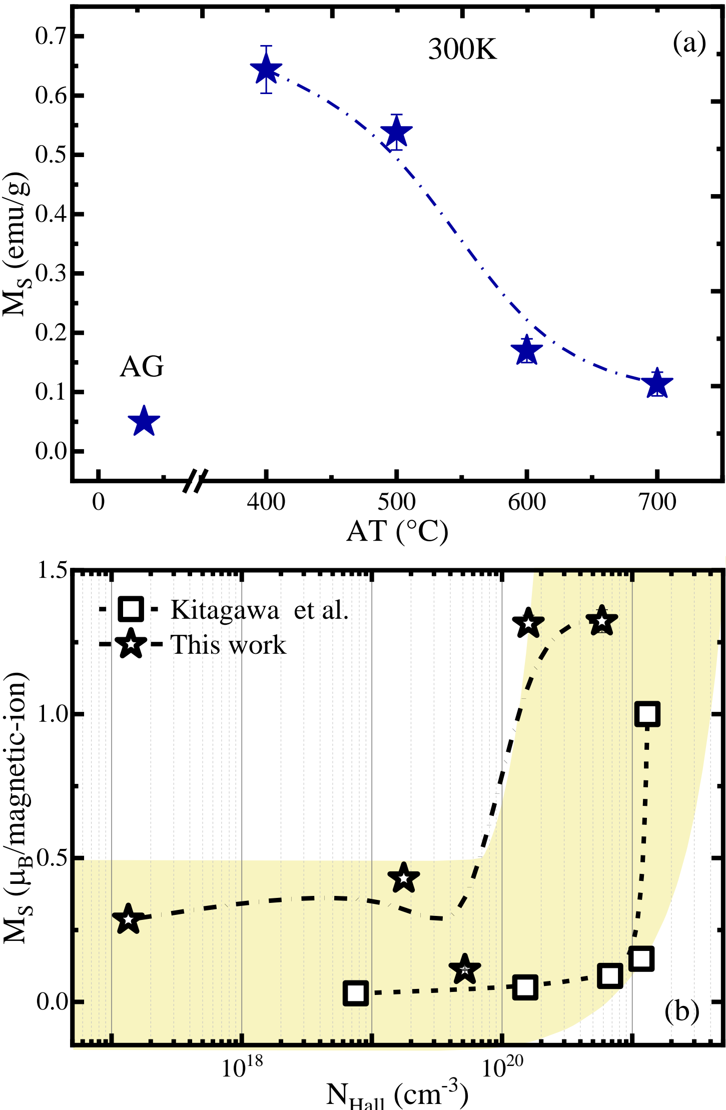

Figure 4.5.8 – (a) Saturation magnetization of the FM contribution (M_S) determined at 300 K as a function of annealing temperature, (b) M_S as a function of carrier concentration. In this plot are included values reported by Kitagawa et al. (KITAGAWA; NAKAMURA, 2025). The yellow shaded region shows the increase in magnetization for larger charge carriers density.

similar effect was observed when the annealing of the films was carried out in air (no showed here), suggesting that the atmosphere is not determinant for this FM increase. We attribute this enhancement instead to the improvement in crystallinity observed by XRD. Ferromagnetism is generally weaker in amorphous solids compared to their crystalline counterparts due to the absence of long-range atomic order (MAURI et al., 1988). Furthermore, the RTFM observed here can be associated with Fe–V_O defects complex. These defects can promote the formation of BMPs, providing an additional channel for exchange interactions between localized Fe magnetic moments and thereby enhancing long-range ferromagnetic ordering (COEY; VENKATESAN; FITZGERALD, 2005; ARAGóN et al., 2016). In contrast, at higher annealing temperatures, the reduction in V_O concentration decreases the polaron density, leaving to the reduction of the FM

contribution as depicted in Figure 4.5.8(a).

On the other hand, Figure 4.5.8(b) shows the dependence of M_S on N_{Hall}, showing a tendency for M_S to increase as the concentration of iron ions increases. This observation suggests that the room-temperature ferromagnetism of Fe-doped ITO films would also be correlated with the number of free carriers, in agreement with the Zener–RKKY interaction model (Ruderman–Kittel–Kasuya–Yosida) (CALDERóN; SARMA, 2007). Although the RKKY model predicts that the effective exchange interaction (S) oscillates in sign with distance between magnetic impurities, leading in general to complex magnetic configurations, under certain conditions an increase in the ratio between the carrier density and the magnetic impurity density (n_c/n_i) results in only ferromagnetism (CALDERóN; SARMA, 2007). This behavior is consistent with our experimental findings. Similar trends have been reported for Mn-doped ITO structures, where an increase in carrier concentration promotes the formation of 3d states near the Fermi level within the conduction band, thereby strengthening the ferromagnetic interaction (KITAGAWA; NAKAMURA, 2025).

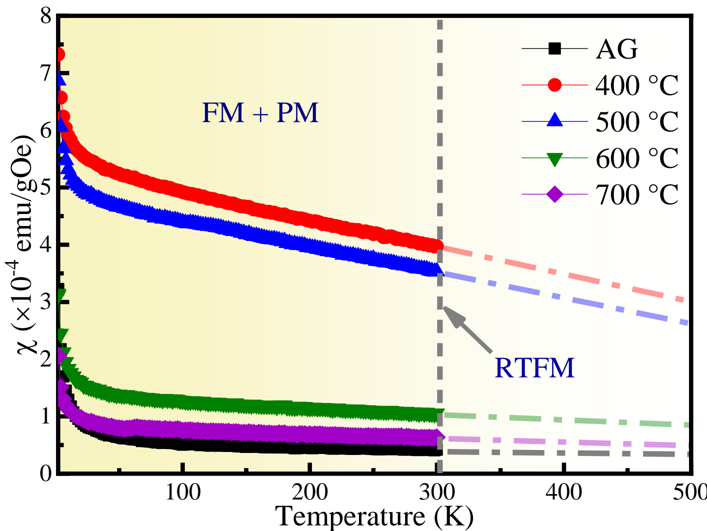

Figure 4.5.9 – Magnetic susceptibility (χ) as a function of temperature for samples annealed at different temperatures.

Figure 4.5.9 shows the magnetic susceptibility as a function of temperature for the as-grown and annealed samples. The overall behavior confirms the coexistence of ferromagnetic and paramagnetic contributions across the entire temperature range. The larger FM contribution is also confirmed by the higher magnetic susceptibility observed for samples annealed at 400 and 500 °C, in agreement with that determined from M vs H curves. The FM contribution shows an almost linear decreasing tendency with the temperature, clearer observed for samples annealed at 400 and 500 °C, where the FM contribution is larger. That trend seems to be screened by the paramagnetism contribution in samples annealed at higher temperatures. The linear trend representing the FM contribution suggests that the Curie temperature must be near above 300K.

4.5.6 Photocurrent

In order to evaluate the influence of light exposure and to elucidate the relationship between the iron ions and the thermal annealing process, the photoresponse behavior of the films was systematically analyzed. Figure 4.5.10(a) displays a representative photocurrent–time (I–t) curve for the Fe-doped ITO film annealed at 600 °C. Upon UV illumination, a sharp increase in photocurrent is observed, evidencing the generation of photoinduced charge carriers and confirming the n-type conduction behavior of the film. When the UV light is turned off, the photocurrent gradually decreases toward its initial value. This slow decay after turning out the UV of illumination can be ascribed to the delayed re-adsorption of oxygen molecules on the film surface, a process strongly affected by the presence of trap states and recombination centers induced by the by Fe doping.

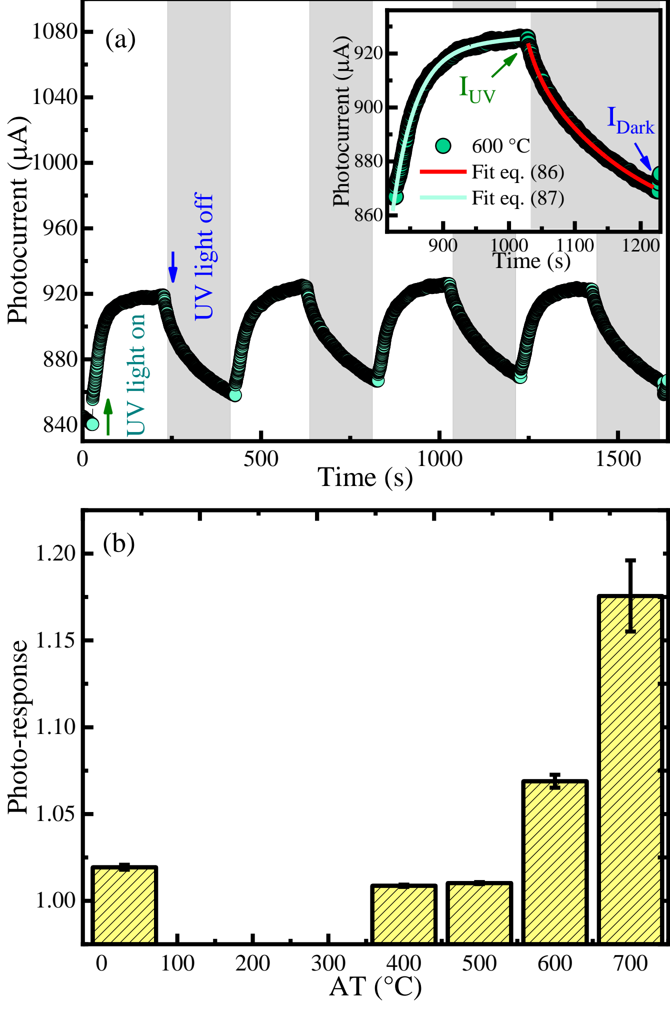

Figure 4.5.10 – Photocurrent as a function of time for the film annealed at 600 °C. The dark-shaded regions indicate the intervals when the sample was not exposed to UV illumination. The inset shows the exponential fitting of the decay curve using Equation 86. (b) Photoresponse ratio (PR = I_{UV}/I_{dark}) as a function of annealing temperature.

To evaluate the temporal decay and gain deeper insight into the photocurrent dynamics,

the experimental data were fitted using the exponential model described by Equation 86 and Equation 87. In this expression, $A_{0,1}$, $B_{0,1}$, and τ, τ_R are fitting parameters; t_0 denotes the time at which the UV illumination is switched off; and τ represents the time constants associated with carrier trapping and recombination processes and τ_R response time. The fitting parameters are summarized in Table 4.5.6. The inset in Figure 4.5.10(a) shows a representative fit for the film annealed at 600 °C, illustrating the excellent agreement between the model and the experimental data.

$$I(t)_{Recovery} = A_0 + B_0 \exp(-(t + t_0)/\tau) \tag{86}$$

$$I(t)_{Response} = A_1 + B_1(1 - \exp(-(t + t_0)/\tau_R)) \tag{87}$$

As shown in Table 4.5.6, the recovery time (τ) exhibits an opposite trend to the photoresponse (PR). A shorter τ corresponds to a faster photocurrent generation and decay, indicating more efficient charge transport and a reduced density of trapping centers. In contrast, longer recovery times are associated with slower carrier dynamics, likely dominated by defect-assisted trapping and recombination processes.

A noticeable decrease in τ is observed for the sample thermally treated at 700 °C. This film exhibits higher crystallinity, as confirmed by XRD and optical analyses, which also reveal a lower Urbach energy consistent with reduced structural disorder. Interestingly, despite being the most resistive among the samples and showing a metal-like behavior at room temperature (see Fig. 5(e)), this film demonstrates the highest photoresponse together with the shortest recovery time. The latter suggests that the defect dynamics, possibly involving oxygen vacancies or Fe-related states, play a key role in the rapid photogeneration carrier and recombination processes that govern the photocurrent behavior.

Table 4.5.6 – Parameters extracted from the exponential fitting of Equation 86, including the response time (τ_R), recovery time (τ), and photoresponse ratio (PR) for the Fe-doped ITO films.

AT (°C)	τ_R (s)	τ (s)	$PR = I_{UV}/I_{dark}$
AG	32.5 ± 0.9	112.0 ± 14.6	1.019 ± 0.001
400	48.9 ± 2.9	103.7 ± 7.1	1.009 ± 0.001
500	45.8 ± 3.2	137.7 ± 9.8	1.010 ± 0.01
600	23.1 ± 2.0	98.5 ± 9.7	1.069 ± 0.004
700	15.8 ± 2.3	55.1 ± 7.8	1.176 ± 0.021

4.5.7 Conclusion

Fe-doped ITO thin films were successfully deposited via RF magnetron sputtering after to post-annealing under vacuum between 400 and 700 °C. XRD and Rietveld analyses confirmed

that all samples retained the cubic bixbyite phase without secondary Fe-related oxides. The lattice parameter and Bragg peaks linewidth decreased with increasing annealing temperature, evidencing reduced structural disorder and improved crystallinity. The preferential (400) orientation observed at lower annealing temperatures gradually weakened with increasing temperature, suggesting that the reduction of oxygen vacancies promotes a more ordered crystallographic structure. Optical transmittance measurements revealed a significant enhancement in transparency, reaching close to 90% after annealing at 600 °C. The optical modeling indicated that vacuum annealing can be used to tune the free carrier concentration and the carrier effective mass, reflecting a renormalization of the bands due to electron-electron/electron-impurity interactions resulting from Fe incorporation and oxygen-vacancy generation. The widening of the optical bandgap and the concurrent reduction in Urbach energy with the increasing of the annealing temperature are consistent with the reduction of localized defect states and lattice disorder. Electrical transport measurements demonstrated that the Fe incorporation stabilizes a semiconducting behavior, suppressing the typical semiconductor–metal transition observed in undoped ITO. At low temperatures, the resistivity shows an anomalous temperature dependence consistent with competing scattering mechanisms, including Kondo-like spin-dependent interactions and two-magnon scattering. The annealing process at low temperatures enhances electrical conductivity due to the improved crystallinity, whereas at higher temperatures may induce defect clustering that partially limits the charge transport. The RTFM observed in Fe-doped ITO samples can be attributed to the coexistence of (i) oxygen vacancies nearby Fe ions favor the formation of BMPs, and (ii) the high carrier concentration characteristic of ITO enables long-range RKKY-like interactions, Overall, these results highlight the interplay between the different magneto-opto-electronic properties, that can be controlled via post deposition vacuum annealing, providing an effective mean to modulate the defect landscape, carrier dynamics, and electronic scattering in Fe-doped ITO films enabling the fine-tuning of their structural, optical, and electrical properties for applications in optoelectronic and spintronic devices.

4.6 Influence of the thermal annealing carried out in different vacuum levels on the optoelectronic, magnetic properties and gas-sensor response of Fe doped ITO films

In this study, we investigated the effects of the thermal annealing under different vacuum levels on the Fe-doped ITO structure grown by co-sputtering, providing insight into mechanisms related to defects such as oxygen vacancies and their interactions with Fe atoms, which govern the structural, optical, electrical and magnetic properties of ITO.

4.6.1 Experimental details

Thin films of Fe-doped ITO were grown via RF magnetron sputtering on quartz substrates. Previously to the films' deposition, the substrates were cleaned in acetone for 10 min in a ultrasonicator machine. For the deposition commercially available targets were used consisted of In_2O_3 (90 wt%) / SnO_2 (10 wt%) target, with a diameter of 2 inches acquired from Plasmaterials, Inc. The metallic Fe target with a diameter of 2 inches was purchased from Beijing Xing Rong Yuan Technology Co. Both targets had a purity of 99.99% . The distance between the targets and the substrate was set to 7.5 cm. These targets were sputtered by co-sputtering applying a power of 60 and 150 W respectively. The base vacuum levels was up to 1.06×10^{-6} mbar. The working pressure was then adjusted to 1.1×10^{-2} mbar by introducing pure Ar/O_2 (35 sccm)/(1 sccm) and by rotating at 50 rpm the growth process lasted 3 hours. After the growth, the films were annealed at different vacuum pressure (10^0 - 10^{-6} mbar) for two hours at 500 °C. Subsequently, the ITO was characterized by X-ray diffraction (XRD) measurements using a Rigaku diffractometer with Cu-Kα radiation (λ = 1.5418 Å) in the range of 20° ≤ 2θ ≤ 80°, The optical properties were determined by UV-Vis spectroscopy and the stoichiometry was determined carrying out EDS measurements by using a scanning electron microscope (SEM) FEI Quanta 650 with a voltage of 6.5 kV. Resistivity measurements were performed at room temperature using the van der Pauw configuration, using a current source and voltmeter (Keithley Instruments), Photocurrent responses under UV illumination were studied at room temperature with an applied bias of 1.5 V in air. Magnetic properties were investigated using a vibrating sample magnetometer (VSM, Quantum Design SQUID) under fields up to ±70 kOe at both 2 K and 300 K.

4.6.2 Structural properties

Figure 4.6.1(a) shows the X-ray diffraction patterns of the Fe-doped ITO films annealed at different vacuum levels (10^0-10^{-6} mbar), showing the (211), (222), (400), (440) and (622) planes corresponding to the cubic crystal structure of In_2O_3 bixbyite (CPDS card no. 6–0416 and space group: Ia3). Within the detection limit of the XRD equipment, no presence of secondary phases associated with Fe or Sn were detected in all the films, suggesting that no secondary phases are

formed. Furthermore, the diffractograms showed a preferential orientation on the (440) plane.

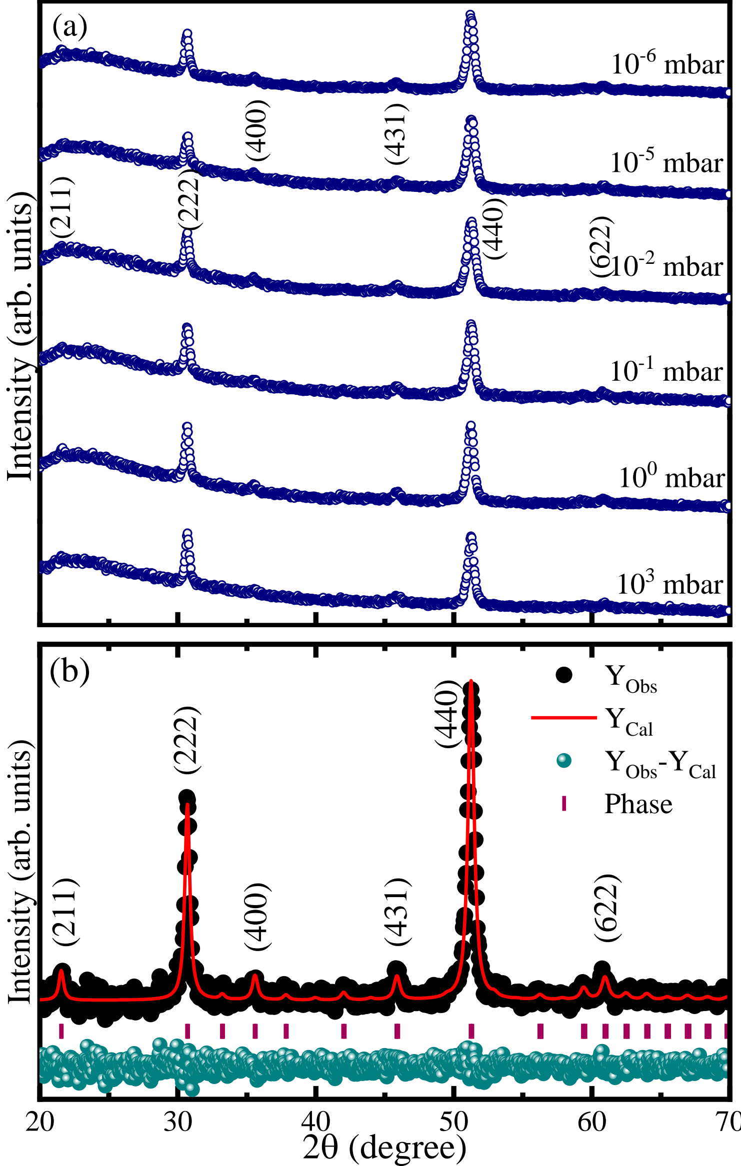

Figure 4.6.1 – (a) X-ray diffraction patterns of the Fe-doped ITO films annealed at different vacuum levels, (b) Rietveld refinement of the XRD pattern of the film annealed in 10^{-6} mbar. The black circles represent the experimental data Y_{Obs}, the blue line represents the fit Y_{Cal}, the green line the difference between Y_{Obs}-Y_{Cal}, the black line the phase and finally wRp/RP=1.26 the quality of the fit.

To quantify the degree of the preferential orientation, the texture coefficient (TC) was calculated using the standard relation:

$$TC(hkl) = \frac{I_{(hkl)}/I_{0(hkl)}}{\frac{1}{N}\sum_{N} I_{(hkl)}/I_{0(hkl)}} \tag{88}$$

where $I_{(hkl)}$ is the measured intensity of the (hkl) diffraction peak, $I_{0(hkl)}$ is the corresponding standard intensity from the ITO (JCPDS card No. 1011258), and N denotes the

number of peaks included in the analysis. The Fe doped ITO films exhibits greater texturing along the (440) plane as shown in the Table 4.6.1. The preferential orientation on the (440) plane may be related to the low surface energy due to the low temperature used during film growth as reported (WANG et al., 2022). In contrast, the (222) plane orientation is favored under oxygen-rich conditions; therefore, as the vacuum level of the thermal annealing, the intensity of this orientation decreases (see Table 4.6.1). This behavior is attributed to the oxygen-poor environment, which promotes the formation of oxygen vacancies, in agreement with the XPS analysis, as discussed below.

Figure 4.6.1(b) shows the Rietveld refinement analysis of the X-ray diffraction pattern for the film annealed in 10^{-6} mbar, using Lorentzian functions implemented in the GSAS software (TOBY; DREELE, 2013). As shown in Figure 4.6.2(a), the lattice parameter a decreased by approximately 0.4 % for the room-pressure annealed film, in comparison to the bulk value, a = 10.117 Å (MAREZIO, 1966), suggesting that Fe^{3+} ions substitute In^{3+} ions, since the ionic radius of Fe^{3+} (0.645 Å) is smaller than that of In^{3+} (0.785 Å). It causes a unit cell volume contraction according to the Vergard's law model, confirming the incorporation of Fe ions into the ITO lattice. Additionally, a slight expansion of the lattice parameter is observed with the increase of the vacuum level (lower pressure). This behavior is accompanied by an increase in oxygen vacancies (V_O) that can facilitate ion migrations within the lattice. However, the combined presence of Fe, Sn, and V_O defects within the lattice is complex, where the interactions between ions and V_O can occur changing the lattice parameter.

The average crystallite size ($< D >$) and residual strain ($< \varepsilon >$) were estimated using the Williamson–Hall (W–H) method. This approach involves plotting $\beta \cos\theta$ versus $\sin\theta$, based on the linearized form of the Williamson–Hall equation,

$$\beta_{Sample} \cos\theta = \frac{K\lambda}{< D >} + 4 < \varepsilon > \sin\theta \tag{89}$$

where, β_{Sample} represents the full width at half maximum ($< FWHM >$) associated with size and/or strain-induced broadening of the crystallites, after subtracting from the instrumental broadening contribution ($\beta_{\text{Sample}} = \beta_{\text{Measurement}} - \beta_{\text{Inst}}$). The constant K is the Scherrer shape factor, which depends on the crystallite morphology; a value of $K \approx 0.9$ is commonly used for approximately spherical particles. As shown in Figure 4.6.2(b), the average crystallite size increases from 24 nm to 43 nm as the vacuum level during annealing increases, attributed to enhanced atomic mobility and diffusion coefficients, leading to atomic transfer from smaller grains to larger grains, which possess higher surface energy thus promoting grain growth (PACHECO-SALAZAR et al., 2020; VILCA-HUAYHUA et al., 2025). However, due to the migration of ions and intrinsic defects, the ITO lattice can be deformed, which would explain the increased $< \varepsilon >$ at higher vacuum pressures levels as show in the Table 4.6.1.

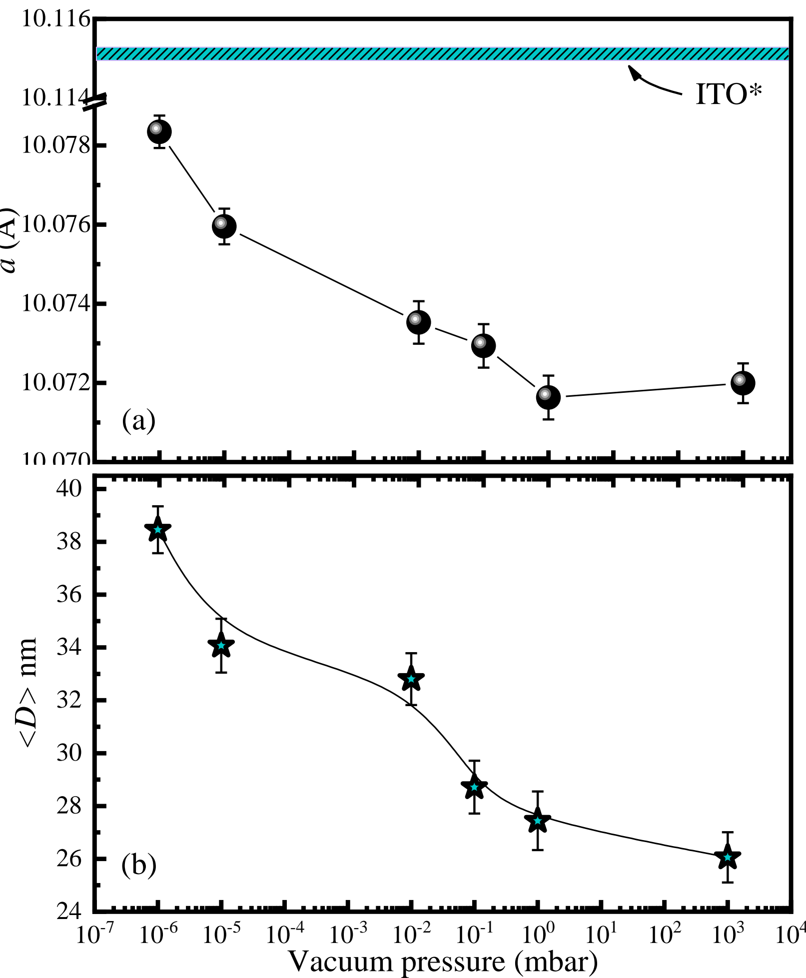

Figure 4.6.2 – (a) Lattice parameter obtained from Rietveld refinements and (b) crystallite size $< D >$, as a function of the vacuum pressure level used during the annealing of the Fe-doped ITO films.

Table 4.6.1 – Results of structural and morphological paramenters of ITO films obtained from the XRD Rietveld refinement. The lattice parameter ($a = b = c$), average crystallite size ($< D >$),and residual strain ($< \varepsilon >$). the texture coefficient (TC) calculated using Equation 88 and goodness-of-fit (G) are also included. Integrated areas of the Sn/In, V_O/O_T, Sn^{4+}/Sn^{2+} ratios obtained by XPS.

VP (mbar)	$a = b = c$ (Å)	$< D >$ (nm)	$< \varepsilon >$ (%)	TC (222)	TC (440)	G	Sn/In	V_O/O_T	Sn^{4+}/Sn^{2+}
1.0×10^{3}	10.072	26.1 ± 1	0.49	0.60	1.61	1.22	0.080	0.45	0.01
1.1×10^{0}	10.072	27.4 ± 1	0.48	0.59	1.65	1.22	0.081	0.51	0.05
1.1×10^{-1}	10.073	28.7 ± 1	0.42	0.57	1.64	1.28	0.079	0.53	0.15
2.0×10^{-2}	10.074	32.8 ± 1	0.89	0.53	1.68	1.23	0.078	0.56	0.25
1.0×10^{-5}	10.076	34.1 ± 1	0.83	0.50	1.68	1.24	0.077	0.58	0.35
2.1×10^{-6}	10.078	38.5 ± 1	0.91	0.52	1.81	1.25	0.079	0.64	0.45

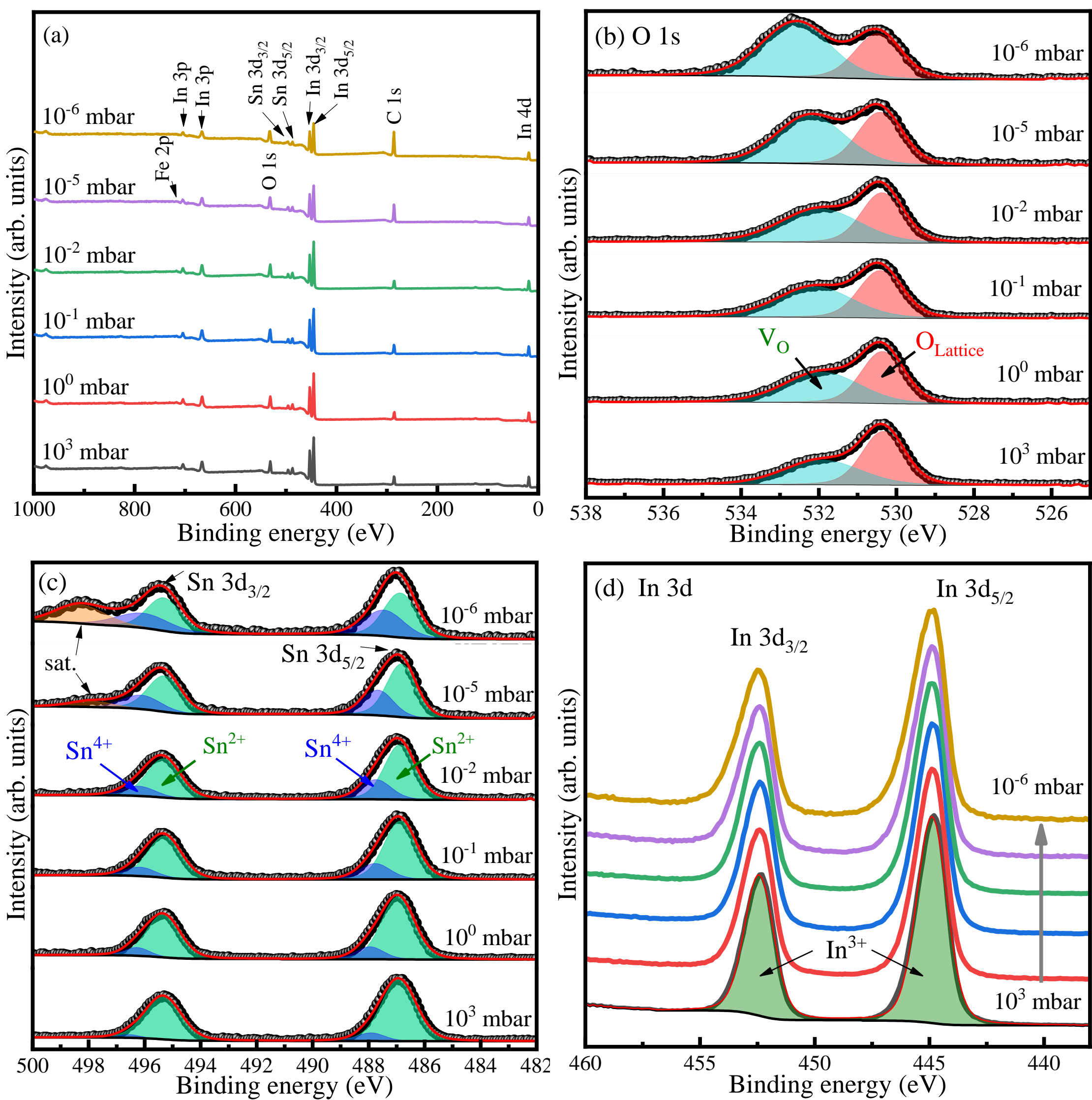

Figure 4.6.3 – XPS spectra of the Fe-doped ITO films annealed at different vacuum pressure levels (a) Survey, (b) O 1s orbital, (c) Tin (Sn) peaks related to $3d_{3/2}$ and $3d_{5/2}$ orbitals, (d) indium (In) peaks related to $3d_{3/2}$ and $3d_{5/2}$ orbitals.

4.6.3 XPS analysis

Figure 4.6.3(a) shows the wide-range survey spectra obtained by X-ray photoelectron spectroscopy (XPS) for the Fe-doped ITO films annealed under different vacuum pressures. The survey spectra reveal the presence of Fe, In, Sn, and O peaks, as well as small amounts of C. The detected carbon is associated with surface-adsorbed carbon accumulated during the sample's exposure to ambient atmosphere. This carbon signal is useful for calibrating the binding energies in the high-resolution spectra of each element in the Fe-doped ITO films by referencing the C 1s peak at 284.8 eV (GRECZYNSKI; HULTMAN, 2022)

Figure 4.6.3(b) presents the high-resolution O 1s spectra fitted using two components associated with lattice oxygen (O_L) and non-stoichiometric oxygen (O_V). The O_L component is located at a lower binding energy (529.37 eV), corresponding to In–O bonds of the bixbyite

In_2O_3 structure, whereas the O_V component appears at higher binding energies (531.87 eV) and is associated with oxygen vacancies (GöKçELI; KARATEPE, 2021). From Figure 4.6.3(b) and Table 4.6.1, a clear increase in the integrated area of the O_V component relative to O_L can be observed as the vacuum pressure level is increased. These results confirm that the annealing in vacuum condition promotes the formation of oxygen vacancies on the surface of the Fe doped ITO films.

Figure 4.6.3(c) shows the high-resolution scans of the Sn 3d spectra, displaying a spin–orbit splitting of ~ 11 eV between the $3d_{3/2}$ and $2p_{5/2}$ peaks. The peak corresponding to the Sn $3d_{5/2}$ orbital reveled the coexistence of Sn^{2+} and Sn^{4+} states, with binding energies of Sn^{2+} (485.6 eV) and Sn^{4+} (486.7 eV) respectively (see Figure 4.6.3). On the other hand, the Sn^{4+}/Sn^{2+} spectral area ratio is 0.01 for the film annealed at room atmosphere pressure 10^3 mbar, which means that the Sn^{2+} ions are dominant. Subsequently, a slight increase in Sn^{4+} ions is observed with the films annealed in higher vacuum levels, reaching a Sn^{4+}/Sn^{2+} ratio of 0.45 for the film annealed at 10^{-6} mbar (see Figure 4.6.3). This indicates that vacuum conditions not only favor the formation of oxygen vacancies (V_O) but also promote the activation of Sn^{4+}. These results are consistent with previous reports, in which the removal of interstitial oxygen (O_i) and the generation of oxygen vacancies contribute to an increase in n-type charge carriers (VILCA-HUAYHUA et al., 2025; HUAYHUA et al., 2025).

The peak positions of In 3d are practically similar for the ITO films annealed at different vacuum pressure levels. Two pairs of peaks are observed (In $3d_{5/2}$ and In $3d_{3/2}$), with binding energies at 425 eV and 458 eV, respectively, separated by 7.6 eV (see Figure 4.6.3(d)); . It suggests that the In^{3+} ion is chemically a single dominant oxidation state of In at the surface of the ITO films. Within the detection limits of the XPS instrument, it was not possible to obtain a well-fitted spectrum for the Fe spin–orbit components. However, magnetic curve analysis revealed the presence of Fe due to the higher sensitivity of that technique, as will be discussed below. On the other hand, the Sn/In ratio of ~0.079 indicates a slight reduction in the Sn content as shown in the Table 4.6.1, which lies below the nominal composition of the 10% in the target (Sn/In~ 0.11). This deviation is likely associated with a stoichiometric imbalance induced by the presence of Fe, which is not accounted for in the current XPS analysis.

4.6.4 Optical and electrical properties

The transmittance spectra were obtained over a range of (250 nm–900 nm), as shown in Figure 4.6.4, for Fe-doped ITO films annealed in different vacuum pressure levels. As shown in Table 4.6.2, the optical transmittance spectra in the visible range exhibit a high average transmittance (%T), exceeding 93% at a wavelength of 600 nm. This makes the material a promising candidate for the optimization of transparent conducting oxides (TCOs). According to previous reports, the thickness values estimated from transmittance measurements provided a good approximation (VILCA-HUAYHUA et al., 2025; HUAYHUA et al., 2025).

Based on these experimental observations, the thickness of the Fe-doped ITO films was determined by employing a multilayer model consisting of air/film/substrate/air. Initially, a fitting was performed on the substrate using a combination of the Cauchy layer and Brendel oscillator models. Subsequently, the Fe-doped ITO film was modeled using the Tauc–Lorentz (T–L) model (LIKHACHEV; MALKOVA; POSLAVSKY, 2015). These models are implemented in the SpectraRay/4 software developed by SENTECH. The thicknesses of the films were found to be around (445.3-478.5 nm), as shown in Table 4.6.2.

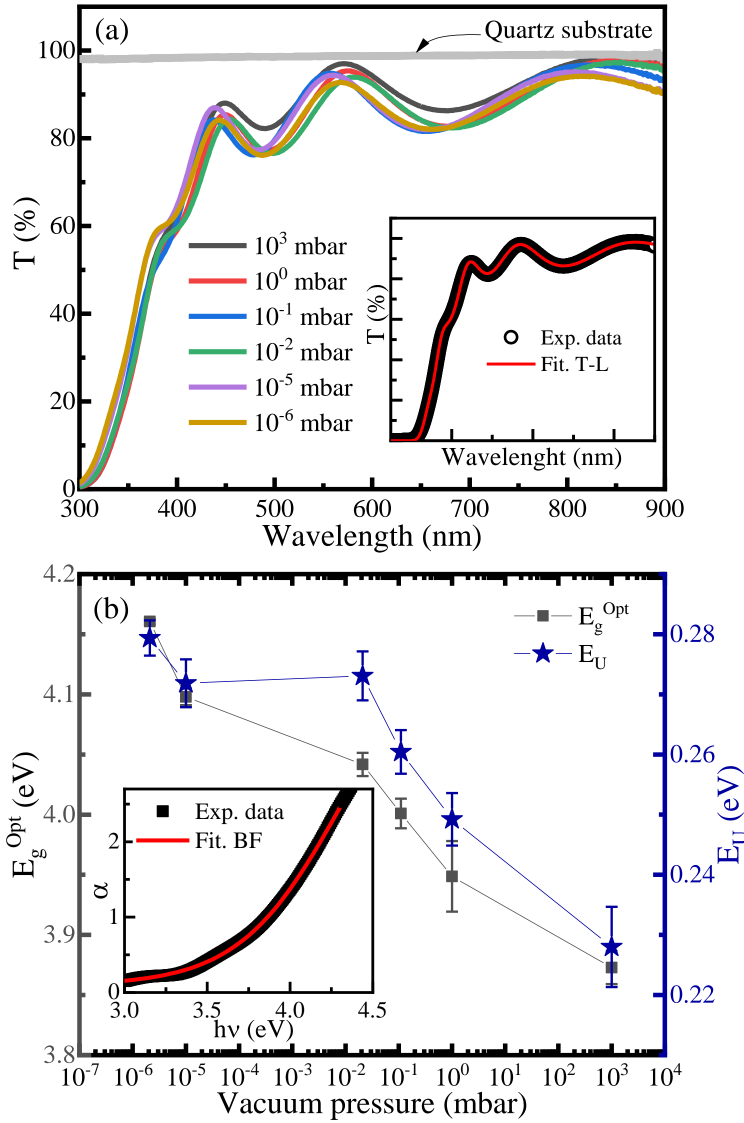

Figure 4.6.4 – (a) UV–Vis transmittance spectra. In the inset is shown the fit using Tauc-Lorentz oscillator layer model. (b) Optical bandgap (E_g^{Opt}), Urbach energy (E_U) as a function of the vacuum pressure level used during the annealing of the Fe-doped ITO films. The inset shows the fit using the band fluctuation model.

In addition, the absorption coefficient (α) for all Fe-doped ITO films was calculated from the transmission spectra using the $\alpha = 4\pi k/\lambda$ relation. Later, the band fluctuation model (BF) for direct transitions was employed (GUERRA et al., 2019) using the following equation:

$$\alpha(h\nu) = (1/2)(A_0/h\nu)\sqrt{\pi/\beta}Li_{1/2}(-e^{\beta(h\nu-E_g)}) \tag{90}$$

Here $h\nu$ is the photon energy, A_0 is a constant in units of $eV^{-1}\cdot cm^{-1}$, β is the inverse of Urbach energy, and Li_j (x) is the $j-th$ order polylogarithm function of x.

According to the literature, the optical bandgap values for Fe-doped ITO are generally lower than those reported for undoped ITO (4.2 eV). This reduction is correlated with the trapping of electrons at specific energy levels. These trapping centers, also known as surface trap states, are formed below the conduction band or above the valence band promoting greater exchange interaction between the electrons in the sp orbitals and the localized d electrons of the Fe atoms (CHAKRABORTY; KALEEMULLA, 2018). However, the minimum observed bandgap was 3.87 eV for the film annealed at 1.0 $\times 10^3$ mbar,and increases for the films annealed in lower vacuum levels, reaching up to 4.2 eV for the film annealed at 10^{-6} mbar. This trend correlates with the increase in charge carrier concentration, implying a Fermi level shift toward the conduction band, consistent with the Burstein–Moss model (BURSTEIN, 1954).

It is well established that the Urbach energy lies below the absorption edge of the material and is determined by structural disorder and stoichiometric imperfections. Our results show a progressive increase of the Urbach energy when the films are annealed in a higher vacuum level, as illustrated in Figure 4.6.4(b). It is attributed to the increase in energetic electronic states caused by oxygen vacancies that increase the Urbach tails.

Table 4.6.2 – Thickness (t), Transmittance (T) values at a wavelength of $\sim$ 580 nm, obtained from the fits of the transmittance spectra using the Tauc Lorentz model, and carrier concentration (n_{Hall}, resistivity (ρ), mobility (μ_{Hall}) determined from Hall effect measurements.

Pressure (mbar)	Thickness t (nm)	N_{Hall} ($\times 10^{19}$cm^{-3})	ρ ($\times 10^{-2}\Omega\cdot$cm)	μ_{Hall} cm^2/Vs	Transmittance (%)
1.0×10^{3}	478.5 ± 3.2	2.3 ± 0.2	3.60 ± 0.23	7.7 ± 1.1	97
1.1×10^{0}	470.7 ± 3.1	2.1 ± 0.3	3.59 ± 0.11	8.3 ± 1.0	95
1.1×10^{-1}	463.9 ± 2.2	3.2 ± 0.1	3.32 ± 0.05	5.9 ± 0.2	95
2.0×10^{-2}	445.3 ± 3.0	3.8 ± 0.4	2.63 ± 0.15	6.2 ± 0.9	93
1.0×10^{-5}	453.4 ± 2.5	5.3 ± 0.5	1.96 ± 0.13	6.0 ± 0.9	94
2.1×10^{-6}	464.1 ± 2.8	8.5 ± 0.7	1.81 ± 0.10	4.6 ± 0.6	93

The electrical resistivity (ρ), carrier concentration (N_{Hall}), and Hall mobility (μ_{Hall}) were measured using the Van der Pauw configuration at room temperature. As shown in Table 4.6.2, these physical parameters are clearly influenced by the vacuum pressure level during the annealing process. Figure 4.6.5 shows an increase in the carrier concentration as the vacuum level is higher, which leads to a decrease in electrical resistivity. This behavior is associated with the generation of oxygen vacancies induced by the higher vacuum levels during thermal annealing, in agreement with our previous findings (VILCA-HUAYHUA et al., 2025).

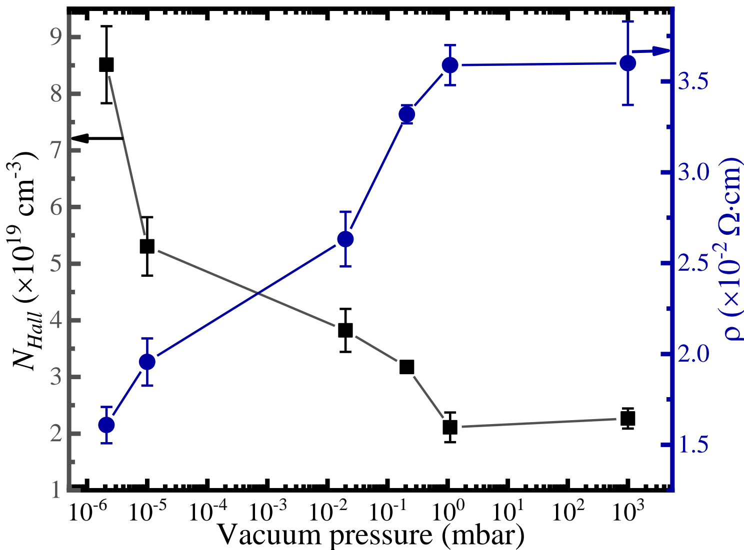

Figure 4.6.5 – Carrier concentration (N_{Hall}) and electrical resistivity (ρ) as a function of the vacuum pressure level used during the annealing of the Fe-doped ITO films.

The values of N_{Hall} obtained are around 10^{19} cm^{-3}, similar values for Fe doped ITO were obtained in the literature (SHEN et al., 2015). The relatively low carrier concentration, compared to values reported for conventional ITO 10^{20}-10^{21} (KHAN et al., 2022; HUAYHUA et al., 2025), is mainly attributed to the dominance of the Sn^{2+} oxidation state, as evidenced by XPS, in addition to the presence of Fe, Sn-O or Vo-Sn defects complexes within the ITO matrix. Iron increases the density of electron traps, which act as acceptor-type dopants, partially compensate the charge carrier provided by the oxygen vacancies and Sn^{4+} ions, thereby reducing the overall carrier density and affecting electrical conductivity, as also reported in the literature (ARAGóN et al., 2021; SHEN et al., 2015). On the other hand, the μ_{Hall} is influenced by several factors, including scattering centers, phonons, dislocations, and grain boundaries. It is commonly reported that an increase in crystallite size reduces electron scattering, thus improving Hall mobility. However, the presence of defects acts as additional scattering centers, leading to the decrease of μ_{Hall}. Our results suggest that impurities such as Fe, Sn, and oxygen vacancies (V_O) predominantly govern the electrical properties of Fe-doped ITO films causing the reduction of the μ_{Hall}.

4.6.5 Electrical properties at low temperature

On the other hand, there are several hoping conduction models that contribute to the understanding of charge transport in semiconductors, such as thermally activated conduction bandgap (TACB), nearest neighbor gap (NNH), and Mott variable range gap (Mott-VRH) (KHAN et al., 2020; BAQIAH et al., 2016). These models contributed to the electrical conduction in different temperature ranges, (see Figure 4.6.6), where the thermally activated conduction band (TACB) dominates at high temperatures (> 200 K) and NNH dominates at medium temperatures (90 K $< T < 200$ K). In general, the TACB and NNH contributions in Fe-doped ITO films can be

described by the equation:

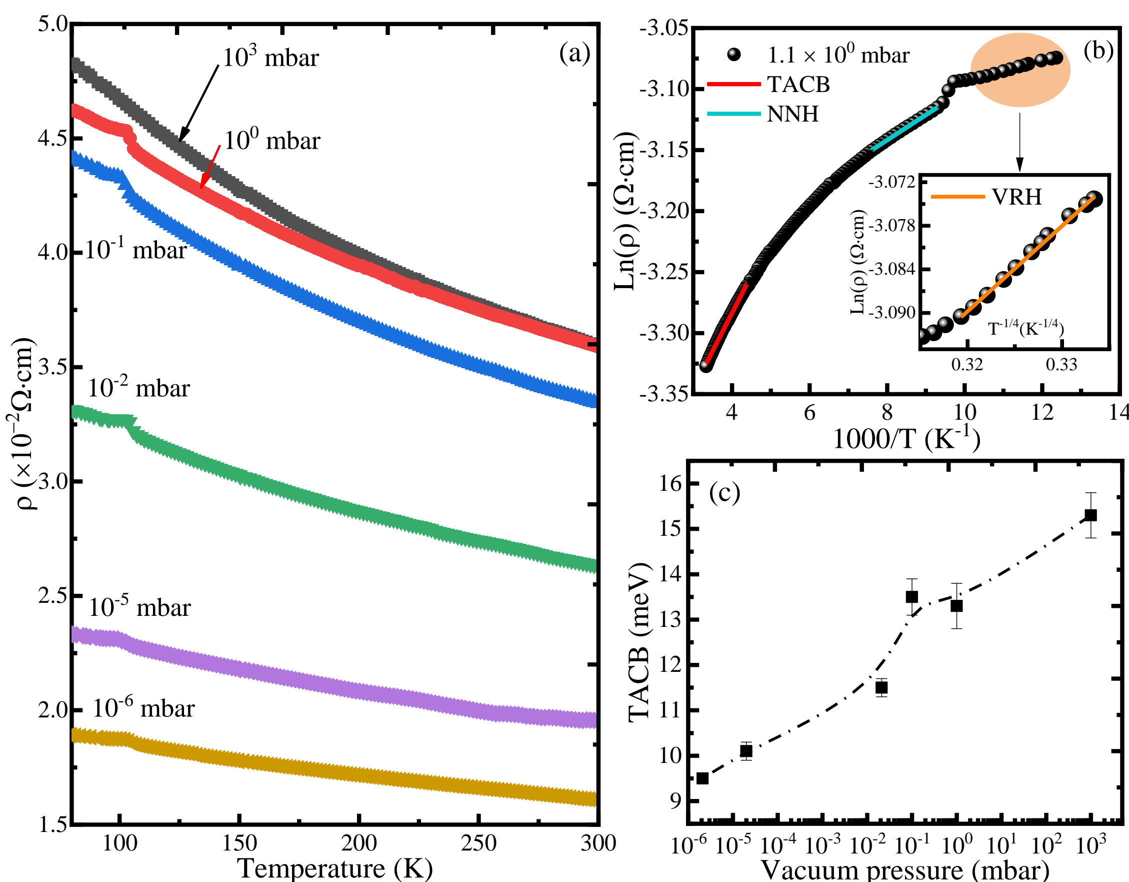

Figure 4.6.6 – (a) Resistivity measured over a temperature range of 80-300K, (b) ln ρ vs. 1000/T, the curves show the fits of the different charge transport mechanisms, the red line represents the fit of the Thermal activation conduction band (TACB), the light blue line represents the nearest neighbor hopping (NNH) behavior, the fit of the Mott-VRH model is shown in the inset of the figure. (c) TACB at vacuum annealing function.

$$\rho(T) = \rho_{01}\exp(E_{TACB}/k_B T) + \rho_{02}\exp(E_{NNH}/k_B T) \tag{91}$$

where $\rho(T)$ is the resistivity, T is the temperature, ρ_{01} and ρ_{02} is the pre-exponential factor, E_{TACB} is the thermal activation energy of the TACB contribution, E_{NNH} is the thermal activation energy of NNH contribution and k_B is the Boltzmann's constant. In order to test the validity of Equation 91, the activation energies E_{TACB} and E_{NNH}, can be obtained from the Arrhenius diagram (ln$\rho(T)$ vs. 1/T) as shown in the inset of Figure 4.6.6. NNH transport mechanism is associated with the hopping of charge carriers in localized states toward the nearest energy states within the bandgap. In the case of ITO, which has n-type charge, mainly due to the presence of Sn^{4+} and oxygen vacancies, these energy states are located near or within the conduction band (VILCA-HUAYHUA et al., 2025). However, the introduction of Fe into the ITO matrix causes new localized states within the bandgap as discussed in the optical properties, allowing some of the electrons to not participate in electrical conductivity because they cannot

move freely, requiring thermal activation to hop to the nearest neighbors. In Table 4.6.3 are presented the values obtained from the fits. As observed, the E_{TACB} value decreases with the vacuum level. This suggests that V_O donor defects seem to provoke the arising of states near the conduction band, facilitating the activation of electrons towards the conduction band. On the other hand, E_{NNH} values are below 5 meV and also decrease with the annealing in higher vacuum level. These low energy values of E_{NNH} are also obtained in the literature (KHAN et al., 2020) showing that electronic energy states become increasingly shorter, requiring less and less energy to jump to the next neighboring state, these results suggest that the increase in the density of energy states, primarily generated by oxygen vacancies, favors electron hopping and, consequently, electrical conduction.

Table 4.6.3 – Thermal activation conduction band (TACB) energy E_{TACB}, nearest neighbor hopping (NNH) activation energy E_{NNH} and Mott characteristic temperature T_{Mott} obtained from different temperature range for Fe-doped ITO films annealed at different vacuum levels.

Films	TACB		NNH		Mott-VRH	
VP (mbar)	T. range (K)	E_{TACB} (meV)	T. range (K)	E_{NNH} (meV)	T range (K)	T_{Mott} (K)
1.0×10^{3}	248-300	15.3 ± 0.5	-	-	80-110	3.52 ± 0.15
1.1×10^{0}	230-300	12.3 ± 0.5	107-130	4.3 ± 0.2	80-103	1.38 ± 0.11
2.1×10^{-1}	260-300	13.7 ± 0.4	107-137	4.6 ± 0.3	80-105	1.35 ± 0.08
2.0×10^{-2}	229-300	11.5 ± 0.2	107-145	4.2 ± 0.2	80-105	0.96 ± 0.03
1.0×10^{-5}	228-260	10.1 ± 0.2	106-135	3.0 ± 0.2	80-105	0.43 ± 0.02
2.1×10^{-6}	244-300	9.5 ± 0.3	108-130	2.6 ± 0.2	80-100	0.38 ± 0.02

The variable range hopping conductivity (VRH) was evaluated in a range of 80 - 110 K, described by the equation:

$$\rho(T) = \rho_{03} \exp(T_{Mott}/T)^{1/4} \tag{92}$$

where ρ_{03} is the value of the residual resistivity and T_{Mott} denotes the characteristic temperature of Mott. Here, electrons move by hopping between localized sites, not necessarily to the nearest neighboring state, but rather seeking the optimal site in space and energy to minimize the total energy during the hop. As observed in the Table 4.6.3, the presence of more oxygen vacancies generated by the annealing in high vacuum level is benefit to this hopping conductivity.

4.6.6 AC electrical properties

In Figure 4.6.7(a)–(b), the frequency dependence of the real (Re, Z) and imaginary $(-Im, Z)$ components of the impedance is shown, measured over a frequency range from 1 kHz to 1 MHz at room temperature. It is well known that the total impedance corresponds to the sum of all contributions from the electronic components (resistive, capacitive, and inductive), which dominate in different frequency regions.

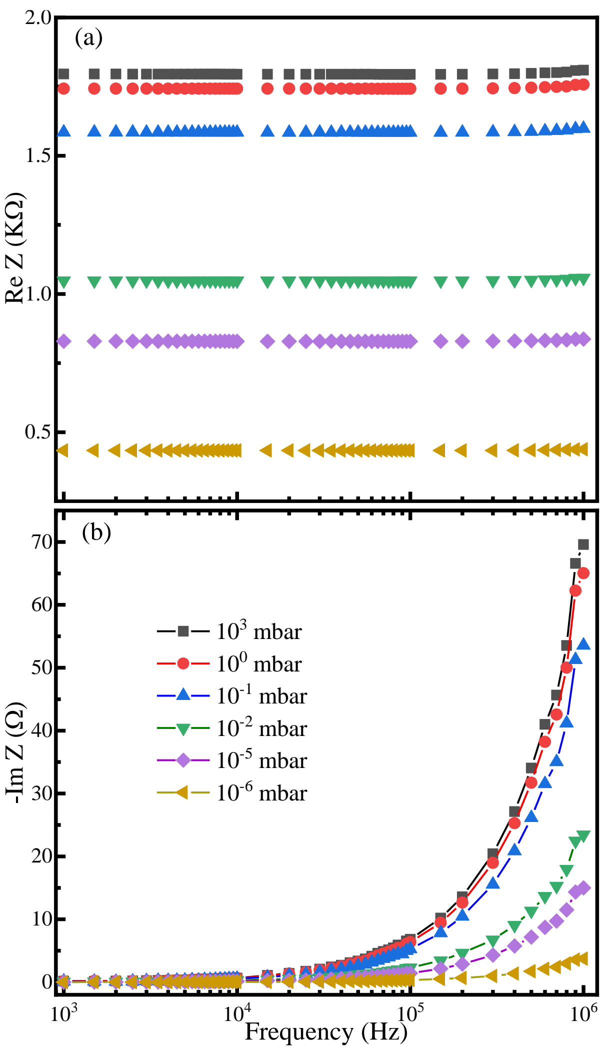

Figure 4.6.7 – (a) Frequency dependence of the Real part (Re Z) and (b) imaginary part (-Im Z) of the AC impedance, for films annealed at different vacuum pressures.

Figure 4.6.7(a) shows that the real component Re, Z does not exhibit significant variations with frequency; however, the imaginary component $-Im, Z$ displays a pronounced variation at high frequencies (> 10^5 Hz), which becomes more evident for films annealed at lower vacuum pressure levels (see Figure 4.6.7(b)). This behavior arises from the fact that inductive and capacitive reactances strongly depend on frequency. Therefore, in order to quantitatively describe these variations, the impedance curves of both the real and imaginary components were fitted using an equivalent electrical circuit, employing the EIS Spectrum Analyzer software, as shown in Figure 4.6.8(a)–(f).

At frequencies $< 10^5$ Hz, the response is capacitive (C_1) in parallel with a resistive component (R_1). The capacitance magnitude ranges from pF to nF, which is typical for bulk capacitance (IRVINE; SINCLAIR; WEST, 1990). Together with the low resistance value, it was concluded that there is no impedance barrier for charge transfer between the metallic electrode and the Fe-doped ITO film, and that the charge carriers are electrons. These low resistance and capacitance values suggest minimal interference in the charge transfer process. At high

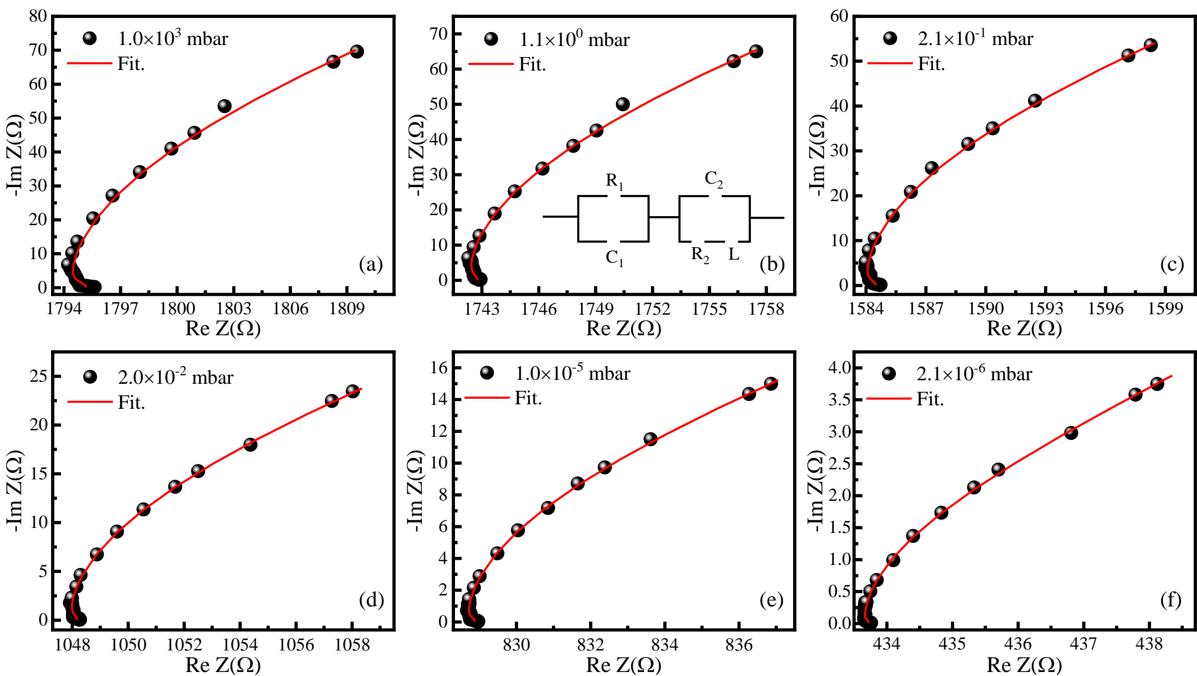

Figure 4.6.8 – (a)-(f) Nyquist plots, fitted EIS curves of ITO films annealed at different vacuum pressure. The inset of figure (b) is shown the equivalent electrical circuit.

frequencies $< 10^5$ Hz, the alternating electric field enables mobile charges to accumulate at grain boundary regions, leading to an increase in electrical resistance due to the potential barriers formed at these interfaces. These micro-potential barriers and charge clusters have a significant impact on the mechanisms governing photocurrent generation and gas sensing, as will be discussed later.

In this frequency regime, the impedance is represented by a resistive component (R_2) in series with an inductor (L); this R_2–L branch is connected in parallel with a capacitor C_2, as shown in the inset of Figure 4.6.8(b). The resistance R_2 is attributed to the resistance of the Fe-doped ITO film, which increases as the vacuum pressure decreases. This behavior is consistent with the DC electrical properties, where smaller crystallite sizes obtained from XRD measurements result in an increased density of grain boundaries, thereby enhancing the resistive nature of the films.

The capacitance values C_2 are on the order of 10^{-6} F. In addition, C_2 increases in films annealed in high vacuum levels. This behavior is consistent to the increase the carrier concentration; as evidenced by Hall measurements. However, from XPS analysis, defects associated with oxygen vacancies contribute to an increase in crystallite size. This suggests that oxygen vacancies may be localized at grain boundaries, coupling charges and leading to an increase in capacitance, as shown in Table 4.6.4. A similar behavior was reported by Li et al., which reported that the annealing under reducing atmospheres caused the migration of defect complexes toward grain boundaries, thereby improving crystallinity (LI et al., 2015).

In contrast, the inductance decreases from 28.5 μH to 7.2 μH the vacuum pressure

level of the annealing is higher. . This reduction is attributed to an increased concentration of charge carriers originating from oxygen vacancies and Sn^{4+}. Under these conditions, electrical conduction is dominated by ions moving in response to the high-frequency alternating field, as suggested in the literature (VILCA-HUAYHUA et al., 2025; HAUFF, 2019).

Table 4.6.4 – Equivalent circuit parameters obtained from the fits of the EIS data of Fe-doped ITO thin films annealed at different vacuum levels.

VP (mbar)	C_1 (pF)	C_2 (μF)	R_1 (Ω)	R_2 (Ω)	L (μH)
1.0×10^{3}	12.2	8.0	0.9	1794.3	28.5
1.1×10^{0}	12.5	11.3	0.5	1742.3	27.9
1.1×10^{-1}	13.5	12.7	0.5	1584.0	25.6
2.0×10^{-2}	18.8	24.3	0.3	1047.9	17.1
1.0×10^{-5}	22.9	47.1	0.2	828.7	13.5
2.1×10^{-6}	41.1	213.7	0.1	433.7	7.2

4.6.7 Gas sensor and Photocurrent Response

The resistance-time curves to methane gas sensing tests exhibit a characteristic behavior of an n-type semiconductor as shown in Figure 4.6.9 (a). Initially, the O_2 molecules of the atmosphere adsorbed in the surface of the Fe doped ITO films can form ionized oxygen species that, depending on the operating temperature during the sensory measurement process, oxygen can transform into three negative ions (O_2^-, O^-, and O_2^-), exhibiting a tendency to attract electrons through the following chemical reactions:

$$O_{2\,(gas)} \rightarrow O_{2\,(ads)}, \tag{93}$$

$$O_{2\,(ads)} + e^- \rightarrow O_{(ads)} \; (T < 373 \text{ K}), \tag{94}$$

$$O^-_{2\,(ads)} + e^- \rightarrow 2O^-{}_{(ads)} \; (373 \text{ K} < T < 473 \text{ K}), \tag{95}$$

$$2O^-_{2\,(ads)} + 2e^- \rightarrow 2O^{2-}{}_{(ads)} \; (T > 473 \text{ K}). \tag{96}$$

Therefore, at high temperatures, the dynamics of oxygen molecules increase, enabling them to capture more electrons from the Fe-doped ITO, thereby enhancing the formation of ionized oxygen species on the material surface. This, in turn, leads to a higher potential barrier (Schottky barrier) formed at the semiconductor grain boundaries, generating a depletion region that hinders the flow of electrons across the grain boundaries, it increases the electrical resistance. When a reducing gas such as methane (CH_4) comes into contact with the film, it interacts with the

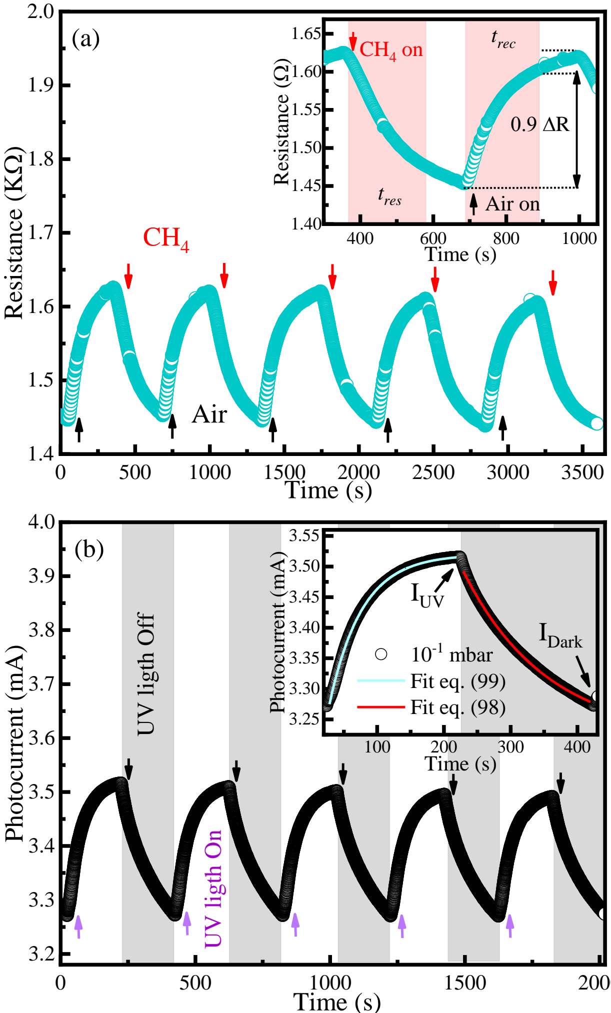

Figure 4.6.9 – (a) Methane (CH_4) gas-sensing response at an operating temperature of 200 °C. (b) Photocurrent response of the Fe-doped ITO film annealed at a pressure of 10^{-1} mbar. The UV light-off periods are represented by the gray shaded regions. The insets display the response and recovery times for gas sensing and photocurrent measurements, respectively.

ionic oxygen species on the surface of the Fe-doped ITO, transferring the trapped electrons back to the conduction band. This process leads to a reduction reaction, as described by Equation 97 at T ≥ 473 K (APARICIO-HUACARPUMA et al., 2025). Consequently, the number of charge carriers in the semiconductor increases, resulting in a decrease in electrical resistance, as expected for n-type semiconductors.

$$2CH_{4\,(gas)} + 8O^{-}{}_{(abs)} \rightarrow 2CO_2 + 4H_2O + 8e^{-} \tag{97}$$

The gas sensor response was measured by the following relation $GSR = R_{air}/R_{gas}$, where R_{air} is the maximum electrical resistance value in the presence of synthetic air and R_{gas} is the minimal electrical resistance value in the presence of the reducing gas (CH_4). The GSR values are listed in Table 4.6.5 and exhibit a dependence on the annealing vacuum pressure level,

decreasing from 1.13 to 1.05 as the vacuum pressure level of the annealing becomes higher. This sensitivity of the ITO may be influenced by several factors such as defects, crystallite size, and morphology . As the films are annealed under oxygen-rich conditions, the average crystallite size decreases, which increases the contact area of the surface of Fe-doped ITO film with the CH_4 gas. This suggests an sensing response enhancement, as shown in Figure 4.6.10. However, the Fe-doped ITO system is complex, and both extrinsic and intrinsic defects also play an important role in the variation of the GSR. To gain a deeper understanding, photocurrent measurements under UV illumination at room temperature were carried out, as will be discussed later.

The response time (t_{res}) and recovery time (t_{rec}) were obtained after analyzing the Resistance–time curves, where 90% of the resistance variation (ΔR) required to reach the maximum saturation value was considered based on the change $\Delta R = R_{Air} - R_{gas}$, as shown in the inset of Figure 4.6.9(a). The values of t_{res} and t_{rec} decrease with the annealing in high vacuum levels, as presented in Table 4.6.5. This behavior is consistent with the evolution of point defects V_O and the migration of defects induced by higher vacuum level during the annealing, which reduce t_{res} and t_{rec}. Similar results were recently reported for ZnO (SILVA et al., 2026).

Figure 4.6.9(b) shows the characteristic photocurrent curves as a function of time in the presence and absence of UV light for the film annealed at $\sim 10^{-1}$ mbar. Initially, when the UV light is switched on, the photocurrent curves increase toward positive values due to the generation of electron–hole pairs. Subsequently, when the UV light is turned off, the electron–hole pairs recombine, causing the photocurrent to decrease until it reaches its initial dark current value. The photoresponse values were calculated using the following relation (I_{UV}/I_{dark}), where I_{UV} represents the maximum photocurrent value under UV illumination and I_{dark} corresponds to the minimum value when the light is switched off. The photoresponse values for films annealed at different vacuum pressure levels are also presented in Table 4.6.5.

It is observed that the photocurrent slightly decreases as the vacuum pressure level of the annealing increases (similar to the gas sensor response). To explain the underlying physical mechanism, two main factors are considered: grain boundaries and defect states. Typically, the rapid initial increase in the photocurrent of Fe-doped ITO is attributed to the excitation of electrons from the valence band to the conduction band, leading to the formation of electron–hole pairs, $hv \longrightarrow h^+ + e^-$. In addition, excitations arising from transitions between defect states and the conduction band also contribute to the photocurrent. During the separation of photogenerated electrons and holes, it is necessary to prevent their recombination in order to increase the carrier lifetime. Therefore, to achieve an excess of photoinduced electrons, the holes must be trapped during the electron–hole pair generation process. In this context, holes can migrate toward the grain boundaries and become trapped in defect levels within the bandgap, which may hinder their recombination with the electrons. These holes swept toward the surface promote the release of adsorbed oxygen (oxygen desorption) according to the reaction $O^{2-} + h^+ \longrightarrow O_2 + e^-$, thereby releasing trapped electrons and increasing the photocurrent. In this scenario, the hole

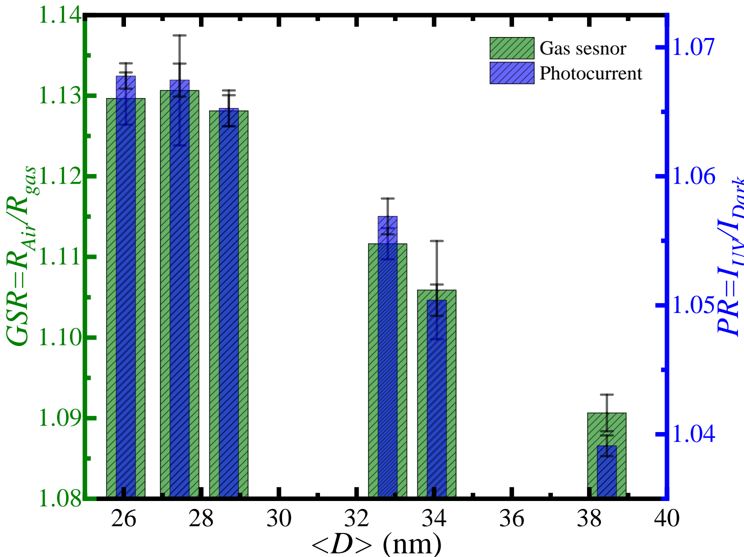

Figure 4.6.10 – Gas sensor response to methane gas and photoresponse under UV illumination as a function of the crystallite size ($< D >$) determined for the Fe-doped ITO films annealed at different vacuum pressure levels.

transported toward grain boundaries, together with a higher density of grain boundaries, reduces the immediate recombination of electron–hole pairs and plays a crucial role in the photocurrent response, as observed in Figure 4.6.10.

On the other hand, this hole migration can be enhanced by an increased density of acceptor-type defects, such as interstitial oxygen, Fe or Sn^{2+}, in degenerate systems such as ITO as discussed in the section 4.2. Consequently, a higher vacuum pressure level during the annealing process reduces these acceptor defects and promotes donor-type defects, such as Sn^{4+} and oxygen vacancies near the conduction band, which do not directly contribute to the enhancement of the photocurrent. This effect explains the lower photocurrent values observed in films annealed in higher vacuum levels.

Table 4.6.5 – Parameters of the methane gas sensing response: response time (t_{res}) and recovery time (t_{rec}); gas sensor response ($GSR = R_{air}/R_{gas}$). Photocurrent parameters: recovery times (τ_{rec}) and response times (τ_{res}); photoresponse ($PR = I_{UV}/I_{dark}$); UV-light-saturated photocurrent (I_{UV}) and saturated dark current (I_{dark}).

VP	Gas sensor			Photocurrent		
(mbar)	t_{rec} (s)	t_{res} (s)	R_{Air}/R_{Gas}	τ_{res} (s)	τ_{rec} (s)	I_{UV}/I_{Dark}
1.0×10^{3}	279.8 ± 25.1	235.5 ± 12.9	1.130	62.2 ± 1.3	151.7 ± 4.3	1.068
1.1×10^{0}	261.8 ± 14.7	223.3 ± 14.0	1.131	57.1 ± 4.2	147.9 ± 9.2	1.067
2.1×10^{-1}	246.3 ± 31.1	217.8 ± 17.5	1.128	52.2 ± 0.5	136.4 ± 4.9	1.065
2.0×10^{-2}	235.8 ± 24.7	211.3 ± 12.3	1.112	52.4 ± 0.9	128.9 ± 9.9	1.057
1.0×10^{-5}	236.7 ± 7.1	203.0 ± 14.0	1.106	43.5 ± 1.1	119.6 ± 7.1	1.050
2.1×10^{-6}	235.7 ± 12.1	212.0 ± 7.0	1.091	45.8 ± 0.6	125.6 ± 3.8	1.039

To evaluate the rise (τ_{res}) and decay times τ_{rec}, the experimental photocurrent–time data were fitted using the exponential model described by Equation 98 and Equation 99, as shown in

the inset of Figure 4.6.9(b). As observed good agreement between the model and the experimental data is obtained. In these expressions, A_0, A_1, B_0, B_1 and τ_{res}, τ_{rec} are fitting parameters; t_0; denotes the time at which the UV illumination is switched off; and τ_{res} represents the time constants associated with carrier trapping and recombination processes, as well as the response time τ_{rec}. The fitting parameters are summarized in Table 4.6.5.

It can be observed that the response times τ_{rec} are longer than the recovery times τ_{rev}, indicating a slow decay of the photocurrent after the UV light is turned off. This behavior can be attributed to the slow surface re-adsorption process of oxygen molecules, caused by the presence of traps and recombination centers on the surface of Fe-doped ITO.

$$I(t)_{Recovery} = A_0 + B_0 \exp(-(t + t_0)/\tau) \tag{98}$$

$$I(t)_{Response} = A_1 + B_1(1 - \exp(-(t + t_0)/\tau_R)) \tag{99}$$

4.6.8 Magnetic properties

Figure 4.6.11(a) shows the magnetic M–H curves for Fe-doped ITO thin films annealed at different vacuum levels. As observed in the magnetic measurements performed at 2 K, the samples exhibit a strong paramagnetic (PM) behavior. This PM contribution outweighs the weak ferromagnetic (FM) contribution observed at 300 K (see Table 4.6.6(a)). Therefore, an initial analysis of the 2K M–H data was carried out by considering only the PM contribution, fitting the data using the Brillouin function:

$$M(H,T) \;=\; M_S\, B_S(y) \;+\; \chi_0\, H \tag{100}$$

$$B_S(y) \;=\; \frac{2S+1}{2S}\coth\left(\frac{2S+1}{2S}y\right) - \frac{1}{2S}\coth\left(\frac{y}{2S}\right) \tag{101}$$

$$y \;=\; \frac{g\,\mu_B\, S\,\mu_0 H}{k_B\,(T - T_0)} \tag{102}$$

where M_S is the saturation magnetization, which defines the maximum contribution of the localized Fe magnetic moments to the total magnetization. $B_S(y)$ is the Brillouin function S, describing the spin angular moment of the iron-ions. The argument y is a dimensionless parameter that incorporates the Landé g-factor, the Bohr magneton μ_B, the applied magnetic field H, and the thermal energy $k_B(T - T_0)$, where T_0 is a phenomenological parameter. The inclusion of T_0 allows the model to account for short range magnetic correlations, with positive (negative) values suggesting predominant ferromagnetic (antiferromagnetic) correlations. The χ_0, represents the temperature-independent susceptibility contribution, as in the case of Pauli or

Van Vleck paramagnetism. In Figure 4.6.11(a), the red continuous line represents the fit obtained using Equation 100. The results obtained from the fits are presented in Table 4.6.6.

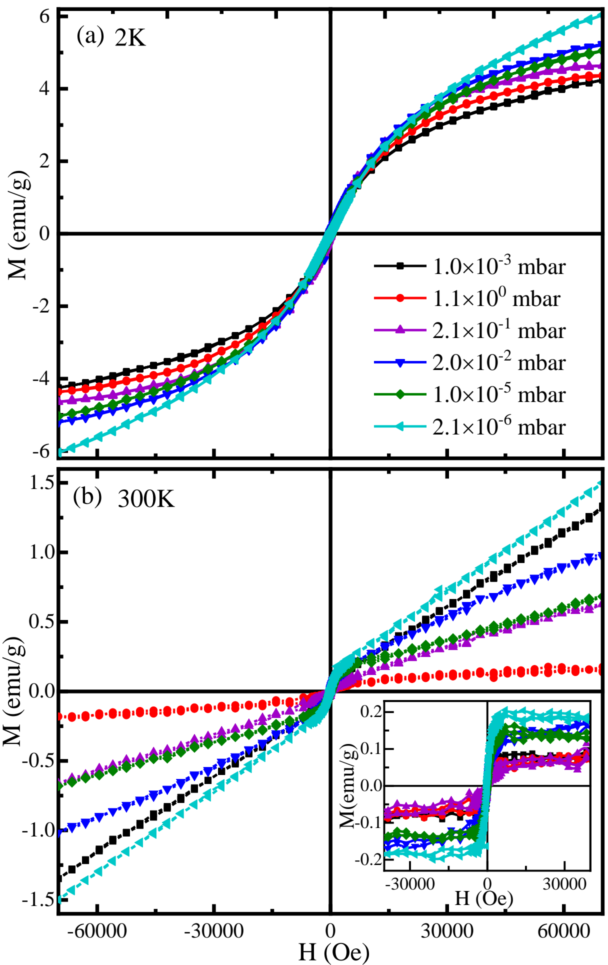

Figure 4.6.11 – Magnetic moment as a function of the applied external magnetic field (H) for Fe-doped ITO films annealed at different vacuum levels, (a) 2 K, inset coercive field, and (b) 300K, inset ferromagnetic contribution curves at room temperature.

From the data fit using Equation 100, it was evidenced that the Fe ions are predominantly in the 3+ oxidation state, as indicated by the S value being close to the theoretical value of $S = 5/2$. In order to determine the fraction of paramagnetic (x_{PM}) ions incorporated into the ITO matrix, the following relation $\mu_{f.u.}(\mu_B/f.u.) = M_S M_{mol}/N_A\mu_B$ was used, where N_A is Avogadro's number, μ_B the Bohr magneton, and M_{mol} the molar mass of the compound. Assuming here that the magnetization arises only from Fe ions substituting In sites, each one contributing with a theoretical moment of $\mu_{Fe}^{theor} = 5\mu_B$, the paramagnetic fraction of Fe was estimated. The obtaining values are in a range of approximately 0.031-0.037. In addition, the positive values of T_0 suggest the presence of weak ferromagnetic correlations, which seems to increase as the vacuum level of the films becomes higher, as shown in Table 4.6.6.

From the M–H curves measured at 300 K, the coexistence of strong paramagnetism with a weak ferromagnetism is observed (see Figure 4.6.11(b)). Therefore, in order to study

the ferromagnetic behavior at room temperature, the paramagnetic contribution was removed, as shown in the inset of Figure 4.6.11(b). The x_{FM} was estimated from the following relation: $x_{FM} = M_S M_{mol}/N_a \mu_B \mu^{Fe}$. In order to determine the Fe concentration, the ferromagnetic fraction (x_{FM}) were added to the paramagnetic fraction of Fe ions (x_{PM}), yielding a total Fe concentration diluted within the ITO matrix of 3.2~3.8%, which is consistent with the values obtained by EDS, as shown in Table 4.6.6.

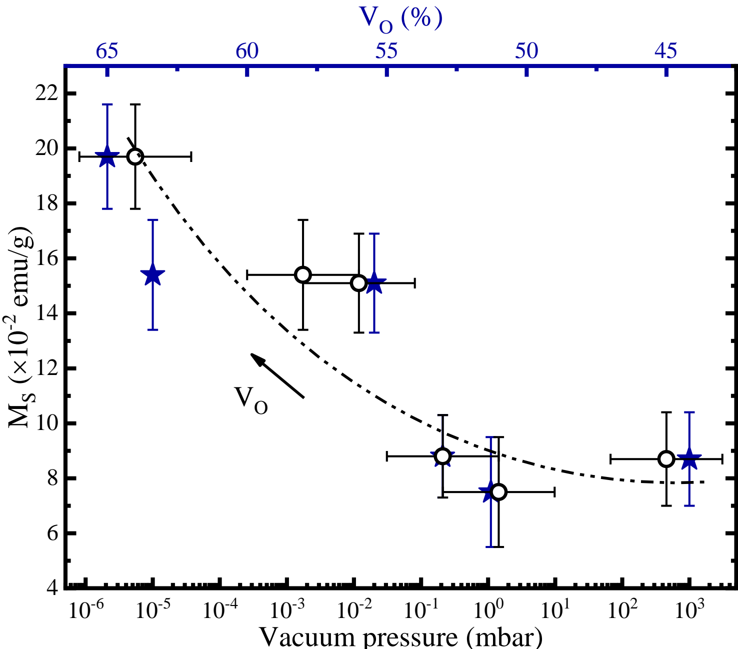

Figure 4.6.12 – Saturation magnetization (M_S) at 300 K as a function of vacuum pressure level used for the annealing process (bottom axis) and oxygen vacancy concentration (top axis) determined from XPS analysis.

Table 4.6.6 – Parameters obtained from the fit of M vs. H curves to the Brilloiun function, M_S (2K) is the saturation magnetization at 2K, temperature independent susceptibility (χ_0), spin angular moment (S), interaction temperature (T_0), fraction paramagnetic of Fe (x_{PM}), M_S (300K) is the saturation magnetization at 300K, fraction ferromagnetic Fe ions (x_{FM}) for the Fe-doped ITO films.

VP (mbar)	M_S (2K) (emu/g)	χ_0 (10^{-5}emu/gOe)	S	T_0 (K)	x_{PM} (%)	x_{FM} (%)	x_{EDS} (%)	M_S (300K) (10^{-2}emu/g)
1.0×10^{3}	3.2±0.7	2.9 ± 0.2	2.51	0.19	3.1 ± 0.1	0.08 ± 0.02	3.7	8.7±1.7
1.1×10^{0}	3.6±0.3	2.3 ± 0.3	2.49	0.18	3.5 ± 0.2	0.07 ± 0.01	-	7.5±2.0
2.1×10^{-1}	3.4±0.5	2.4 ± 0.4	2.50	0.30	3.3 ± 0.3	0.09 ± 0.02	-	8.8±1.5
2.0×10^{-2}	3.8±0.8	3.1 ± 0.3	2.51	0.21	3.7 ± 0.2	0.15 ± 0.03	-	15.1±1.8
1.0×10^{-5}	3.6±0.2	3.0 ± 0.2	2.52	0.35	3.5 ± 0.2	0.15 ± 0.03	-	15.4±2.0
2.1×10^{-6}	3.2±0.9	8.1 ± 0.2	2.54	0.65	3.2 ± 0.1	0.19 ± 0.02	-	19.7±1.9

The saturation magnetization of the ferromagnetic contribution (M_S) obtained for the film annealed at a pressure of 10^3 mbar was 0.087 emu/g. It is determined that the M_S increases with the vacuum level during thermal annealing, reaching 0.197 emu/g for the film annealed

at 10^{-6} mbar. Additionally, this behavior is accompanied by an increase in the oxygen vacancy density, as observed in Figure 4.6.12. Therefore, due to the absence of secondary phases as evidenced by XRD, we suggest that the weak ferromagnetism is intrinsic and is induced by the presence of oxygen vacancies and Fe ions in the semiconducting matrix. Several models have been proposed in the literature to explain this ferromagnetism, the most common being spin-polarized carrier-mediated exchange (RKKY) and/or bound magnetic polaron formation, particularly for systems with low concentrations of magnetic ions. However, due to the low charge carrier concentration obtained for Fe-doped ITO $\sim 10^{19}$ cm^{-3} (see Table 4.6.6), the ferromagnetism is likely to be predominantly influenced by the formation of F centers, consisting of oxygen vacancies that trap an electron and form V_O–Fe complexes. Based on Hund's rule and the Pauli exclusion principle, the spin of the trapped electrons and the neighboring Fe ions must align, leading to the room-temperature ferromagnetism (RTFM). These oxygen vacancies are favored by increasing the vacuum level, enhancing long-range interactions. This demonstrates that RTFM can be tuned by controlling the vacuum levels during annealing.

4.6.9 Conclusion

In this work, the effect of annealing under different vacuum levels on the optoelectronic, magnetic, and sensing properties of Fe-doped ITO thin films prepared by RF magnetron sputtering was systematically investigated. X-ray diffraction analyses confirmed the formation of a single-phase cubic bixbyite structure. UV–Vis measurements revealed optical transmittance values exceeding 90%, together with a wide optical bandgap that increases for films annealed in higher vacuum level, which was attributed to the increase of charge carrier concentration related to oxygen vacancies, as evidenced by XPS and Hall measurements. The presence of oxygen vacancies interacting with Fe atoms leads to an increase in the Urbach energy. Magnetization measurements indicate a predominantly paramagnetic behavior with a weak ferromagnetic contribution at room temperature; this ferromagnetism is associated with oxygen vacancies forming bound magnetic polarons. Furthermore, photocurrent and methane gas sensing measurements exhibit typical n-type semiconductor behavior, where films annealed at lower vacuum level show higher sensor response values due to their larger surface area and the presence of acceptor-type defects. Finally, temperature-dependent resistivity measurements performed in the range of 80–300 K reveal semiconducting behavior for all films.

5

General conclusions

In this thesis work, we present a systematic study on the control and manipulation of intrinsic and extrinsic defects and their influence on the physical properties of Sn- and Fe-doped In_2O_3 thin films. The defect engineering was achieved through precise control of film thickness, Sn concentration, annealing temperature, vacuum level of the annealing, and Fe incorporation. The Sn-doped In_2O_3 films were grown by DC sputtering using high-purity metallic targets fabricated at the LSNCM laboratory. The Sn concentration was successfully controlled while preserving the In_2O_3 matrix. At a Sn concentration of ~10%, the films exhibited enhanced electrical and optical properties. Subsequently, these properties were optimized by varying the vacuum pressure during the thermal annealing process. High-vacuum annealing conditions were found to promote the generation of intrinsic defects associated with oxygen vacancies and the removal of interstitial oxygen, thereby activating Sn^{4+} donors and increasing the carrier concentration of ITO films. This process also induced a widening of the optical band gap up to 4.2 eV, in agreement with the Burstein–Moss model. These experimental findings are consistent with the theoretical calculations obtained by DFT. Furthermore, it was demonstrated that reducing the film thickness to ~200 nm resulted in a maximum carrier concentration (~10^{21} cm^{-3}), which is comparable to or even an exceeding value when compared to reported values for commercial ITO. In contrast, this high carrier concentration provokes the shift of the metal–semiconductor transition temperature from 146 to 109 K.

Films annealed at temperatures below to 500 °C exhibited the coexistence of oxygen vacancies and Sn^{2+} species and provoked the enhancement of the photocurrent response. Additionally, it was determined that for Sn concentrations above ~10%, interstitial oxygen defects became more prominent. These defects improved methane gas sensitivity and photocurrent performance, showing an strong dependence on the surface area and acceptor-type defects states. On the other hand, the Fe incorporation modified both the optical and electrical properties, leading to anomalous low-temperature resistivity behavior and the emergence of room-temperature ferromagnetism. This magnetic behavior was controlled by adjusting the vacuum level during

thermal annealing. It was observed that the saturation magnetization at 300 K increased with the oxygen vacancy concentration, suggesting that the ferromagnetism is intrinsic and likely related to bound magnetic polarons (BMPs). Moreover, annealings carried out below 500 °C under vacuum optimized the room-temperature ferromagnetic properties, achieving a maximum magnetization value of 0.64 emu/g. This enhancement can be attributed to the generation of single-electron occupied oxygen vacancies near Fe ions, which favors the percolation of BMPs, enabling long-range magnetic interactions. Overall, this research contributes to the advancement of defect-mediated engineering of magneto-optoelectronic properties in Fe-doped ITO systems.

6

Future works

Based on the results obtained in this thesis, the presence of interstitial oxygen in the ITO structure constitutes a defect that deserves further investigation. Additional characterization techniques, such as photoluminescence (PL) spectroscopy, would help to corroborate the presence of these defects, thereby enabling optimization of growth parameters and the improved control over the formation of intrinsic defects. Low-temperature resistivity measurements (approaching 2 K) would be necessary to carefully investigate the metal–semiconductor transitions and the anomalous transport behavior observed in Fe-doped ITO systems. Such studies would allow for a more accurate evaluation of quantum corrections.

Additional, conversion electron Mössbauer spectroscopy (CEMS) measurements, employing both ^{119}Sn and ^{57}Fe sources measurements would be required to obtain the hyperfine interactions in order to determine the site occupancy of Sn and Fe ions at the b and d crystallographic sites. Depending on the specific location of the Fe atoms within the lattice, their presence may significantly influence the environment of both Sn and Fe, and consequently the magnetic properties. Furthermore, the incorporation of other transition metals or rare-earth elements into the ITO matrix, at varying concentrations, should be explored to systematically study the rising of room-temperature ferromagnetism. These experimental efforts should be complemented by computational modeling to provide a comprehensive understanding of the magnetic interaction mechanisms, charge carrier dynamics, and intrinsic defect states, thereby enabling the prediction, optimization, and manipulation of the physical properties of ITO.

Additionally, gas-sensing measurements under different gas atmospheres would be necessary to evaluate the influence of the defects on the oxidation-reduction process, as well as to assess the sensor selectivity. Such studies would contribute to the development of multifunctional devices that combine the magnetic and electrical properties of doped ITO thin films for applications in sensors and photodetectors.

Bibliography

AFRE, R. A. et al. Transparent conducting oxide films for various applications: A review. *REVIEWS ON ADVANCED MATERIALS SCIENCE*, Walter de Gruyter GmbH, v. 53, n. 1, p. 79–89, jan. 2018. ISSN 1605-8127. Disponível em: <http://dx.doi.org/10.1515/rams-2018-0006>. Citado na página 34.

AGRAWAL, N.; SARKAR, M.; GANESAN, V. Low temperature anomalies and room temperature magnetism in in0.95fe0.05sb dilute magnetic semiconducting film. *Journal of Applied Physics*, AIP Publishing, v. 126, n. 21, dez. 2019. ISSN 1089-7550. Disponível em: <http://dx.doi.org/10.1063/1.5126297>. Citado na página 149.

AHMED, M. et al. The main role of thermal annealing in controlling the structural and optical properties of ito thin film layer. *Optical Materials*, Elsevier BV, v. 113, p. 110866, mar. 2021. ISSN 0925-3467. Disponível em: <http://dx.doi.org/10.1016/j.optmat.2021.110866>. Citado na página 129.

APARICIO-HUACARPUMA, B. et al. Influence of the thickness effect on the structural, morphological, vibrational, optical, electrical and gas sensor properties of polycrystalline cuo films. *Journal of Alloys and Compounds*, Elsevier BV, v. 1014, p. 178681, fev. 2025. ISSN 0925-8388. Disponível em: <http://dx.doi.org/10.1016/j.jallcom.2025.178681>. Citado na página 172.

APARICIO-HUACARPUMA, B. D. et al. Thickness dependence of the room-temperature ethanol sensor properties of cu2o polycrystalline films. *Nanotechnology*, IOP Publishing, v. 35, n. 32, p. 325705, maio 2024. ISSN 1361-6528. Disponível em: <http://dx.doi.org/10.1088/1361-6528/ad47cc>. Citado na página 81.

ARAGÓN, F. H. et al. Structural and surface study of praseodymium-doped sno2 nanoparticles prepared by the polymeric precursor method. *The Journal of Physical Chemistry C*, American Chemical Society, v. 119, n. 16, p. 8711–8717, Apr 2015. ISSN 1932-7447. Disponível em: <https://doi.org/10.1021/acs.jpcc.5b00761>. Citado 2 vezes nas páginas 70 and 86.

ARAGóN, F. et al. Characterization of polycrystalline sno2 films deposited by dc sputtering technique with potential for technological applications. *Journal of the European Ceramic Society*, Elsevier BV, v. 37, n. 10, p. 3375–3380, ago. 2017. ISSN 0955-2219. Disponível em: <http://dx.doi.org/10.1016/j.jeurceramsoc.2017.04.014>. Citado na página 133.

ARAGóN, F. et al. Fe content effects on structural, electrical and magnetic properties of fe-doped ito polycrystalline powders. *Journal of Alloys and Compounds*, Elsevier BV, v. 867, p. 158866, jun. 2021. ISSN 0925-8388. Disponível em: <http://dx.doi.org/10.1016/j.jallcom.2021.158866>. Citado 3 vezes nas páginas 31, 144, and 166.

ARAGóN, F. H. et al. Fe doping effect on the structural, magnetic and surface properties of sno2 nanoparticles prepared by a polymer precursor method. *Journal of Physics D: Applied Physics*, IOP Publishing, v. 49, n. 15, p. 155002, mar 2016. Disponível em: <https://doi.org/10.1088/0022-3727/49/15/155002>. Citado na página 153.

ASADIAN, Z.; BAKOUEI, A.; GHAMSARI, M. S. Sol–gel derived ito thin films with (400) preferred orientation. *Discover Materials*, Springer Science and Business Media LLC, v. 6, n. 1, fev. 2026. ISSN 2730-7727. Disponível em: <http://dx.doi.org/10.1007/s43939-026-00565-y>. Citado na página 31.

BABU, S. H. et al. Indium oxide: A transparent, conducting ferromagnetic semiconductor for spintronic applications. *Journal of Magnetism and Magnetic Materials*, Elsevier BV, v. 416, p. 66–74, out. 2016. ISSN 0304-8853. Disponível em: <http://dx.doi.org/10.1016/j.jmmm.2016.05.007>. Citado na página 35.

BADGUJAR, A. C. et al. Room temperature sputtered aluminum-doped zno thin film transparent electrode for application in solar cells and for low-band-gap optoelectronic devices. *ACS Omega*, American Chemical Society (ACS), v. 7, n. 16, p. 14203–14210, abr. 2022. ISSN 2470-1343. Disponível em: <http://dx.doi.org/10.1021/acsomega.2c00830>. Citado na página 74.

BAQIAH, H. et al. Physical properties of fe doped in2o3 magnetic semiconductor annealed in hydrogen at different temperature. *Journal of Magnetism and Magnetic Materials*, Elsevier BV, v. 401, p. 102–107, mar. 2016. ISSN 0304-8853. Disponível em: <http://dx.doi.org/10.1016/j.jmmm.2015.10.013>. Citado na página 166.

BARDEEN, J.; SHOCKLEY, W. Deformation potentials and mobilities in non-polar crystals. *Physical Review*, American Physical Society (APS), v. 80, n. 1, p. 72–80, out. 1950. ISSN 0031-899X. Disponível em: <http://dx.doi.org/10.1103/PhysRev.80.72>. Citado na página 40.

BINCZYCKA, H. et al. Hyperfine interactions and site occupancy in sn-doped in2o3 (ito). *physica status solidi (b)*, Wiley, v. 242, n. 5, p. 1100–1107, mar. 2005. ISSN 1521-3951. Disponível em: <http://dx.doi.org/10.1002/pssb.200402129>. Citado 3 vezes nas páginas 10, 65, and 67.

BLAIR, S. F. J. et al. Photonic characterisation of indium tin oxide as a function of deposition conditions. *Nanomaterials (Basel)*, v. 13, n. 13, jun. 2023. Citado na página 142.

BLöCHL, P. E. Projector augmented-wave method. *Physical Review B*, American Physical Society (APS), v. 50, n. 24, p. 17953–17979, dez. 1994. ISSN 1095-3795. Disponível em: <http://dx.doi.org/10.1103/physrevb.50.17953>. Citado 2 vezes nas páginas 64 and 119.

BREWER, S. H.; F, S. Calculation of the electronic and optical properties of indium tin oxide by density functional theory. *Chemical Physics*, Elsevier BV, v. 300, n. 1–3, p. 285–293, maio 2004. ISSN 0301-0104. Disponível em: <http://dx.doi.org/10.1016/j.chemphys.2003.11.039>. Citado 4 vezes nas páginas 18, 115, 116, and 136.

BURSTEIN, E. Anomalous optical absorption limit in insb. *Physical Review*, American Physical Society (APS), v. 93, n. 3, p. 632–633, fev. 1954. ISSN 0031-899X. Disponível em: <http://dx.doi.org/10.1103/PhysRev.93.632>. Citado 2 vezes nas páginas 105 and 165.

CALDERóN, M.; SARMA, S. D. Theory of carrier mediated ferromagnetism in dilute magnetic oxides. *Annals of Physics*, Elsevier BV, v. 322, n. 11, p. 2618–2634, nov. 2007. ISSN 0003-4916. Disponível em: <http://dx.doi.org/10.1016/j.aop.2007.01.010>. Citado na página 154.

CHAKRABORTY, D.; KALEEMULLA, S. No signature of room temperature ferromagnetism in fe-doped ito thin films. *Journal of Superconductivity and Novel Magnetism*, Springer Science and Business Media LLC, v. 32, n. 3, p. 729–737, jun. 2018. ISSN 1557-1947. Disponível em: <http://dx.doi.org/10.1007/s10948-018-4745-1>. Citado na página 165.

CHAKRABORTY, D. et al. Influence of surface spin alignment and f-centers on the magnetic behavior of ib thin films. *Journal of Superconductivity and Novel Magnetism*, Springer Science and Business Media LLC, v. 33, n. 7, p. 2043–2050, fev. 2020. ISSN 1557-1947. Disponível em: <http://dx.doi.org/10.1007/s10948-020-05460-y>. Citado 2 vezes nas páginas 31 and 32.

CHAKRABORTY, D. et al. Synthesis and characterization of fe doped ito nanoparticles. In: *THE 1ST INTERNATIONAL CONFERENCE ON PHYSICS AND APPLIED PHYSICS (THE 1ST ICP&AP) 2019: Fundamental and Innovative Research for Improving Competitive Dignified Nation and Industrial Revolution 4.0*. AIP Publishing, 2020. v. 2221, p. 110001. ISSN 0094-243X. Disponível em: <http://dx.doi.org/10.1063/5.0003080>. Citado na página 144.

CHAUHAN, R. N.; ANAND, R.; KUMAR, J. Structural, electrical and optical properties of radio frequency sputtered indium tin oxide thin films modified by annealing in silicon oil and vacuum. *Thin Solid Films*, Elsevier BV, v. 556, p. 253–259, abr. 2014. ISSN 0040-6090. Disponível em: <http://dx.doi.org/10.1016/j.tsf.2014.02.023>. Citado na página 127.

CHEN, A. et al. A new investigation of oxygen flow influence on ito thin films by magnetron sputtering. *Solar Energy Materials and Solar Cells*, Elsevier BV, v. 120, p. 157–162, jan. 2014. ISSN 0927-0248. Disponível em: <http://dx.doi.org/10.1016/j.solmat.2013.08.036>. Citado 3 vezes nas páginas 31, 113, and 135.

CHEN, Z. et al. Electronic structures and transport properties of n-type-doped indium oxides. *The Journal of Physical Chemistry C*, American Chemical Society (ACS), v. 119, n. 9, p. 4789–4795, fev. 2015. ISSN 1932-7455. Disponível em: <http://dx.doi.org/10.1021/jp5104164>. Citado 4 vezes nas páginas 18, 99, 113, and 136.

CHEN, Z. et al. Increased photocurrent of cuwo4 photoanodes by modification with the oxide carbodiimide sn2o(ncn). *Dalton Transactions*, Royal Society of Chemistry (RSC), v. 49, n. 11, p. 3450–3456, 2020. ISSN 1477-9234. Disponível em: <http://dx.doi.org/10.1039/C9DT04752B>. Citado na página 71.

COEY, J. M. D.; VENKATESAN, M.; FITZGERALD, C. B. Donor impurity band exchange in dilute ferromagnetic oxides. *Nature Materials*, Springer Science and Business Media LLC, v. 4, n. 2, p. 173–179, jan. 2005. ISSN 1476-4660. Disponível em: <http://dx.doi.org/10.1038/nmat1310>. Citado 2 vezes nas páginas 52 and 153.

CORSO, A. D. Pseudopotentials periodic table: From h to pu. *Computational Materials Science*, v. 95, p. 337–350, 2014. Citado na página 99.

DAMSHEKAN, Z.; MOGHIM, I.; BAHROLOLOOM, M. E. Preparation of porous indium tin oxide thin films via saccharin aided sol gel process for carbon monoxide gas sensing applications. *Journal of Materials Science: Materials in Electronics*, Springer Science and Business Media LLC, v. 34, n. 11, abr. 2023. ISSN 1573-482X. Disponível em: <http://dx.doi.org/10.1007/s10854-023-10261-9>. Citado na página 30.

DEY, A. Semiconductor metal oxide gas sensors: A review. *Materials Science and Engineering: B*, Elsevier BV, v. 229, p. 206–217, mar. 2018. ISSN 0921-5107. Disponível em: <http://dx.doi.org/10.1016/j.mseb.2017.12.036>. Citado na página 54.

DIETL, T. et al. Zener model description of ferromagnetism in zinc-blende magnetic semiconductors. *science*, American Association for the Advancement of Science, v. 287, n. 5455, p. 1019–1022, 2000. Citado na página 51.

DIXON, S. C. et al. n-type doped transparent conducting binary oxides: an overview. *Journal of Materials Chemistry C*, Royal Society of Chemistry (RSC), v. 4, n. 29, p. 6946–6961, 2016. ISSN 2050-7534. Disponível em: <http://dx.doi.org/10.1039/C6TC01881E>. Citado na página 34.

DOLGONOS, A.; MASON, T. O.; POEPPELMEIER, K. R. Direct optical band gap measurement in polycrystalline semiconductors: A critical look at the tauc method. *Journal of Solid State Chemistry*, Elsevier BV, v. 240, p. 43–48, ago. 2016. ISSN 0022-4596. Disponível em: <http://dx.doi.org/10.1016/j.jssc.2016.05.010>. Citado 2 vezes nas páginas 106 and 131.

DONG, W. J. et al. Effect of ultraviolet–ozone on ito/p3ht interface for pedot:pss-free polymer solar cells. *Solar Energy Materials and Solar Cells*, Elsevier BV, v. 109, p. 240–245, fev. 2013. ISSN 0927-0248. Disponível em: <http://dx.doi.org/10.1016/j.solmat.2012.10.023>. Citado na página 86.

EFAFI, B. et al. Aluminum doped zno sol–gel derived nanocrystals: Raman spectroscopy and solid solubility characterization. *physica status solidi (a)*, Wiley, v. 211, n. 10, p. 2426–2430, jun. 2014. ISSN 1862-6319. Disponível em: <http://dx.doi.org/10.1002/pssa.201431075>. Citado na página 34.

EFFECT of working pressure on Sn/In composition and optoelectronic properties of ITO films prepared by high power impulse magnetron sputtering. *Vacuum*, v. 196, p. 110762, 2022. ISSN 0042-207X. Citado na página 125.

EL Gana, L. et al. Iron doping effects on the structural, optical, magnetic, and photocatalytic properties of spray-deposited cerium oxide thin films. *Ceramics International*, v. 51, n. 4, p. 4206–4216, 2025. ISSN 0272-8842. Citado na página 144.

ELLMER, K.; MIENTUS, R. Carrier transport in polycrystalline transparent conductive oxides: A comparative study of zinc oxide and indium oxide. *Thin Solid Films*, Elsevier BV, v. 516, n. 14, p. 4620–4627, maio 2008. ISSN 0040-6090. Disponível em: <http://dx.doi.org/10.1016/j.tsf.2007.05.084>. Citado na página 41.

ELSHARAWY, A. I. et al. Transition-metal blends incorporated into cuo nanostructures: Tuning of room temperature spin-ferromagnetic order. *Solid State Sciences*, Elsevier BV, v. 139, p. 107166, maio 2023. ISSN 1293-2558. Disponível em: <http://dx.doi.org/10.1016/j.solidstatesciences.2023.107166>. Citado na página 35.

ENRIQUE, L. A. et al. Revisiting the optoelectronic properties of sputtered aluminium-doped zinc oxide: a study combining advanced optical dispersion models. *Journal of Physics D: Applied Physics*, IOP Publishing, v. 58, n. 9, p. 095104, jan. 2025. ISSN 1361-6463. Disponível em: <http://dx.doi.org/10.1088/1361-6463/ada168>. Citado 2 vezes nas páginas 129 and 142.

ERHART, P. et al. Band structure of indium oxide: Indirect versus direct band gap. *Physical Review B*, American Physical Society (APS), v. 75, n. 15, abr. 2007. ISSN 1550-235X. Disponível em: <http://dx.doi.org/10.1103/PhysRevB.75.153205>. Citado na página 81.

FENG, Y. et al. Effects of sn doping content on the structure, morphology, optical and electrical properties of ito thin films prepared by microwave-assisted spray pyrolysis. *RSC Advances*, Royal Society of Chemistry (RSC), v. 16, n. 8, p. 7538–7548, 2026. ISSN 2046-2069. Disponível em: <http://dx.doi.org/10.1039/D5RA09041E>. Citado na página 30.

FEREIDOONI, M. et al. On the co2 photocatalytic reduction over indium tin oxide (ito) ultra-thin films in water vapor: Experimental and theoretical study. *Fuel*, Elsevier BV, v. 349, p. 128652, out. 2023. ISSN 0016-2361. Disponível em: <http://dx.doi.org/10.1016/j.fuel.2023.128652>. Citado na página 31.

FERNANDES, M. et al. Photocurrent multiplication in ito/siox/si optical sensors. *Vacuum*, Elsevier BV, v. 65, n. 1, p. 67–71, fev. 2002. ISSN 0042-207X. Disponível em: <http://dx.doi.org/10.1016/S0042-207X(01)00407-9>. Citado na página 54.

FRANK, G.; KöSTLIN, H. Electrical properties and defect model of tin-doped indium oxide layers. *Applied Physics A Solids and Surfaces*, Springer Science and Business Media LLC, v. 27, n. 4, p. 197–206, abr. 1982. ISSN 1432-0630. Disponível em: <http://dx.doi.org/10.1007/BF00619080>. Citado 5 vezes nas páginas 30, 73, 83, 107, and 121.

FUKUMURA, T. et al. Exploration of oxide-based diluted magnetic semiconductors toward transparent spintronics. *Applied Surface Science*, Elsevier BV, v. 223, n. 1–3, p. 62–67, fev. 2004. ISSN 0169-4332. Disponível em: <http://dx.doi.org/10.1016/S0169-4332(03)00898-5>. Citado na página 37.

GHEIDARI, A. M. et al. Effect of sputtering pressure and annealing temperature on the properties of indium tin oxide thin films. *Materials Science and Engineering: B*, Elsevier BV, v. 136, n. 1, p. 37–40, jan. 2007. ISSN 0921-5107. Disponível em: <http://dx.doi.org/10.1016/j.mseb.2006.08.058>. Citado na página 122.

GHOSH, S.; BASAK, D. Correlation between hall mobility and optical mobility in aluminum-doped zno films via boundary scatterings and estimation of donor compensation ratio. *physica status solidi (b)*, Wiley, v. 257, n. 5, dez. 2019. ISSN 1521-3951. Disponível em: <http://dx.doi.org/10.1002/pssb.201900682>. Citado na página 108.

GIANNOZZI, P. et al. Quantum espresso: a modular and open-source software project for quantum simulations of materials. *Journal of Physics: Condensed Matter*, IOP Publishing, v. 21, n. 39, p. 395502, set. 2009. ISSN 1361-648X. Disponível em: <http://dx.doi.org/10.1088/0953-8984/21/39/395502>. Citado 2 vezes nas páginas 99 and 119.

GONZáLEZ, G. B. et al. Neutron diffraction study on the defect structure of indium–tin–oxide. *Journal of Applied Physics*, AIP Publishing, v. 89, n. 5, p. 2550–2555, mar. 2001. ISSN 1089-7550. Disponível em: <http://dx.doi.org/10.1063/1.1341209>. Citado 3 vezes nas páginas 30, 73, and 106.

GRECZYNSKI, G.; HULTMAN, L. Referencing to adventitious carbon in x-ray photoelectron spectroscopy: Can differential charging explain c 1s peak shifts? *Applied Surface Science*, Elsevier BV, v. 606, p. 154855, dez. 2022. ISSN 0169-4332. Disponível em: <http://dx.doi.org/10.1016/j.apsusc.2022.154855>. Citado 3 vezes nas páginas 69, 85, and 162.

GUERRA, J. A. et al. Band-fluctuations model for the fundamental absorption of crystalline and amorphous semiconductors: a dimensionless joint density of states analysis. *Journal of Physics D: Applied Physics*, IOP Publishing, v. 52, n. 10, p. 105303, jan. 2019. ISSN 1361-6463. Disponível em: <http://dx.doi.org/10.1088/1361-6463/aaf963>. Citado 4 vezes nas páginas 105, 131, 144, and 164.

GUILLEN-BACA, Y. B. et al. Lattice strain effects on the structural properties and band gap tailoring in columnarly grown fe-doped sno2 films deposited by dc sputtering. *Journal of*

Physics D: Applied Physics, IOP Publishing, v. 52, n. 46, p. 465306, set. 2019. ISSN 1361-6463. Disponível em: <http://dx.doi.org/10.1088/1361-6463/ab3968>. Citado na página 104.

GUILLéN, C.; HERRERO, J. Comparing metal oxide thin films as transparent p-type conductive electrodes. *Materials Research Express*, IOP Publishing, v. 7, n. 1, p. 016411, dez. 2019. ISSN 2053-1591. Disponível em: <http://dx.doi.org/10.1088/2053-1591/ab600e>. Citado na página 34.

GUO, E.-J. et al. Structure and characteristics of ultrathin indium tin oxide films. *Applied Physics Letters*, v. 98, n. 1, p. 011905, 01 2011. Citado 3 vezes nas páginas 13, 125, and 126.

GöKçELI, G.; KARATEPE, N. Investigation of hydrogen post-treatment effect on surface and optoelectronic properties of indium tin oxide thin films. *Journal of Alloys and Compounds*, Elsevier BV, v. 851, p. 156861, jan. 2021. ISSN 0925-8388. Disponível em: <http://dx.doi.org/10.1016/j.jallcom.2020.156861>. Citado 2 vezes nas páginas 70 and 163.

HAFNER, J. Ab-initiosimulations of materials using vasp: Density-functional theory and beyond. *Journal of Computational Chemistry*, Wiley, v. 29, n. 13, p. 2044–2078, jul. 2008. ISSN 1096-987X. Disponível em: <http://dx.doi.org/10.1002/jcc.21057>. Citado na página 64.

HAI-BO, F. et al. Investigation of oxygen vacancy and interstitial oxygen defects in zno films by photoluminescence and x-ray photoelectron spectroscopy. *Chinese Physics Letters*, IOP Publishing, v. 24, n. 7, p. 2108–2111, jun. 2007. ISSN 1741-3540. Disponível em: <http://dx.doi.org/10.1088/0256-307X/24/7/089>. Citado na página 70.

HAMBERG, I. et al. Band-gap widening in heavily sn-doped in_2o_3. *Phys. Rev. B*, American Physical Society, v. 30, p. 3240–3249, Sep 1984. Disponível em: <https://link.aps.org/doi/10.1103/PhysRevB.30.3240>. Citado 2 vezes nas páginas 106 and 108.

HAUFF, E. von. Impedance spectroscopy for emerging photovoltaics. *The Journal of Physical Chemistry C*, American Chemical Society, v. 123, n. 18, p. 11329–11346, May 2019. ISSN 1932-7447. Disponível em: <https://doi.org/10.1021/acs.jpcc.9b00892>. Citado 2 vezes nas páginas 113 and 171.

HERRANZ, G. et al. Weak localization effects in some metallic perovskites. *The European Physical Journal B - Condensed Matter and Complex Systems*, v. 40, n. 4, p. 439–444, Aug 2004. Citado 2 vezes nas páginas 125 and 126.

HOHENBERG, P.; KOHN, W. Inhomogeneous electron gas. *Physical Review*, American Physical Society (APS), v. 136, n. 3B, p. B864–B871, nov. 1964. ISSN 0031-899X. Disponível em: <http://dx.doi.org/10.1103/PhysRev.136.B864>. Citado 2 vezes nas páginas 64 and 118.

HSU, C.-M. et al. Preparation and characterization of ni–indium tin oxide cosputtered thin films for organic light-emitting diode application. *Thin Solid Films*, Elsevier BV, v. 474, n. 1–2, p. 19–24, mar. 2005. ISSN 0040-6090. Disponível em: <http://dx.doi.org/10.1016/j.tsf.2004.08.005>. Citado na página 45.

HUANG, T. et al. Ion behavior impact on ito thin film fabrication via dc magnetron sputtering with external anode. *Vacuum*, Elsevier BV, v. 221, p. 112848, mar. 2024. ISSN 0042-207X. Disponível em: <http://dx.doi.org/10.1016/j.vacuum.2023.112848>. Citado na página 31.

HUAYHUA, C. A. V. *Efeitos produzidos pelo tratamento térmico nas propriedades estruturais, morfológicas, ópticas, elétricas e sensoriais de filmes de In_2O_3 dopados com Sn*. 2022. <https://repositorio.unb.br/handle/10482/43284>. Citado 2 vezes nas páginas 13 and 127.

HUAYHUA, C. A. V. et al. Tuning the structural, electrical, and optical properties of ito thin films via thickness control and vacuum annealing. *Materials Today Communications*, Elsevier BV, v. 48, p. 113605, set. 2025. ISSN 2352-4928. Disponível em: <http://dx.doi.org/10.1016/j.mtcomm.2025.113605>. Citado 11 vezes nas páginas 31, 40, 45, 72, 74, 90, 140, 142, 146, 163, and 166.

IRVINE, J. T. S.; SINCLAIR, D. C.; WEST, A. R. Electroceramics: Characterization by impedance spectroscopy. *Advanced Materials*, Wiley, v. 2, n. 3, p. 132–138, mar. 1990. ISSN 1521-4095. Disponível em: <http://dx.doi.org/10.1002/adma.19900020304>. Citado na página 169.

JACKSON, J. D. *Classical electrodynamics*. [S.l.]: John Wiley & Sons, 2021. Citado na página 49.

KARAZHANOV, S. Z. et al. Phase stability, electronic structure, and optical properties of indium oxide polytypes. *Physical Review B*, American Physical Society (APS), v. 76, n. 7, ago. 2007. ISSN 1550-235X. Disponível em: <http://dx.doi.org/10.1103/PhysRevB.76.075129>. Citado na página 133.

KAUSHIK, D. K.; KUMAR, K. U.; SUBRAHMANYAM, A. Metal-insulator transition in tin doped indium oxide (ito) thin films: Quantum correction to the electrical conductivity. *AIP Advances*, AIP Publishing, v. 7, n. 1, jan. 2017. ISSN 2158-3226. Disponível em: <http://dx.doi.org/10.1063/1.4974157>. Citado 4 vezes nas páginas 13, 45, 125, and 126.

KAUSHIK, D. K.; KUMAR, K. U.; SUBRAHMANYAM, A. Metal-insulator transition in tin doped indium oxide (ito) thin films: Quantum correction to the electrical conductivity. *AIP Advances*, v. 7, n. 1, p. 015109, 01 2017. Citado na página 126.

KHAN, A. et al. Structural, optical and electrical transport properties of sn doped in2o3. *Solid State Sciences*, Elsevier BV, v. 109, p. 106436, nov. 2020. ISSN 1293-2558. Disponível em: <http://dx.doi.org/10.1016/j.solidstatesciences.2020.106436>. Citado 6 vezes nas páginas 10, 34, 73, 127, 166, and 168.

KHAN, A. et al. Role of deposition temperature and sn content on structural, optical & electrical properties of in2o3 thin films. *Current Applied Physics*, Elsevier BV, v. 38, p. 49–58, jun. 2022. ISSN 1567-1739. Disponível em: <http://dx.doi.org/10.1016/j.cap.2022.03.004>. Citado 4 vezes nas páginas 10, 30, 73, and 166.

KHAN, M. M. et al. Structural and optical properties of in2o3 nanostructured thin film. *Materials Letters*, v. 79, p. 119–121, 2012. ISSN 0167-577X. Disponível em: <https://www.sciencedirect.com/science/article/pii/S0167577X12004715>. Citado 3 vezes nas páginas 12, 105, and 107.

KIM, J.-H. et al. The effects of film thickness on the electrical, optical, and structural properties of cylindrical, rotating, magnetron-sputtered ito films. *Applied Surface Science*, Elsevier BV, v. 440, p. 1211–1218, maio 2018. ISSN 0169-4332. Disponível em: <http://dx.doi.org/10.1016/j.apsusc.2018.01.318>. Citado na página 31.

KIM, S. et al. Free-carrier absorption and burstein–moss shift effect on quantum efficiency in heterojunction silicon solar cells. *Vacuum*, v. 108, p. 39–44, 2014. ISSN 0042-207X. Citado na página 148.

KIM, T.-H. et al. Influence of substrate temperature and o2 flow on the properties of rf-magnetron-sputtered indium-tin-oxide thin films. *Journal of The Korean Physical Society - J KOREAN PHYS SOC*, v. 51, 08 2007. Citado na página 140.

KITAGAWA, S.; NAKAMURA, T. Effect of crystallinity on magnetic properties in manganese-doped indium tin oxide films. In: *2023 IEEE International Magnetic Conference (INTERMAG)*. IEEE, 2023. v. 294, p. 1–5. Disponível em: <http://dx.doi.org/10.1109/INTERMAG50591.2023.10265075>. Citado 2 vezes nas páginas 32 and 36.

KITAGAWA, S.; NAKAMURA, T. Carrier concentration dependence of optical and magnetic properties in epitaxial manganese-doped indium tin oxide films with different manganese concentrations. *Current Applied Physics*, Elsevier BV, v. 69, p. 60–69, jan. 2025. ISSN 1567-1739. Disponível em: <http://dx.doi.org/10.1016/j.cap.2024.11.008>. Citado 4 vezes nas páginas 15, 32, 153, and 154.

KLEIN, J. et al. Limitations of the tauc plot method. *Advanced Functional Materials*, Wiley, v. 33, n. 47, set. 2023. ISSN 1616-3028. Disponível em: <http://dx.doi.org/10.1002/adfm.202304523>. Citado na página 144.

KOC, M.; KALELI, M.; ÖZTÜRK, M. Effect of nitrogen flow rate during annealing on structural and electro-optical properties of ito thin films deposited by ultrasonic spray pyrolysis. *Arabian Journal for Science and Engineering*, Springer Science and Business Media LLC, v. 47, n. 6, p. 7707–7716, jan. 2022. ISSN 2191-4281. Disponível em: <http://dx.doi.org/10.1007/s13369-021-06553-z>. Citado na página 30.

KOCH, R. The intrinsic stress of polycrystalline and epitaxial thin metal films. *Journal of Physics: Condensed Matter*, IOP Publishing, v. 6, n. 45, p. 9519, 1994. Citado na página 104.

KOHN, W.; SHAM, L. J. Self-consistent equations including exchange and correlation effects. *Physical Review*, American Physical Society (APS), v. 140, n. 4A, p. A1133–A1138, nov. 1965. ISSN 0031-899X. Disponível em: <http://dx.doi.org/10.1103/PhysRev.140.A1133>. Citado 2 vezes nas páginas 64 and 118.

KRESSE, G.; FURTHMüLLER, J. Efficient iterative schemes forab initiototal-energy calculations using a plane-wave basis set. *Physical Review B*, American Physical Society (APS), v. 54, n. 16, p. 11169–11186, out. 1996. ISSN 1095-3795. Disponível em: <http://dx.doi.org/10.1103/physrevb.54.11169>. Citado 2 vezes nas páginas 64 and 119.

KUMAR, M. et al. Carrier concentration dependence of donor activation energy in n-type gan epilayers grown on si (111) by plasma-assisted mbe. *Materials Research Bulletin*, v. 47, n. 6, p. 1306–1309, 2012. ISSN 0025-5408. Disponível em: <https://www.sciencedirect.com/science/article/pii/S0025540812001316>. Citado na página 150.

KUMAR, N.; SHUKLA, R.; SRIVASTAVA, A. Faster photoswitching and amplified nbe emission from mg doped sol-gel derived zno thin films. *Materials Technology*, Informa UK Limited, v. 39, n. 1, jan. 2024. ISSN 1753-5557. Disponível em: <http://dx.doi.org/10.1080/10667857.2023.2296182>. Citado na página 77.

LEE, H. et al. Strong dependence of photocurrent on illumination-light colors for zno/graphene schottky diode. *Current Applied Physics*, Elsevier BV, v. 17, n. 4, p. 552–556, abr. 2017. ISSN 1567-1739. Disponível em: <http://dx.doi.org/10.1016/j.cap.2017.02.001>. Citado na página 53.

LI, Q. et al. Defects evolution and their impacts on conductivity of indium tin oxide thin films upon thermal treatment. *Journal of Applied Physics*, AIP Publishing, v. 118, n. 2, jul. 2015. ISSN 1089-7550. Disponível em: <http://dx.doi.org/10.1063/1.4923392>. Citado 4 vezes nas páginas 106, 116, 139, and 170.

LIKHACHEV, D.; MALKOVA, N.; POSLAVSKY, L. Modified tauc–lorentz dispersion model leading to a more accurate representation of absorption features below the bandgap. *Thin Solid Films*, Elsevier BV, v. 589, p. 844–851, ago. 2015. ISSN 0040-6090. Disponível em: <http://dx.doi.org/10.1016/j.tsf.2015.07.035>. Citado 2 vezes nas páginas 47 and 164.

LIN, B.-T. et al. Temperature dependence of resistance and thermopower of thin indium tin oxide films. *Thin Solid Films*, v. 518, n. 23, p. 6997–7001, 2010. ISSN 0040-6090. Citado 3 vezes nas páginas 13, 125, and 126.

LIU, T. et al. Nano cone ito thin films prepared by pulsed laser deposition for surface measurement of high-temperature components. *Journal of Alloys and Compounds*, Elsevier BV, v. 959, p. 170538, out. 2023. ISSN 0925-8388. Disponível em: <http://dx.doi.org/10.1016/j.jallcom.2023.170538>. Citado na página 30.

LLONTOP, P. et al. Indirect excitation and luminescence activation of tb doped indium tin oxide and its impact on the host's optical and electrical properties. *Journal of Physics D: Applied Physics*, IOP Publishing, v. 55, n. 21, p. 210002, feb 2022. Disponível em: <https://doi.org/10.1088/1361-6463/ac52fc>. Citado 2 vezes nas páginas 105 and 108.

LU, W. et al. Influences of vacuum annealing induced oxygen defects on the transfer characteristics of a-ito thin-film transistors. *Materials Letters*, Elsevier BV, v. 311, p. 131565, mar. 2022. ISSN 0167-577X. Disponível em: <http://dx.doi.org/10.1016/j.matlet.2021.131565>. Citado na página 30.

MADRIGAL-DIAZ, S. d. C. et al. Synthesis and characterization of ito films via forced hydrolysis for surface functionalization of pet sheets. *Coatings*, MDPI AG, v. 16, n. 1, p. 120, jan. 2026. ISSN 2079-6412. Disponível em: <http://dx.doi.org/10.3390/coatings16010120>. Citado na página 30.

MAGAR, H. S.; HASSAN, R. Y. A.; MULCHANDANI, A. Electrochemical impedance spectroscopy (eis): Principles, construction, and biosensing applications. *Sensors*, MDPI AG, v. 21, n. 19, p. 6578, out. 2021. ISSN 1424-8220. Disponível em: <http://dx.doi.org/10.3390/s21196578>. Citado na página 41.

MAIER, S. A. et al. *Plasmonics: fundamentals and applications*. [S.l.]: Springer, 2007. v. 1. Citado na página 40.

MAJUMDAR, H. S. et al. Ferromagnetism in indium tin-oxide (ito) electrodes at room temperature. *Synthetic Metals*, Elsevier BV, v. 160, n. 3–4, p. 303–306, fev. 2010. ISSN 0379-6779. Disponível em: <http://dx.doi.org/10.1016/j.synthmet.2009.04.010>. Citado na página 35.

MAREZIO, M. Refinement of the crystal structure of in2o3 at two wavelengths. *Acta Crystallographica*, International Union of Crystallography (IUCr), v. 20, n. 6, p. 723–728, nov. 1966. ISSN 0365-110X. Disponível em: <http://dx.doi.org/10.1107/S0365110X66001749>. Citado 6 vezes nas páginas 36, 65, 87, 104, 120, and 160.

MARKOV, L. et al. Formation of the structured indium tin oxide films by magnetron sputtering. *Thin Solid Films*, Elsevier BV, v. 774, p. 139848, jun. 2023. ISSN 0040-6090. Disponível em: <http://dx.doi.org/10.1016/j.tsf.2023.139848>. Citado na página 30.

MATSUMOTO, Y. et al. Room-temperature ferromagnetism in transparent transition metal-doped titanium dioxide. *Science*, American Association for the Advancement of Science (AAAS), v. 291, n. 5505, p. 854–856, fev. 2001. ISSN 1095-9203. Disponível em: <http://dx.doi.org/10.1126/science.1056186>. Citado na página 35.

MATTONI, G. *Metal Insulator Transitions in Heterostructures of Quantum Materials*. Tese (Doutorado) — Delft University of Technology, 2017. Disponível em: <http://resolver.tudelft.nl/uuid:695c7410-ac2d-4fee-879b-2501a0d72421>. Citado na página 44.

MAURI, D. et al. Observation of the exchange interaction at the surface of a ferromagnet. *Physical Review Letters*, American Physical Society (APS), v. 61, n. 6, p. 758–761, ago. 1988. ISSN 0031-9007. Disponível em: <http://dx.doi.org/10.1103/PhysRevLett.61.758>. Citado na página 153.

MOMMA, K.; IZUMI, F. Vesta: a three-dimensional visualization system for electronic and structural analysis. *Journal of Applied Crystallography*, International Union of Crystallography (IUCr), v. 41, n. 3, p. 653–658, maio 2008. ISSN 0021-8898. Disponível em: <http://dx.doi.org/10.1107/S0021889808012016>. Citado 2 vezes nas páginas 65 and 119.

MUGIRANEZA, S.; HALLAS, A. M. Tutorial: a beginner's guide to interpreting magnetic susceptibility data with the curie-weiss law. *Communications Physics*, v. 5, n. 1, p. 95, Apr 2022. ISSN 2399-3650. Disponível em: <https://doi.org/10.1038/s42005-022-00853-y>. Citado na página 152.

MURMU, P. P. et al. Role of phase separation in nanocomposite indium-tin-oxide films for transparent thermoelectric applications. *Journal of Materiomics*, Elsevier BV, v. 7, n. 3, p. 612–620, maio 2021. ISSN 2352-8478. Disponível em: <http://dx.doi.org/10.1016/j.jmat.2020.10.015>. Citado na página 30.

NAJWA, S. et al. In-situ tuning of sn doped in2o3 (ito) films properties by controlling deposition argon/oxygen flow. *Applied Surface Science*, Elsevier BV, v. 479, p. 1220–1225, jun. 2019. ISSN 0169-4332. Disponível em: <http://dx.doi.org/10.1016/j.apsusc.2019.01.123>. Citado 2 vezes nas páginas 31 and 122.

NEUBERT, T. et al. Investigations on oxygen diffusion in annealing processes of non-stoichiometric amorphous indium tin oxide thin films. *Thin Solid Films*, Elsevier BV, v. 513, n. 1–2, p. 319–324, ago. 2006. ISSN 0040-6090. Disponível em: <http://dx.doi.org/10.1016/j.tsf.2006.02.007>. Citado na página 126.

NORTON, D. et al. Ferromagnetism in zno doped with transition metal ions. In: ____. *Zinc Oxide Bulk, Thin Films and Nanostructures*. Elsevier, 2006. p. 555–576. ISBN 9780080447223. Disponível em: <http://dx.doi.org/10.1016/B978-008044722-3/50016-6>. Citado na página 35.

OHNO, T. et al. Magnetic and electric properties of fe-doped ito thin films. *Journal of Magnetism and Magnetic Materials*, Elsevier BV, v. 310, n. 2, p. e717–e719, mar. 2007. ISSN 0304-8853. Disponível em: <http://dx.doi.org/10.1016/j.jmmm.2006.10.781>. Citado 2 vezes nas páginas 32 and 143.

PACHECO-SALAZAR, D. et al. Engineering of the band gap induced by ce surface enrichment in ce-doped sno2 nanocrystals. *Applied Surface Science*, Elsevier, v. 527, p. 146794, 2020. Citado 2 vezes nas páginas 104 and 160.

PARK, K.-S. et al. The effect of the concentration and oxidation state of sn on the structural and electrical properties of indium tin oxide nanowires. *Nanotechnology*, IOP Publishing, v. 22, n. 28, p. 285712, jun. 2011. ISSN 1361-6528. Disponível em: <http://dx.doi.org/10.1088/0957-4484/22/28/285712>. Citado 3 vezes nas páginas 10, 30, and 67.

PAZ-CORRALES, K. J. et al. Tuning intrinsic defects in zno films by controlling the vacuum annealing temperature: an experimental and theoretical approach. *Physica Scripta*, IOP Publishing, v. 97, n. 7, p. 075811, jun. 2022. ISSN 1402-4896. Disponível em: <http://dx.doi.org/10.1088/1402-4896/ac758b>. Citado na página 100.

PELECKIS, G.; WANG, X.; DOU, S. X. High temperature ferromagnetism in ni-doped in2o3 and indium-tin oxide. *Applied Physics Letters*, AIP Publishing, v. 89, n. 2, jul. 2006. ISSN 1077-3118. Disponível em: <http://dx.doi.org/10.1063/1.2220529>. Citado 2 vezes nas páginas 32 and 51.

PERDEW, J. P.; BURKE, K.; ERNZERHOF, M. Generalized gradient approximation made simple. *Physical Review Letters*, American Physical Society (APS), v. 77, n. 18, p. 3865–3868, out. 1996. ISSN 1079-7114. Disponível em: <http://dx.doi.org/10.1103/PhysRevLett.77.3865>. Citado 3 vezes nas páginas 64, 99, and 119.

PFLUG, A. et al. Optical characterization of aluminum-doped zinc oxide films by advanced dispersion theories. *Thin Solid Films*, Elsevier BV, v. 455–456, p. 201–206, maio 2004. ISSN 0040-6090. Disponível em: <http://dx.doi.org/10.1016/j.tsf.2004.01.006>. Citado 6 vezes nas páginas 14, 50, 93, 128, 129, and 142.

PISARKIEWICZ, T.; ZAKRZEWSKA, K.; LEJA, E. Scattering of charge carriers in transparent and conducting thin oxide films with a non-parabolic conduction band. *Thin Solid Films*, Elsevier BV, v. 174, p. 217–223, jul. 1989. ISSN 0040-6090. Disponível em: <http://dx.doi.org/10.1016/0040-6090(89)90892-4>. Citado na página 41.

POLYANSKIY, M. N. Refractiveindex.info database of optical constants. *Scientific Data*, v. 11, n. 1, p. 94, Jan 2024. ISSN 2052-4463. Disponível em: <https://doi.org/10.1038/s41597-023-02898-2>. Citado 3 vezes nas páginas 19, 143, and 144.

RAMAIAH, K. S. et al. Optical, structural and electrical properties of tin doped indium oxide thin films prepared by spray-pyrolysis technique. *Semiconductor Science and Technology*, IOP Publishing, v. 15, n. 7, p. 676–683, jun. 2000. ISSN 1361-6641. Disponível em: <http://dx.doi.org/10.1088/0268-1242/15/7/305>. Citado na página 40.

RAMANATHAN, R. et al. Facile surface modification process of sn-doped in2o3 electron transport layer for enhanced perovskite solar cell performance. *Solar Energy Materials and Solar Cells*, Elsevier BV, v. 284, p. 113481, jun. 2025. ISSN 0927-0248. Disponível em: <http://dx.doi.org/10.1016/j.solmat.2025.113481>. Citado na página 30.

REN, Y. et al. The key of ito films with high transparency and conductivity: Grain size and surface chemical composition. *Journal of Alloys and Compounds*, v. 893, p. 162304, 2022. ISSN 0925-8388. Disponível em: <https://www.sciencedirect.com/science/article/pii/S0925838821037142>. Citado 4 vezes nas páginas 106, 107, 116, and 125.

REY, G. et al. Electron scattering mechanisms in fluorine-doped sno2 thin films. *Journal of Applied Physics*, AIP Publishing, v. 114, n. 18, nov. 2013. ISSN 1089-7550. Disponível em: <http://dx.doi.org/10.1063/1.4829672>. Citado na página 40.

RUSKE, F. et al. Optical modeling of free electron behavior in highly doped zno films. *Thin Solid Films*, v. 518, n. 4, p. 1289–1293, 2009. ISSN 0040-6090. Transparent Conductive Oxides. Disponível em: <https://www.sciencedirect.com/science/article/pii/S0040609009007470>. Citado na página 109.

SAHAI, A.; GOSWAMI, N. Probing the dominance of interstitial oxygen defects in zno nanoparticles through structural and optical characterizations. *Ceramics International*, v. 40, n. 9, Part B, p. 14569–14578, 2014. ISSN 0272-8842. Disponível em: <https://www.sciencedirect.com/science/article/pii/S0272884214009353>. Citado na página 70.

SALES, M. P. *Modelamiento de las Propiedades Óptico-Eléctricas de Películas Delgadas de Óxido de Indio Dopado con Estaño: Una Evaluación Crítica*. 2022. Citado 4 vezes nas páginas 49, 50, 74, and 130.

SANTOS, A. R. d. *Análise por impedância eletroquímica "on-line" de conjuntos eletrodo/membrana (MEA) de células a combustível a membrana polimérica (PEMFC)*. Tese (Doutorado) — Universidade de Sao Paulo, Agencia USP de Gestao da Informacao Academica (AGUIA), 2007. Disponível em: <http://dx.doi.org/10.11606/T.85.2007.tde-16052012-093213>. Citado na página 43.

SATO, K. S. K.; KATAYAMA-YOSHIDA, H. K.-Y. H. Stabilization of ferromagnetic states by electron doping in fe-, co-or ni-doped zno. *Japanese Journal of Applied Physics*, IOP Publishing, v. 40, n. 4A, p. L334, 2001. Citado na página 52.

SATO, Y. et al. Carrier density dependence of optical band gap and work function in sn-doped in2o3films. *Applied Physics Express*, IOP Publishing, v. 3, n. 6, p. 061101, jun. 2010. ISSN 1882-0786. Disponível em: <http://dx.doi.org/10.1143/APEX.3.061101>. Citado 2 vezes nas páginas 10 and 73.

SHANKER, G. S. et al. Doping controls plasmonics, electrical conductivity, and carrier-mediated magnetic coupling in fe and sn codoped in2o3 nanocrystals: Local structure is the key. *Chemistry of Materials*, American Chemical Society (ACS), v. 27, n. 3, p. 892–900, jan. 2015. ISSN 1520-5002. Disponível em: <http://dx.doi.org/10.1021/cm5040936>. Citado na página 32.

SHANNON, R. Revised effective ionic radii and systematic studies of interatomic distances in halides and chalcogenides. *Acta Cryst*, v. 32, p. 751–767, 01 1976. Citado na página 104.

SHARIKA, E. et al. Factors influencing mobility in ito thin films and the consequent effects on optical and nir surface plasmon resonance properties. *Materials Today: Proceedings*, Elsevier BV, v. 49, p. 2131–2135, 2022. ISSN 2214-7853. Disponível em: <http://dx.doi.org/10.1016/j.matpr.2021.08.325>. Citado 4 vezes nas páginas 30, 40, 75, and 108.

SHEN, L. et al. Effect of fe doping on magnetoresistance and exchange coupling of fe-doped ito films. *Journal of Alloys and Compounds*, Elsevier BV, v. 632, p. 218–221, maio 2015. ISSN 0925-8388. Disponível em: <http://dx.doi.org/10.1016/j.jallcom.2015.01.187>. Citado na página 166.

SHIN, S. et al. Low resistivity indium tin oxide films deposited by unbalanced dc magnetron sputtering. *Thin Solid Films*, Elsevier BV, v. 341, n. 1–2, p. 225–229, mar. 1999. ISSN 0040-6090. Disponível em: <http://dx.doi.org/10.1016/S0040-6090(98)01531-4>. Citado na página 90.

SILVA, V. C. et al. Effect of the working pressure on the structural, morphological, optical, electrical and gas sensor properties of zno films grown by dc magnetron sputtering. *Thin Solid Films*, Elsevier BV, v. 835, p. 140863, fev. 2026. ISSN 0040-6090. Disponível em: <http://dx.doi.org/10.1016/j.tsf.2026.140863>. Citado 4 vezes nas páginas 53, 79, 96, and 173.

SOBRI, M. et al. Effect of annealing on structural, optical, and electrical properties of nickel (ni)/indium tin oxide (ito) nanostructures prepared by rf magnetron sputtering. *Superlattices and Microstructures*, Elsevier BV, v. 70, p. 82–90, jun. 2014. ISSN 0749-6036. Disponível em: <http://dx.doi.org/10.1016/j.spmi.2014.02.010>. Citado na página 45.

SRINIVASAN, C. et al. Measurement of thickness of thin films by the x-ray diffraction method. Jul 1979. Citado na página 123.

STANKIEWICZ, J.; VILLUENDAS, F.; BARTOLOMé, J. Magnetic behavior of sputtered co-doped indium-tin oxide films. *Physical Review B*, American Physical Society (APS), v. 75, n. 23, jun. 2007. ISSN 1550-235X. Disponível em: <http://dx.doi.org/10.1103/PhysRevB.75.235308>. Citado na página 31.

STEIN, T. 2019. See <https://xraytools.com/> for "Absorption Coefficient Calculator". Citado na página 123.

SZMYTKOWSKI, J. The photocurrent quantum efficiency dependence on the applied voltage in organic solar cells. *Semiconductor Science and Technology*, IOP Publishing, v. 22, n. 12, p. 1329–1331, nov. 2007. ISSN 1361-6641. Disponível em: <http://dx.doi.org/10.1088/0268-1242/22/12/016>. Citado na página 54.

SZYMANIEC, M. et al. Scalable fabrication of transparent conductive ito thin films using chemical methods: Optimization of parameters and applications in functional glass technologies. *Journal of Alloys and Compounds*, Elsevier BV, v. 1032, p. 181195, jun. 2025. ISSN 0925-8388. Disponível em: <http://dx.doi.org/10.1016/j.jallcom.2025.181195>. Citado na página 30.

TAYLOR, S. R.; GILEADI, E. Physical Interpretation of the Warburg Impedance. *Corrosion*, v. 51, n. 9, p. 664–671, 09 1995. Citado na página 113.

THIRUMOORTHI, M.; PRAKASH, J. T. J. Structure, optical and electrical properties of indium tin oxide ultra thin films prepared by jet nebulizer spray pyrolysis technique. *Journal of Asian Ceramic Societies*, Taylor & Francis, v. 4, n. 1, p. 124–132, 2016. Citado na página 104.

TIEN, C.-L. et al. Effect of oxygen flow rate on the optical, electrical, and mechanical properties of dc sputtering ito thin films. *Advances in Condensed Matter Physics*, v. 2018, n. 1, p. 2647282, 2018. Disponível em: <https://onlinelibrary.wiley.com/doi/abs/10.1155/2018/2647282>. Citado 2 vezes nas páginas 91 and 123.

TOBY, B. H. R factors in rietveld analysis: How good is good enough? *Powder Diffraction*, v. 21, n. 1, p. 67–70, 2006. Citado na página 139.

TOBY, B. H.; DREELE, R. B. V. Gsas-ii: the genesis of a modern open-source all purpose crystallography software package. *Journal of Applied Crystallography*, International Union of Crystallography (IUCr), v. 46, n. 2, p. 544–549, mar. 2013. ISSN 0021-8898. Disponível em:

<http://dx.doi.org/10.1107/S0021889813003531>. Citado 7 vezes nas páginas 65, 87, 103, 118, 120, 139, and 160.

TOGO, A.; TANAKA, I. First principles phonon calculations in materials science. *Scripta Materialia*, Elsevier BV, v. 108, p. 1–5, nov. 2015. ISSN 1359-6462. Disponível em: <http://dx.doi.org/10.1016/j.scriptamat.2015.07.021>. Citado na página 119.

TORASA, C.; SRITHANACHAI, I. Optimization of electrical and optical properties of ito thin films by annealing in air and nitrogen. *Materials Today: Proceedings*, Elsevier BV, v. 65, p. 2439–2441, 2022. ISSN 2214-7853. Disponível em: <http://dx.doi.org/10.1016/j.matpr.2022.06.073>. Citado na página 31.

TRIPATHI, M. N. et al. First-principles analysis of structural and opto-electronic properties of indium tin oxide. *Journal of Applied Physics*, AIP Publishing, v. 111, n. 10, maio 2012. ISSN 1089-7550. Disponível em: <http://dx.doi.org/10.1063/1.4719980>. Citado na página 65.

TRIPATHY, S. R.; BARAL, S. S. Defect engineering in semiconductor photocatalysts: Enhancing photocatalytic activity for green energy production. *Advanced Energy and Sustainability Research*, Wiley, v. 6, n. 11, maio 2025. ISSN 2699-9412. Disponível em: <http://dx.doi.org/10.1002/aesr.202500110>. Citado na página 37.

VELASQUEZ-ORDOñEZ, J. R. et al. Impact of the thickness on the optical and electronic and structural properties of sputtered cu2s thin films. *Journal of Applied Physics*, v. 135, n. 6, p. 065703, 02 2024. Citado 2 vezes nas páginas 105 and 123.

VENKATESAN, M. et al. Room temperature ferromagnetism in mn- and fe-doped indium tin oxide thin films. *Journal of Applied Physics*, AIP Publishing, v. 103, n. 7, mar. 2008. ISSN 1089-7550. Disponível em: <http://dx.doi.org/10.1063/1.2835476>. Citado na página 32.

VILCA-HUAYHUA, C. et al. Tailoring structural, electrical, and optical properties of ito thin films via vacuum-pressure annealing: An experimental and theoretical study. *Journal of Alloys and Compounds*, Elsevier BV, p. 178909, jan. 2025. ISSN 0925-8388. Disponível em: <http://dx.doi.org/10.1016/j.jallcom.2025.178909>. Citado 19 vezes nas páginas 74, 75, 81, 91, 94, 121, 122, 123, 125, 131, 136, 142, 143, 148, 160, 163, 165, 167, and 171.

VILCA-HUAYHUA, C. et al. Growth and vacuum post-annealing effect on the structural, electrical and optical properties of sn-doped in2o3 thin films. *Thin Solid Films*, Elsevier BV, v. 709, p. 138207, set. 2020. ISSN 0040-6090. Disponível em: <http://dx.doi.org/10.1016/j.tsf.2020.138207>. Citado na página 65.

VYGRANENKO, Y.; LAVAREDA, G. Extended tauc-lorentz model for amorphous materials with non-exponential band tails. *IEEE Electron Device Letters*, Institute of Electrical and Electronics Engineers (IEEE), v. 45, n. 11, p. 2146–2149, nov. 2024. ISSN 1558-0563. Disponível em: <http://dx.doi.org/10.1109/LED.2024.3458392>. Citado na página 47.

WALSH, A. et al. Nature of the band gap of in2o3 revealed by first-principles calculations and x-ray spectroscopy. American Physical Society, 2022. Disponível em: <https://tuprints.ulb.tu-darmstadt.de/id/eprint/21183>. Citado 2 vezes nas páginas 36 and 95.

WALSH, A. et al. Nature of the band gap of in2o3 revealed by first-principles calculations and x-ray spectroscopy. American Physical Society, 2022. Disponível em: <https://tuprints.ulb.tu-darmstadt.de/id/eprint/21183>. Citado 2 vezes nas páginas 75 and 131.

WANG, K. et al. Ito films with different preferred orientations prepared by dc magnetron sputtering. *Optical Materials*, Elsevier BV, v. 134, p. 113040, dez. 2022. ISSN 0925-3467. Disponível em: <http://dx.doi.org/10.1016/j.optmat.2022.113040>. Citado 3 vezes nas páginas 89, 90, and 160.

WANG, V. et al. Vaspkit: A user-friendly interface facilitating high-throughput computing and analysis using vasp code. *Computer Physics Communications*, Elsevier BV, v. 267, p. 108033, out. 2021. ISSN 0010-4655. Disponível em: <http://dx.doi.org/10.1016/j.cpc.2021.108033>. Citado na página 65.

WANG, Y.; ZHANG, C.; DING, G. Fabrication and characterization of ito thin film resistance temperature detector. In: *2016 IEEE International Nanoelectronics Conference (INEC)*. IEEE, 2016. p. 1–2. Disponível em: <http://dx.doi.org/10.1109/INEC.2016.7589456>. Citado na página 90.

WEN, S. et al. Electrical properties of pure in2o3 and sn-doped in2o3 single crystals and ceramics. *Journal of Solid State Chemistry*, Elsevier BV, v. 101, n. 2, p. 203–210, dez. 1992. ISSN 0022-4596. Disponível em: <http://dx.doi.org/10.1016/0022-4596(92)90176-V>. Citado 2 vezes nas páginas 10 and 73.

XING, P.; CHEN, Y.; SUN, S. Effect of sn-doping on the structural, electrical and magnetic properties of (in0.95xsnxfe0.05)2o3films. *Journal of Semiconductors*, IOP Publishing, v. 34, n. 2, p. 023002, fev. 2013. ISSN 1674-4926. Disponível em: <http://dx.doi.org/10.1088/1674-4926/34/2/023002>. Citado na página 32.

XU, W.-J. et al. Defect and doping synergistic optimization for efficient and durable alkaline seawater hydrogen production. *Journal of Colloid and Interface Science*, Elsevier BV, v. 690, p. 137354, jul. 2025. ISSN 0021-9797. Disponível em: <http://dx.doi.org/10.1016/j.jcis.2025.137354>. Citado na página 37.

YAMAGUCHI, M. et al. Characteristics of indium tin oxide thin films prepared using electron beam evaporation. *Thin Solid Films*, Elsevier BV, v. 447–448, p. 115–118, jan. 2004. ISSN 0040-6090. Disponível em: <http://dx.doi.org/10.1016/j.tsf.2003.09.033>. Citado na página 30.

YAN, S. et al. Effects of site occupancy and valence state of fe ions on ferromagnetism in fe-doped in2o3 diluted magnetic semiconductor. *Applied Physics Letters*, AIP Publishing, v. 104, n. 6, fev. 2014. ISSN 1077-3118. Disponível em: <http://dx.doi.org/10.1063/1.4865102>. Citado na página 38.

YOSIDA, K. *Theory of magnetism.: Edition en anglais*. [S.l.]: Springer Science & Business Media, 1996. v. 122. Citado na página 51.

YU, Z. et al. Indium tin oxide as a semiconductor material in efficient p-type dye-sensitized solar cells. *NPG Asia Materials*, v. 8, n. 9, p. e305–e305, Sep 2016. ISSN 1884-4057. Disponível em: <https://doi.org/10.1038/am.2016.89>. Citado na página 144.

ZATSEPIN, D. et al. Bulk in2o3 crystals grown by chemical vapour transport: a combination of xps and dft studies. *Journal of Materials Science Materials in Electronics*, v. 30, p. 18753–18758, 10 2019. Citado na página 86.

ZEGHBROECK, B. J. V. Principles of semiconductor devices. Bart Van Zeghbroeck University of Colorado, CO, 2011. Citado 2 vezes nas páginas 115 and 136.

ZENER, C. Interaction between the d-shells in the transition metals. ii. ferromagnetic compounds of manganese with perovskite structure. *Physical Review*, APS, v. 82, n. 3, p. 403, 1951. Citado na página 52.

ZHAO, M.-J. et al. Effect of power density on compositional and structural evolution of ito thin film by hipims method. *Vacuum*, Elsevier BV, v. 200, p. 111034, jun. 2022. ISSN 0042-207X. Disponível em: <http://dx.doi.org/10.1016/j.vacuum.2022.111034>. Citado na página 86.

ZHENG, J. et al. Efficient monolithic perovskite–si tandem solar cells enabled by an ultra-thin indium tin oxide interlayer. *Energy & Environmental Science*, Royal Society of Chemistry (RSC), v. 16, n. 3, p. 1223–1233, 2023. ISSN 1754-5706. Disponível em: <http://dx.doi.org/10.1039/d2ee04007g>. Citado na página 30.

ZHENG, J. et al. Design and fabrication of indium tin oxide for high performance electro-optic modulators at the communication wavelength. *Optical Materials*, v. 148, p. 114931, 2024. ISSN 0925-3467. Disponível em: <https://www.sciencedirect.com/science/article/pii/S0925346724001083>. Citado na página 142.

ZHOU, T. et al. Effects of sn doping on the morphology and properties of fe-doped in2o3 epitaxial films. *Nanoscale Research Letters*, Springer Science and Business Media LLC, v. 7, n. 1, nov. 2012. ISSN 1556-276X. Disponível em: <http://dx.doi.org/10.1186/1556-276X-7-661>. Citado na página 32.

ZHU, B. et al. Combined effects of substrate temperature and film thickness on structure and optical-electrical properties of ito films prepared by rf magnetron sputtering. *Materials Chemistry and Physics*, Elsevier BV, v. 357, p. 132375, jun. 2026. ISSN 0254-0584. Disponível em: <http://dx.doi.org/10.1016/j.matchemphys.2026.132375>. Citado na página 31.

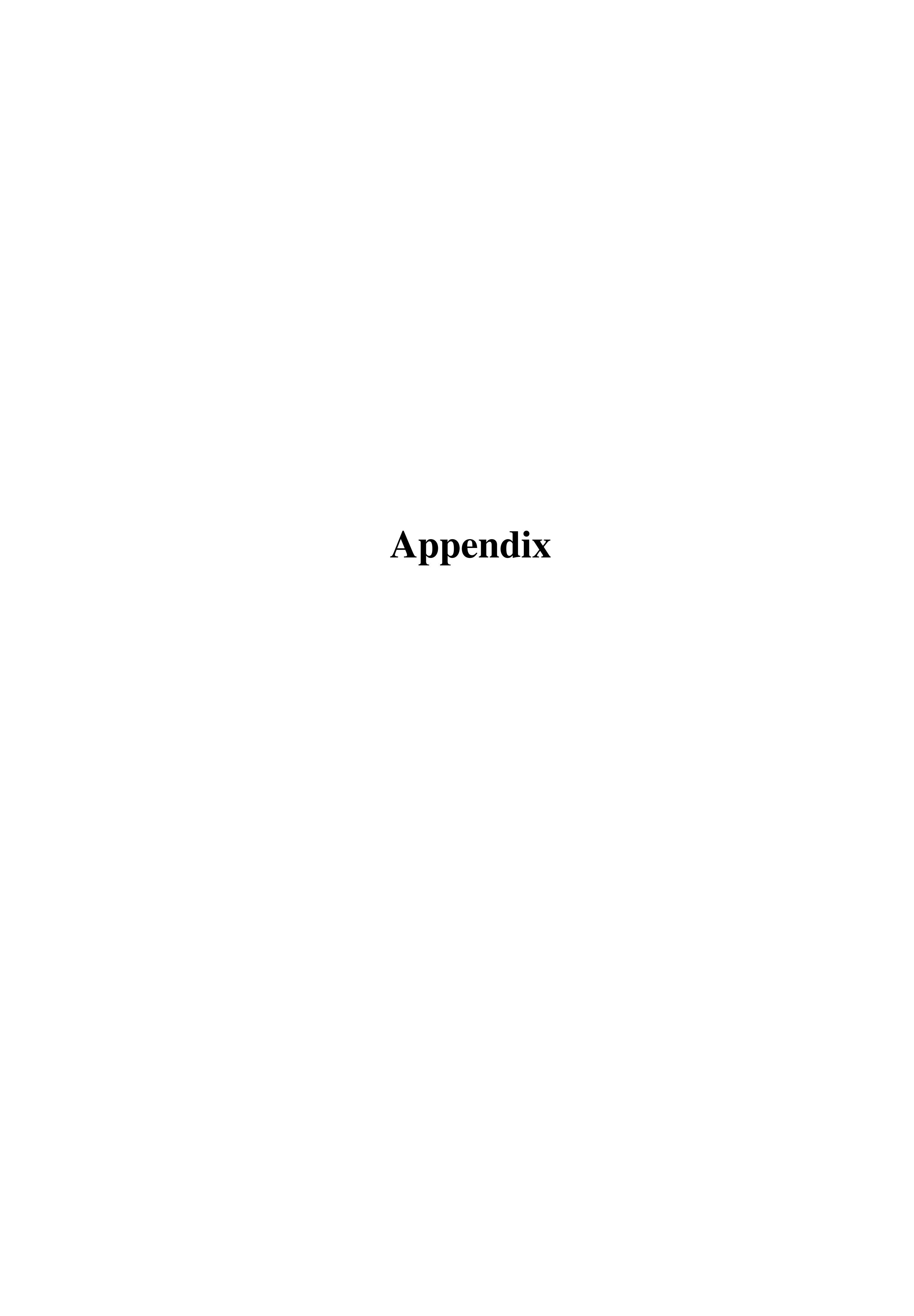

Appendix

APPENDIX A – Articles published within the context of this thesis

Journal of Alloys and Compounds 1017 (2025) 178909

Contents lists available at ScienceDirect

Journal of Alloys and Compounds

journal homepage: www.elsevier.com/locate/jalcom

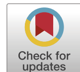

Tailoring structural, electrical, and optical properties of ITO thin films via vacuum-pressure annealing: An experimental and theoretical study

C.A. Vilca-Huayhua [a], S. Mishra [b], M.A.R. Martinez [a], J.A. Guerra [b], L. Villegas-Lelovsky [c], F.F.H. Aragón [a,b,*], J.A.H. Coaquira [a]

[a] Núcleo de Física Aplicada, Instituto de Física, Universidade de Brasília, Brasília, DF 70910-900, Brazil
[b] Departamento de Ciencias, Sección Física, Pontificia Universidad Católica del Perú, Av. Universitaria 1801, San Miguel, Lima 32, Peru
[c] Departamento de Física, IGCE, Universidade Estadual Paulista, Rio Claro, SP 13506-900, Brazil

ARTICLE INFO

Keywords:
Sn-doped In_2O_3 (ITO) thin films
Thermal annealing
Burstein-Moss effect
Carrier concentration
Oxygen vacancies
Optoelectronic applications

ABSTRACT

This study explores the structural, optical, and electronic properties of polycrystalline Sn-doped In_2O_3 (ITO) thin films deposited via DC sputtering method and annealed at 600° C for 2 h under different vacuum pressures (VPs) ranging from 1 to 10^{-6} mbar. The bandgap energy increases from 3.8 eV to 4.1 eV with the vacuum, driven by the Burstein-Moss effect, accompanied by the reduction of Urbach energy, crystallinity improvement and reduction of disorder. This reduction is likely due to enhanced migration of interstitial oxygen ions with vacuum during the annealing. The electrical resistivity decreases significantly when the carrier concentration increases, meanwhile, the effective mass increases (from 0.3 to $0.5m_e$), which is linked to a transition from parabolic to non-parabolic density of states. Near-infrared optical analysis reveals higher optical mobility than Hall mobility, particularly in samples annealed under lower vacuum, which was assigned to the predominant grain boundary scattering process. Photocurrent generation correlates with photoabsorption, Urbach energy, and crystallite size, which decrease as the vacuum is increased. Impedance analysis shows a reduction of the resistance and inductance, with an increase of the capacitance and carrier concentration with the vacuum of the annealing. DFT calculations confirm oxygen vacancies enhance charge density and widen the bandgap, aligning with experimental findings. These results highlight the role of oxygen vacancies in tuning ITO properties for optoelectronic applications.

1. Introduction

Technologies composed of thin films based on transparent conductive oxides (TCOs) are currently attracting great interest, mainly due to their attractive properties, ideal for constructing various optoelectronic devices [1]. It is known that In_2O_3 when doped with Sn (ITO) presents the characteristic of possessing low electrical resistivity with $\backsim 10^{-4}$ ohm-cm whilst maintaining a high optical transmittance in the visible spectrum. These properties together lead to applications in surface plasmon resonance [2], transistors [3], thermoelectric [4], solar cells [5], gas sensors [6], among other. There are several methods of obtaining these materials, such as DC sputtering [7], electron beam evaporation [8], pulsed laser [9], ultrasonic spray pyrolysis [10]. Understanding the microstructure of ITO is fundamental, as it depends on the manufacturing technique, conditions and growth parameters such as deposition temperature and oxygen pressure [11]. The sputtering pressure and post-deposition thermal treatments under vacuum conditions play a crucial role in the sputtering technique, significantly enhancing the electrical and optical properties [12]. Meanwhile, to the best of our knowledge, the effect of post-thermal annealing change the vacuum pressure has not been explored in the literature. This process could have a significant impact on the electrical properties, as the low oxygen environments may promote the formation of oxygen vacancies (defects engineering). In the present work, we aim to investigate this phenomenon in detail, analyzing how variations in vacuum pressure during annealing impact the structural, electrical, and optical properties of the films. Having control of vacuum pressures during film growth or annealing leads to the generation of oxygen vacancies V_O or modification of defects complexes, which act as donor defects in the ITO structure, thereby increasing the concentration of electronic charge carriers. Furthermore, the formation of oxygen vacancies can be enhanced via post-growth thermal treatments in low oxygen concentration

* Corresponding author at: Núcleo de Física Aplicada, Instituto de Física, Universidade de Brasília, Brasília, DF 70910-900, Brazil.
E-mail address: ffharagon@gmail.com (F.F.H. Aragón).

https://doi.org/10.1016/j.jallcom.2025.178909
Received 2 November 2024; Received in revised form 13 January 2025; Accepted 28 January 2025
Available online 30 January 2025
0925-8388/© 2025 Elsevier B.V. All rights are reserved, including those for text and data mining, AI training, and similar technologies.

Materials Today Communications 48 (2025) 113605

Contents lists available at ScienceDirect

Materials Today Communications

journal homepage: www.elsevier.com/locate/mtcomm

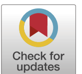

Tuning the structural, electrical, and optical properties of ITO thin films via thickness control and vacuum annealing

Carlos A. Vilca Huayhua [a,*], Bill D. Aparicio Huacarpuma [b], L.A. Ribeiro Junior [b], J.A. Guerra [c], F.F.H. Aragón [a,c,**], J.A.H. Coaquira [a]

[a] LSNCM, Institute of Physics, University of Brasília, Campus Universitario Darcy Ribeiro, Brasília, 70910-900, DF, Brazil
[b] LCCMat, Institute of Physics, University of Brasılia, Brasilia, Campus Universitario Darcy Ribeiro, 70910-900, DF, Brazil
[c] Departamento de Ciencias, Sección Física, Pontificia Universidad Católica del Perú, Av. Universitaria 1801, San Miguel, Lima 32, Peru

ARTICLE INFO

Keywords:
Oxygen vacancies
Interstitials oxygen
Vacuum annealing
Defect engineering
Semiconductor-to-metal transition temperature
DFT calculation

ABSTRACT

This study examines the correlation between vacuum postthermal annealing and film thickness, and their effects on the structural, electrical, and optical properties of tin-doped indium oxide thin films. Vacuum annealing proves to be more effective in thinner films, promoting the diffusion of oxygen atoms and the reduction of interstitial oxygen defects. This oxygen removal critically alters the structural properties, causing changes in the lattice constants and a systematic increase in the texture coefficient along the [400] direction. Electrical measurements reveal that the carrier concentration increases as the film thickness decreases, indicating enhanced oxygen vacancy formation and fewer interstitial oxygens due to annealing. Resistivity versus temperature data show a semiconductor-to-metal transition, with the transition temperature depending on the carrier density. Optical studies indicate band gap widening in thinner films, attributed to increased carrier concentration from vacuum annealing. This behavior is explained by the Burstein–Moss effect, where the upward shift of the Fermi level broadens the optical band gap. These findings are supported by density functional theory calculations, which confirm that the removal of oxygen-related defects modifies the electronic structure, increasing the bandgap, and enhancing the n-type conductivity. Overall, the results highlight how vacuum annealing and film thickness interplay to control defect chemistry and electronic properties in sputtered ITO films.

1. Introduction

Transparent Conductive Oxides (TCO) are widely investigated due to their high transmittance in the visible spectral region and their low electrical resistivity, being attractive for the fabrication of optoelectronic devices [1,2]. Among these materials, indium tin oxide (ITO) stands out for its excellent performance. It is conductivity arises from the degenerated character obtained by the ion substitution of In^{3+} ions with Sn^{4+} which increases the charge carrier shifting the Fermi level to the conduction band enhancing the electrostatic screening and inducing the delocalization of electrons. There are several techniques to deposit ITO thin films, such as magnetron Sputtering [3,4], chemical vapor deposition [5], Sol gel [6], electron beam evaporation [7], spray pyrolysis [8]. Among them, the techniques based on sputtering are the most common for obtaining ITO thin films and are well established in industry, due to their good reproducibility and good control of the growth conditions. Furthermore, although post-deposition thermal annealing in vacuum is commonly used to enhance the crystallinity of ITO thin films and improve their electrical conductivity, the specific influence of the low pressure in a vacuum environment on defect formation and evolution is still not fully understood. In addition, growths under oxygen-deficient conditions cause changes in the preferential orientations in the (222), (400) planes [9,10], which contribute to the change in the ITO microstructure. Additionally, some controversies have been reported regarding the lattice parameter shift in the ITO structure, where they were associated with deformation effects, derived from increased thickness, oxygen deficiency, and a mismatch in the thermal expansion coefficient between the film and substrate [7,11,12]. On the other hand, it is commonly reported that the substitutional introduction of Sn^{4+} ions in place of In^{3+} would cause a reduction in the lattice parameter, due to the smaller ionic radius of Sn^{4+}. However, Gonzalez et al. and Neri et al. observed that the activation of Sn^{4+} charge would result in an increase of the lattice constant due to

* Corresponding authors.
** Correspondence to: Institute of Physics, University of Brasília.
E-mail addresses: cavilcahu@gmail.com (C.A.V. Huayhua), fherrera@unb.br, fherreraa@pucp.edu.pe (F.F.H. Aragón).

https://doi.org/10.1016/j.mtcomm.2025.113605
Received 17 July 2025; Received in revised form 13 August 2025; Accepted 16 August 2025
Available online 26 August 2025
2352-4928/© 2025 Elsevier Ltd. All rights are reserved, including those for text and data mining, AI training, and similar technologies.

APPENDIX B – Articles published outside the context of this thesis

J Mater Sci (2024) 59:16884–16899

Ceramics

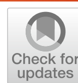

Crystal structure and magnetic properties of the $Y_{2.97}Gd_{0.03}Fe_{5-x}La_xO_{12}$ compound: an experimental and theoretical investigation

M. Gonçalves[1], J. Matilla-Arias[2], J. Penha-Caland[3], C. Vilca-Huayhua[3], J. A. H. Coaquira[3], F. Guerrero[4], Y. Guerra[5], Bartolomeu C. Viana[1,6], and Ramón R. Peña-Garcia[1,7,*]

[1] *Pós-Graduação em Ciência e Engenharia dos Materiais, Universidade Federal do Piauí, Teresina, PI, Brazil*
[2] *Facultad de Ciencias Técnicas, Departamento de Ciencias Básicas e Informática Aplicada, Universidad de Granma, Bayamo, Cuba*
[3] *Instituto de Física, Universidade de Brasília, Brasilia, DF, Brazil*
[4] *Departamento de Física, Universidade Federal do Amazona, Manaus, AM, Brazil*
[5] *Instituto de Física, Universidade Federal de Alagoas, Maceió, AL, Brazil*
[6] *Departamento de Física, Universidade Federal do Piauí, Teresina, PI, Brazil*
[7] *Unidade Acadêmica do Cabo de Santo Agostinho, Universidade Federal Rural de Pernambuco, Cabo de Santo Agostinho, PE, Brazil*

Received: 23 July 2024
Accepted: 5 September 2024
Published online: 14 September 2024

© The Author(s), under exclusive licence to Springer Science+Business Media, LLC, part of Springer Nature, 2024

ABSTRACT

In the present work, we have investigated the crystal structure and magnetic properties of the $Y_{2.97}Gd_{0.03}Fe_{5-x}La_xO_{12}$ (Gd-La co-doped YIG) compound ($0.00 \leq x \leq 0.05$) obtained by the citrate sol–gel method. Rietveld refinement of the X-ray diffraction patterns provided the lattice parameter (a) values, which increased from 12.387(2) to 12.468(2) Å as the La^{3+} content increased. Raman measurements confirmed the single-phase formation, whereas transmission electron microscopy (TEM) revealed elongated and irregular particles. The Mössbauer spectroscopy confirmed the presence of Fe^{3+} and Fe^{2+} cations and the coexistence of Fe^{2+} and La^{3+} cations in the octahedral and tetrahedral sites. Nonetheless, using a phenomenological model, it was suggested that the Fe^{2+} and La^{3+} ions tend to occupy preferentially the octahedral sites in the YIG structure. Further, the correspondence between the experimental and theoretically predicted saturation magnetization values indicated that the compound stoichiometry can be described by the chemical formula ${Y^{3+}}_{2.97}{Gd^{3+}}_{0.03}{Fe^{3+}}_{5-x-y}{La^{3+}}_x{Fe^{2+}}_y{O^{2-}}_{12-y/2}$. Magnetic parameters such as saturation magnetization, anisotropy constant, remanent magnetization, and coercive field values were computed and discussed as a function of cations distribution in the YIG crystal structure.

Handling Editor: David Cann.

Address correspondence to E-mail: rraudelp@gmail.com; ramon.raudel@ufrpe.br

Journal of Alloys and Compounds 1014 (2025) 178681

Contents lists available at ScienceDirect

Journal of Alloys and Compounds

journal homepage: www.elsevier.com/locate/jalcom

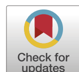

Influence of the thickness effect on the structural, morphological, vibrational, optical, electrical and gas sensor properties of polycrystalline CuO films

B.D. Aparicio-Huacarpuma [a,*], C.A. Vilca-Huayhua [a], A. Pandolfo Silveira [b], Sônia Nair Báo [b], S.W. da Silva [c], J.A.H. Coaquira [a]

[a] *LSNCM/NFA, Institute of Physics, Campus Universitário Darcy Ribeiro, University of Brasília, Brasília, DF 70910-900, Brazil*
[b] *Laboratory of Microscopy and Microanalysis, Department of Cell Biology, Institute of Biological Sciences, University of Brasília, Brasília, DF 70910-900, Brazil*
[c] *Institute of Physics, Campus Universitário Darcy Ribeiro, University of Brasília, Brasília, DF 70910-900, Brazil*

ARTICLE INFO

Keywords:
Polycrystalline CuO films
Film thickness effects
Crystal size effects
DC sputtering
Methane gas sensor

ABSTRACT

Polycrystalline CuO films with different thickness were successfully produced by the DC magnetron sputtering technique and subsequent thermal annealing at 500°C in air atmosphere. The formation of the monoclinic phase was confirmed via XRD data analysis in consistency with Raman spectroscopy. Furthermore, larger residual strain was determined for the thinner film, which was assigned to the occurrence of strong tensile strain related to structural disorder likely coming from the film/substrate interface region. That resulting strain goes to relaxations as the film thickness increases. The positions of the Raman modes determined for the thinner film show a blueshift to values expected for bulk CuO as the thickness increases. Cross-sectional SEM micrographs indicate that the film thickness ranges from 256 to 1230 nm. UV-Vis spectroscopy revealed that the optical band gap and Urbach energy decreases with increasing thickness which was attributed to the relaxation of the tensile strain as the film thickness increases. Additionally, methane gas sensitivity tests at 473 K revealed higher response for the thinner film, which was associated with its smaller grain size (larger surface area), which seems to be the determining parameter in order to improve the sensing response. Our obtained results suggest that CuO films are promising for gas sensing applications.

1. Introduction

Currently, science has allowed great advances in different areas, for example, semiconducting metal oxide nanomaterials are of interest for different applications, due to their low cost and accessible synthesis, non-toxicity, thermal and mechanical stabilities, excellent electrical and electronic properties [1]. In this sense, cupric oxide (CuO) is an intrinsic p-type semiconductor material and, along with other copper oxides, it has been interesting for photothermal or photoconductive applications [2] and in recent times it has been extensively investigated [3,4]. The semiconductor properties of CuO are related to the “Cu” vacancies in the structure, which generate holes and are responsible for electrical conduction [5]. CuO presents a monoclinic structure, with lattice constants a = 4.684 Å, b = 3.425 Å, c = 5.129 Å and angle $\alpha = \gamma = 90^\circ$, $\beta = 99.47^\circ$. CuO is a direct band gap semiconductor that lies in the range of ~ 1.2–1.7 eV [6–8] and could reach 1.9 eV [9] or more depending on its properties.

CuO has the potential to be used in various technological applications such as manufacturing gas sensors [10,11], solar cells [12], manufacturing diodes [13], materials for the production of photoelectrons [14], energy storage [15], catalysts and field emitters [16,17]. Thin or thick CuO films can be obtained by various deposition techniques such as thermal evaporation [6], RF magnetron sputtering [18], spray pyrolysis [19,20], spin-coating [9], SILAR (Successive Ion Layer Adsorption and Reaction) dip coating technique [21], physical vapor deposition [22], sol gel technique [23] and others. Among them, the magnetron sputtering technique presents low cost, great benefit for depositing in large areas, ease and excellent uniformity in obtaining films [24].

Bhowmick and co-workers [25] synthesized CuO film by sol gel spin coating technique, they showed that CuO present a good ethanol and acetone sensing varying the thickness of the film. Gas sensing response

* Corresponding author.
E-mail address: bdaparicioh@gmail.com (B.D. Aparicio-Huacarpuma).

https://doi.org/10.1016/j.jallcom.2025.178681
Received 2 September 2024; Received in revised form 11 January 2025; Accepted 14 January 2025
Available online 17 January 2025
0925-8388/© 2025 Elsevier B.V. All rights are reserved, including those for text and data mining, AI training, and similar technologies.

Article

Tailoring the Properties of Magnetite/PLA Nanocomposites: A Composition-Dependent Study

Mariana Martins de Melo Barbosa [1,*], Juliene Oliveira Campos de França [1], Quezia dos Santos Lima [1], Sílvia Cláudia Loureiro Dias [1], Carlos A. Vilca Huayhua [2], Fermín F. H. Aragón [2,3], José A. H. Coaquira [2,*] and José Alves Dias [1,*]

[1] Laboratório de Catálise, Instituto de Química, Universidade de Brasília, Campus Universitário Darcy Ribeiro, Asa Norte, Brasília 70910-900, DF, Brazil; julienechemistry@gmail.com (J.O.C.d.F.); quezia.sl198@gmail.com (Q.d.S.L.); scdias@unb.br (S.C.L.D.)

[2] Laboratório de Síntese de Nanomateriais e Caracterização Magnética-Núcleo de Física Aplicada, Instituto de Física, Universidade de Brasília, Brasília 70910-900, DF, Brazil; cavilcahu@gmail.com (C.A.V.H.); ffharagon@gmail.com (F.F.H.A.)

[3] Departamento de Ciencias, Sección Física, Pontificia Universidad Católica del Perú, Av. Universitaria 1801, Lima 15088, Peru

* Correspondence: marimm.barbosa@gmail.com (M.M.d.M.B.); coaquira@unb.br (J.A.H.C.); jdias@unb.br or josediasunb@gmail.com (J.A.D.); Tel.: +55-61-3107-7771 (J.A.H.C.); +55-61-3107-3846 (J.A.D.); Fax: +55-61-3107-3900 (J.A.D.)

Abstract: This study focused on composites of magnetite magnetic nanoparticles (MNP) and poly(lactic acid) (PLA) prepared via sonochemical synthesis. The evaluation of MNP loadings (2, 5, 10, 15, and 20 wt.%) provided insights into the structural and reactivity properties of the materials. Methods used included XRD, FT-IR and Raman spectroscopy, SEM and TEM microscopy, textural and thermal analysis (TG and DTA), and magnetic property measurements. The agreement between theoretical and experimental MNP loadings was good. XRD patterns showed predominantly MNP and semicrystalline phases, with a minor maghemite phase detected by FT-Raman and magnetic measurements. FT-IR analysis revealed interactions between MNP and PLA, confirmed by thermal analysis showing higher transition temperatures for the composites (145 °C) compared to pure PLA (139 °C). FT-Raman spectra also indicated that PLA helps prevent iron oxide oxidation, enhancing nanoparticle stability. SEM and TEM micrographs showed well-dispersed, spherical nanoparticles with minimal agglomeration, dependent on MNP loading. The nanocomposites exhibited low N_2 adsorption, resulting in low surface area (~2.1 m^2/g) and porosity (~0.03 cm^3/g). Magnetic analysis indicated that in the 2MNP/PLA sample, MNP were in a superparamagnetic-like regime at 300 K, suggesting good dispersion of 2 wt.% MNP in the PLA matrix.

Keywords: Poly(lactic acid)-PLA; magnetite; magnetic nanoparticles (MNP); nanocomposites MNP/PLA; PLA biocompatible polymer

check for updates

Academic Editor: Aparna Beena Unni

Received: 3 June 2025
Revised: 15 June 2025
Accepted: 16 June 2025
Published: 19 June 2025

Citation: Barbosa, M.M.d.M.; de França, J.O.C.; Lima, Q.d.S.; Dias, S.C.L.; Huayhua, C.A.V.; Aragón, F.F.H.; Coaquira, J.A.H.; Dias, J.A. Tailoring the Properties of Magnetite/PLA Nanocomposites: A Composition-Dependent Study. *Polymers* **2025**, *17*, 1713. https://doi.org/10.3390/polym17121713

Copyright: © 2025 by the authors. Licensee MDPI, Basel, Switzerland. This article is an open access article distributed under the terms and conditions of the Creative Commons Attribution (CC BY) license (https://creativecommons.org/licenses/by/4.0/).

1. Introduction

Poly(lactic acid), or polylactide (PLA), is one of the main bioplastics produced in the world [1]. In 2020, it was reported that 40% of the bioplastics market consisted of common bio-based plastics such as polylactic acid (PLA), polyhydroxyalkanoates (PHA), and thermoplastic starch (TPS) [2]. PLA is used in a variety of applications, including the packaging industry, automotive industry, air filtration, and the biomedical field [3,4]. Since the work of Kulkarni and coworkers [5], who demonstrated the biocompatibility of PLA,

Thin Solid Films 835 (2026) 140863

Contents lists available at ScienceDirect

Thin Solid Films

journal homepage: www.elsevier.com/locate/tsf

Effect of the working pressure on the structural, morphological, optical, electrical and gas sensor properties of ZnO films grown by DC magnetron sputtering

V. Cerqueira Silva [a], Bill D. Aparicio Huacarpuma [b], Carlos A. Vilca Huayhua [a,*], F.F.H. Aragón [a,c,**], J.A.H. Coaquira [a]

[a] LSNCM, Institute of Physics, University of Brasilia, Campus Universitario Darcy Ribeiro, Brasilia, 70910-900, DF, Brazil
[b] LCCMat, Institute of Physics, University of Brasilia, Campus Universitario Darcy Ribeiro, Brasilia, 70910-900, DF, Brazil
[c] Departamento de Ciencias, Sección Física, Pontificia Universidad Católica del Perú, Av. Universitaria 1801, Lima 15088, Peru

ARTICLE INFO

Keywords:
ZnO thin films
Working pressure
Activation energy
Gas sensor
Photocurrent

ABSTRACT

In this work, ZnO thin films were deposited by DC magnetron sputtering under varying working pressures and subsequently annealed in air, followed by vacuum thermal annealing. The increase of working pressure drive to the reduction of the film thickness, crystallite size, lattice constants, and to the strengthening of the (002) X-ray diffraction peak, suggesting changes in the in oxygen vacancy concentration. Scanning electron microscopy revealed the formation of randomly distributed nanorods, while UV–Vis spectroscopy data analysis evidenced the presence of defect-related levels inside the band gap. As the thickness decreases, Hall measurements show a noticeable drop in charge carrier density and mobility, which is linked to the combined impact of defects and the decreasing size of crystallites. This suggests that thicker films exhibited a higher density of zinc interstitials, whereas thinner films exhibit more oxygen vacancies (V_O), mainly associated with surface states, as supported by temperature-dependent resistance measurements and photocurrent analysis. Gas detection tests demonstrated a superior response to methane (CH_4) for thinner films at 200 °C, attributed to their higher oxygen vacancy concentration. Photocurrent and gas sensing measurements showed similar trends, indicating a common defect-driven mechanism. These results highlight the potential of tuning defect chemistry in ZnO films to optimize their performance for gas sensing and optoelectronic devices.

1. Introduction

Nanostructured oxides have played an important role in various fields of chemistry, physics, and materials science. Among these materials, zinc oxide (ZnO), an n-type semiconductor with a bulk energy band gap around 3.37 eV at room temperature [1] is of great interest. ZnO has a hexagonal ($P6_3mc$) wurtzite crystal structure, with lattice constants $a = b = 3.250$ Åand $c = 5.207$ Å [2]. The electrical resistivity can range from $5{\times}10^4$ Ω-cm to $3{\times}10^5$ Ω-cm, [3]. Due to its low cost, non-toxicity, and potential in various optical, electronic, and optoelectronic applications [4], ZnO is a suitable candidate for the manufacturing of solar cells [5], UV devices [6,7], photocatalysts [8,9], and antibacterial materials [10].

ZnO thin films offer several advantages, particularly due to their reduced dimensionality. Confining the material along one axis allows for the modulation of various physical properties, including the structural, morphological, optical, and electrical properties. These tunable properties are not solely intrinsic to ZnO but are also strongly influenced by the fabrication technique employed, which affects the crystallinity, defect concentration, grain orientation, and film morphology [11]. There are several techniques for fabricating thin films. Among which we can mention chemical and physical methods. Chemical approaches include chemical vapor deposition (CVD) [12], the hydrothermal method [13], spray pyrolysis [4], and spin coating [14]. Physical techniques, meanwhile, include thermal evaporation [15], electron beam evaporation [16], and sputtering deposition [6]. The latter technique offers several advantages, including high deposition rates and good reproducibility of the films [17]. Moreover, it allows precise control over various deposition parameters, such as sputtering power, substrate temperature, base pressure (prior to deposition), working pressure (during deposition), and deposition time, enabling the fabrication of films with tailored structural, morphological, and functional properties.

* Corresponding author.
** Corresponding author at: LSNCM, Institute of Physics, University of Brasilia, Campus Universitario Darcy Ribeiro, Brasilia, 70910-900, DF, Brazil.
E-mail addresses: cavilcahu@gmail.com (C.A.V. Huayhua), fherrera@unb.br, fherreraa@pucp.edu.pe (F.F.H. Aragón).

https://doi.org/10.1016/j.tsf.2026.140863
Received 28 September 2025; Received in revised form 7 January 2026; Accepted 13 January 2026
Available online 14 January 2026
0040-6090/© 2026 Elsevier B.V. All rights are reserved, including those for text and data mining, AI training, and similar technologies.

Physica E 177 (2026) 116453

Contents lists available at ScienceDirect

Physica E: Low-dimensional Systems and Nanostructures

journal homepage: www.elsevier.com/locate/physe

Electronic structure and light-harvesting efficiency of Janus XSO (X = Sn, Ge) monolayers

Bill D. Aparicio Huacarpuma [a,b,*], Muhammad Irfan [a,b], Carlos A. Vilca Huayhua [c], Fábio L. Lopes de Mendonça [d], Carlos M.O. Bastos [e], Alexandre C. Dias [e], Luiz A. Ribeiro Junior [a,b]

[a] Institute of Physics, University of Brasília, Brasília, 70910-900, DF, Brazil
[b] Computational Materials Laboratory, LCCMat, Institute of Physics, University of Brasília, Brasília, 70910-900, DF, Brazil
[c] LSNCM, Institute of Physics, University of Brasilia, 70910-900, Brasilia, DF, Brazil
[d] College of Technology, Department of Electrical Engineering, University of Brasilia, 70910-900, Brasilia, Federal District, Brazil
[e] Institute of Physics and International Center of Physics, University of Brasilia, 70910-900, Brasilia, DF, Brazil

ARTICLE INFO

Editor: Ming-Wei Wu

Dataset link: https://vasp.at/, https://github.com/ac-dias/wantibexos, https://vaspkit.com/, https://jp-minerals.org/vesta/en/

Keywords:
2D-materials
DFT
Janus SnSO and GeSO
Exciton
PCE
Solar harvesting

ABSTRACT

The urgent global demand for clean and efficient energy has intensified the search for novel low-dimensional materials with photovoltaic potential. Two-dimensional (2D) materials, particularly Janus materials, are emerging as promising candidates for solar cell applications owing to their electronic properties. However, the literature lacks studies that analyze the impact of excitons on their optical properties and power conversion efficiency (PCE) for such devices. In this work, we perform a comprehensive first-principles investigation of the structural, thermodynamic, electronic, and optical properties of 2D Janus XSO (X = Sn, Ge) monolayers, analyzing the impact of excitonic effects on photovoltaic devices. Both systems are identified as direct-gap semiconductors, with band gaps of 0.86 eV and 0.59 eV at the PBE level, increasing to 1.74 eV and 1.52 eV within the HSE06 functional, respectively. Their optical response, evaluated through a Wannier basis tight-binding Hamiltonian combined with the Bethe–Salpeter equation, reveals pronounced excitonic effects, with binding energies of 315 meV for SnSO and 256 meV for GeSO. The photovoltaic performance, assessed via the Shockley–Queisser limit, yields theoretical power conversion efficiencies of up to 32.46 %. These results demonstrate that 2D Janus SnSO and GeSO monolayers are promising candidates for next-generation solar energy technologies, combining suitable band gaps with intense light–matter interactions.

1. Introduction

The depletion of oil reserves is intensifying the global energy crisis, emphasizing the finite nature of fossil fuel resources. This urgent challenge underscores the need for renewable and environmentally friendly energy alternatives to meet growing energy demands while mitigating environmental impacts [1,2].

Solar cells based on novel two-dimensional (2D) semiconductors have attracted significant attention due to their potential for high power conversion efficiencies (PCE) [3]. Solar radiation, one of the most abundant energy sources, is already harnessed through photovoltaic devices, thermoelectric generators, and solar thermal technologies [4].

Since the discovery of graphene in 2004 [5], its absence of an intrinsic band gap has motivated the search for alternative 2D materials. To overcome this limitation, several material families have been synthesized experimentally and investigated theoretically, including transition-metal dichalcogenides (TMDs) [6–9], hexagonal boron nitride [10,11], 2D carbon allotropes [12–14], MXenes [15–17], phosphorenes [18,19], carbon nitrides [20], and group-IV dichalcogenides [21–24].

The potential of 2D materials has recently been demonstrated across a broad spectrum of applications, including sensors, batteries, catalysis, optoelectronic devices, and solar cells [25,26]. Well-known examples such as MoS_2 [27] and $Ti_3C_2T_x$ [28–30] are already widely employed for these purposes. These materials can also be engineered in Janus form. For example, Janus MoSSe has been successfully synthesized [31], and its asymmetric atomic configuration confers properties that are enhanced relative to conventional non-Janus counterparts [8,32,33]. Beyond MoSSe, other Janus structures have also been investigated, including MoXY (X, Y = S, Se, Te) [34,35], VSeTe [36], SnSSe [37,38], among others [39–41] for energy conversion applications.

Recently, the Janus semiconductor SnSSe, with a band gap of

* Corresponding author.
E-mail address: bdaparicioh@gmail.com (B.D.A. Huacarpuma).

https://doi.org/10.1016/j.physe.2025.116453
Received 9 October 2025; Received in revised form 13 December 2025; Accepted 23 December 2025
Available online 23 December 2025
1386-9477/© 2025 Elsevier B.V. All rights reserved, including those for text and data mining, AI training, and similar technologies.

Computational Condensed Matter 46 (2026) e01213

Contents lists available at ScienceDirect

Computational Condensed Matter

journal homepage: www.elsevier.com/locate/cocom

Excitonic and photovoltaic properties of Janus Sc_2C and Y_2C MXenes from first-principles calculations

Bill D. Aparicio-Huacarpuma [a,b,*], Carlos M.O. Bastos [c], C.A. Vilca Huayhua [a], Alysson M.A. Silva [d], Leander Michels [a,e,f], Alexandre C. Dias [c], Luiz A. Ribeiro Junior [a,b,*]

[a] Institute of Physics, University of Brasília, Brasília, 70910-900, DF, Brazil
[b] Computational Materials Laboratory, LCCMat, Institute of Physics, University of Brasília, Brasília, 70910-900, DF, Brazil
[c] Institute of Physics and International Center of Physics, University of Brasília, 70919-970, Brasília, DF, Brazil
[d] University of Brasilia, College of Technology, Department of Mechanical Engineering, 70910-900, Brasilia, Brazil
[e] Chemical Sciences Division, Lawrence Berkeley National Laboratory, Berkeley, CA 94720, USA
[f] Innovation Department, Elkem Silicon Products (ESP), Fiskåveien 100 4621, Kristiansand, Norway

ARTICLE INFO

Keywords:
Janus MXenes
Density functional theory
Optoelectronic properties
Excitonic effects
Power conversion efficiency

ABSTRACT

Janus MXenes represent a promising class of two-dimensional materials with tunable electronic and optical properties arising from their intrinsic structural asymmetry. Here, we investigate the structural, electronic, excitonic, and photovoltaic properties of Janus Sc_2CTT' and Y_2CTT' monolayers (T = Br, Cl, F; T′ = H), employing density functional theory (DFT) combined with a maximally localized Wannier based tight-binding plus Bethe–Salpeter equation framework. We confirm the stability of these materials using cohesive energies, phonon dispersions, elastic constants, and AIMD simulations. Furthermore, the calculated elastic moduli reveal nearly isotropic mechanical responses. Electronic band structures, obtained with the HSE06 functional, show indirect band gaps in the range of 1.7 eV to 1.9 eV, attributed to strong orbital contributions from transition-metal d states at the conduction band edge. To capture excitonic effects, we apply the Bethe–Salpeter equation, which yields excitonic binding energies up to 0.49 eV, demonstrating robust quasiparticle effects. The optical spectra, as a result, exhibit broad absorption from the visible to ultraviolet regions, along with clear exciton-induced anisotropy. Finally, power conversion efficiencies, evaluated using the Shockley–Queisser and spectroscopy-limited maximum efficiency models, reach values above 32 % for Y-based Janus MXenes. These findings highlight Janus Sc- and Y-based MXenes as stable and efficient candidates for next-generation photovoltaic and optoelectronic devices.

1. Introduction

Two-dimensional (2D) materials such as hexagonal boron nitride [1], black phosphorus [2], graphene [3], and transition-metal dichalcogenides [4–6] (TMDs) have attracted intense interest due to their rich physical properties and wide range of technological applications [7]. Within this class, MXenes compose a large family of transition-metal carbides and nitrides with the general formula $M_{n+1}X_nT_x$ (where M is a transition metal, X is C or N, and T_x represents surface terminations such as O, F, Cl, H, or OH) [8–10], which stand out as versatile candidates for next-generation devices [11,12]. Their tunable surface chemistry, high carrier mobility, and structural robustness have enabled applications in supercapacitors [13], ion batteries [14–17], catalysis [18], sensing [19], and optoelectronics [20].

A subset of these compounds is the so-called *Janus* MXenes [21–23], where asymmetric surface terminations ($T \neq T'$) break out-of-plane symmetry. This broken symmetry can generate intrinsic dipole moments, modify band alignments, and enhance light–matter interactions [24]. As a result, Janus MXenes are expected to exhibit good performance in photocatalysis, spintronics, and solar energy harvesting [25]. Recent studies on halogen-functionalized MXenes (e.g., Sc_2CClF, Y_2CClF) have demonstrated favorable electronic and optical properties, including indirect band gaps below 2 eV and strong absorption in the ultraviolet region [26,27]. Additionally, recent work on 2D materials has investigated the structural, optical, and electronic responses in asymmetric Janus γ-Si_2XY (X/Y = S, Se, Te) monolayers, offering promise for photonics and nanoelectronic applications [28]. However, most previous reports have been limited to

* Corresponding authors.
E-mail addresses: bdaparicioh@gmail.com (B.D. Aparicio-Huacarpuma), ribeirojr@unb.br (L.A.R. Junior).

https://doi.org/10.1016/j.cocom.2026.e01213
Received 28 October 2025; Received in revised form 30 December 2025; Accepted 6 January 2026
Available online 23 January 2026
2352-2143/© 2026 Elsevier B.V. All rights are reserved, including those for text and data mining, AI training, and similar technologies.

Physica B 727 (2026) 418364

Contents lists available at ScienceDirect

Physica B: Condensed Matter

journal homepage: www.elsevier.com/locate/physb

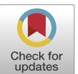

Sintering-temperature effects on cation redistribution and magnetic response of the $Y_{2.97}Gd_{0.03}Fe_{4.97}La_{0.03}O_{12}$ ceramic

M. Gonçalves [a], J. Penha-Caland [b], C. Vilca-Huayhua [b], J.A.H. Coaquira [b], J. Matilla-Arias [c], F. Guerrero [d], Samuel F. Rodrigues [a], Bartolomeu C. Viana [a,e], Ramón R. Peña-Garcia [a,f,*]

[a] Universidade Federal do Piauí, Pós-Graduação em Ciência e Engenharia dos Materiais, Teresina, PI, Brazil
[b] Instituto de Física, Universidade de Brasília, Brasilia, DF, Brazil
[c] Universidad de Granma, Facultad de Ciencias Técnicas, Departamento de Ciencias Básicas e Informática Aplicada, Bayamo, Cuba
[d] Universidade Federal do Amazona, Departamento de Física, Manaus, AM, Brazil
[e] Universidade Federal do Piauí, Departamento de Física, Teresina, PI, Brazil
[f] Universidade Federal Rural de Pernambuco, Unidade Acadêmica do Cabo de Santo Agostinho, Cabo de Santo Agostinho, PE, Brazil

A R T I C L E I N F O

Keywords:
Yttrium iron garnet (YIG)
Sintering temperature
Mössbauer
Magnetic properties

A B S T R A C T

In this work, we report a comprehensive investigation of the influence of sintering temperature (900, 1000, and 1100 °C) on the structural, morphological, and magnetic properties of the $Y_{2.97}Gd_{0.03}Fe_{4.97}La_{0.03}O_{12}$ garnet-type ceramic synthesized by the sol–gel method. Structural refinement confirms the predominance of the garnet phase in all samples and reveals a thermally induced emergence of a $YFeO_3$ secondary phase, quantified as 3.7 % at 1000 °C and 9.9 % at 1100 °C. Increasing the sintering temperature enhances crystallinity, increases the average crystallite size from 45 to 68 nm (≈51 %), and reduces the microstrain by ≈ 33 %. Infrared vibrational analysis shows red shifts in Fe–O stretching modes, indicating bond elongation and local lattice relaxation. Electron microscopy reveals grain growth and reduced porosity at 1000 °C, followed by abnormal coarsening and localized porosity at 1100 °C. Mössbauer spectroscopy demonstrates a temperature-dependent redistribution of Fe^{3+} across octahedral and tetrahedral sublattices and confirms the persistence of Fe^{2+} associated with oxygen-vacancy stabilization. This redistribution governs the magnetic response: the saturation magnetization increases from 15.37 emu g^{-1} (900 °C) to 18.46 emu g^{-1} at 1000 °C (≈20 %), then decreases to 15.27 emu g^{-1} at 1100 °C in parallel with the growth of the secondary phase. Remanent magnetization follows the same trend, whereas the remanent-to-saturation ratio remains nearly constant at ≈0.3, consistent with a multi-domain configuration. Coercivity decreases from 62 to 46 Oe (≈26 %), reflecting grain-size-assisted domain-wall motion. Collectively, these results show that sintering temperature provides a quantitative route to tune structural relaxation, cation redistribution, and magnetic behavior in this co-doped garnet system. The sample sintered at 1000 °C exhibits the most favorable combination of crystallinity, controlled porosity, and maximized magnetization, offering a mechanism-based framework for designing soft-magnetic and microwave-grade ceramics.

1. Introduction

The Yttrium-iron garnet ($Y_3Fe_5O_{12}$ – YIG), recognized for its complex structure, with space group *Ia*3*d* and cubic symmetry, is a multifunctional compound distinguished for its microwave and spintronics applications [1–5]. The YIG crystal structure, organized into three sublattices $\{Y_3^{3+}24c\}[Fe_2^{3+}16a](Fe_3^{3+}24d)O_{12}96h$, facilitates antiferromagnetic coupling between iron ions at distinct crystallographic sites [6–10]. This structural configuration generates unique magnetic behavior, making the YIG a suitable material for several applications [11,12]. Several methodologies have been applied to expand the YIG compound's properties and applications, such as isovalent or heterovalent ion substitutions in the sites occupied by the Fe^{3+} and Y^{3+} ions in the YIG sublattices [13–17]. The 4*f*-5*d* electronic transitions and crystal field interactions, facilitated by metal-ligand bonds, lead to the splitting of energy levels, positioning rare earth cations as strategic dopants [18]. The inclusion of these dopant ions can substantially alter superexchange mechanisms, modify magnetocrystalline anisotropy, and influence the material's overall magnetization [19]. The incorporation of rare-earth as dopant ions into the $Y_3Fe_5O_{12}$ compound has been extensively studied

* Corresponding author. Universidade Federal Rural de Pernambuco, Unidade Acadêmica do Cabo de Santo Agostinho, Cabo de Santo Agostinho, PE, Brazil.
E-mail address: rraudelp@gmail.com (R.R. Peña-Garcia).

https://doi.org/10.1016/j.physb.2026.418364
Received 23 September 2025; Received in revised form 28 January 2026; Accepted 1 February 2026
Available online 3 February 2026
0921-4526/© 2026 The Authors. Published by Elsevier B.V. This is an open access article under the CC BY license (http://creativecommons.org/licenses/by/4.0/).